An experimental Rayleigh laser guide star ground layer adaptive optics system for the William Herschel telescope

T. J. Morris

An Experimental Rayleigh Laser Guide Star Ground Layer Adaptive Optics System for the William Herschel Telescope

T. J. Morris

A Thesis presented for the degree of

Doctor of Philosophy

Centre for Advanced Instrumentation

Department of Physics

University of Durham

September 2005

An Experimental Rayleigh Laser Guide Star Ground Layer Adaptive Optics System for the William Herschel Telescope

T. J. Morris

Submitted for the degree of Doctor of Philosophy

September 2005

Abstract

The design of an experimental ground layer adaptive optics (GLAO) system that uses a low altitude Rayleigh laser guide star as a wavefront reference source is presented. GLAO is a technique for achieving wide-field partial adaptive optics correction of the aberrations in a wavefront due to the effects of propagation through a turbulent atmosphere. The theoretical performance of the GLAO sub-systems, such as the laser launch system, wavefront sensor and optical train are analysed and compared, where possible, to measurements taken both under laboratory conditions and on-sky at the William Herschel Telescope.

Declaration

The work in this thesis is based on research carried out in the Centre for Advanced Instrumentation, the Department of Physics, the University of Durham, United Kingdom. No part of this thesis has been submitted elsewhere for any other degree or qualification and it is all my own work unless referenced to the contrary in the text.

Acknowledgements

I'd like to start off at the beginning by thanking my wonderful girlfriend Becca who has had to put up with me spending all my time over the last year writing this thesis. I would not have been able to write this without you, your constant support and almost infinite patience as I stare night after night at a computer screen. Next I'd like to thank my parents. I couldn't have got here without you! Thanks also to Simon (for getting me interested in telescopes in the first place), Rachel, and especially Joff who has somehow managed to put up with me for all these years without resorting to (too much) violence. Others that have helped me outside of the wonderful world of work, including the mighty Lawson and G'Dave (who found love in the end!).

There has been a large team of people who have helped me over the course of this work, without whom this system would not have made it to the WHT. I'd like to thank all of the ING staff who have helped with this project, especially Tom, Rene, Gordon, Kevin, Doug and Servando. Thanks for giving me the time off to write up too!

Here in Durham, I'd like to thank everyone in the Instrumentation group who has worked on the project. Paul C, thanks for jumping ship to the wonderful world of VISTA, leaving fresh-faced ol' me to run the project and work with that damned laser. Colin, I learnt almost everything I know about optics from watching you set up my newest crazy AO design in a cramped GHRIL enclosure. Chris, our resident programming monkey with a wxPython fetish, I believe the score is 7-6 to me. Tim B, thanks for warning me, and the rest of the world, to the danger that badgers pose to wavefront measurements. Nirmal, for letting me steal shiny new computer kit. And to everyone else who has been happy to help whenever I've discovered some new

problem with the optics/DM/electronics/Laser/Fisba/data* (*delete as appropriate) including Richard W, Nigel, Gordon, Paul B, the two Alis, Graham, Stephen and Francois and all the people who have had to put up with me as an office mate; Harold, Tom, Jason, Tim and Chris.

Finally I'd like to thank my supervisor, Richard Myers, for steering me through the murky waters of LGS AO towards the light. And I saw it was green...

Contents

Chapter 1: Introduction

1.1 Introduction

Telescope design is driven by the desire to observe fainter objects in greater detail. The collecting area of a telescope primary mirror not only determines how many photons that a telescope will capture from a given source, but in theory, also increases the angular resolution with which an object can be imaged. A steady increase in ground-based optical/infrared telescope diameters over the years has resulted in the 8-10m diameter mirrors that are currently in use at locations around the world and the 30-100m diameter mirrors that are being planned. The vast light-collecting power of these telescopes does allow astronomers to view very faint objects, but the resolving power at optical and near infrared wavelengths is still limited by atmospheric turbulence to that of a telescope with a far smaller aperture.

Adaptive Optics (AO) systems are designed to correct wavefront distortions in light that has propagated through a turbulent medium, such as the Earth's atmosphere. Regardless of their application, all AO systems require a method to measure the wavefront distortions present, an adaptive optical element to correct them, and finally a control system linking these two components together. Each stage in this process can be studied and optimised separately, but the overall system design will be determined by the application for which it is intended. Astronomy is one field where AO has been in use for decades, because the turbulent effects of the Earth's atmosphere (referred to as atmospheric 'seeing') causes images of stars to become blurred, resulting in a loss of resolution and hence, scientific information.

It is to counter this loss of information that astronomical AO systems are used, ideally leading to an AO-enabled telescope with a performance not limited by the atmosphere, which we have no control over, but by the optics of the telescope and the performance of the AO system, which can be designed to almost any standard. This thesis describes the design and implementation of an AO system for the 4.2m William Herschel Telescope (WHT) on La Palma in the Canary Islands to give a partial compensation of atmospheric effects over a wide field with high sky coverage. To achieve this aim, a laser guide star (LGS) must be created at a low (~10km) altitude above the observing telescope so that a large percentage of the sky can be observed while still sampling the effect of atmospheric turbulence accurately.

1.2 Project Description

Using a low-altitude LGS to achieve correction over a wide-field has not to date been experimentally demonstrated, and this thesis details the work undertaken to prove this concept on the WHT. To achieve this aim, several modifications to an existing laboratory-based AO system had to be made. There were various constraints placed on this task in terms of budget, available manpower and project timescale which impacted the final design and performance of the fielded system. Specific cases where these constraints have impacted the system design has been indicated at appropriate points throughout the text.

As stated, the primary aim of this work is to demonstrate wide-field AO correction from a low-altitude LGS. As detailed further in chapters 4, 6 and 8, the major critical components, specifically the laser and AO system, had already been purchased and

partially tested. However, integrated designs for the laser launch system and LGS AO system had not progressed past the conceptual/preliminary design phase. Both systems required designing, modelling, integration and optimisation both in the laboratory and on-sky. Software tools for system calibration and control also required development.

The hardware budget to achieve this task was limited to approximately £30K, a value an order of magnitude below systems attempting the same task. This budget had to cover the complete laser launch system, the optics for the redesigned AO system and electronics related to closed-loop control. Little staff effort had been officially allocated to this project, although technical and engineering support was provided for laser launch system construction. A small team of four to five people was taken out during on-sky commissioning primarily to provide software integration with launch system electronics and WFS cameras, and also for optical alignment of the AO system. The software tools and alignment procedures have not been extensively described in this work; as such, unless explicitly stated otherwise, the work described in this thesis was performed solely by the author.

The timeline for this project also injected severe constraints on the order that tasks were undertaken. For example, the design and integration of the AO and laser launch systems were undertaken before the modelling of the LGS and LGS WFS interaction. Constraints such as this were dictated by the allocated telescope time. The project timeline is shown in Table 1.1 and shows the order in which tasks were completed.

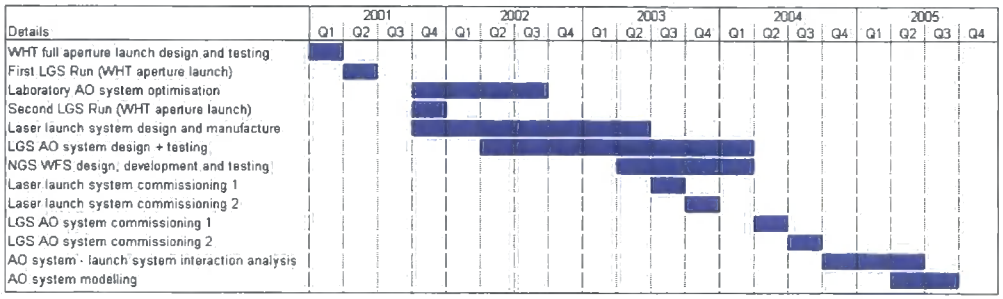

Table 1.1 Prototype Rayleigh LGS project timeline indicating experimental LGS runs at the WHT (light blue) and research and development work carried out in Durham (dark blue). The author of this work joined the project in Q4 '01.

1.3 Project Aims

As stated, this project aims to demonstrate on the WHT, AO correction using a low-altitude LGS as a wavefront reference. Although the ultimate test of the wide-field AO performance would be achieved from imaging a dense star field through the AO system, there are numerous tests that should be undertaken before this step if performance is to be characterised. These tests can be summarised by the following questions:

- How should the launch system perform and does it perform as expected?
- Does this performance provide a stable wavefront reference for the AO system?
- Can the laboratory AO system be modified to use a LGS as a wavefront reference?
- What degree of correction should we observe from the AO system using the LGS, and does it achieve this performance?

If these questions can be answered, the viability of a low-altitude LGS as a wavefront reference for wide-field AO will be confirmed. There are several key steps that must be taken to achieve this aim, and these are summarised in Table 1.2 along with the chapter of this thesis where the problem is studied.

Task	Sub-tasks	Thesis Chapter
Optimise laboratory AO system	Optimise closed-loop performance	8
	Remove static aberrations	6
AO system design	Examine alternative LGS AO system designs	3
	Design AO system	6
	Closed-loop Tip-tilt correction system	6
	Integrate NGS and LGS closed loop systems	6
	Test AO system	6, 8
Launch system design	Examine alternative launch system design	3
	Design launch system	4
	Test launch system	4
System performance estimates	Model launch system	5
	Model AO system	7
	System performance from integrated model	7
Science verification	Define verification tests	4, 6, 8
	Measure launch system performance	4
	Measure AO system performance	8

Table 1.2 Table showing key project tasks and associated sub-tasks. The chapter where a description of how these tasks were addressed is indicated.

1.4 Thesis Synopsis

This thesis describes the prototype Rayleigh Laser Guide Star AO system on the WHT, from design through to integration and testing, both in the laboratory and on-sky at the WHT. After an introduction detailing the physics behind atmospheric turbulence and how to correct for its effects, each of the subsequent chapters looks at a different aspect of the design and discusses the issues and physical processes that must be studied when designing an LGS-enabled AO system.

1.4.1 Chapter 2

This chapter examines the theoretical aspects and the limitations of using an LGS as a wavefront reference. The use of an LGS as a wavefront reference allows great versatility in the method that the wavefront is sensed, and two concepts are introduced here as examples of this. Ground Layer AO (GLAO) is a method for achieving partial AO correction over wide-field is one such concept. Several systems that rely on, or can utilise this technique examined.

1.4.2 Chapter 3

Chapter 3 examines in greater detail a selection of past and current AO systems that utilise laser guide stars, and the problems that are encountered when trying to correct the wavefront sensed from an LGS. Studying similar systems and examining successes and shortcomings of a variety of system designs can highlight critical aspects of the AO system design described in this work. This chapter also includes a discussion of the types of laser that can be used and a comparison of their relative merits.

1.4.3 Chapter 4

The specific issues that are involved in equipping the WHT with a laser guide star are studied in this chapter. Also included are details of the laser used and the laser launch

system design as well as on-sky measurements of the laser launch system performance.

1.4.4 Chapter 5

This chapter examines the performance of the laser launch system using a model of the interaction between the LGS and Wavefront Sensor (WFS). Parameters that optimise the theoretical performance of the LGS and WFS interaction are also presented. This analysis provides data used to optimise the AO system design.

1.4.5 Chapter 6

This chapter looks at the requirements of the LGS AO system and how the design addressed these. Performance estimates for various parts of the system are given. System calibration and control techniques are discussed here.

1.4.6 Chapter 7

Results of numerical simulations of the end-to-end system performance of the AO system are given here. Simulations of the performance of two LGS concepts are made and analysed, showing the expected performance of the GLAO system demonstrator and also the performance of a related LGS novel concept.

1.4.7 Chapter 8

On-sky and laboratory testing results of the closed loop AO system are presented in chapter 8.

1.4.8 Chapter 9

Conclusions are presented in Chapter 9 as well as an outline of the future work and modifications planned for the experimental system.

1.5 Imaging through atmospheric turbulence

The intensity function of a point source resolved by a circular aperture is an Airy pattern (Figure 1.1). The angular resolution of a circular aperture is defined as

$$R = \frac{1.22\lambda}{D} \qquad \text{- 1.1}$$

where R is the minimum angular distance in between two resolved point sources of equal magnitude and D is the diameter of the circular aperture. λ is the wavelength at which the observation is being made. Two sources are said to be resolved when the peak of the intensity function of one source lies in the first minimum of the other. This is the Rayleigh diffraction criterion. Note that this is a definition of a 'resolved image', and in practice, sources that are separated by less than $1.22\lambda/D$ can be discerned in actuality, both by eye and using post-processing techniques.

Figure 1.1 Diffraction limited Airy pattern formed at the focus of a telescope with circular aperture. The central obscuration present in most astronomical telescopes causes a slight increase in the diameter of the central core and a suppression of the intensity of the diffracted rings in comparison with the image presented above.

The plane wavefront that would form the image shown in Figure 1.1 is given a random phase profile by passage through the atmosphere. If the time-averaged wavefront collected by a telescope is examined (by looking at a long exposure image), the random phase fluctuations present will produce a blurred image, the resolution of which will be limited not only by the size and shape of the aperture, but also by the properties of the atmosphere. Dependent on atmospheric conditions, typical exposures between 30 seconds and 2 minutes must be used to image the time-averaged wavefront. Analysis of the time-averaged image shows the atmosphere reduces the resolving power of the telescope in a way that is directly analogous to decreasing the size of the telescope aperture, giving Equation 1.2:

$$R = \frac{1.22\lambda}{r_0} \qquad \text{- 1.2}$$

where r_0 is the so-called Fried parameter, which will be described in section Figure 1.2. At visible wavelengths in premier observing sites, r_0 ranges between 5 and 20cm depending on atmospheric conditions.

Shorter camera exposure times (of the order of 1ms) give an instantaneous snapshot of the current effect of the atmosphere on a propagating plane wavefront. A typical short exposure image is shown in Figure 1.2. The light has been scattered inside an envelope function (identical to the intensity profile of the long-exposure image) with the size of the individual speckles determined by the diffraction limit of the telescope.

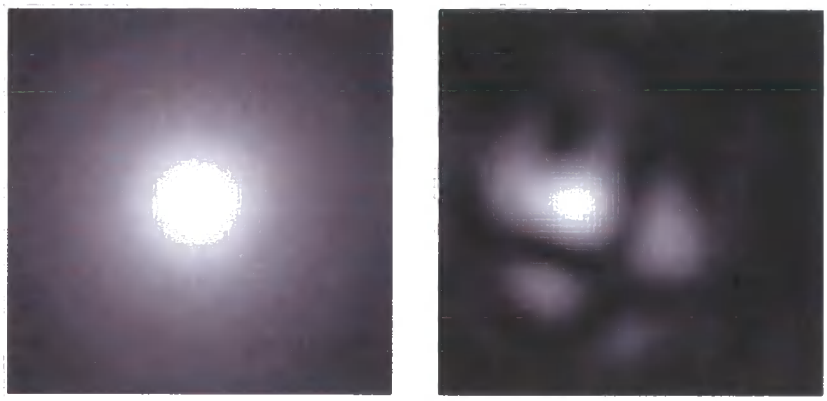

Figure 1.2 Long (left) and short (right) exposure images of a point source taken through a turbulent atmosphere. Intensity has been scaled in short exposure image to enhance speckle pattern visibility. A D/r_0 value of 6 was used to generate the speckled image.

1.6 Atmospheric turbulence profiles

Because r_0 is a statistical property of the atmosphere it does not describe the precise structure of atmospheric turbulence itself. However, r_0 is an extremely useful parameter with which to characterise the overall effect of the atmosphere on an incoming plane wavefront. While simple models of AO system performance can be made with knowledge of r_0 alone, to fully predict AO system performance the structure of turbulence within the atmosphere must be described in far greater detail.

Turbulence in the atmosphere is caused by the cascade of thermal energy from large to smaller scales. Kolmogorov [1] introduced the idea of structure functions to

describe non-stationary random functions, such as the changing refractive index profile that is characteristic of atmospheric turbulence. The velocity structure function describes the spatial and temporal properties of turbulence within the atmosphere. Tatarskii [2] introduces the effect of temperature as a "passive additive" to the system. A passive additive is one that does not change the statistical properties of the observed structure function.

The local temperature variations lead to refractive index fluctuations in the air which can distort an incoming stellar wavefront. The magnitude of the refractive index fluctuations is greatest at lower altitudes, where air density is higher, and decreases exponentially with altitude. This is the reason why most astronomical observatory sites are at a high altitude. The fluctuations are greatest during daylight hours, when solar heating causes large temperature variations, and hence creates a highly turbulent medium. The refractive index fluctuations act as a random array of irregular lenses in the sky, introducing a random optical phase into the wavefront. Being a turbulent system, the phase fluctuations (and hence transmitted wavefront) change continuously. The power spectrum of Kolmogorov turbulence in one dimension is given by

$$\phi(k) \propto k^{-5/3} \qquad \text{- 1.3}$$

where k, the spatial wave-number for a turbulent eddy of scale size l is defined as $k = 2\pi/l$. Obviously this approximation breaks down at very small and very large values of l, so this relation is only valid in the range $l_0 < l < L_0$, where l_0 and L_0 are the so-called inner and outer scales of turbulence respectively. When the size of a turbulent eddy falls below l_0, the viscosity of the air dissipates the fluctuation. The

outer scale, L_0 must also be specified; the power spectrum of turbulence on the larger scales would otherwise tend towards infinity. This implies infinite energy input, which is clearly unphysical. The actual size of the outer scale is not well characterised at present with model values ranging from 10m to 300m [3]. The effect of L_0 on an atmospheric turbulence profile can be physically interpreted as the magnitude of the overall wavefront slope in a wavefront. The larger the L_0, the greater the global slope in a perturbed wavefront can be. Higher spatial frequency terms will be superimposed on this slope, until the spatial scale reaches l_0, below which the atmosphere induces no turbulence.

The inclusion of the outer scale has a large effect on the optical properties of the atmosphere. The effect of the outer scale is too complex to include in many of the simple approximations presented here (and frequently used in AO literature). Under identical seeing conditions, the seeing measured by a telescope with large aperture can be far better than a telescope with small aperture. The magnitude of this effect is given by [4]:

$$d_{vK} \approx d_K \left[1 - 2.183 \left(r_0 / L_0 \right)^{0.356} \right]^{\frac{1}{2}} \qquad \text{- 1.4}$$

where d_{vK} is the FWHM diameter of the seeing limited image from a von Karman-type atmosphere that includes the effect of an atmospheric outer scale on the power spectrum of turbulence, and d_K is the FWHM diameter of the seeing limited image from a Kolmogorov-type atmosphere. By measuring the strength of refractive index fluctuations at all altitudes, an accurate map of the vertical structure of atmospheric turbulence can be made.

The structure function, $D_n(r)$, is defined as the average difference between two values that describe a random process. In the case of atmospheric turbulence, the two 3D vectors describing a position (x) in the atmosphere, and the refractive index (n) at a point a distance r from x on an incoming wavefront.

$$D_n(r) = \left\langle |n(x) - n(x+r)|^2 \right\rangle = C_n^2 r^{2/3} \qquad - 1.5$$

C_n^2 is the refractive index (vertical) structure parameter and is derived by integrating the strength of the refractive index fluctuations over all altitudes, from the telescope aperture to the edge of the atmosphere. Once C_n^2 is known, the precise instantaneous effect of the atmosphere on an incoming wavefront can be determined.

C_n^2 is, not a simple thing to measure from a telescope aperture. The vertical distribution of the turbulence cannot be determined by measuring the phase at the pupil plane of the telescope as this encodes no information on the altitude at which the phase change was induced. Balloon measurements [6], analysis of differential intensity patterns [7] or wavefront measurements from binary stars [8] are all methods that have been used to determine the C_n^2 profile.

Similarly to the spatial structure function defined above, we can define a temporal structure function for the evolution of the wavefront at any single point above a telescope aperture between time $t = 0$ and $t = \tau$,

$$D_n(\tau) = \left\langle |n(x,t) - n(x,t+\tau)|^2 \right\rangle \qquad - 1.6$$

Although the structure of the turbulence evolves with time due to temperature fluctuations, these changes are small when compared with the far greater variation in a wavefront caused by wind blowing atmospheric inhomogeneities across the

telescope aperture. This leads to equation 1.7, showing the effect of the wind velocity on the structure function.

$$D_n(v\tau) = \left\langle \left| n(x,t) - n(x+v\tau,t) \right|^2 \right\rangle = C_n^2 |v\tau|^{2/3} \qquad - 1.7$$

where v is the velocity with which the turbulence is changing and τ the time taken for the turbulence to move a distance r. If the turbulence is contained within a single layer, v is the wind speed at that layer. When the entire atmosphere is collapsed into a single invariant (frozen) layer moving across a telescope aperture, this is called the Taylor approximation.

Modelling all atmospheric turbulence as a single turbulent phase screen translating across a telescope aperture is an oversimplification of the chaotic nature of the atmosphere, as both wind speed and direction of motion of turbulence can evolve with altitude. Studies [8,9] of the atmosphere above observatory sites have shown that the turbulence within the atmosphere is primarily contained within a set of discrete turbulent layers. When dealing with adaptive optics system design and modelling, the approximation that all turbulence within the atmosphere is stratified into a set of layers each with separate velocities and directions is made.

The optical effects of turbulence can be calculated by integrating the C_n^2 profile over height with several different weighting functions. These functions can be expressed as full and partial turbulence moments. The full turbulence moment of order m is defined as:

$$\mu_m = \int_0^\infty dh\, C_n^2(h)\, h^m \qquad - 1.8$$

This can be separated into partial turbulence moments at an altitude H, by integrating between 0 and H for the so-called lower turbulence moment, μ^-, and H and ∞ for the upper turbulence moment, μ^+. By changing the order of the turbulence moment, different atmospheric properties can be defined. Zero-order (m=0) turbulence moments are used for calculating r_0. Five-thirds order (m=5/3) turbulence moments are used for calculating anisoplanatic and temporal errors (see section 1.10), while second-order (m=2) moments are used for calculating overall tilt errors.

Atmospheres modelled using the equations given above, having a power spectrum indicative of a Kolmogorov structure function, are said to be Kolmogorov atmospheres. The optical effect of turbulence is characterised by the three dimensional refractivity power spectrum, which for Kolmogorov turbulence,

$$\phi(k,h) = 0.033 C_n^{\,2}(h) k^{-11/3}, \qquad \text{- 1.9}$$

where h is the altitude. For atmospheric turbulence with a Kolmogorov power spectrum, the structure function across a telescope pupil is given by:

$$D_\phi(r) = 6.88\left(\frac{|r|}{r_0}\right)^{5/3} \qquad \text{- 1.10}$$

where r is a 2D displacement across the telescope pupil and

$$r_0 = \left(0.423 k^2 \sec\theta \int C_n^2(z)\, dz\right)^{-3/5} \qquad \text{- 1.11}$$

θ is the zenith angle at which observations are being made that must be included to account for the effect of changing airmass with telescope elevation. r_0 (introduced in equation 1.2) has the useful property that it is the diameter over which the wavefront

phase variance has a mean-square value of 1 rad^2 for a given wavenumber k. This approximately corresponds to a $\lambda/4$ peak-to-valley (P-V) wavefront error, assuming that the 3σ deviation from the mean describes the root-mean-square (rms) wavefront error. A residual wavefront variance of 1 rad^2 is significant for the performance of the system as it describes the maximum wavefront variance of a system that is classically 'diffraction-limited'. If the wavefront variance exceeds the critical value of 1 rad^2 the image quality rapidly degrades. This value defines the level of correction that an AO system must provide to achieve 'diffraction-limited' performance. The effect of wavefront error on image quality is quantified in section 1.10.

The power spectrum of the atmosphere may be obtained by performing a Fourier transform of the atmospheric C_n^2 profile. Studies have shown [10,11,12] that the fit of measured atmospheric power spectra to theoretical Kolmogorov turbulence profiles shows a good correlation. However, as was mentioned, the Kolmogorov power spectrum must be modified to take into account the finite size of the outer scale. The outer scale is included in the Modified Von Karman (MVK) power spectrum. The power spectrum of the phase fluctuations in the MVK spectrum is given by [13]

$$\phi_{MVK}(k,h) = 0.033 C_n^2(h)(k + L_0)^{-11/6} \exp\left(-k^2 / l_0^2\right) \qquad \text{- 1.12}$$

where L_0 and l_0 are the atmospheric outer and inner scales previously defined.

1.7 Temporal Properties of the Atmosphere

The Taylor hypothesis describes how a translation of a phase screen across the aperture of a telescope affects the phase structure function. Using equations 1.7 and

1.10 it can be shown that the time for the rms of the change of a wavefront perturbed by atmospheric turbulence to reach the 'critical value' of 1 radian is given by:

$$\tau_0 = 0.314\frac{r_0}{v} \qquad \text{- 1.13}$$

Equation 1.13 assumes that turbulence is concentrated in a single layer that moves with a velocity v across the telescope aperture. τ_0, the coherence time of the atmosphere, can be thought of as being the time over which the atmosphere will not change an image. A qualitative way of describing the effect of τ_0 on an image distorted by turbulence is as follows: If an observation lasts for a time less than or equal to the coherence time, the atmosphere will have a single refractive index profile and the incoming light will form a static, albeit distorted, image.

1.8 Modal representation of turbulence

Any wavefront perturbed by the atmosphere can be represented by a series of orthogonal modes of increasing spatial frequency. A set of orthogonal 2D functions, called Zernike polynomials are widely used in optical systems to describe wavefront shape. Low-order Zernike modes correspond to familiar and correctable wavefront aberrations, such as wavefront tilt, defocus, astigmatism and coma. Zernike polynomials are defined in polar coordinates on a unit circle as functions of both azimuthal and radial frequency, denoted by m and n respectively. Noll [14] defined a numbering scheme that is commonly used when describing atmospheric turbulence using Zernike polynomials. The set of Zernike polynomials is defined as:

$$\begin{aligned} Z_{even} &= \sqrt{n+1}R_n^m(r)\sqrt{2}\cos(m\theta), & m \neq 0 \\ Z_{odd} &= \sqrt{n+1}R_n^m(r)\sqrt{2}\sin(m\theta), & n \neq 0 \\ Z &= \sqrt{n+1}R_n^0(r), & m = 0 \end{aligned} \qquad \text{- 1.14}$$

where

$$R_n^m(r) = \sum_{S=0}^{(n-m)/2} \frac{(-1)^S (n-S)! r^{n-2S}}{S![(n+m)/2-S]![(n-m)/2-S]!} \qquad \text{- 1.15}$$

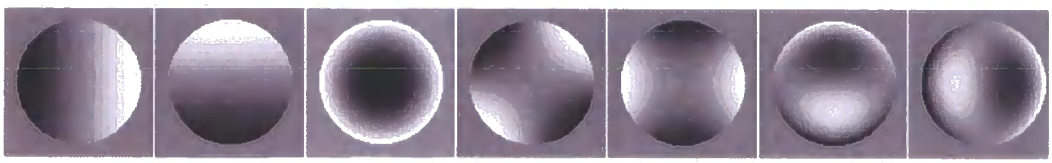

Figure 1.3 Zernike modes 2-8. Mode 1 is a piston of the wavefront. Low order modes correspond to classical wavefront aberrations. Modes 2 and 3 correspond to wavefront tip and tilt, 4 is focus, 5 and 6 are wavefront astigmatism. Modes 7 and 8 represent coma.

Zernike modes are described over a circular and not the annular aperture that exists at most telescopes. This allows for some ambiguity in the measurement of zernike modes from a wavefront e.g. differing higher-order radially symmetric terms can appear identical if the central 25% of a circular aperture is removed. An equivalent annular set of Zernike modes [15] can be used to reduce this error. However, both annular and circular Zernikes are not statistically independent when being used to describe Kolmogorov turbulence. This means that subtracting a given number of modes from a Kolmogorov wavefront will result in a residual wavefront error that is higher than optimal. As such, a related set, based on Karhunen-Loeve (KL) functions [16] was defined to create an orthonormal set of modes that were configured to be statistically independent of each other when describing wavefronts distorted by Kolmogorov turbulence. KL modes give the minimum residual wavefront error for a

fixed number of fitted modes when compared to any other orthonormal set, such as circular or annular Zernike modes.

1.9 Adaptive Optics system architecture

At the most basic level, an AO system requires a method for sensing an incoming wavefront, a method for controlling the wavefront and a control system to link the two. AO systems are normally designed as a closed feedback loop where the wavefront sensor (WFS) measures the wavefront after the wavefront corrector (normally a deformable mirror, or DM) has applied a correction. The WFS requires a reference source that is bright enough to allow WFS exposures with a sufficient signal-to-noise ratio (SNR) at integration times less than τ_0, the coherence time of the atmosphere. This layout is shown in Figure 1.4.

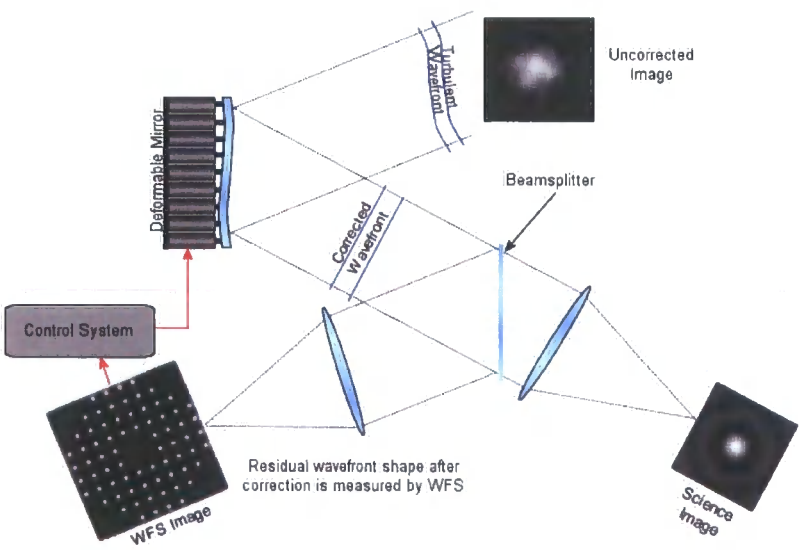

Figure 1.4 Closed-loop feedback AO system using a Shack-Hartmann WFS and piezo-stack DM. Red lines denote the data-flow providing closed-loop feedback

1.10 Error Sources in AO

One commonly used metric to indicate the performance of an AO system is the Strehl ratio. It is defined as the ratio between peak intensity of the diffraction limited PSF and the peak intensity of the long-exposure image. A Strehl ratio of 1 describes a diffraction limited image. AO system performance is often given in terms of Strehl ratio improvement. For wavefront errors below approximately 1 rad^2 rms, the Strehl ratio is given by Equation 1.16.

$$S = \exp\left(-\sigma^2\right), \qquad \text{- 1.16}$$

where σ^2 is the wavefront variance in square radians. The Strehl Ratio is highly sensitive to small wavefront errors. However, a Strehl ratio of 0.8 still gives performance corresponding to the Rayleigh diffraction limit. This corresponds to an rms wavefront error of $\lambda/13.3$. Strehl ratio is not always the best metric with which to define the performance of an AO system when coupled to a scientific instrument. Other metrics, such as image FWHM, or in the case of a spectrograph, in-slit energy can be used.

The sources of error in an adaptive optics system that contribute to the wavefront variance, σ^2, are numerous and depend on both the properties of the atmosphere and the components that make up the AO system as is shown in Figure 1.5.

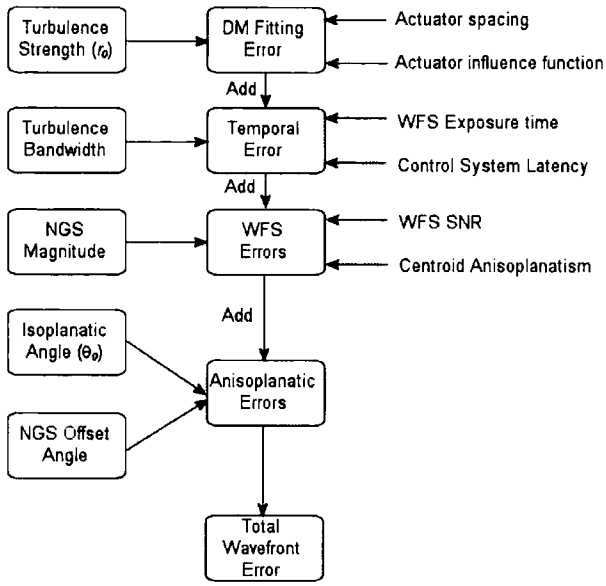

Figure 1.5 Sources of Error in an AO system using an NGS as a wavefront reference. Diagram adapted from Hardy [17].

To arrive at the global system error, the magnitude of each error source shown in Figure 1.5 must be combined. When errors in an adaptive system are calculated in terms of wavefront variance, the system performance is described by the sum of the wavefront variances due to each individual error source. A system error calculated in this way often gives a pessimistic impression of system performance as errors (particularly spatial errors) can be counted multiple times [18]. Analysis of AO system performance in terms other than wavefront variance produces a system error that easily demonstrates the scientific potential of the AO system, but introduces difficulties in system error budgeting as the sensitivity of a metric to a specific error source can decrease [19]. One example of this is the use of in-slit energy, which is a standard design parameter for describing the operation of a spectrograph. Inslit energy is defined as the ratio of energy within the slit to the total energy incident on the slit and slit mask i.e. the energy in the PSF.. As an example, an AO-fed spectrograph has

a slit width of 0.2". Under seeing-limited conditions, a small fraction of the energy in the PSF will pass through the slit. If the AO system is turned on the inslit energy will increase. However, if the sources of error in the AO system are then reduced, there will come a point where the inslit energy reaches 1, but there may still be some residual error in the system. At this point, further reduction of system error does not improve the performance in terms of inslit energy and alternative metric would have to be used.

1.10.1 Wavefront Fitting Error

The wavefront fitting error is a measure of how well the wavefront correcting element, usually some kind of DM, can match the shape of the wavefront caused by turbulence present in the atmosphere. Obviously, as the strength of the turbulence increases i.e. r_0 decreases, the DM must recreate a higher spatial frequency wavefront. There are many different types of deformable mirror, each with a different way of recreating a wavefront. Here, the fitting error for a DM with inter-element spacing of d to a Kolmogorov turbulence profile is given.

$$\sigma_{fit}^2 = \alpha\left(\frac{d}{r_0}\right)^{5/3} \qquad \text{- 1.17}$$

The scaling factor α depends on the type of corrector being used. The inter-element spacing of a DM is also defined by the corrector type and normally cannot be varied without changing DM. Typical values of α range from 0.14 to 1.26 whilst inter-element spacings range between 100um and 7mm. To achieve the Strehl ratio of 0.8 that indicates classical Rayleigh diffraction-limited performance, for an α of 0.28, (the

value for a continuous phase sheet deformable mirror, such as those manufactured by Xinetics Inc. and of the type used in this project), the ratio d/r_0 must be less than 0.873. For an original Xinetics-type mirror with 11x11 actuators, (i.e. 10x10 corrective segments), deployed on a 4.2m telescope each segment will correct a 42cm 'patch' of the atmosphere. To achieve the ratio of d/r_0 given above requires an atmospheric r_0 of 36.75cm, which is a typical value for atmospheric r_0 at Near-Infrared (NIR) wavelengths. NIR wavelengths cover the so called J-band at 1.25μm, H-band at 1.65μm, and K-bands centred at 2.2μm. Diffraction-limited AO correction at shorter wavelengths therefore requires a DM with a greater number of corrective elements. In the above example, a Xinetics-type DM would require an actuator spacing of approximately 9cm across the telescope pupil to correct strong atmospheric turbulence with an r_0 of 10cm. An r_0 of 10cm is a typical value observed in the V-band. This corresponds to a 48x48 actuator grid, which is an order of magnitude greater than the actuator resolution available in current civilian astronomical AO systems.

1.10.2 Temporal Errors

The fact that the system cannot respond instantaneously to changes in an incoming wavefront gives rise to temporal error. Temporal error sources depend on many factors, both atmospheric and internal to the system. The characteristic frequency of the atmosphere is dependant on the strength and distribution of atmospheric turbulence i.e. the C_n^2 profile, as well as the integrated wind speed profile. This is referred to as the Greenwood frequency and is given by

$$f_G = \left[0.102k^2 \sec\theta \int_0^\infty C_n^2(h) v^{5/3}(h) dh \right]^{3/5} \qquad \text{- 1.18}$$

For the case of a single turbulent layer with a wind velocity v, the Greenwood frequency reduces to

$$f_G = 0.427 \frac{v}{r_0} \qquad \text{- 1.19}$$

The error associated with the characteristic frequency of the atmosphere depends on the response time of the AO system. The wavefront error due to a finite time delay of duration, τ_s between the end of the WFS exposure and the corrective shape being displayed on the DM is given by

$$\sigma^2_{delay} = \left(\frac{\tau_s}{\tau_0} \right)^{5/3} \qquad \text{- 1.20}$$

where τ_0 is defined in equation 1.13. For a single layer of turbulence, τ_0 can be expressed in terms of the Greenwood frequency,

$$\tau_0 = \frac{0.134}{f_G} \qquad \text{- 1.21}$$

The wavefront error can then be expressed as

$$\sigma^2_{delay} = 28.4 (\tau_s f_G)^{5/3} \qquad \text{- 1.22}$$

At a good astronomical site, the magnitude of the Greenwood frequency is typically of the order of tens of Hz. To achieve a closed loop correction bandwidth that approaches this value, the system loop frequency, given by $1/\tau_s$, must be many times

greater than the Greenwood frequency. AO systems run with loop speeds ranging from 100Hz for low-order wavefront correction, up to 3kHz for proposed ExAO ('Extreme' Adaptive Optics) systems that would be capable of providing true diffraction-limited performance at visible wavelengths.

The closed loop bandwidth that will be achieved by an AO system also helps to define what spatial frequency of turbulence can be corrected. Higher spatial frequency turbulence has a short characteristic lifetime when compared with low spatial frequency turbulence (such as a global tilt across a wavefront) [20]. Determining the closed loop bandwidth of a system involves careful study of the performance of all elements of the AO system, and in particular, the predicted performance of the control system.

1.10.3 WFS Errors

Sensing the wavefront introduces further sources of error, which are due in part to the very short exposure times that are required to allow the system to run with loop speeds of up to 3kHz, and also due to the very faint wavefront reference sources that must be used. WFSing in astronomical AO usually operates in a photon-sparse environment, with typical WFS signals of the order of 100 photons per control channel. Accurately measuring the phase of an incoming wavefront from a source other than the Sun therefore requires very sensitive detectors with very low noise levels.

The errors associated with WFSing are particular to each type of WFS. Throughout this work, only the errors associated with the Shack-Hartmann WFS (SH-WFS) will

be discussed. A SH-WFS works by placing an array of lenslets at a point in the light path conjugate to a given altitude. Each lenslet then samples a fraction of the total incoming wavefront. In the absence of any wavefront aberrations, i.e. a plane wavefront, a regularly spaced array of spots is created in the focal plane of the lenslets. If a wavefront gradient is present across a lenslet, then the corresponding focussed spot becomes offset by an amount proportional to the wavefront gradient. This is shown in Figure 1.6. A detector array, normally a CCD, is placed at the focal plane of the lenslets to measure the offset positions of the spots. A cluster of four (or more) Avalanche Photodiodes (APDs) can be placed behind each lenslet instead of a CCD pixel array. Large APD arrays are costly, fragile and in quad-cell mode, provide a less accurate measure of spot offset than a higher-resolution array of CCD pixels.

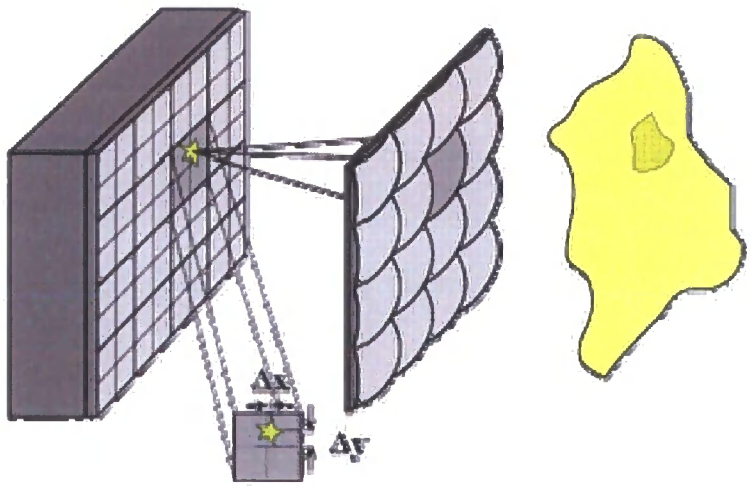

Figure 1.6 A Shack-Hartmann WFS works by measuring the slope of a wavefront across an array of lenslets. If an incoming turbulent wavefront (shown in yellow) exhibits a slope across a lenslet, the resulting focused spot formed by the lenslet will be offset by an amount proportional to the wavefront slope.

By recombining the slopes from each lenslet, the entire wavefront can be reconstructed. Obviously, the extent to which the reconstructed wavefront matches the actual wavefront depends on the number of lenslets present in the array. Because the

wavefront contains a small finite number of photons, as the number of lenslets sampling a wavefront is increased, the signal-to-noise (SNR) decreases correspondingly. The SNR is further reduced as the photons within each subaperture must then be distributed across a number of CCD pixels.

There are three main error sources in CCDs; photon shot noise in the signal, noise generated in the CCD readout electronics, and noise derived from the production of thermal electrons in the CCD substrate. Thermal noise can be minimised by cooling the CCD to the point where it is a small fraction of the total noise level. Photon shot noise is a fundamental property of the quantum nature of light, giving rise to a Poissonian distribution in the total number of photons incident onto the CCD over a given time interval. The noise on a signal associated with a Poissonian distribution is equal to the square root of the population. Due to the low numbers of photons that are present in a WFS image, the error associated with photon noise can be large.

Noise generated in the readout electronics, particularly in the on-chip preamplifier is a large factor in the accuracy with which a wavefront can be determined. The job of the readout electronics is to convert the charge stored in each CCD pixel to a digital value. Scientific-grade astronomical CCDs have around 2Kx2K pixels and a readout time of around 100s, corresponding to a readout rate of 40kPixels/s. Typically, a few electrons rms readout noise per pixel would be observed on a CCD image. A WFSing CCD requires far fewer pixels (~80x80 pixels for low-order NIR AO systems on a 4-8m telescope), but using a 40kPixels/s readout rate would add a delay of 160ms before a WFS exposure could be fully analysed by the AO control system. This would be the dominant error term affecting the system performance (see equation 1.20). Faster readout electronics must therefore be used, but increasing the readout speed

also increases the level of readout noise observed. Multiple readout ports from a single CCD can also be employed to effectively increase the readout rate [24], and frame transfer CCDs used to maximise the CCD duty cycle [25]. Frame-transfer CCDs have a charge storage area which is an array of masked pixels identical to the photosensitive section of the chip. The photoelectrons present in the light-sensitive half of the chip at the end of an exposure can be rapidly transferred to the masked portion of the chip almost noiselessly. The next WFS exposure can then start immediately while the charge is being read out of the masked section of the chip. Typical WFS CCDs exhibit a readout delay of 1ms or less, and have read noise levels of between 3 and 8 electrons rms.

Temporal errors associated with the integration time of the WFS, although present, are small as long as the $t_{exp} << \tau_0$. The readout speed of the CCD can introduce an appreciable latency into the system. Latency is a major source of error in an AO system and is caused due to the fact that all operations within the AO system take a finite amount of time. WFS exposure time, readout time and wavefront reconstruction in the control system are not instantaneous, and any time taken during these steps means the atmosphere has changed and the correction applied to the DM will be incorrect. The effect of increasing system latency on performance is modelled in Chapter 7.

The final source of error that is present within a wavefront sensor observing a natural guide star is centroid anisoplanatism. Centroid anisoplanatism is caused by wavefront

modes within a subaperture[1] causing an apparent wavefront gradient. A simple example of this is coma, which causes a centroid offset due to the resulting non-gaussian intensity pattern. This offset is interpreted by the centroiding algorithm as an extra component of the wavefront tilt. Yura et al [21] calculated the effect of centroid anisoplanatism and showed that the effect is small. The effect of centroid anisoplanatism is inversely proportional to the detected wavelength of the reference source.

$$\sigma^2_{centroid} = -\ln\left(\left(1+0.015\left(d/r_0\right)^{5/3}\right)^{-1}\right) \qquad \text{- 1.23}$$

where for a SH-WFS, d is the effective diameter of each WFS subaperture projected onto the telescope primary aperture.

Modal decomposition of a wavefront (Section 1.8) can be used as a basis to control an AO system. Modal control (rather than zonal where the wavefront is analysed as a series of discrete zones, as is the case with a SH-WFS) is better suited to some types of corrector/DM and WFS than zonal control. This is brought about the inability of the WFS to sense wavefront distortions at the order of spatial correction being displayed on the DM. The combination of a curvature sensor with a bimorph DMs is a common example of a situation where the modal control of an AO system would show an improvement in performance over the zonal control of the bimorph DM using a SH-WFS.

---

[1] Note that modes across a subaperture are not Zernike modes, as these are defined over a circular aperture, not the square (or sometimes hexagonal) subaperture geometry of a SH-WFS

1.10.4 Anisoplanatic Errors

Angular anisoplanatism is caused by inadequate sampling of the atmosphere. Figure 1.7 demonstrates the cause of angular anisoplanatism.

If the object under study i.e. the science target, is bright enough to act as a wavefront reference (a condition referred to as self-referencing AO) the path that a wavefront travels through the atmosphere is identical for the reference and science beams. If the science object is too dim to be used as a wavefront reference source, either an off-axis guide star or LGS must be used. As the angle between the science target and guide star increases, the variance between the wavefront from the science target and that from the guide star also increases. The AO system only corrects aberrations observed in the wavefront from the reference source, which will not be exactly the same as those that are present in the science target wavefront.

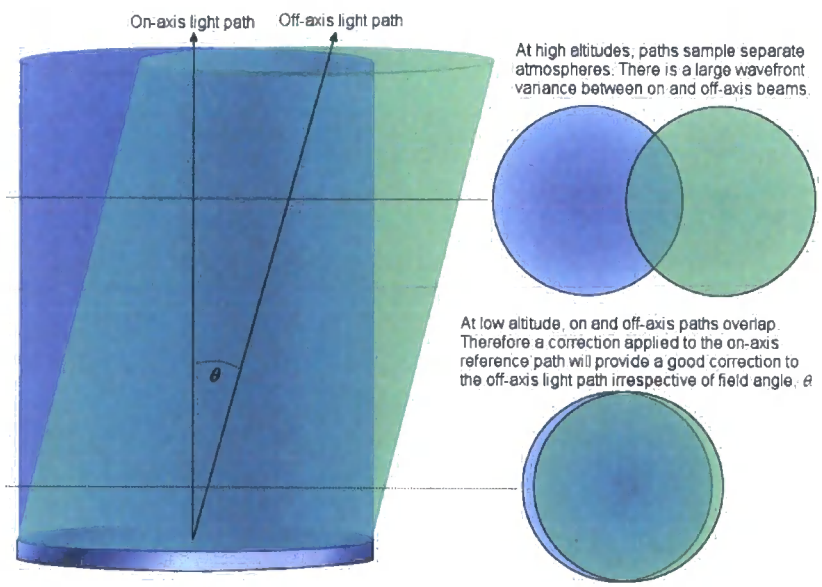

Figure 1.7 Cause of angular anisoplanatism in AO

The isoplanatic angle, θ_0, is a property of the turbulence distribution within the atmosphere and is defined as [22]

$$\theta_0 = \left[2.941 k^2 (\sec\theta)^{8/3} \int C_n^2(h) h^{5/3} dh \right]^{-3/5}, \qquad \text{- 1.24}$$

where h is the height of a turbulent layer, θ is the telescope elevation angle, and k is the wavenumber. For a single layer of turbulence, equation 1.24 reduces to

$$\theta_0 = 0.314(\cos\theta)\frac{r_o}{h} \qquad \text{- 1.25}$$

The wavefront error due to angular anisoplanatism for any off-axis angle, θ, may be expressed as

$$\sigma_\theta^2 = \left(\frac{\theta}{\theta_0}\right)^{5/3} \qquad \text{- 1.26}$$

Angular anisoplanatism limits the field of view that can be corrected by an AO system. Once the angular offset between an object and the bright NGS increases beyond the isoplanatic angle, the degree of correction falls off rapidly. The limited corrected field of an AO system can be overcome by using multiple reference sources located in and around the scientific field of interest in order to measure wavefronts through many different turbulent paths through the atmosphere. Using multiple wavefront reference sources provides data about the vertical distribution of turbulence as shown in Figure 1.8.

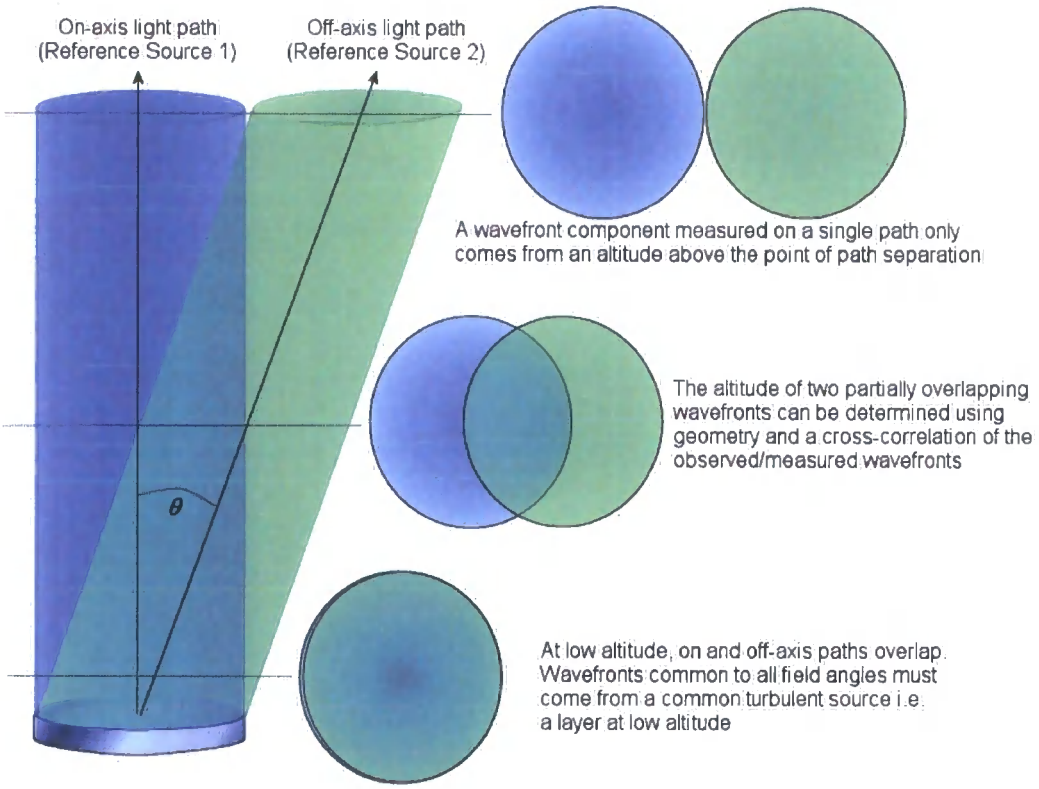

Figure 1.8 Wavefronts from two reference sources being used to determine vertical distribution of turbulence. Reference source 1 is on-axis, and reference source 2 is off-axis. Observed wavefront from each source is common where wavefronts overlap.

1.11 Multiple Conjugate AO

By correlating the wavefronts from two or more reference sources, multiple DMs can be controlled. The WFS signals can be analysed to determine what proportion of the observed wavefront is common to all paths through the atmosphere (i.e. the turbulence that is concentrated in the lowest layer of the atmosphere), and that which is specific to a single path through the atmosphere (i.e. turbulence that exists at higher layers in the atmosphere). As the geometry of the guide stars is known, a tomographic picture of distribution of turbulent layers within the atmosphere can be determined.

For a multiple DM system, the DMs are normally conjugated to different altitudes within the atmosphere, with the AO control system performing analysis of the WFS signals to split the turbulence between low and high altitude DMs. This technique is commonly referred to as Multiple-Conjugate AO (MCAO).

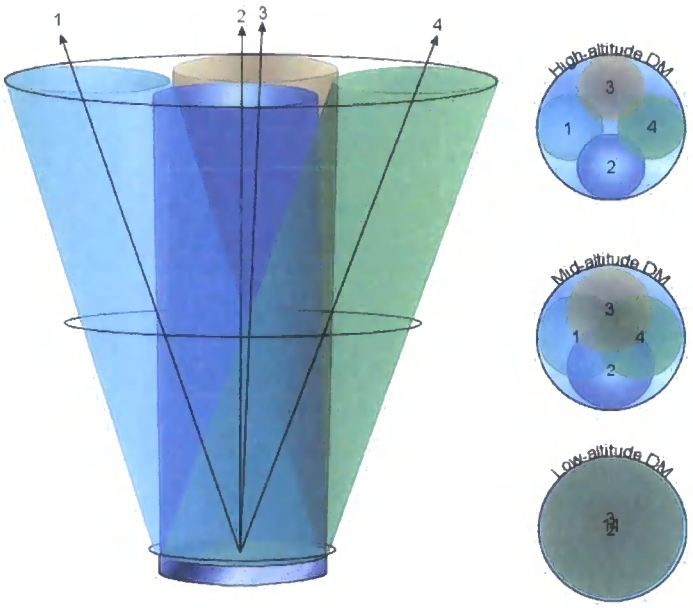

Figure 1.9 WFS geometry and associated beam footprints of a 3-layer MCAO system with DMs conjugated to low, mid and high altitude layers. A 4-star asterism is used.

There are two flavours of performing MCAO that are called 'star-oriented' and 'layer oriented' [26]. Star-oriented (SO) MCAO has a number of guide stars (four are shown in Figure 1.9), each observed by a dedicated WFS. Knowledge of the geometric overlap of the reference wavefronts at the layers in the atmosphere conjugate to each DM provides knowledge of the vertical distribution of the turbulence. The observed turbulence is separated into a set of discrete layers that are conjugated to the set of DMs. In a star-oriented MCAO system, the control system performs the task of discretising the turbulence profile into layers by comparison of the measured wavefront from each source (see Section 1.10.4).

Layer-oriented (LO) MCAO is similar in concept to SO-MCAO, except that the light from all guide stars are optically [27] co-added on a single WFS rather than processed in the control system to provide the MCAO correction.. In LO-MCAO, for each turbulent layer that requires correction, there must exist a WFS that is conjugated to that layer. Each turbulent layer is then re-imaged onto the WFS plane which allows a WFS to control a single DM without the complex control algorithms that are required for tomographic reconstruction of the turbulent atmosphere and the mapping of different turbulent layers onto separate DMs. The LO-MCAO concept is shown in Figure 1.10.

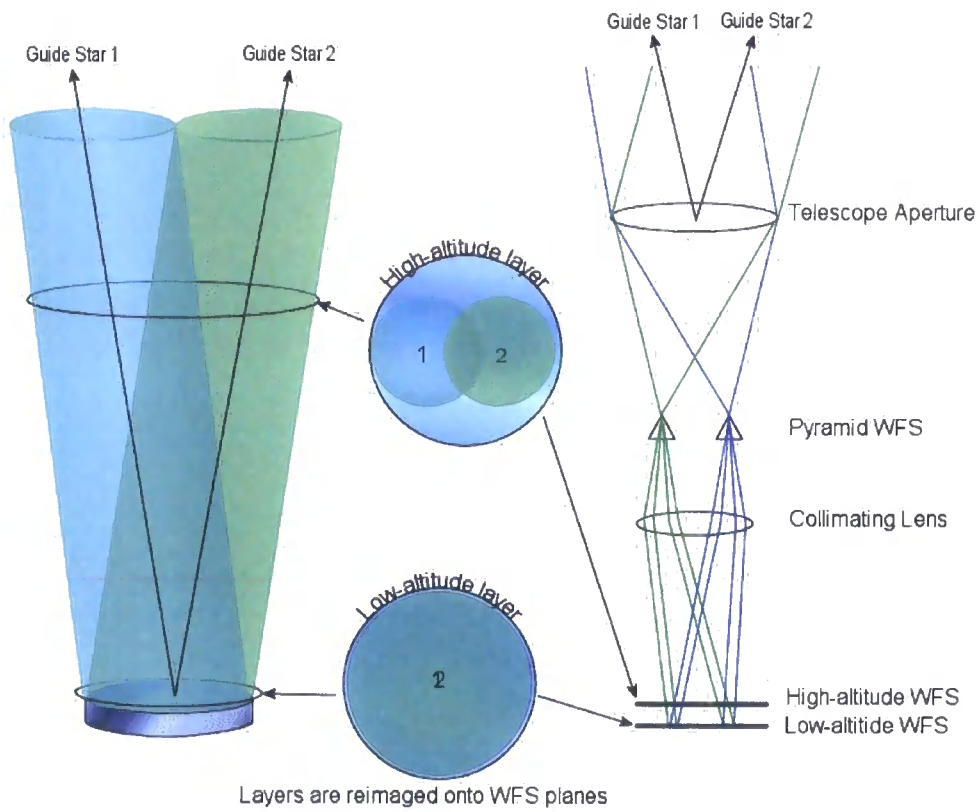

Figure 1.10 Layer-oriented MCAO showing WFS geometry and re-imaging of a turbulent layer onto a conjugated WFS CCD.

Layer-oriented MCAO holds several advantages over SO-MCAO in that the control system is greatly simplified with a single WFS required to control each DM, creating an independent closed loop system for each WFS-DM pairing. The optical co-adding of light also increases the signal on the WFS, allowing fainter objects to be used and thereby increasing sky-coverage. It is also possible to tune both the temporal and the spatial sampling for the temporal (τ_0) and spatial frequencies (r_0) characteristic of the layer which the detector is conjugated to, thereby improving performance by minimizing both pixel scales and WFS integration times. It is also possible to co-add the individual wavefronts numerically [28]. Each WFS in a LO-MCAO system can use a different field-of-view. If the field of view of the ground-conjugated layer is significantly increased, sky-coverage can be greatly increased. This technique is called multiple-field-of-view (mFoV) LO-MCAO [29].

Both SO and LO MCAO can provide wide-field correction. Using the SO rather than the LO approach improves AO correction across the field, although in all MCAO cases the magnitude and distribution of available guide stars will determine the degree of correction across the field. Numerous studies have shown [30,31,32] that AO corrected fields that measure arcminutes in diameter can be created with little angular anisoplanatism, and MCAO has been demonstrated [33] in the photon-rich environment of solar AO, where the sun can be used as a bright wavefront reference.

1.12 Sky Coverage

As most astronomical AO systems currently in use do not employ MCAO, angular anisoplanatism often becomes the limiting factor in the scientific use of many NGS

AO systems, as the following example demonstrates. As a typical AO system requires approximately 100 photons per r_0 element for high-order wavefront sensing, the choice must be made between the order of correction (or alternatively the minimum wavelength where adequate correction will be observed) and the required magnitude of the guide star. For example, wavefront sensing for a 48 element SH-WFS system requires a guide star with half the apparent intensity of a 96 element system, yet this increase in wavefront resolution only corresponds to increasing the WFS geometry from 8x8 to 10x10 elements (defined across a circular pupil with a central obscuration). From equation 1.17, the increased resolution corresponds to a respectable decrease in wavefront fitting error of 45%. However, by doubling the required brightness of the guide star, the number of NGSs that are suitably bright is more than halved [34]. The decrease in NGS density means that either the search radius for a bright NGS must be expanded, increasing the error due to angular anisoplanatism, or that a fainter NGS must be used, increasing WFS error as longer exposures are used or lower SNR wavefronts are detected. Indeed, the lack of a suitable NGS near the target object means that many objects of scientific interest are unobservable with AO systems as the errors become so great that little or no image improvement is seen.

For a given limiting magnitude, the distribution of suitably bright NGSs is concentrated towards the galactic core. Figure 1.11 shows the probability of finding a star brighter R=18 within 1.5' of the science object, showing almost 100% sky coverage in and around the galactic plane, but falling to approximately 20% sky coverage near the galactic poles. NGS AO systems generally require guide stars brighter than 15^{th} magnitude, which would reduce the probability of finding a suitably

bright NGS even near the galactic plane. A guide star with an R-band magnitude of 18 is not suitable for a conventional NGS AO system, so an alternative means of providing a high-order wavefront reference must be found.

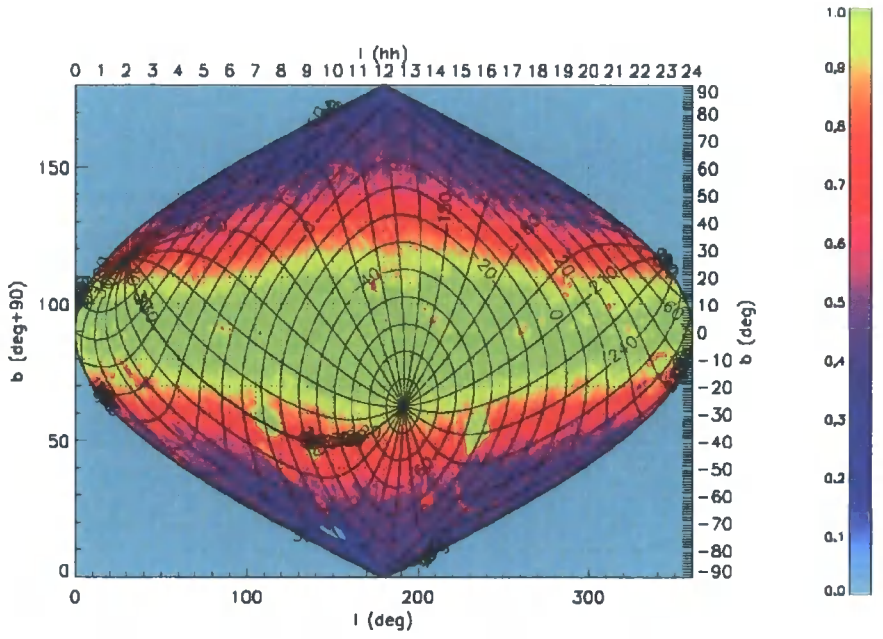

Figure 1.11 Sky coverage map showing probability of finding a star brighter R=18mag star within 1.5' of science object. The sky coverage map was created by locating and examining the area of sky around R=18 and brighter stars from sky survey data (Courtesy R. Stuik, Leiden University)

The solution to the problem of sky coverage is to generate a non-natural reference source. The creation of a bright, artificial laser guide star (LGS) that can be superimposed over, or positioned near, to the target object solves the problem of sky coverage. A perfect example of this is the NAOMI AO system that has a 10% sky coverage in the galactic plane when using an NGS. NAOMI should achieve 100% sky coverage within 30° of the galactic plane when using an LGS, falling to ~30% near the galactic poles. Whilst increasing sky coverage, the use of an LGS as a wavefront

reference does introduce many additional sources of error into an AO system. Laser Guide stars are studied in more detail in Chapter 2.

1.13 References

1. Kolmogorov, A. N. '*Dissipation of energy in locally isotropic turbulence*', Doklady Akad. Nauk SSSR **32**, 16 (1941)
2. Tatarskii, V. I., '*Wave Propagation in a Turbulent Medium*' McGraw-Hill, New York, (1961)
3. Agabi, A., Borgnino, J., Martin, F., Tokovinin, A., Ziad, A., '*G.S.M: A Grating Scale Monitor for atmospheric turbulence measurements. II. First measurements of the wavefront outer scale at the O.C.A*', A&A Suppl. **109** p557-562 (1995)
4. Tokovinin, A., '*From Differential Image Motion to Seeing*', PASP, **114**, p1156-1166 (2002)
5. Azouit, M., Vernin, J., '*Optical Turbulence Profiling with Balloons Relevant to Astronomy and Atmospheric Physics*', PASP **117** p536-543 (2005)
6. J. Vernin and F. Roddier '*Experimental determination of two-dimensional spatiotemporal power spectra of stellar light scintillation. Evidence for a multi-layer structure of the air turbulence in the upper atmosphere*'. J. Opt. Sci. Am. **63** 270-273 (1973)
7. Wilson, R.W., '*SLODAR: measuring optical turbulence altitude with a Shack-Hartmann wavefront sensor*', MNRAS **337** p103-108 (2002)
8. Vernin, J., and Munoz-Tunon, C., '*Optical seeing at La Palma Observatory. 2: Intensive site testing campaign at the Nordic Optical Telescope*', A&A **284** p311-318 (1994)
9. Taylor, G.I., '*The Spectrum of Turbulence*', Proc. R. Soc. London A **164** p476-490 (1938)
10. Nicholls, T. W., Boreman, G. D. and Dainty, J.C. '*Use of a Shack–Hartmann wavefront sensor to measure deviations from a Kolmogorov phase spectrum*', Opt. Lett. **20**, 2460–2463 (1995).
11. Dayton, D., Pierson, B., Spielbusch, B., and Gonglewski, J., '*Atmospheric structure function measurements with a Shack–Hartmann wave-front sensor*', Opt. Lett. **17**, 1737–1739 (1992)
12. Silbaugh, E.E., Welsh, B.M., Roggemann, M.C., '*Characterization of atmospheric turbulence phase statistics using wave-front slope measurements*', J. Opt. Sci. Am. A **13** p2453-2460 (1996)
13. Goodman, J.W., '*Statistical Optics*' Wiley-Interscience, New York, p388-393 (1985)

14. Noll, R.J., '*Zernike Polynomials and Atmospheric Turbulence*', J. Opt. Sci. Am. **66**, p207-211 (1976)

15. Mahajan, V. N., *Zernike annular polynomials for imaging systems with annular pupils*, J. Opt. Soc. Am., **71**, 75 (1981)

16. Holmes, P., Lumley, J. L. and Berkooz, G., '*Turbulence, coherent structures, dynamical systems and symmetry*', Cambridge university press, 1998

17. Hardy, J.W. '*Adaptive Optics for Astronomical Telescopes*', Oxford University Press, New York (1998)

18. Parenti, R.R., and Sasiela, R.J., '*Laser guide-star systems for astronomical applications*', J. Opt. Sci. Am. A **11** p288-309 (1994)

19. Tyler, D.W., Ellerbroek, B.L., '*Spectrometer slit-power-coupling calculations for natural and laser guide-star adaptive optics*', Appl. Opt. **37**, p4569-4576 (1998)

20. Whiteley, M.R., Roggemann, M.C., Welsh, B.M., '*Temporal properties of the Zernike expansion coefficients of turbulence-induced phase aberrations for aperture and source motion*' J. Opt. Sci. Am. A **15**, p993-1005 (1998)

21. Yura, H.T. and Tavis, M.T, '*Centroid anisoplanatism*', J. Opt. Sci. Am. A **2**, p765-773 (1985)

22. Dainty, J.C., 'Optical *Effects of Atmospheric Turbulence*' in '*Laser Guide Star Adaptive Optics for Astronomy*', eds. Ageorges, N. and Dainty, C., NATO ASI Series C:551, Kluwer Academic Publishers, Dordrecht. (2000)

23. Rousset, G, '*Wave-front Sensors*', appears in '*Adaptive Optics for Astronomy*', ed. Roddier, F, Cambridge University Press, Cambridge (1999)

24. J. C. Geary, '*Rapid-framing CCDs with 16 output ports for laser guide star sensors*', Proc SPIE **2201** p607-612

25. Janesick, J. '*Fundamentals of Scientific Charge Coupled Devices*', SPIE **PM38**, SPIE Press (2001)

26. Beckers, J.M., '*Increasing the Size of the Isoplanatic Patch with Multiconjugate Adaptive Optics*', in 'Very Large Telescopes and their Instrumentation', ed Marie-Helene Ulrich. ESO Conference and Workshop Proceedings, p.693 (1988)

27. Ragazzoni, R., Farinato, J., Marchetti, '*Adaptive optics for 100-m-class telescopes: new challenges require new solutions*', Proc. SPIE **4007**, 1076 (2000)

28. Bello, D., Conan, J-M, Rousset, R., Ragazzoni, R., '*Signal to noise ratio of layer-oriented measurements for multiconjugate adaptive optics*', A&A, **410**, p1101–1106 (2003)

29. Ragazzoni, R., Diolaiti, E., Farinato, J., Fedrigo, E., Marchetti, E., Tordi, M. and Kirkman, D., '*Multiple field of view layer-oriented adaptive optics. Nearly whole sky coverage on 8m class telescopes and beyond*', A&A **396** p731-744

30. Carbillet, M., Femenia, B., Esposito, S., Brusa, G., Correia, S., '*Closed-loop performances of a modal MCAO system using real star configurations: the young open cluster NGC2362 as seen by MAD*', in '*Beyond conventional adaptive optics: a conference devoted to the development of adaptive optics for ELTs*' Edited by E. Vernet, R. Ragazzoni, S. Esposito, and N. Hubin. ESO Conference and Workshop Proceedings, **58**, p25 (2002)

31. Diolaiti, E., Ragazzoni, R., Tordi, M., '*Closed loop performance of a layer-oriented multi-conjugate adaptive optics system*', A&A **372**, p710-718 (2001)

32. Johnston, D.C., Welsh, B.M., '*Analysis of multiconjugate adaptive optics*', J. OPT. SCI. AM. A **11** p394-408 (1994)

33. Langlois, M., Moretto, G., Richards, K., Hegwer, S., Rimmele, T.R., '*Solar multiconjugate adaptive optics at the Dunn Solar Telescope: preliminary results*' Proc SPIE **5490** p59-66 (2004)

34. Simons, D., '*Longitudinally averaged R-band field star counts across the entire sky*', Gemini Technical note **30** (1995)

Chapter 2: LGS AO Systems

2.1 Introduction

As was demonstrated in Chapter 1, NGS AO systems suffer from the shortcoming of poor sky coverage. To improve sky coverage, an LGS that is bright enough to act as a high-order wavefront reference can be created near to the object of interest.

The most common ways of creating a wavefront reference source in the atmosphere using a laser rely on photon scattering processes within the atmosphere. Elastic scattering processes within the atmosphere give rise to so-called Rayleigh LGSs, sometimes also called Rayleigh beacons. An alternative and commonly used method creates a sodium guide star by stimulating emission from a thin layer of sodium atoms that are present between 80 and 100km above the Earth's surface. Sodium LGSs are in use as wavefront references for AO systems at various astronomical [1,2] and military sites [3] around the world. The concept of using an LGS as a wavefront reference for an AO system [4] was initially classified as part of a military investigation into high-energy laser propagation, although the idea was independently introduced into the astronomical community at a later date [5].

2.2 LGS types

Although this work is primarily concerned with the study of Rayleigh LGSs, an examination of the relative merits of both Rayleigh and sodium guide stars points to many applications where one type of beacon is more suitable than the other.

2.2.1 Sodium LGS

Sodium LGSs are created by illuminating a layer of sodium atoms situated between 80 and 100km above the surface of the Earth with light tuned to an electronic transition within the sodium atom. The strongest of these lines for the sodium atom is the D2 line, centred at 589nm. The generation of a laser tuned to the sodium 589nm line is complex, making current sodium lasers bulky and expensive. Fibre-based lasers do not currently output 589nm light with the required power to create a suitably-bright LGS. Approximately 5-10W of laser power are required to create a sodium LGS.

The return flux from a sodium beacon is dependent on numerous factors which result in highly variable return from a sodium LGS on a night-to-night basis. The sodium density at 90km varies with season, with a greater sodium density observed during the winter than the summer [6,7,8]. The sodium layer can also separate into distinct layers, reducing WFS performance. An upper limit on the flux that can be obtained from a sodium LGS is reached when the excited states of the sodium atoms being illuminated becomes saturated [9,10]. Further increases in return flux from the sodium layer can be found through techniques such as matching the Doppler broadened linewidth of sodium at the LGS focal altitude, and controlling the output polarisation state of the laser. However, there is a finite limit on the sodium return flux that is dependent on the sodium column density. To increase the return flux beyond the saturation point, a larger number of sodium atoms must be excited. This involves increasing the LGS spot size, but this can have an adverse effect on the WFS performance, as discussed in Chapter 5.

2.2.2 Rayleigh LGS

A Rayleigh LGS is formed when photons are elastically backscattered from molecules within the atmosphere. By using a pulsed laser, a temporal range gate can be employed to select a small vertical section of the Rayleigh plume. A high-speed WFS shutter is used to create the range gate. Many methods of creating a high-speed shutter exist [11,12]. Normally, Pockels cells that switch at the laser repetition rate (usually 5-10kHz) are used to rotate the polarisation state of an incoming wavefront and hence provide a means for modulating the amplitude of the beam into the WFS. The cells are placed between crossed polarisers to form a high-speed shutter. The range gate depth and distance from the launch aperture of the LGS are products of the timings input to the shutter. Each pulse from the laser is not emitted instantaneously, but has a pulse width that is defined by the FWHM of the pulse energy. A typical pulse has a profile as shown in Figure 2.1.

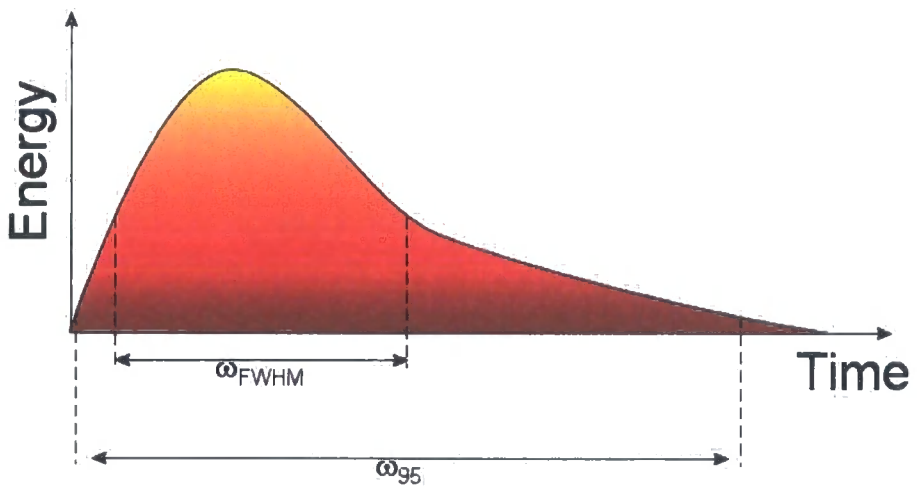

Figure 2.1 Typical pulse profile of a pulsed laser. The pulse width is normally quoted as a FWHM value. Typcial value for the pulse width range in value from femtoseconds to hundreds of nanoseconds.

The FWHM pulse width is dependent on the laser gain medium used. The standard gain medium used in commercially available lasers suitable for the creation of a

Rayleigh LGS is normally Nd:YAG, although other materials, such as Yb:YAG can be used. A Nd:YAG has a pulse width of approximately 120ns FWHM, while Yb:YAG has a longer pulse width of 400ns FWHM. For a Rayleigh LGS, the pulse width defines the minimum range gate depth that can be achieved before the shutter system starts to chop the tail of the pulse, decreasing signal on the WFS. It is better to specify the pulse width of a Rayleigh laser in terms of a full width at a given percentile of the total pulse energy.

To create a 200m range gate at 20km requires the shutter to open after the outgoing light pulse has travelled to the lowest point of the range gate, i.e. 19.9km distant, and the backscattered light has had time to return. The shutter must then remain open for the time taken for the pulse to travel the 200m to the top of the range gate in the atmosphere and return the same distance. Table 2.1 describes the system timing required to create the above range gate where the shutter is opened after the pulse has travelled a distance of 39.8km and closes after the light has travelled a distance of 40.2km

Time (μsecs)	Event Description
0.0	Laser Q-switch opens (laser pulse starts)
0.020	Leading 95% percentile energy point exits laser aperture
0.087	Leading 95% percentile energy point exits BLT launch aperture
0.620	Trailing 95% percentile energy point exits laser aperture
0.687	Trailing 95% percentile energy point exits BLT launch aperture
66.420	Leading edge reaches bottom of range gate at 19.9km
67.020	Trailing edge reaches bottom of range gate at 19.9km
67.087	Leading edge reaches top of range gate at 20.1km
67.687	Trailing edge reaches top of range gate at 20.1km
132.853	Leading edge backscatters from bottom of range gate into shutter (shutter opens)
133.453	Trailing edge backscatters from bottom of range gate into shutter
134.187	Leading edge backscatters from top of range gate into shutter (shutter closes)
134.787	Trailing edge backscatters from top of range gate into shutter
200.000	Next pulse generated (Initial pulse at 60km)

Table 2.1 Laser pulse chronology for an LGS created at a distance of 20km with a range gate depth of 200m. The laser pulse rate is 5Khz and there is a 20m path length between laser head and beam launch telescope.

The photon return from a Rayleigh LGS is dependent on the molecular density in the atmosphere. The exponential decay of atmospheric pressure with increasing altitude results in a lower photon return as the Rayleigh LGS altitude is increased. This limits the maximum altitude for a Rayleigh LGS to approximately 35km above sea level using currently available commercial lasers. This altitude can be increased if more powerful lasers are used. Although the output power of lasers is continually increasing, there is a power level where the laser itself can induce turbulence in the atmosphere. At this level the suitability of a Rayleigh LGS AO system for the correction of an astronomical wavefront is reduced.

2.3 LGS Error Sources

The comparison of Rayleigh with sodium beacons first requires an examination of the sources of error associated with using a LGS.

2.3.1 Finite Altitude of the LGS

The creation of an LGS within the atmosphere means that there will always be a proportion of the turbulent atmosphere above the LGS. This is not a problem if the object one is trying to observe lies within the atmosphere, but for astronomical AO where the object of interest always lies outside the atmosphere, unsensed atmosphere above the LGS can introduce significant errors between the turbulence-induced wavefront from the LGS and the object of interest. Most aberrations in a turbulent wavefront are induced at altitudes below 20km in the atmosphere, and the further above this altitude that the LGS can be created, the smaller the difference between the

wavefront measured from the LGS and wavefront of the target object. The error source brought about by the limited altitude of atmospheric sampling and projection effects due to conical rather than cylindrical illumination is called focal anisoplanatism. Figure 2.2 illustrates the cause of focal anisoplanatism, which is also referred to as the 'cone effect'.

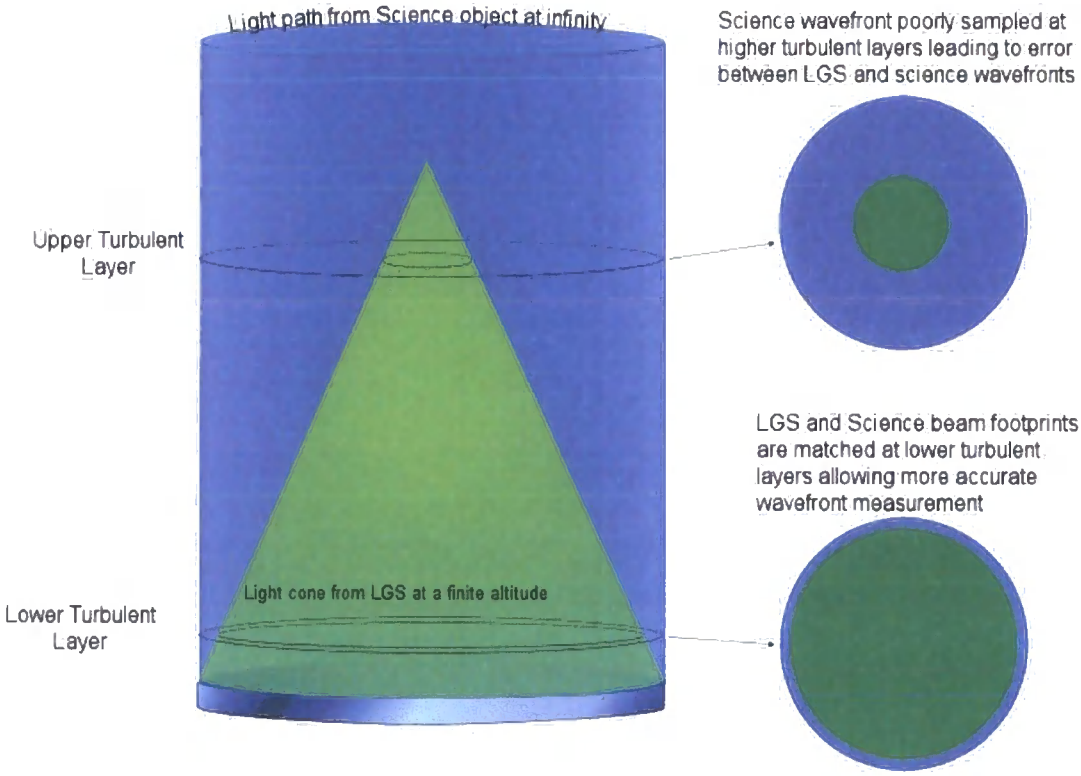

Figure 2.2 Cone Effect caused by using a wavefront reference at a finite altitude

Focal anisoplanatism (FA) is caused by parts of the turbulent atmosphere that are sensed by a wavefront originating from an astronomical source (effectively infinity) and the turbulence sensed by a wavefront originating from the LGS. FA is the major source of error present between science and LGS wavefronts. The wavefront variance between the measured LGS wavefront, and actual wavefront incoming from the target object is dependent on the vertical distribution of turbulence, given by the C_n^2 profile. The wavefront variance due to focal anisoplanatism is given by [13]:

$$\sigma_{FA}^2 = 0.207k^2 \int_0^\infty C_n^2(h)dh \int f(\kappa)g(\gamma,\kappa,z)d\kappa \qquad \text{- 2.1}$$

where k is the temporal wavenumber of the propagating wave,

κ is the spatial wavenumber transverse to the h direction,

$f(\kappa)$ is the two-dimensional turbulence spectrum (normally Kolmogorov).

The wavefront variance due to the cone effect can be added to the overall system wavefront variance (Equation 1.15) to determine the system Strehl ratio. An alternative form for this equation was derived by Fried and Belsher [14] reducing the effect of focal anisoplanatism to a single parameter, d_0, the LGS equivalent of the Fried parameter, r_0.

$$\sigma_{FA}^2 = \left(D/d_o\right)^{5/3} \qquad \text{- 2.2}$$

It was shown by Sasiela [15] that d_0 can be expressed in terms of turbulence moments (introduced in Chapter 1) by

$$d_0 = \left\{ k^2 \left[0.057\mu_0^+(H_{LGS}) + 0.500\frac{\mu_{5/3}^-(H_{LGS})}{H_{LGS}^{5/3}} - 0.452\frac{\mu_2^-(H_{LGS})}{H_{LGS}^{2}} \right] \right\}^{-3/5}, \qquad \text{- 2.3}$$

where H_{LGS} is the focal altitude of the LGS. The basic concept of an LGS involves creating an artificial star at as high an altitude in the atmosphere as possible to increase d_0 and therefore limit the cone effect. However, this approach does not provide good off-axis performance as the corrected field of view is limited by the effects of angular anisoplanatism and the isoplanatic patch size.

2.3.2 WFS Spot Elongation

Both sodium and Rayleigh LGSs have a finite depth in the sky. In the case of a sodium LGS, this depth is dependent on the sodium column depth, which is of the order of 10km. For a Rayleigh LGS, the depth is usually externally defined through temporal range gating of the Rayleigh plume. When using a SH-WFS, the finite depth of the LGS exhibits itself as an elongation of the WFS spot within a subaperture in the direction of propagation. Spot elongation of a z-extended LGS is a geometrical problem and can be modelled. Chapter 5 examines the error associated with wavefront sensing from a z-extended reference. The optical z-axis is a common definition in optics describing the direction of propagation of a beam.

2.3.3 WFS Launch Jitter

Launch jitter is the name given to any global LGS spot motion that is observed on the LGS WFS. Launch jitter is caused by vibrations in the launch optics, pointing stability of the laser, and differential tilt between the launch and return paths the laser travels through the atmosphere. The effect of launch jitter is to place a spurious tilt across the LGS wavefront. Launch jitter can be simply removed using a closed-loop tilt correction system controlled by the tip/tilt signal from the LGS WFS. A fast-steering mirror (FSM) correcting the launch jitter is normally placed in the optical train of the laser launch system [16], giving rise to pre-launch jitter correction. However, the WFS jitter can also be corrected with a FSM that corrects the LGS wavefront only. This is known as post-launch launch jitter correction.

Performance of a SH-WFS can be seriously degraded when the magnitude of the launch jitter approaches the boundary of a subaperture, as vignetting can occur. The field of view of the lenslet must then be further increased beyond that required to accommodate any spot elongation. However, this can degrade the accuracy of subaperture centroid determination, and hence reduce WFS performance.

2.3.4 LGS Tilt Reciprocity

One of the major sources of error in the wavefront coming from an LGS is caused by the double propagation of the laser through the atmosphere. This problem is demonstrated when the full aperture of the telescope is used to project and observe the LGS.

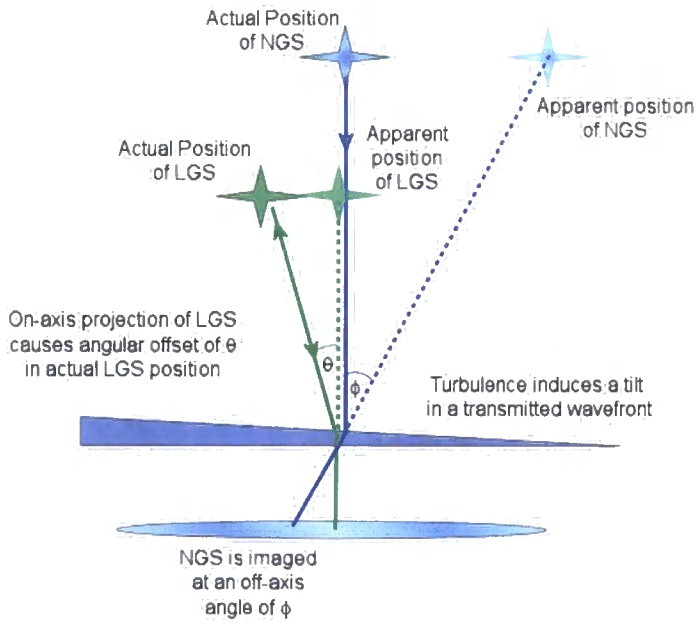

Figure 2.3 Diagram showing cause of atmospheric tilt reciprocity. If the LGS is launched using the full aperture of the telescope, the angle θ is identical on both uplink and downlink LGS paths (shown by the green arrows) and no LGS spot motion is observed. θ can not therefore be determined. For turbulent layers where the LGS and NGS beam diameters are not equal $\theta \neq \phi$.

For the simple case shown in Figure 2.3, a single turbulent layer injects a tilt on the LGS on the uplink, offsetting the LGS spot on the sky in relation to the wavefront coming from the science object at infinity. The offset in the LGS position is cancelled by the double pass through the turbulent layer when the LGS light is collected by the telescope. The LGS therefore will appear stationary when observed by the telescope. The science light however, only makes a single pass through the atmosphere so experiences the full atmospheric tilt. To determine the wavefront tilt for science objects, a separate NGS must be used to measure tip-tilt. Sensing only atmospheric tip-tilt reduces the required NGS intensity as the light does not need to be separated between individual subapertures, as is the case with a high-order NGS AO system, and longer integration times can be used. Longer integration times will not increase wavefront temporal errors as wavefront tip-tilt changes at a much lower rate than higher spatial frequency modes. The combination of an LGS with tip-tilt NGS can give near 100% sky-coverage for AO correction.

The above example, whereby the wavefront tilt is completely reciprocal, is not a true description of AO systems that utilise a secondary BLT to create the LGS. The differential tilt on uplink and downlink LGS paths results in apparent LGS motion and an NGS is still required to stabilise the position of the science image. The differential spot motion means that any global tilt observed by the LGS WFS should be ignored by the AO system, although in many cases it is used to stabilise the position of the LGS spot on the sky using an independent closed-loop LGS fast steering system.

2.4 Ground Layer AO

As with NGS MCAO systems, multiple LGSs can be used to give wide-field AO correction. However, as an LGS can be positioned at any point in the sky, an LGS MCAO system can provide a far more uniform degree of AO correction across a given field of view. All MCAO systems are complex and expensive, requiring multiple WFSs, DMs and if being used, multiple LGSs.

The technique of correcting the lowest layers of turbulence only was proposed as 'restricted-conjugate' AO by Sharples et al [17] and later by Rigaut [18] under the name 'ground-layer' AO, which has been adopted as the term used to describe the technique ever since. Correcting low-altitude turbulence only provides a low-level of AO correction over a wide field of view because low-altitude turbulence is common to all field angles. Whilst Ground-Layer AO (GLAO) does not provide the high-strehl correction over a wide field that a full MCAO system would, it is often referred to as a 'seeing-improvement' system, greatly improving the efficiency of telescope observations.

The definition of the atmospheric ground layer is site-dependent. At Cerro Paranal in Chile, the site of the Very Large Telescope (VLT), there is a good indication that the ground layer is normally contained within the first 100m above the observatory [19], however at sites such as La Palma it can be found at altitudes up to 500m [20]. At these altitudes the surrounding topology can influence the maximum altitude of the ground layer and can be dependent on wind direction. Obviously, the lower the altitude of the ground layer, the wider the GLAO corrected field becomes. The suitability of GLAO to a particular site, or at least particular weather conditions, is increased whenever low-altitude turbulence becomes dominant.

There are various methods for achieving selective correction of the ground-layer. The first is to use a low-altitude LGS that only samples the lowest layers of turbulence. This is the simplest method, using only a single LGS, DM and WFS, but is sensitive to the maximum altitude of the ground layer. The second method is a by-product of an MCAO system as the ground layer wavefront can be obtained by co-adding the WFS images from each guide star sampled within the AO control system. This process 'blurs' the high-layer turbulence unique to each field angle, leaving only the ground-layer component of the observed turbulence.

2.4.1 Rotating LGS

A novel methodof measuring a ground layer wavefront, presented here for the first time, is to change the position of the LGS on the sky during a single WFS frame, and to correct the resulting apparent tilt with an LGS FSM conjugated to the telescope pupil on the return path. The performance of an AO system utilising this technique has not been studied prior to this work. If the phase and amplitude of the LGS on-sky rotation is matched by the correction of the LGS FSM, this will result in an apparently static LGS. The LGS wavefront will then be dominated by the wavefront terms that are common to all return paths of the LGS i.e. ground layer turbulence. Obviously the LGS FSM cannot receive a control signal from the LGS WFS as the frequency of LGS motion is, by definition, higher than the closed-loop speed of the WFS. This means the FSM must receive an open-loop signal from the LGS offset system, as shown in Figure 2.4.

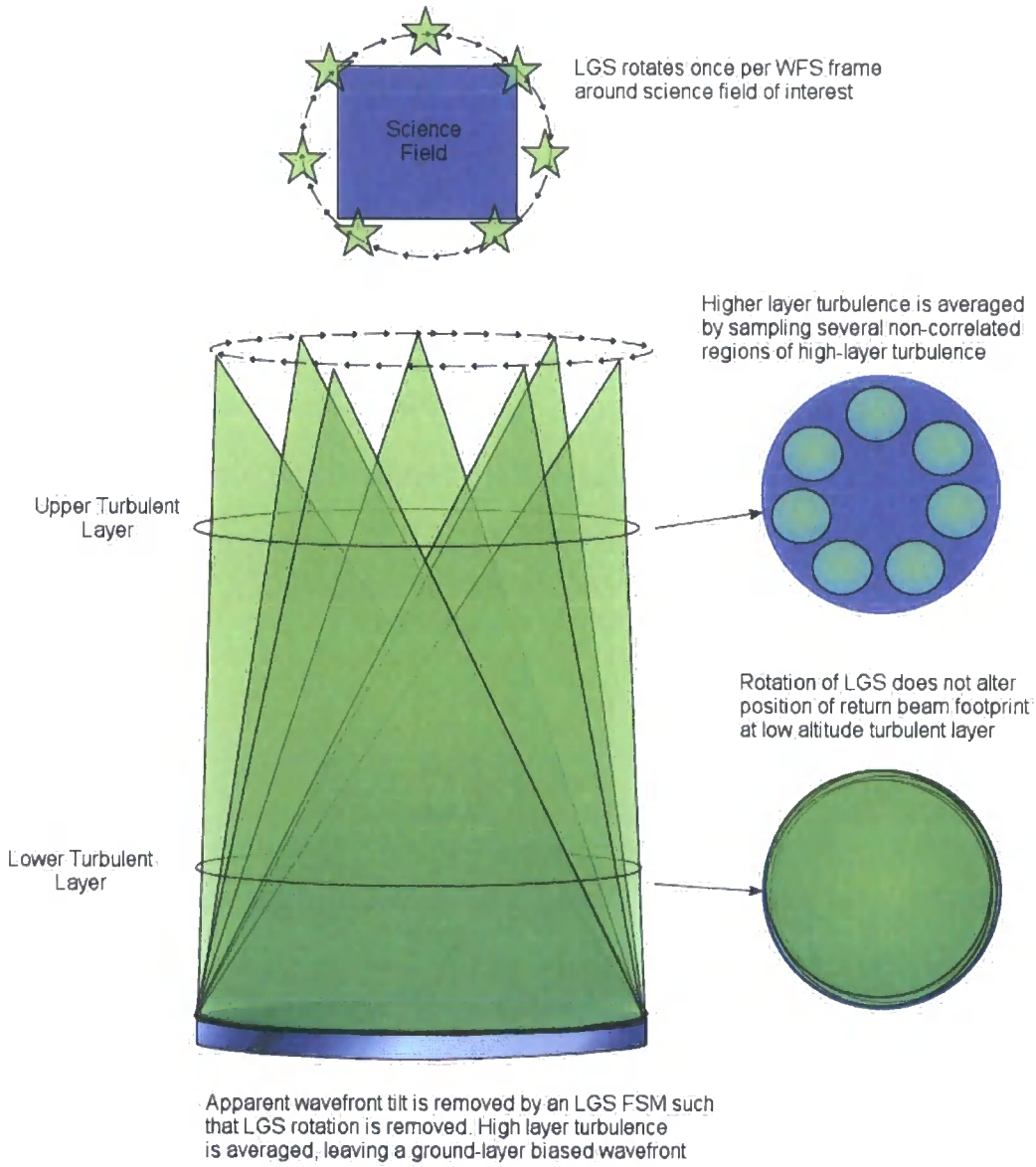

Figure 2.4 Scheme for rotating guide star to achieve ground layer only correction from a single, high-altitude LGS

The simplest scheme for the launch offset and then post-correction of the LGS described above is to rotate the LGS around the centre of the science field. This allows two sinusoidal DC offsets to the FSM (with a suitable amplitude and phase delay) to correct for the launch offset signal. A simple scheme for adapting the

demonstrator launch system (described in Chapter 4) is shown in Figure 2.5. This scheme then approximates the optimum LGS configuration for GLAO correction on an ELT [21].

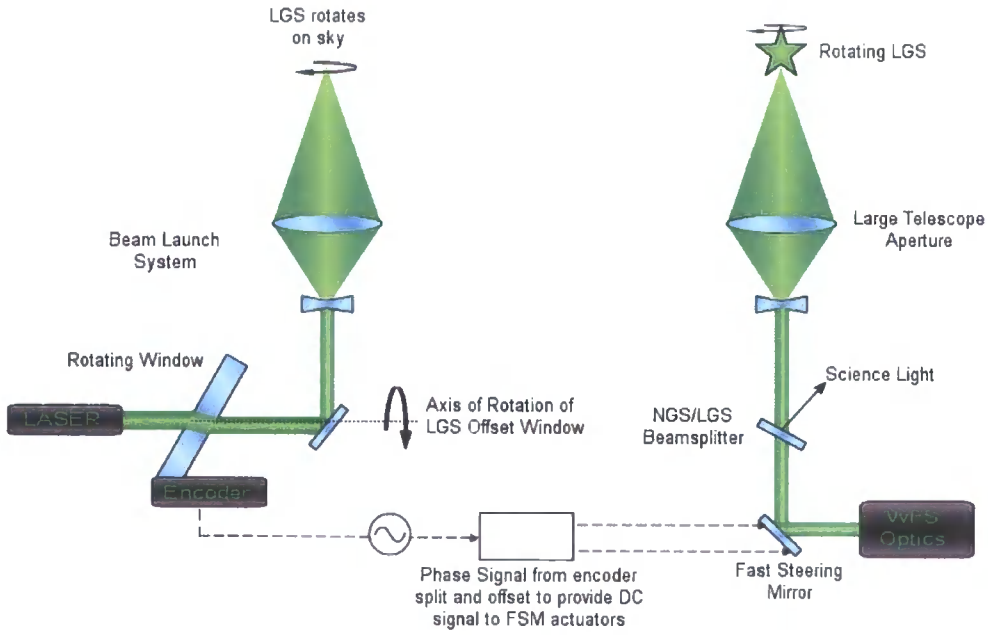

Figure 2.5 Launch system concept to generate rotating guide star. The LGS offset window works by moving the virtual focus formed by the diverging lens around the optical axis of the launch lens. This moves the focal position of the LGS on the sky in a circular path on the sky.

The performance of a rotating laser guide star for measuring a ground-layer wavefront is determined by several factors, including angular magnitude of offset, vertical distribution of turbulence, laser launch and return aperture diameters, and frequency of LGS rotation. The effect of the LGS rotation reduces WFS SNR as the spot motion due to high layer turbulence is blurred within a subaperture. A performance model of a rotating LGS was made and the results of this study are presented in the Chapter 7 which concentrates on AO system modelling.

Each of the three methods described above can determine a ground-layer wavefront, although in the case of the two simplest methods, this may be more accurately described as a ground-layer *biased* wavefront. The method chosen for achieving ground-layer AO with the Durham demonstrator system was to create a low-altitude guide star. This is the least technically demanding implementation of a GLAO system, and was chosen primarily for the relative simplicity of the technique, although the power of the Rayleigh laser also limited the altitude from which the signal on the WFS would provide an accurate measure of the wavefront. An analysis of the LGS parameter space is presented in Chapter 5.

2.4.2 LGS GLAO performance

Several analyses of the performance of GLAO wavefront determination have been published [22,23] as well as the results from several GLAO simulations [24,25]. More recently, the results of on-sky analysis of ground-layer wavefronts from MCAO systems have been presented [26,27], although on-sky GLAO correction has not been demonstrated. As with any GLAO system, regardless of GLAO method, the off-axis performance of the system is highly dependent on the vertical distribution of turbulence. For a low-level LGS, the optimum case is found when there is a single layer of turbulence at the ground, and high-layer turbulence exists at an altitude above the focal altitude of the LGS. Turbulence that exists at altitudes between the ground layer and the focal altitude of the LGS contaminates the WFS signal, causing poor correction of the infinity focused science field. The optimum altitude of a low-level LGS is therefore (atmospheric) condition dependent, which in turn is dependent on the observatory site.

Characterisation of the atmosphere on La Palma [28] has shown that a 3-layer atmosphere, with layers at 0km, 2.5km and 7.5km with a 0.4:0.4:0.2 turbulence strength split, can be used to describe a 'standard' La Palma atmosphere. The optimum altitude at which a low-level LGS can determine a ground layer wavefront is determined in Chapter 7 as a result of running numerical simulations.

The numerical simulations of GLAO performance have shown that while GLAO will not provide anything near diffraction limited performance, some correction will be observed. Once the ground layer correction is coupled with the fact that, for long exposure images, the corrected FOV exhibits an extremely uniform PSF across a large field of view (as described at the start of section 2.4), GLAO becomes an attractive technique for astronomical observations. The performance of GLAO has often been referred to as a seeing-improvement system as is has the potential to turn a 'bad-seeing' night into a 'good-seeing' night, thus greatly increasing the efficiency of telescope observation programs. As has been observed by site-monitoring campaigns [29,30] that have examined low-altitude turbulence, the 'ground' layer can vary in strength and mean altitude considerably, requiring careful scheduling to optimise telescope efficiency.

2.4.3 GLAO systems

Although GLAO has not been successfully demonstrated on-sky yet, several experimental and facility-class GLAO systems have been proposed are in various stages of development. This work describes the first instrument to attempt GLAO correction on-sky.

ESO are building the Multiconjugate Adaptive Optics Demonstrator (MAD) [31]. MAD was due to be commissioned on one of the VLT UTs (Unit Telescopes) in the summer of 2005, although the system is still in laboratory testing phase. MAD takes the wavefronts from 3 to 8 NGSs to perform atmospheric tomography and correct the observed wavefront using two DM's. One DM is conjugated to the ground layer and therefore GLAO can be tested. MAD has both star-oriented and layer-oriented MCAO configurations.

MANU-CHAO [32] is a GLAO demonstrator for the TNG (Telescope Nazional Galileo) which uses four pyramid wavefront sensors to optically co-add the light from 4 NGSs within the telescope field of view. The measured wavefront will be corrected using a single 96 actuator DM conjugated near to the telescope pupil providing ground-layer correction.

The 4.2m SOAR (Southern Astrophysical Research) telescope is currently in the design phase for a GLAO system that utilises a low-altitude RLGS. SAM (SOAR Adaptive Module), [33] will project a 20W 355nm laser to 10km and correct the return using a 97-actuator DM. The SAM project bears many resemblances to this work, although it will deliver a facility-class GLAO system, rather than a experimental system. SAM is planned to be operational in 2007-2008.

Both ESO and Gemini observatories are studying almost identical GLAO systems using a 4-star sodium LGS asterism. Gemini have completed an extensive modelling of the problem [25] showing that they will be able to achieve a 0.3" ± 0.03" FWHM across a 10' field under typical atmospheric conditions for Cerro Pachón. Median seeing at Cerro Pachón is 0.717". Importantly, the study also suggested that the

efficiency of the Gemini telescope will be increased by 50%, thereby increasing science productivity.

A GLAO WFS is being tested on the Magellan telescopes [34] to examine the correction across the 23' Magellan FOV. The WFS will be made using relatively coarse 0.6m subapertures at a 100Hz frame rate.

The 6.5m MMT (Multiple Mirror Telescope) is being fitted with a RLGS which creates a 5-star asterism. The MMT RLGS system incorporates a dynamic refocus mechanism that allows the 5 guide stars to be created at a distance of 20km using 30W of laser power at 532nm. The MMT will use a deformable secondary mirror to correct the wavefront. On-sky WFS tests have shown that the 5 Rayleigh LGS asterism can expect to correct a field of 2 arcminutes in diameter using GLAO correction.

2.5 Conclusion

The error sources associated with using an LGS at a finite altitude have been presented and the concept of GLAO has been introduced. Various methods of determining a ground-layer wavefront have also been presented.

As can be seen by the large number of proposed instruments that will utilise GLAO, the concept is one that is attractive to the astronomical community as a method of improving seeing, and thereby increasing telescope scientific output. All observations will benefit from the increased resolution and uniform PSF that GLAO can provide.

2.6 References

1. Wizinowich, P.L., Le Mignant, D., Bouchez, A., Chin, J., Contos, A., Hartman, S., Johansson, E., Lafon, R., Neyman, C., Stomski, P., Summers, D., van Dam, M.A., '*Adaptive optics developments at Keck Observatory*', SPIE 5490, p. 1-11 (2004)
2. Gavel, D.T., Gates, E.L., Max, C.E., Olivier, S.S., Bauman, B.J., Pennington, D.M., Macintosh, B.A., Patience, J., Brown, C.G., Danforth, P.M., Hurd, R.L., Severson, S.A., Lloyd, J.P., '*Recent science and engineering results with the laser guide star adaptive optic system at Lick Observatory*', SPIE 4839, p354-359 (2003)
3. Fugate, R. Q., Fried, D. L., Ameer, G. A., Boeke, B. R., Browne, S. L., Roberts, P. H., Ruane, R. E., & Wopat, L. M., '*Measurement of Atmospheric Optical Distortion Using Scattered Light from a Laser Guide Star*', Nature, 353, 144 (1991)
4. Feinlib, J. proposal 82-P4, Adaptive Optics Associates, Cambridge, Mass. (1982)
5. Foy, R., Labeyrie, A., '*Feasibility of adaptive telescope with laser probe*', A&A 152, , pL29-L31 (1985)
6. L. Michaille et al, 'Characterisation of the mesospheric sodium layer at La Palma', MNRAS 328 p993-1000 (2001)
7. Papen G. C., Gardner C. S., Yu G., Adaptive Optics 13, OSA Technical Digest Series 96. (1996)
8. Megie G., Blamont J. E., '*Laser sounding of atmospheric sodium interpretation in terms of global atmospheric parameters*', Planet Space Sci., 25, 1093 (1977)
9. Milonni P., Fugate R., Telle J. M., '*Analysis of measured photon returns from sodium beacons*', J. Opt. Soc. Am. A, 15, 217 (1998)
10. Milonni P.W., Fearn H., Telle J. M., Fugate R. Q., '*Theory of continuous-wave excitation of the sodium beacon*', J. Opt. Soc. Am. A, 16, 2555 (1999)
11. Thompson, L.A., Teare, S.W., Crawford, S.L., Leach, R.W., '*Rayleigh Laser Guide Star Systems: UnISIS Bow-Tie Shutter and CCD39 Wavefront Camera*', PASP 114 p1143-1149 (2002)
12. Reich, R.K., Mountain, R.W, McGonagle, W.H., Huang, J., Twichell, J.C., Kosicki, B.B., Savoye, E.D., '*Integrated Electronic Shutter for Back-illuminated Charge-Coupled Devices*', IEEE Trans. Elec. Dev. 40 p1231-1236
13. Hardy, J.W., '*Adaptive Optics for Astronomical Telescopes*', Oxford University Press, Oxford (1998)
14. Fried, D.L., Belsher, J.F. '*Analysis of fundamental limits to artificial guide star adapvtive optics system performances for astronomical imaging*', J. Opt. Sci. Am. A 11, p277-287 (1994)

15. Sasiela, R.J., '*Wave-front correction by one or more synthetic beacons*', J. Opt. Sci. Am. A 11, p379-393 (1994)

16. d'Orgeville, C., Bauman, B., Catone, J., Carter, C., Ellerbroek, B., Gavel, D., Hunten, M., James, E., Sheehan, M., '*Gemini Laser Launch Telescope Requirements Document*', Gemini Observatory, (2001)

17. Sharples, R. M., Myers, R.M., Walton, N.A., '*MOSAIC: A Multi-Object Spectrograph with Adaptive Image Correction*' Proc. SPIE 4008 p228-236 (2000)

18. F. Rigaut, '*Ground-Conjugate Wide Field Adaptive Optics for ELTs*', in '*Beyond conventional adaptive optics: a conference devoted to the development of adaptive optics for ELTs*' Edited by E. Vernet, R. Ragazzoni, S. Esposito, and N. Hubin. ESO Conference and Workshop Proceedings 58, p25 (2002)

19. Sarazin, M., '*Double star Cn2 profiler - SLODAR: Slope Detection and Ranging*', ESO, http://www.eso.org/gen-fac/pubs/astclim/paranal/asm/slodar/, (3/9/2005)

20. Hoegemann, C.K., Chueca, S., Delgado, J.M., Fuensalida, J.J., Garcia-Lorenzo, B., Mendizabal, E.G., Reyes, M., Verde, M., Vernin, J., '*Cute SCIDAR: presentation of the new Canarian instrument and first observational results*', Proc. SPIE 5490, p774-784 (2004)

21. Tokovinin, A., Le Louarn, M., Sarazin, M., '*Isoplanatism in a multiconjugate adaptive optics system*', J. Opt. Sci. Am. A 17, p1819-1827 (2000)

22. M. Chun, '*Gains from ground-only adaptive optics system*', Proc. SPIE, 4839, pp. 94-98, 2003

23. Tokovinin, '*Seeing improvement with ground-layer adaptive optics*', PASP, 116, pp. 941-951, 2004

24. Hubin, N., Le Louarn, M., Conzelmann, R., Delabre, B., Fedrigo, E., Stuik, R., '*Ground layer AO correction for the VLT MUSE project*', Proc SPIE, 5490, pp. 846-857 (2004).

25. '*Gemini Ground Layer Adaptive Optics Feasibility Study Report*', http://www2.keck.hawaii.edu/optics/aowg/GLAO-FSR.pdf (23/2/2005)

26. Stalcup, T.E., Jr., Georges, J.A., III, Snyder, M., Baranec, C., Putnam, N., Milton, N.M., Angel, J.R.P., Lloyd-Hart, M., '*Field tests of wavefront sensing with multiple Rayleigh laser guide stars and dynamic refocus*', Proc. SPIE 5490, p1021-1032 (2004)

27. Baranec, C.J., Lloyd-Hart, M., Codona, J.L., Milton, N. M., '*Sky demonstration of potential for ground-layer adaptive optics correction*', SPIE 5169, p341-348 (2003).

28. Wilson, R.W., '*Results of the JOSE site evaluation project for adaptive optics at the William Herschel Telescope*', New Astronomy Reviews, 42, p465-469. (1998)

29. Wilson, R. W., O'Mahony, N., Packham, C., Azzaro, M., '*The seeing at the William Herschel Telescope*', MNRAS, 309, p379-387. (1999)

30. Sarazin, M. , Butterley, T., Tokovinin, A., Travouillon, T., Wilson R., '*The Tololo SLODAR Campaign*', ESO Website (2005)

31. Marchetti, Enrico; Hubin, Norbert N.; Fedrigo, Enrico; et al., '*MAD the ESO multi-conjugate adaptive optics demonstrator*', Proc. SPIE, Volume 4839, pp. 317-328 (2003)

32. Farinato, Jacopo; Ragazzoni, Roberto; Arcidiacono, Carmelo; et al., '*Layer-Oriented on Paper, Laboratory and soon on the Sky*', Proc. SPIE, Volume 5382, pp. 578-587 (2004)

33. S. Thomas, '*SAM - the SOAR Adaptive Module*', EAS Publications Series, 12 p177-184 (2004)

34. Athey, A.E., Shectman, S., Schechter, P., Lane, B., '*The GMT ground-layer AO experiment at the Magellan telescopes*', Proc. SPIE, Volume 5490, p960-965 (2004)

Chapter 3: AO Systems – Past and Present

3.1 Introduction

The astronomical use of AO to correct for atmospheric turbulence was first proposed in 1953 by Horace Babcock [1], and even though the technology required to achieve partial AO correction was available, a system that was able to compensate real-time high-order atmospheric turbulence was not realised until the 1970s. Since then, many astronomical AO systems have been built, using a wide variety of technologies. This chapter describes the basic layout of any AO system and then goes on to examine the designs of many past and present NGS and LGS AO systems. Solar AO systems are also studied. For each example presented, aspects of the system design that are applicable to the low-level GLAO system design are identified and analysed.

3.2 Generic AO system

This section describes a generic AO system that could be employed at any 2-10m class telescope, while ignoring telescope-specific issues such as the optical input, space constraints, telescope diameter etc. The generic AO system introduces many of the concepts that are present in most astronomical AO systems and is a useful yardstick against which to compare an existing AO system.

An AO system consists of three elements, a wavefront sensor (WFS), a wavefront corrector (normally a deformable mirror, or 'DM') and a control system linking the two. AO systems generally operate in a closed-feedback loop, where the WFS is positioned after the DM in the optical train such that any change that the DM makes to the wavefront is observed by the WFS. A secondary corrective element is usually

included in the optical train to take out global atmospheric tip and tilt out of the wavefront. This is necessary as DM's cannot be manufactured to run at the frequencies required for high-order atmospheric correction if they have a mechanical stroke large enough to correct tip and tilt. Figure 3.1 shows the general layout of an AO system.

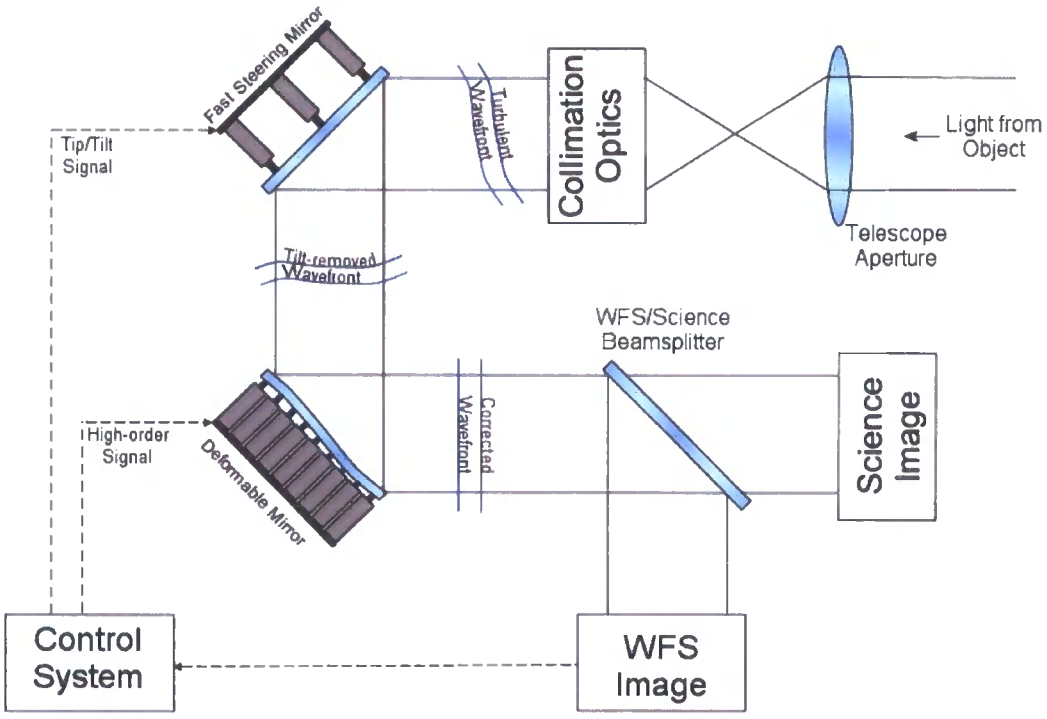

Figure 3.1 Generic AO system

A DM consists of a number of separate corrective elements that allow phase distortion of a wavefront. The optical design of an AO system is driven by the DM aperture and corrective element density. Light entering the AO system is collimated to fill a central part of the DM. The full aperture of a DM is not normally used due to either effects at the DM edge that are caused by corrective elements that are not bound on all sides, or because there may not be enough light incident on the WFS to allow higher-order correction. Normally, matched off-axis parabolic (OAP) mirrors are used to collimate the beam onto the DM and refocus the beam into the WFS. OAP elements give an

unvignetted field of view and diffraction-limited on-axis performance. A Fast Steering Mirror (FSM) is placed before collimation optics to remove gross tip-tilt from the system. Placing the FSM at this point reduces any off-axis angle present in the beam, thus reducing any static aberration caused by the off-axis propagation of the beam through the collimation optics.

The DM is then placed at the point in the collimated beam conjugate to the primary mirror of the telescope. The conjugation of the DM to the telescope aperture accomplishes two tasks. First, any point in the optical system conjugate to the pupil plane of the telescope is fixed in x and y directions (z is the direction of light propagation) so the return beam does not wander over the surface of the DM. Secondly, at most astronomical sites turbulence due to the ground layer can contribute up to 60% of the full turbulence strength [2] Placing the DM conjugate to the ground layer (or the telescope pupil) allows for the best optical registration to the observed turbulence (Figure 3.2).

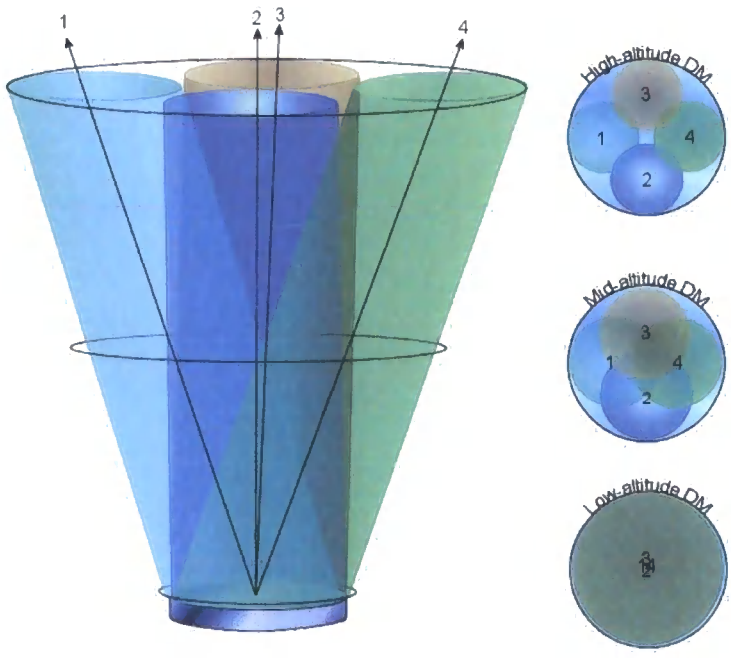

Figure 3.2 DM conjugation to ground and altitude

After the wavefront has been corrected by the DM, the light is focused by the second OAP. This removes the aberrations imposed on the wavefront by the first off-axis parabolic mirror. After this, the light is separated using a dichroic beamsplitter. Visible (or LGS, if used) wavelengths are directed towards the WFS, while the longer wavelengths are directed towards the science camera. Longer wavelengths are affected less by passage through a turbulent atmosphere. Although they exhibit almost the same amount of optical path difference in metres as a wavefront at shorter wavelength, image quality is dependent on the optical path difference in terms of wavelengths. This means a $\lambda/2$ distortion present in a visible wavefront at a wavelength of 500nm results in a $\lambda/4$ distortion at a wavelength of 1μm. A quarter-wave distortion is the classical definition of a diffraction limited system. Conversely, correction applied to a wavefront in the visible results in better correction in the IR. For this reason, most AO systems sense wavefront distortions in the visible, where the system efficiency is highest, and apply this correction to a longer wavelength observation. This allows small degrees of correction at visible wavelengths to provide diffraction-limited observations at longer wavelengths.

Astronomical AO systems operate in a photon-sparse environment because the rate at which the WFS must run to compensate for atmospheric turbulence dictates a very short exposure time (~1ms). Thus there is a requirement for a high optical throughput to the WFS, as well as the obvious requirement of a high science throughput. For this reason, the number of surfaces in the system must be kept to an absolute minimum. LGS AO systems have an advantage over NGS AO systems in this respect, as the WFS only works at a single wavelength, so all optical components can use a narrowband coating, allowing efficiencies greater than 99%, while the broadband

coatings required by NGS AO systems have a maximum 98% efficiency, although this efficiency will not be available across the entire wavelength range of operation.

Many optical components that would be present in a facility-class astronomical AO system were not included in the description of the generic AO system above. Items such as the derotator and atmospheric dispersion compensator (ADC) were not mentioned, as although they may be essential for scientific observations, their presence is not integral to the performance of the AO system. Other components may be required to allow for the optical design to fit into a particular space envelope. Due to their complexity, AO systems are generally housed at a dedicated focus of the telescope, or as is becoming the case, are integrated into the original telescope design. The space envelope would not be a constraint in this case, but many telescopes still have quite stringent weight and space limits, so this must be taken into consideration. The presence of any extra elements in the system only reduces optical throughput to the WFS and consequently reduces on-sky AO performance.

3.2.1 Control System

The tasks carried out by the AO control system linking the WFS to the DM are analysis of the WFS image, reconstruction of the wavefront and calculation of the correct form to display on the DM. The primary requirement is that this takes place within a time less than the coherence time of the atmosphere, τ_0, otherwise temporal errors can dominate system performance.

In the past, the above set of tasks has been carried out by customised Digital Signal Processor (DSP) hardware. To minimise processing time, several DSPs are used in parallel to carry out the calculations. The parallelisation over several DSPs results in a

complex hardware architecture that is often difficult and expensive to maintain and update. Recently, continuing advances in the processing power of PC microprocessors have allowed the control system to be placed within a single x86 architecture PC, vastly reducing control system cost and complexity, and often reducing latency too. This also allows further system development to be undertaken by anyone with general programming skills, rather than requiring a DSP specialist for system modifications, reducing running and training costs.

For more complex AO systems, such as MCAO where extra wavefront processing is carried out, or an ELT AO system where the data volumes are extremely large, parallelised control systems are still used, although normally a parallelised PowerPC-based architecture. Future advances involve using Field Programmable Gate Arrays (FPGAs) as a high-speed (re)configurable maths co-processor. Processor intensive applications that can be parallelised (examples include centroiding, Fourier transfers and matrix multiplications) benefit from large speed increases when carried out inside an FPGA. Taking the process a step further, an entire control system within an FPGA has been demonstrated, including WFS interface and DM control [3].

One required input that the control system requires is an interaction matrix that measures the WFS response to changes in DM shape. In the case of a SH-WFS and Xinetics DM, this involves offsetting each actuator in turn from the default mirror value and measuring the resulting spot motion on the WFS. The WFS-DM interaction matrix produced by this process can then be inverted so that the control system has knowledge of what correction to apply to the DM when a spot motion is measured during closed loop operations. An inverted interaction matrix is called the control matrix.

Measuring the interaction matrix can be complicated, especially if it is difficult to find a suitable calibration source. This is the case with telescopes that will employ an adaptive secondary mirror, where only on-sky calibrations or theoretical models of DM performance can be used to generate the interaction matrix. Interaction matrices for MCAO systems are also complicated through offset beam footprints on DMs conjugated to an altitude above the ground-layer.

3.3 NGS AO Systems

NGS AO systems use light from a bright star (normally brighter than 15^{th} magnitude [4]) to determine the wavefront distortions caused by the atmosphere. NGS AO systems are in common use at many observatories around the world, and a full study of each one is not required to illustrate all the design options/trade-offs that can be made. There is no 'perfect' AO system design, although all AO systems are designed to optimise science performance for a particular telescope and often, a particular instrument. The optimisation of science performance is less of an issue for a technical demonstrator system, where optical throughput to science cameras is not of primary concern.

3.3.1 PUEO

PUEO was installed on the 3.6m Canada-France-Hawaii Telescope (CFHT) in 1996. PUEO consists of a 19-subaperture curvature sensor coupled to a 19-element bimorph DM. A full description of the design and performance of PUEO is given in Chapter 9 of Roddier's book, *Adaptive Optics in Astronomy* [5], and is not required here,

although several results are presented from the above reference source. The design of PUEO is shown below.

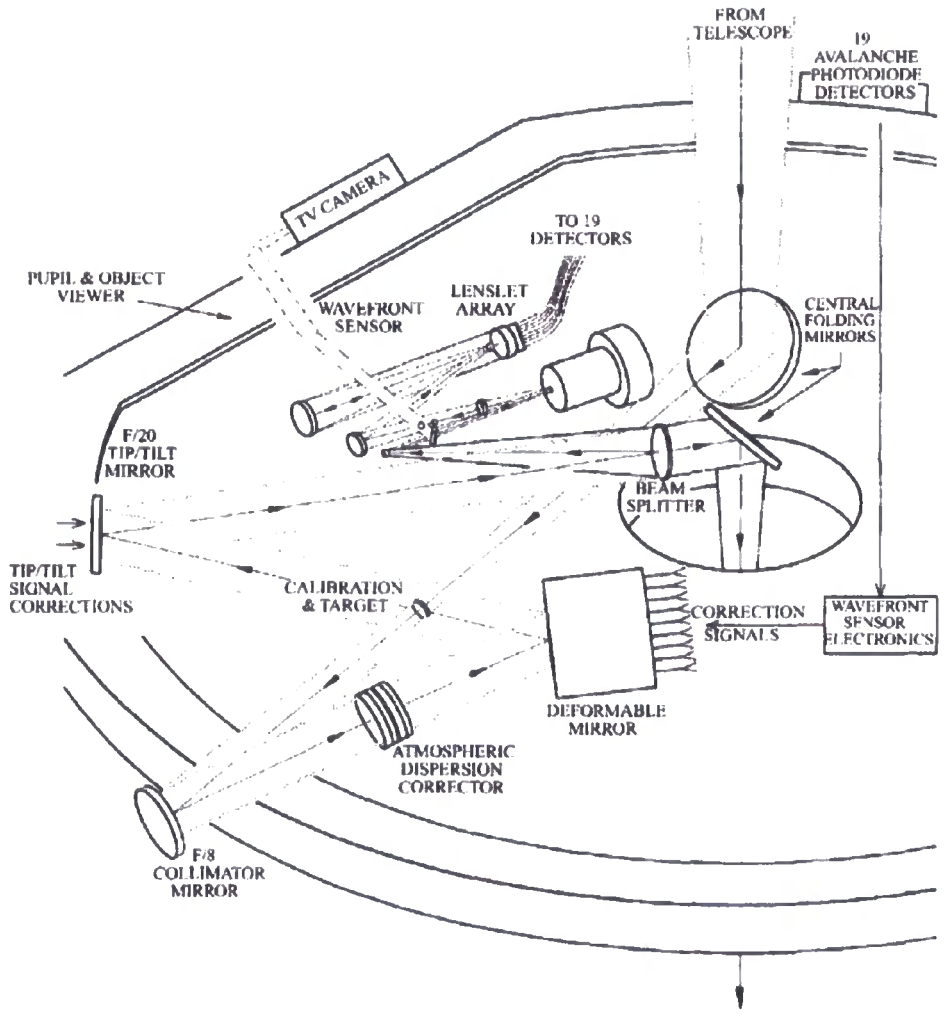

Figure 3.3 PUEO AO system schematic. Taken from '*Adaptive Optics in Astronomy*' [5]

The performance of PUEO is obviously limited to a relatively small field of view, employing only a single DM conjugated to the ground layer, as is shown by off-axis measurements of PUEO performance. The correction is also of a very low-order due to the limited number of DM elements and 19-element WFS. Large degrees of correction are restricted to longer wavelength observations only.

The PUEO design is 'transparent' to telescope operations in that the insertion of the two central folding mirrors into the beam path (see Figure 3.3) does not affect the f/ratio or focal length of the telescope. This allows the AO system to be used with any telescope instrument or removed to maximise throughput if high-angular resolution observations are not required.

The initial design of PUEO used a 52-actuator piezo-stack DM, but this mirror required a secondary SH-WFS and reference source to initially flatten the mirror, therefore this design was rejected due to the added expense. A SH-WFS being required to calibrate the deformable mirror such that it could be used closed-loop with a curvature based WFS demonstrates the necessity of matching DM and WFS geometries for optimum AO performance.

3.3.2 ALTAIR

Altair is the Gemini North AO system and consists of a 177 actuator DM with 208 subaperture WFS. Like PUEO, it is transparent to telescope operations, having an f/16 input and output beam, so can provide an AO corrected field to any current Gemini instrument.

The design of Altair was based around the idea of conjugating the DM to an altitude other than the ground layer. Characterisation of the atmospheric turbulence above Mauna Kea had been interpreted as showing that the strongest layer of turbulence was found at an altitude approximately 6.5km above the telescope. By optically conjugating the DM to this layer, the off-axis performance would theoretically be improved [6]. Significant time and effort was invested in optimising the control system to cope with the non-pupil conjugation of the DM however, the eventual off-

axis performance of Altair did not reach the level simulations predicted. Further site characterisation suggests that while strong turbulent layers existed at high altitude, turbulence at the ground layer was still significant. The apparent mis-conjugation demonstrates the importance of accurate site characterisation when designing an AO system that corrects for large fields of view.

For an MCAO system, the altitudes at which DMs should be conjugated can only be determined by site characterisation [7]. For an AO system with single DM, whilst conjugating the DM to an average height of turbulence will improve performance (e.g. two equal strength layers exist at the ground layer and 2km above ground; the average height to conjugate the DM to would be around 1km) the hour-to-hour variation of the altitude of turbulent layers that all site characterisation campaigns have shown [8,30] mean an AO system will, in general, perform better if the DM is conjugated to the ground layer. Obviously for a GLAO system, the DM should always be conjugated to (or as near as possible to) the telescope pupil.

Another important point to note in the design of Altair is that the DM does not utilise all the DM actuators present, increasing the wavelength at which diffraction-limited correction can occur. The first reason for this is to optimise sky-coverage, as larger WFS subapertures increase light collecting area, therefore allowing fainter guide stars to be used. Secondly, as the DM is not conjugated to the telescope pupil, the WFS and science beam footprints do not completely coincide. This means that the correction has to be extrapolated for some actuators, resulting in a highly complex control system, which will introduce further latencies and system errors, although these will have been accounted for in the error budget.

3.3.3 NAOMI

Due to the involvement of Durham University in the development of the NAOMI (Natural guide-star Adaptive Optics system for Multi-purpose Instrumentation) real-time control system, both the hardware and software in use in the NAOMI control system is similar to that used for the Durham experimental GLAO system. Coupled with the fact that NAOMI is also deployed on the William Herschel Telescope (WHT), and therefore subject to the same optical constraints and atmospheric conditions that the GLAO system will encounter, a close study of NAOMI is essential before an AO system is designed for the WHT.

NAOMI is installed at one of the Nasmyth foci on the 4.2m WHT on La Palma in the Canary Islands. The system uses a 76-element segmented mirror, arranged in a 10x10 matrix, with each segment having full tip/tilt and piston control. A SH-WFS is used to determine the wavefront slopes across each mirror segment. 17 parallel C40 DSP's control the system. To improve sky-coverage, the current configuration utilised 8x8 segments of the DM.

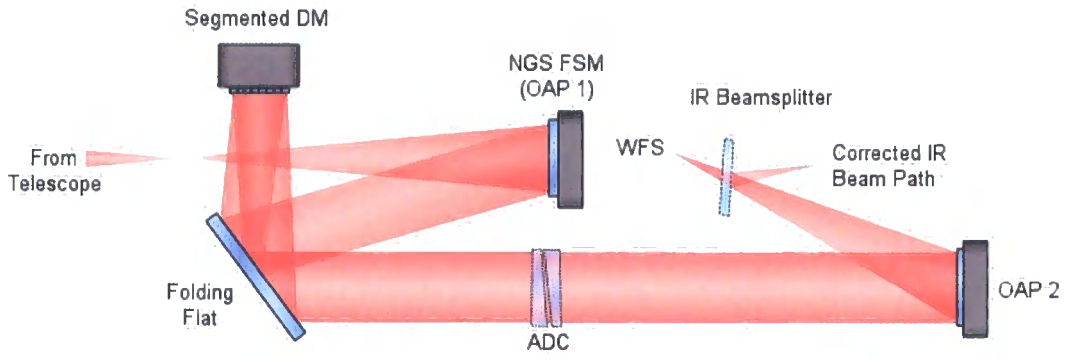

Figure 3.4 Optical layout of NAOMI

The optical layout of NAOMI (Figure 3.4) differs from the generic AO layout in several important ways. The first of these is that the collimating OAP also acts as the

FSM. This injects a small optical aberration into the system that is observed by the NGS WFS, and can therefore be corrected when running closed-loop, but this reduces DM stroke.

The second important point to note about NAOMI is that it uses a segmented DM to achieve high-order wavefront correction. Each segment on the DM is aligned to a single WFS subaperture. This allows the DM to achieve a closer fit to a given turbulent wavefront as edges of segments need not necessarily be aligned. The improvement in DM performance for a given number of WFS subapertures that a segmented mirror allows over a 'conventional' continuous phase sheet DM (e.g. SILAS, Xinetics, OKOTech) is balanced by the added complexity of having three actuators per segment. Unlike continuous phase sheet DMs, mirror segmentation can also allow piston errors to occur between adjacent segments without registering on the WFS. A secondary strain-gauge sensing control loop is employed to detect and correct actuator hysteresis and solve the piston problem.

The control system for the optimal DM-WFS geometry that DM segmentation allows is greatly simplified and scales well to larger aperture telescopes as the conventional actuator-subaperture interaction matrix does not have to be determined and then inverted to find a system control matrix. This allows the wavefront to be reconstructed from the WFS image using a technique called Successive Over-Relaxation (SOR) although at present an interaction matrix is used for wavefront reconstruction. SOR is computationally less intensive that the conventional method of wavefront reconstruction, and scales well to high-order AO systems with many control channels. Although the segmented DM is also infinitely scalable, the costs are prohibitive for a large aperture telescope. MEMS (Micro-Electro-Mechanical Systems) [10] devices

can give a similar DM response to a segmented mirror without the high cost and complexity.

Another effect of segmentation is on the output PSF. The small gaps in between segments effectively create a diffraction grating resulting in the diffraction pattern shown below. The percentage of energy in the extended diffraction pattern is small compared to the energy in the central core of the PSF, but can cause problems, particularly if faint objects are being observed near to a bright guide star.

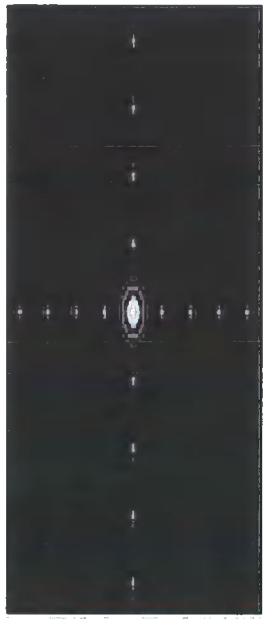

Figure 3.5 NAOMI theoretical diffraction-limited PSF showing diffraction pattern caused by DM segmentation. Intensity has been scaled to enhance diffracted orders.

3.4 LGS AO Systems

Most current LGS-enabled AO systems utilise the photon return generated by exciting atoms in the sodium layer at 90km. A LGS created at this altitude samples a greater volume of the atmosphere between the LGS and the telescope aperture, allowing for

better correction. Because of this, Rayleigh guide stars have not been used for wavefront reference sources since the 1980s. It is only recently that cheap high-power, high-quality lasers have become available, and it is only with this availability that there has been a resurgence of interest in Rayleigh LGS's.

Two Rayleigh LGS-enabled AO systems are studied here. As will be seen, the presence of a LGS not only extends the operational limit of these systems, but also introduces a whole set of technologies and technical challenges that an NGS AO system need not consider.

3.4.1 UnISIS

UnISIS is unique in the field of astronomical AO in that it is the only AO system that employs a Rayleigh LGS as a closed-loop wavefront reference source. UnISIS is employed on the 2.5m Mt. Wilson telescope and uses a 177-actuator Xinetics DM and 13x13 WFS. An excimer laser, outputting 351nm light at a pulse rate of 333Hz is used to create the LGS. With a 90mJ output per pulse this gives the laser an output power of 30W. A sub-arcsecond LGS is created at a fixed distance 18km away from the telescope with a range gate depth of 2.2km.

The UnISIS system uses a shared-launch technique to create the LGS. A shared launch refers to the use of the telescope primary mirror to both launch the outgoing and observe the return beam from the LGS. Using a secondary launch telescope was not an option due to the large beam divergence output by the excimer laser. The output divergence of the laser is approximately 300μrad, which corresponds to an LGS spot size of 238" – far too large to use as a conventional LGS. The diameter of the launch optic must therefore be large in order to reduce the beam divergence. By

expanding the 24mm output beam to fill the 2.5m diameter primary mirror, the beam divergence can be reduced by a factor of 100 and an LGS with a spot size of 0.62" on-sky can be created.

With a shared launch, the alignment between LGS and telescope should be retained over all zenith angles although slight misalignments can easily occur and require slow-loop beam steering that can update at a rate similar to the telescope tracking rate. The effect of launch jitter due to telescope vibrations is common to both paths and therefore not observed. The shared launch also means that the LGS is tilt reciprocal, reducing differential uplink/return path jitter. The reduction in apparent LGS motion means that no high-speed tip-tilt correction is required in the LGS return beam path and the WFS pattern is stable on the WFS CCD.

There are several problems with the technique used to generate the UnISIS LGS that any shared launch system must address. The first of these is the fluorescence of any optical components in the shared path. In the case of UnISIS, this includes the coudé beam path relay mirrors and the primary and secondary mirrors. Dust on each of these surfaces will absorb the high-intensity laser light and fluoresce. Structures in the beam path such as the secondary mirror spider can also absorb laser light. Fluorescence of shared components by definition occurs at longer wavelengths that the UV photons output by the laser, and dust (primarily silica compounds) fluoresce mainly in the IR region of the spectrum. Fluoresced light can contaminate science images, although suitable filters can reduce this effect.

An efficient method of multiplexing the launch and return beams is essential to the operation of the shared launch system. Multiplexing within UnISIS is performed by a transparent spinning disk with small reflective spots that rotates in synchronisation with the output laser pulses. The synchronisation between laser and disk ensures that

when a pulse from the laser reaches the spinning disk, a reflective spot directs the pulse into the main coudé beam path and hence to sky. When the pulsed light is backscattered from the LGS focal altitude, the spot has rotated out of the coudé beam path and the return pulse passes through the transparent disk. This allows the return photons to pass into the AO system where they can be detected by the WFS. The presence of the spots in the return beam path reduces throughput to the science camera by approximately 5%.

UnISIS is a very high order system for a 2.5m telescope with 0.19m subapertures, which should theoretically provide diffraction limited correction in the I-band (~850nm). However, due to the effects of focal anisoplanatism this will not be achieved. At 355nm, each subaperture can create a diffraction-limited LGS spot with FWHM 0.03" – far smaller than the LGS diameter. The WFS operates in quad-cell mode, with the light from each WFS subaperture being divided between 4 pixels. For small centroid offsets, a quad-cell will provide an accurate a determination of centroid position. However, for large centroid offsets, detector arrays with greater number of pixels provide a more linear response as the WFS subaperture image will not be concentrated within a single quadrant, but rather over several pixels. A quad-cell will provide better performance at low-light levels as the photons are distributed over the minimum number of pixels, resulting in increased SNR. An 8x8 pixel array behind each subaperture is normally used [11] as this achieves a good balance between linear response to centroid offsets and WFS SNR.

3.4.2 Starfire Optical Range Generation I and II Systems

The first LGS AO systems were built by the United States Air Force at the Starfire Optical Range (SOR) [14]. Their first generation (Gen I) system used a 1.5m aperture telescope to observe and then a 149-actuator continuous phase sheet mirror to correct the return from a Rayleigh LGS formed by focussing the output of a 75W copper vapour laser at an altitude of 10km. The LGS range gate depth was 2.4km. Copper vapour lasers emit at 511nm (green-blue) and 578nm (orange). The beam quality of the copper-vapour laser meant that like UnISIS, a shared launch must be used to geometrically reduce the beam divergence. The system suffered from the problems of fluoresced and scattered light from the launch pulse. Launch return multiplexing was carried out using a polarising beamsplitter cube. Although successful, this early attempt at multiplexing highlighted the problems of shared optic fluorescence which was overcome by the spinning multiplexer used in UnISIS.

The Gen I system used an intensified 64x64 pixel Reticon array in a Shack-Hartmann configuration for WFSing. Range-gating the Rayleigh plume was achieved by turning the intensifiers on and off at the required times to created the 2.4km LGS at a distance of 10km. Reticon arrays are not normally used due to their low QE of 0.1 compared to a CCD QE of 0.85 around the wavelength 500-550nm, but the Gen I system was constructed before CCD technology had matured to the point where it could be used as a WFS.

The use of image intensifiers to range gate the signal can introduce errors into the wavefront measurement. At the time of the Gen I system, image intensifiers had a low QE, even current intensifiers have at best, a QE of 0.7. An image intensifier introduces noise into the WFS signal due to decay lifetime of the intensified image on

the phosphor screen. Polarisation dependent range gates and electronically shuttered systems have replaced the use of intensified CCDs in LGS AO. The Reticon array was replaced with a CCD array in the second generation (Gen II) system that increased the return optics throughput from 0.075 to 0.25.

The Gen II system upgraded several components including the DM, WFS and laser. The copper vapour laser was upgraded from 75W to 200W, although the range gate depth and distance to LGS remained the same. The number of subapertures was increased from 124 to 208, requiring a reduction in subaperture size from 10.8cm to 9.2cm on each side. The photon flux that was detected from the Gen I LGS was 50-80 photons/subaperture for every six pulses of the laser. The Gen II system measured a photon flux of 190 photons/subaperture for every five pulses of the laser. As the photon return from a Rayleigh LGS is highly dependent on altitude, these numbers cannot be compared to one another unless the zenith angles at which each measurement was made are known.

Both Gen I and II systems made use of pre-launch correction of the LGS beam. Pre-launch correction allows the spot size of the LGS to be minimised on-sky by reflecting the laser off the DM and FSM before it has been launched. This causes shared path fluorescence from a far greater number of components, but will increase WFS SNR. Use of this technique was essential due to the poor seeing conditions that are often observed at the SOR. 2.5-3" seeing is quoted, whereas values greater than 1.5" will rarely be observed at a good astronomical site.

The performance of the Gen II system significantly exceeded the best performance of the Gen I system on the first night of operation. That this was achieved on the first night of LGS observations ably demonstrates the importance of experience when working with LGS AO systems.

The measured Strehl ratio of the Gen II system using the LGS was 0.321±0.071 at 880nm. This was within the predicted performance range of the LGS system, although correction using the NGS was worse than predicted. Whether this was due to changes in the atmosphere or inaccuracy within the model cannot be determined from the provided data.

3.5 Solar AO

Solar AO operates using the same principles as night-time AO, except it can use the surface of the sun as a wavefront reference. Many of the technical challenges associated with night-time AO, such as WFS SNR and sky coverage are removed. The large number of photons allows rapid development of advanced AO concepts. Indeed, while the first experimental night-time MCAO system is progressing towards being commissioned, MCAO systems have already been implemented at solar observatories [16].

Using the sun as a wavefront reference is not as simple as using a sub-arcsecond point of light observed with an NGS or LGS. To find a wavefront reference point on the sun, solar AO observers use dark sunspots or filaments that appear on the surface of the sun and track their motion. This is achieved by reimaging the dark spot using a lenslet array and cross-correlating the subaperture image with all other subaperture images. The output of the cross-correlation resembles a standard SH-WFS spot pattern. This spot pattern can then be used to control a DM in an identical manner to a night-time AO system. The intensity variation between the bright photosphere of the sun and the dark filaments is of the order of 13%. To accurately perform a cross-correlation, between 8x8 and 32x32 pixels per subaperture are used. As the WFS photon flux is so high, this large number of pixels does not reduce WFS SNR.

The other great advantage of the large photon flux is the high SNR in the WFS. This allows both the higher resolution subaperture images and very fast frames rates. The science detector can also take exposures at the same frame rate as the WFS without concern about the penalty of increased read-noise when the images are co-added. Each science frame can therefore be associated with a residual wavefront and a correction can be applied, based on the stored wavefront during post-processing. Phase-diverse speckle imaging also work well to correct the residual aberrations present after AO correction and can be used to increase field of view [17].

3.6 Conclusions

The design of several commissioned AO systems utilising both LGS and NGS as wavefront references have been studied and compared to a generic AO system design. Several aspects of each design have been highlighted as novel, or areas where caution must be taken when designing an AO system. These points are summarised in Table 3.1.

System	Type	Telescope	Reasons for Study
PUEO	NGS	CFHT	Curvature WFS with bimorph mirror - demonstrates importance of matching DM/WFS geometry Example of a 'transparent' AO system able to feed any telescope instrument
Altair	NGS	Gemini N	DM conjugated to non-zero altitude for wide field imaging Demonstrates trade-off between increased correction and sky covergae
NAOMI	NGS	WHT	Installed on the WHT Simplified control system allowed by the use of a segmented DM (application to MEMS devices) Effect of DM segmentation on PSF
UnISIS	LGS	Mount Wilson	Uses a Rayleigh LGS Full-aperture shared launch system required for generating LGS High-order correction allowed (~20cm diameter subapertures) from LGS Subaperture offsets provided by a quad-cell of CCD pixels - non-linear response to offsets
Starfire (Gen I)	LGS	Starfire	First LGS AO System LGS projected to a low altitude (10km) Very-high order system, not diffraction limited due to focal anisoplanatism Demonstrates an alternative method of range gating a Rayleigh plume
Starfire (Gen II)	LGS	Starfire	Upgraded Gen I system with higher-order correction Errors in modelling AO system performance - careful definition of problem required
Solar AO	Sun	Various	Demonstrates limits of current technology when a bright reference is available

Table 3.1 Table of examined systems, giving type of wavefront reference, telescope (or observatory) the system is installed and reasons for study.

While not all aspects of the studied designs are directly applicable to the GLAO system demonstrator (e.g. use of a segmented DM, or a curvature-based WFS), several conclusions can be drawn that will influence the design of the AO system:

- Most astronomical AO systems are designed around the same basic concept described in section 3.2, with differences brought about due to different types of WFSX, DM and wavefront reference. The generic AO system design is therefore an adequate start point for the conceptual design.
- The DM and WFS geometries must be matched for optimum performance. For the GLAO system, this means careful alignment of the DM to the SH-WFS. An alignment procedure will have to be implemented.
- A transparent AO system allows current telescope instruments to benefit from an AO-corrected feed. The AO system output should mimic the WHT Nasmyth focus to take advantage of commissioned WHT instruments, if required.
- The DM must be conjugated to the telescope pupil i.e. the ground layer.
- Focal ansioplanatism will be the limiting performance factor when using a low-altitude LGS.
- Shared-launch LGS WFSing is possible, although scattered/fluoresced light from common path optics can saturate the WFS
- The number of pixels to use per subaperture must be defined, along with the subaperture FOV.

- More advanced AO concepts, such as MCAO, and therefore by definition GLAO, are possible using similar equipment.

These conclusions will be fed into the GLAO system design and analysis, presented in the following chapters.

3.7 References

1. Babcock, H. W., '*The Possibility of Compensating Astronomical Seeing*', PASP, Vol. 65, No. 386, p.229 (1953)
2. Rigaut, F., '*Ground-Conjugate Wide Field Adaptive Optics for ELTs*', in '*Beyond conventional adaptive optics: a conference devoted to the development of adaptive optics for ELTs*' Edited by E. Vernet, R. Ragazzoni, S. Esposito, and N. Hubin. ESO Conference and Workshop Proceedings 58, p25 (2002)
3. Saunter, C.D., Love, G.D., Johns, M., Holmes, J., '*FPGA technology for high speed, low cost adaptive optics*', Proc. SPIE, Volume 6018, p60181G-1 (2005)
4. Ellerbroek, B. L.; Tyler, D. W., '*Adaptive Optics Sky Coverage Calculations for the Gemini-North Telescope*', PASP Volume 110, Issue 744, pp. 165-185. (1998)
5. Roddier, F., Rigaut, F., '*Adaptive Optics in Astronomy*', p205-234 (1999)
6. Racine, Rene; Ellerbroek, Brent L., '*Profiles of nighttime turbulence above Mauna Kea and isoplanatism extension in adaptive optics*', Proc. SPIE Vol. 2534, p. 248-257 (1995)
7. Fuensalida, Jesus J.; Garcia-Lorenzo, Begona; Castro, Julio; Chueca, Sergio; Delgado, Jose Miguel; Gonzalez-Rodriguez, Jose M.; Hoegemann, Claudia K.; Reyes, Marcos; Verde, Manuel; Vernin, Jean, '*Statistics of atmospheric parameters for multiconjugated adaptive optics for the Observatorio del Roque del los Muchachos*', Proc. SPIE, Volume 5572, pp. 1-9 (2004).
8. Fuensalida, Jesus J.; Chueca, Sergio; Delgado, Jose M.; Garcia-Lorenzo, Begona; Rodriguez-Gonzalez, Jose M.; Hoegemann, Claudia K.; Mendizabal, Esteban G.; Reyes, Marcos; Verde, Manuel; Vernin, Jean, '*Vertical structure of the turbulence above the observatories of the Canary Islands: parameters and statistics for adaptive optics*', Proc SPIE, Volume 5490, pp. 749-757 (2004)
9. Sarazin, M. , Butterley, T., Tokovinin, A., Travouillon, T., Wilson R., '*The Tololo SLODAR Campaign*', ESO Website (2005)

10. Zamkotsian, F.; Camon, H.; Fabre, N.; Conedera, V.; Moreaux, G., '*Microdeformable mirror for next-generation adaptive optical systems*', SPIE, Volume 4839, pp. 711-720 (2003).

11. Soechting, Ilona K.; Wilson, Richard W.; Myers, Richard M.; Longmore, Andy J.; Benn, Chris R.; Ostensen, Roy; Els, Sebastian; Goodsell, Steven; Gregory, Tom; Talbot, Gordon, '*Influence of restricted FOV and CCD binning in SH-WFS on the performance of NAOMI*', Proc SPIE, Volume 5490, pp. 574-579 (2004).

12. Fugate, R.Q. et al, '*Experimental Demonstration of Real Time Atmospheric Compensation with Adaptive Optics Employing Laser Guide Stars*', BAAS Vol. 23, p898F (1991)

13. Fugate, R.Q., '*Observations of faint objects with laser beacon adaptive optics*', Proc. SPIE Vol. 2201, p. 10-21

14. Fugate, R.Q., Ellebroek, B.L., Higgins, C.H., et al '*Two generations of laser-guide-star adaptive optics experiments at the Starfire Optical Range*', J. Opt. Sci. Am. A, Vol 11, p310-324 (1994)

15. Spinhirne, J.M. et al., '*Starfire Optical Range 3.5-m telescope adaptive optical system*', Proc. 1998 SPIE Vol. 3353, p. 22-33

16. Langlois, M., Moretto, G., Richards, K., Hegwer, S., Rimmele, T.R., '*Solar multiconjugate adaptive optics at the Dunn Solar Telescope: preliminary results*', Proc. SPIE, Volume 5490, pp. 59-66 (2004).

17. Denker, C., Mascarinas, D., Xu, Y., Cao, W., Yang, G., Wang, H., Goode, P.R., Rimmele, T., '*High-Spatial-Resolution Imaging Combining High-Order Adaptive Optics, Frame Selection, and Speckle Masking Reconstruction*', Solar Physics, Volume 227, Issue 2, pp.217-230 (2005)

Chapter 4: Laser Launch System

4.1 Introduction

This chapter describes the overall design of the demonstrator LGS system on the WHT. The laser launch system (LLS) is one of the two main components of the GLAO system that this thesis describes. The LLS consists of three main components; the laser itself, the beam relay system (BRS) for transporting light from the laser to the main launch optics, and the actual launch optics, which is normally referred to as a beam launch telescope (BLT). The following is a description of the laser launch system and the factors affecting the performance of each subsystem.

4.2 Laser

The choice of laser is one that determines many aspects of the laser launch system, and the GLAO system as a whole. For the creation of a Rayleigh LGS, the laser must satisfy a number of criteria. Firstly, the laser must output enough power at the correct wavelength for a sufficiently bright LGS to be generated at a suitable altitude. Secondly, the laser must exhibit a high beam quality and low beam divergence. Unless the beam quality requirements are met, the LGS spot created at the focal altitude would not be tightly focused enough to allow WFSing. Finally, the laser must also be pulsed with a repetition rate that does not limit the altitude at which the LGS can be created. Unless the laser light is pulsed at a suitable frequency, the altitude at which the LGS is to be created may not be able to be selected. The pulse length of each laser pulse can also affect the performance of the LGS. If the pulse is too long, light may be lost in the system range gate, or if the pulse length is too short, higher

peak powers are encountered in the system and all of these points are addressed in greater detail below. This is followed by a technical description of the laser selected.

4.3 Photon return from the LGS

The first, and most important question to address is the altitude at which the LGS can be created. This determines how much of the atmosphere is sampled and sets limits on the performance requirements of the LLS, which then help define the performance of the LGS-enabled AO system as a whole. The starting point for any Rayleigh LGS system is the LIDAR equation [1,2,3] governing the photon return due to Rayleigh backscattering in the atmosphere. The LIDAR equation and photon return from a Rayleigh LGS are examined in greater detail in Chapter 5.

$$N_\gamma = \frac{Q\sigma T_{sys} QE_{CCD} \lambda \rho_H D_{slice} A}{4\pi hc H_{LGS}^2 f_L} \qquad - 4.1$$

where N_γ is the number of detected photons for a single pulse,

Q is the output laser power in watts,

σ is the molecular scattering cross-sectional area in m^2,

T_{sys} is the end-to-end system optical throughput,

QE_{CCD} is the QE of the WFS CCD at the LGS wavelength,

ρ_H is the atmospheric scattering particle density at a height H_{LGS},

D_{slice} is the scattering depth in the atmosphere,

A is the diameter of the collecting area of the WFS subaperture being studied,

f_L is the laser repetition rate.

The amount of light that is backscattered from the plume via the process of Rayleigh scattering is proportional to λ^{-4}. This appears to make the choice of laser wavelength simple, with shorter wavelengths giving a better photon return for the same output power. However, what must be kept in mind is that by using an LGS we are trying to increase the signal on the WFS. So any study of photon return must also take into account the efficiency of all the optical elements that are used to observe the LGS and direct light into the WFS. These display a dependency on wavelength that is a function of the material used to coat the optical surfaces. Whilst any optical system can be optimised for a particular wavelength of light, achieving a broadband throughput optimisation from the UV to the NIR is complex and expensive.

The repetition rate of the laser pulses determines the maximum altitude at which an LGS can be created. A range gate shutter is synchronised to the laser pulses such that the altitude of the LGS is selected by opening the shutter after the light has travelled a distance twice that of the desired focal height of the LGS. If the laser pulses too rapidly, the shutter will open at the correct moment to allow light returning from the LGS altitude, but will also transmit light from the subsequent pulse. As the subsequent pulse is by definition at a lower altitude than the LGS, the resulting photon return from the lower altitude pulse is greater than that from the LGS. Preceding pulses at a higher altitude cannot be observed as the photon return is negligible. Although this effect can be reduced by introducing optical elements into the beam that cause light entering the system from the incorrect focal altitude to be vignetted, overlapping of the laser pulses in this manner is obviously a situation that should be avoided.

The lower limit on the pulse rate is set by the coherence time of the atmosphere. For optimum sampling of the turbulence, the WFS must run at a rate greater than the

Greenwood frequency (defined in Chapter 1). The minimum pulse rate of the laser must therefore be greater than this frequency, otherwise there will be insufficient pulses to provide correct temporal sampling of the atmosphere. Low pulse rates also imply high peak intensities in each laser pulse for a given laser power. This introduces extra safety considerations and costs to the system.

The final aspect of the pulsed laser system is the length of the laser pulse. The minimum range gate depth is defined by the pulse length. If the range gate shutter opens for a time less than the laser pulse length a portion of the return pulse is blocked by the range gate, and the signal detected by the WFS is reduced. The pulse length of the laser must therefore be short enough so that the desired range gate depth can be achieved without loss of light to the WFS. The pulse must not be so long as to require an increase in range gate depth, resulting in an increase in apparent LGS spot size, but long enough so that the peak intensity in the pulse does not require the use of custom high-power optics.

With all these issues in mind, a model describing the photon return from the LGS was made. Atmospheric optical transmission for LGS at different altitudes was determined by extrapolation from data measuring the V-band atmospheric extinction at the WHT. [5]. Figure 4.1 gives the resulting wavelength dependency of the LGS photon return. This model includes the transmission of all components in the system, using data on the throughput of the WHT and wavelength dependency of transmission for the GLAO system design as detailed in Chapter 6.

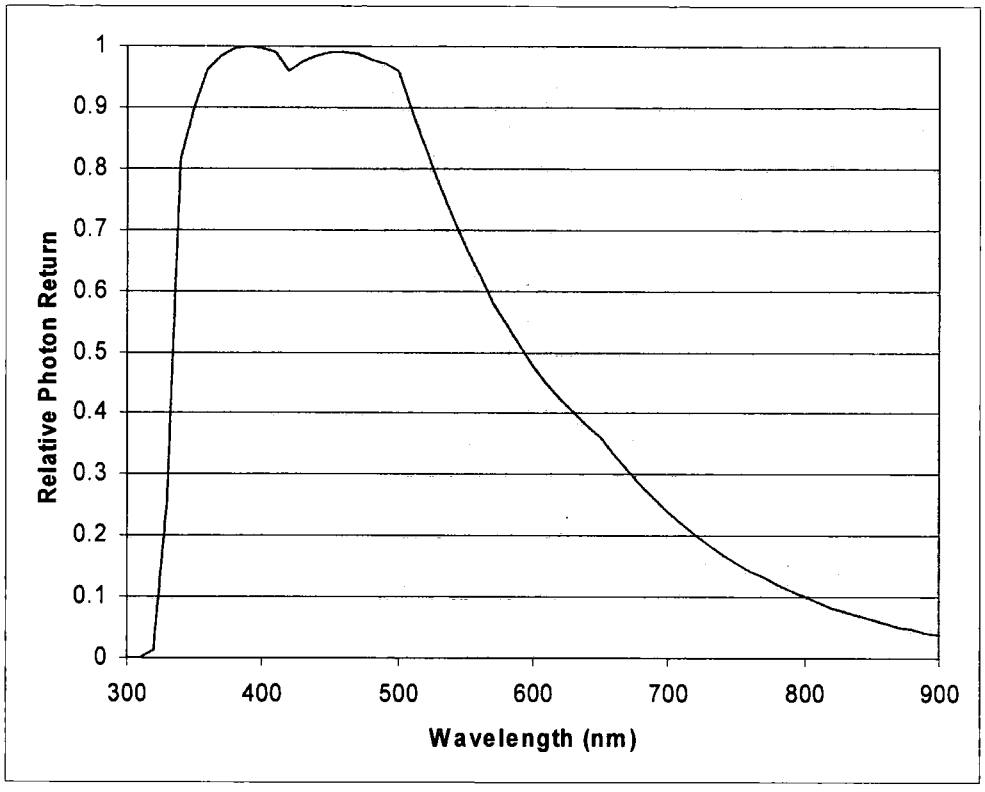

Figure 4.1 Photon return versus wavelength of LGS photon return. The optical system models the GLAO design containing 9 silver surfaces, 6 aluminium surfaces and an EEV39 WFS CCD. Atmospheric transmission is included and assumes that the LGS altitude is above 20km.

The wavelength dependency of the photon return shows the optimum wavelength for a Rayleigh LGS is limited by the optical transmission of the atmosphere and the reflectance curves of the return optics, rather than the wavelength dependence of the Rayleigh backscatter. Although the number of photons which are Rayleigh backscattered is greater at shorter wavelengths, the optical transmission of the atmosphere is also reduced via the same process. Below a wavelength of 400nm, the poor intrinsic UV reflectance of the silver-coated optics effectively cancels the advantages of using a short wavelength laser. This effect can be reduced by coating the main optics of the telescope with aluminium, but this then reduces the visible and IR throughputs of the telescope. A reduction in system efficiency at the main observational wavelengths of the telescope in this way, purely for optimisation of the

LGS photon return was not an option for this demonstrator system, and effectively precluded the use of a UV laser for the LGS.

The probability of multiple scattering is also increased for shorter wavelengths, and photons with an arbitrary polarisation state may be observed. However, multiple scattering events are rare as the cross section of Rayleigh scattering is very small [6] i.e. $5.45\times10^{-32} m^2 sr^{-1}$ at 550nm.

The laser that had been purchased for the generation of the LGS was a frequency-doubled Nd:YLF laser, which outputs a nominal 5W of 523nm light at a 7kHz repetition rate. The 7kHz repetition rate limits the maximum altitude for LGS to 21.43km otherwise consecutive pulses start to overlap on the sky. This range can be slightly increased by the use of low altitude baffling of the return beam and also by taking advantage of the vignetting of the WHT from low altitude photon return when the laser is launched from behind the WHT secondary mirror. Before determining the maximum altitude at which the LGS can be created the WFS geometry and optical design must first be examined. This is because increasing the range gate depth is a very simple way to increase the return number of photons (doubling the range gate effectively doubles the photon return from the LGS). However, a larger range gate also affects the spot geometry on the WFS in several ways. The lenslet array transforms the pupil of the primary telescope into an array of smaller telescopes. For a 10 x 10 lenslet array on a 4.2m telescope, each lenslet effectively creates a 42cm telescope positioned at the primary mirror. The position of the lenslet in the pupil plane means that lenslets always view the LGS off-axis, with the off-axis angle increasing with increasing lenslet distance from the centre of the primary mirror. The off-axis angle transforms the z-extension of the LGS spots into an offset on the plane of the WFS CCD. This causes the LGS spots to appear elongated, spreading the LGS

light over more pixels. Furthermore, the WFS CCD can only be conjugated to a single altitude so the extremities of the LGS appear defocused on the WFS. The degree with which increasing the gate depth degrades the performance of a WFS depends on the lenslet geometry, lenslet focal length, the plate scale at the WFS CCD and WFS pixel size.

The WFS optical design is detailed in chapter 6 of this thesis, while a study of the maximum permissible spot elongation is included in Chapter 5. Using the LIDAR equation (equation 4.1), the required range gate depth to detect a given number of photons within a WFS subaperture can be determined for each altitude. Any range gate depth can then be expressed as a spot elongation when viewed from a point on the WHT pupil. The maximum spot elongation is observed at a subaperture positioned at the pupil edge. For a 10x10 Shack-Hartmann WFS on a 4.2m pupil, each subaperture has a 0.42m diameter. Square subapertures positioned around the edge of an annular aperture have a fill factor defined by the area of overlap between the telescope pupil and subapertures. If only subapertures that are over 60% filled are included in the WFS pattern, the maximum off-axis pupil position is approximately 2m. The maximum elongation within the WFS spot pattern is shown in Figure 4.2.

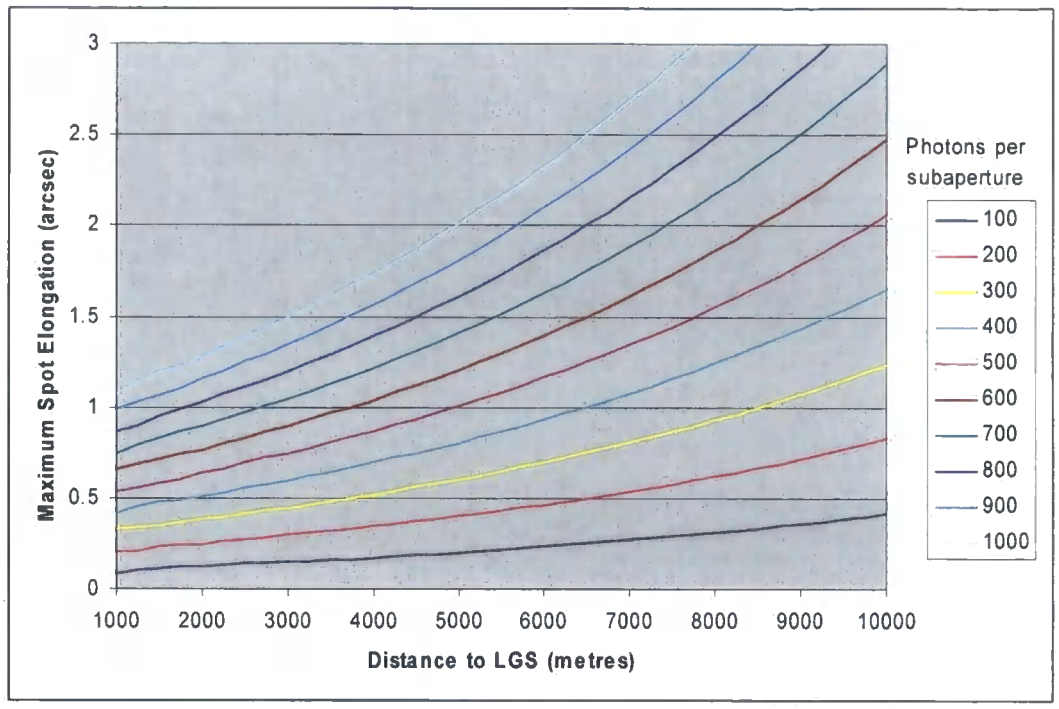

Figure 4.2 Observed spot elongation at a given LGS distance for a subaperture positioned at the edge of the 2.1m radius WHT primary aperture.

4.4 Launch Methods

There are various methods for projecting the light from the laser onto the sky. The simplest, conceptually, is to share the laser launch and return optics by projecting the laser from the primary mirror of the telescope being used (in this case the 4.2m primary mirror of the WHT). This method does not require any separate launch optics and the laser can be quickly and easily aligned to the optical axis of the telescope at a Nasmyth focus. This method also allows the return system to be physically close to the laser pulse timing controller so no long cabling is required to link the laser to the range-gate system.

However, the use of a shared laser launch introduces problems. With the high laser powers that are associated with the generation of a Rayleigh LGS, the amount of light that is scattered from all the surfaces in the launch path becomes much greater than

the photon return from the LGS itself. Off-axis or scattered light from the telescope mirrors and the vanes of the spider supporting the secondary mirror cell can defeat the range gate and enter the WFS. Figure 4.3 shows a composite Photomultiplier Tube (PMT) trace of the photon return from a Rayleigh LGS created using a shared launch[8]. The intensity of the scattered launch pulse is far greater than the light returning from the LGS itself. One final point to note about this trace is that the bright launch pulse does not vanish instantly, but decays over the course of 10μs. Two broadband filters centred on 500nm and 630nm were used to determine the wavelength of the decay. These measurements showed the slow decay was far greater at the red end of the visible spectrum suggesting the decay was due to fluorescence from dust on the primary, secondary and Nasmyth mirrors.

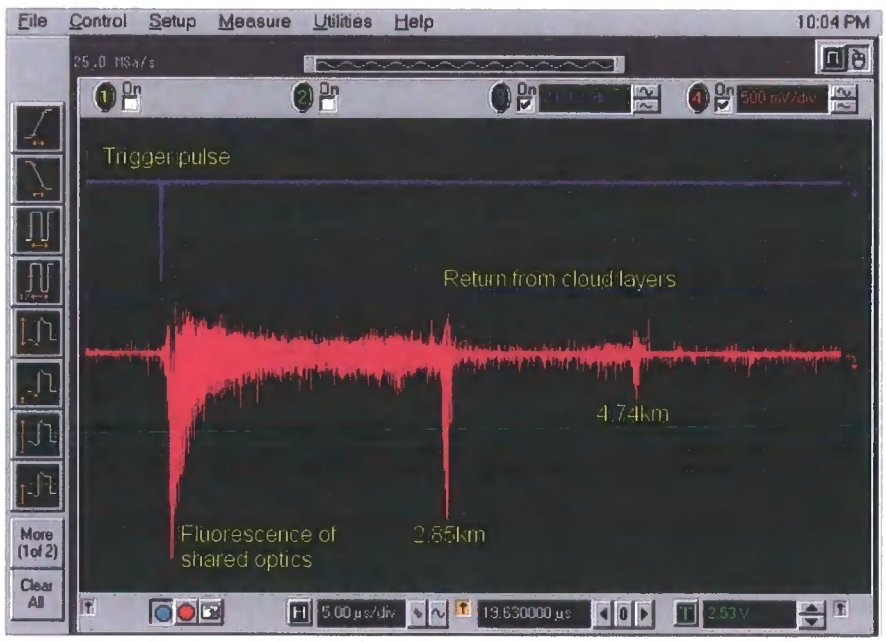

Figure 4.3 Composite trace of PMT showing the decay of fluoresced light from optics shared by the launch and return paths. The peaks mark the bright photon return from two cloud layers at 2.85km and 4.74km from the telescope pupil.

Suppression of light scattered and/or fluoresced as part of the launch pulse can be achieved through the use of a mechanical shutter that physically blocks the fluoresced

light observed within the first 10μs after the initial launch pulse. This must be separate from the range gate, as the high speed range gate (normally a Pockels cell placed between crossed polarisers) may not have an extinction ratio capable of blocking the large number of photons scattered from the inside of the dome and from any optical components shared between the launch and return paths. Having a separate shutter on the return path also blocks the scattered light from entering any detectors in the system used to observe non-laser wavelengths, such as NGS tip-tilt sensors or the science camera itself.

If a shared launch is ruled out, a separate Beam Launch Telescope (BLT) must be employed to project the laser onto the sky. Although the use of a separate BLT removes the problems of scattering and fluorescence, it introduces a number of separate difficulties that must be overcome. BLT's can essentially be subdivided into two groups: those situated on the optical axis of the main telescope, and those situated off-axis. Each type of BLT has merits over the other such that, for single guide stars, the use of off-axis BLT's is biased towards sodium guide stars, and on-axis BLT's towards Rayleigh guide stars.

Off-axis BLT's have been more widely used in past LGS enabled AO systems, mainly due to the complexity and size of the equipment required for laser generation. The creation of high power laser light tuned precisely to the sodium D2 line is especially difficult requiring complex dye or sum-frequency mixing systems. By housing the laser head in an off-axis location away from the main observing telescope, both space and operational constraints of these complex systems can be eased. Projecting the guide star from an off-axis location to a point in the field of view of the main observing telescope also has the effect of hiding most of the Rayleigh plume (Figure 4.4). This can be advantageous for sodium LGS's, as the sodium LGS spot is spatially

separated from the unwanted return light from the Rayleigh plume, and therefore no complex baffling or range-gating is required for its removal. This aspect of an off axis launch is less beneficial for Rayleigh LGS's where the ability to observe the plume along its entire length is often beneficial for testing and alignment purposes.

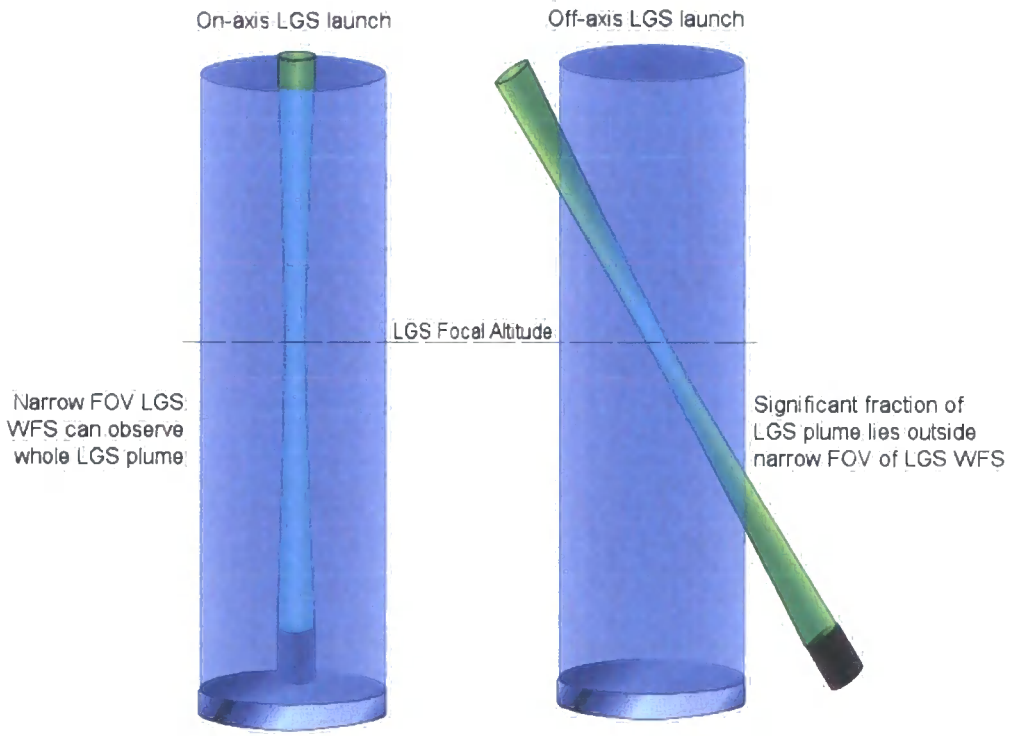

Figure 4.4 Shadowing of Rayleigh plume by off-axis BLT. With an on-axis launch, the LGS plume (shown in green) travels within the FOV of the LGS WFS (shown in blue), therefore allowing some light from any altitude into the WFS. With the off-axis launch, a significant fraction of the LGS plume lies outside the FOV of the WFS and cannot be observed.

The main disadvantage of an off-axis guide star is spot elongation on the WFS. Unlike a star, LGSs have a physical depth on the sky. For a sodium LGS, this is the depth of the sodium column in the atmosphere, while for a Rayleigh LGS, it is set by the depth of the range gate. An on-axis guide star projects this range along the optical axis of the observing telescope, whilst an off-axis guide star projects the range across the pupil of the observing telescope. Using the Shack-Hartmann WFS as an example, the

elongated LGS spot is re-imaged onto the WFS CCD, and therefore each Shack-Hartmann spot is also elongated. If the degree of elongation causes the WFS spot to approach, or even overlap an adjacent spot, the accuracy with which the WFS can measure the wavefront is impaired. In principle, any enlargement or elongation of a subaperture spot may degrade the signal-to-noise ratio of the wavefront measurement.

By using an on-axis guide star, spot elongation is reduced because the projected depth of the LGS now lies along the optical axis of the observing telescope. If the BLT were positioned at the edge of the mirror (as is the case with the Keck observatory BLT), then not only would the maximum off-axis distance double, but the maximum spot elongation would also double accordingly.

The creation of an on-axis LGS requires the BLT to be positioned behind the secondary mirror of the primary telescope. This constraint means a method for getting laser light to this point must be found. One method is to situate the laser behind the secondary mirror, giving a very short, and therefore stable, light path into the BLT. This method is complicated by the resultant need to provide services (power, coolant, controllers, etc.) to a point behind the secondary mirror without compromising the clear aperture of the observing telescope. The laser head itself must also exhibit insensitivity to the variable gravity vector that is present at the secondary mirror. If the laser head is mounted behind the secondary mirror, the space envelope must also be considered because the BLT and laser compete directly for the limited space that is available. Modern Rayleigh lasers are relatively compact, and placing the laser head in this limited space is not an overly complex issue. Sodium lasers are (currently) rather complex systems, and they require significantly more space than their Rayleigh counterparts. The physical size of a sodium laser system often precludes positioning the laser head behind the secondary mirror. Where this is the case, a method of

relaying the beam from the point where the laser light is generated to the BLT must be found.

4.5 Beam Relay System

The purpose of the Beam Relay System (BRS) is to transport the laser light from the point where it is generated to the BLT. A 'perfect' BRS does not adversely affect the laser beam in any way and provides a motion-stable input to the BLT with a high optical throughput. Both optical fibres and relay mirrors have been used in the past, although difficulties are encountered with both methods.

Optical fibres are an attractive solution to the BRS problem as they only require alignment at the two fibre ends, and are insensitive to telescope orientation. Alternatively, using relay mirrors to steer the beam requires active compensation for telescope structural vibrations and orientation. However, it is not a simple task to transmit through optical fibres the high laser powers that are inherent to LGS generation. High power transmission within optical fibres is simpler within fibres that have large core diameters. If the core is too small, non-linear optical effects can be stimulated within the waveguide, and this leads to a drop in throughput. Conversely, if the core is too large, the output beam quality suffers because a greater number of transverse modes are guided. The basic requirement is that the fibre must have a core large enough to transmit the power without exhibiting any non-linear effects or beam quality degradation. The use of fibres in a Rayleigh LGS relay system is further complicated by the fact that Rayleigh lasers must be pulsed, and that non-linear effects within optical fibres (such as Stimulated Brillouin Scattering, SBS) [9] depend on peak power. Rayleigh LGS require pulsed lasers, which greatly increases the power density at the coupling point to the fibre. New technologies, such as Photonic

Crystal Fibres (PCF), [10] may allow higher-power densities to be transmitted within fibres. 10W of CW [2] laser at 532nm has been transmitted through PCF with a core diameter of 30 microns [11,12]. At this core diameter and wavelength a PCF exhibits single mode wave-guiding, whereas conventional step-index fibres do not exhibit single-mode operation with core diameters greater than approximately 5 microns. However, the dependency of non-linear effects that are present in optical fibres on peak input power have until now precluded their use as pulsed laser relay systems. Air-guiding hollow-core PCF's may allow pulsed laser light [13] to be relayed in the future, but the use of high-power reflective mirrors is currently the only realistic option to relay light to a BLT situated behind the secondary mirror of a telescope.

The use of a reflective relay system has a completely separate range of problems that must be overcome if a stable input to the BLT is to be provided. Fortunately, these problems are not due to physical limitations of the technology in use, such as the non-linear effects that were encountered with the use of optical fibres, but instead are opto-mechanical, and simple solutions exist for their compensation. The simplest place to situate the laser is at a gravity stable point on the telescope structure that rotates with the azimuthal axis of the telescope e.g. at a Nasmyth platform. This ensures that the BRS only observes motion in one dimension (telescope elevation), and greatly simplifies the opto-mechanical design. If the laser is placed on the Nasmyth optical

---

[2] CW, or continuous wave lasers differ from pulsed lasers in that the photons are output from the lasing medium continuously at a low rate. A pulsed laser builds up the electron population in the excited state before releasing them in a short burst. Pulsed lasers therefore have much higher peak power than an equivalent power CW laser. Some CW lasers are actually 'quasi-CW', in that they have a pulse repetition rate of several MHz, therefore appearing to be CW lasers to most optical detectors.

axis, then a simple mirror attached to the primary mirror support structure will automatically direct the light to the top end of the telescope (Figure 4.5). The problem with this simple method is due to the Serrurier truss, which is used in most large telescopes to ensure that alignment is maintained between the primary and secondary mirrors over all elevation angles. Such a truss does not keep the telescope top-end, (where the BLT is mounted) stationary with respect to the primary mirror cube, where the rotating fold mirror that directs light from the Nasmyth optical axis towards the top-end is positioned. When the WHT is horizontal, the sag that is observed [14] between the top-end ring and the primary mirror cube is 2mm. There are two solutions for this.

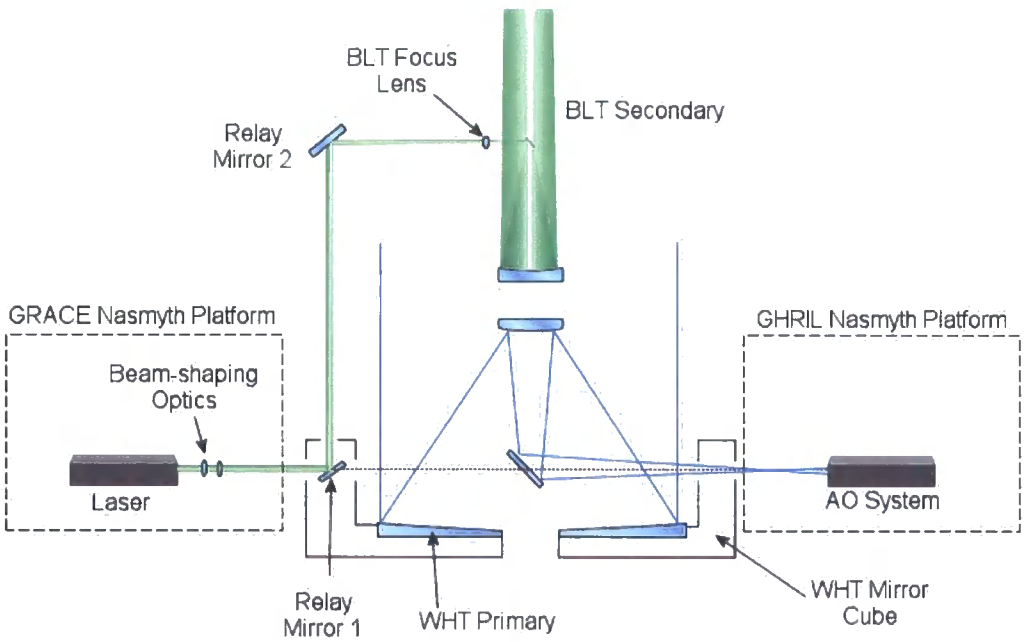

Figure 4.5 BRS schematic showing position of laser and relay mirrors in respect to telescope and AO system. Laser is housed in a temperature controlled environment in the GRACE Nasmyth platform. The Laser and Relay mirror 1 are aligned to the Nasmyth optical axis. Relay Mirror 1 rotates with changes in the telescope altitude axis. The return light (shown in blue) enters the AO system housed in the GHRIL Nasmyth platform.

The first method is attractive, if somewhat complex. By including active beam steering elements in the BRS, not only can the effects of telescope sag be removed, but also of any telescope vibrations, e.g., vibrations due to wind-shake. This method requires closed-loop tip-tilt correction of the beam at one or two points in the BRS structure, and also a reasonably complex diagnostics package to determine the beam position at the input to the BLT and provide a control signal to the steering mirrors. It is due to this complexity that the second, and simpler method, may be considered. This method involves limiting the operational angle over which the LGS would be used. Up to 30 degrees from zenith the WHT top-end sag is approximately 1mm. A sag this small, although it will affect the apparent position of the LGS on the sky, can be compensated by increasing the off-axis tolerance of the BLT, over sizing any BRS optics, and also by aligning the BLT at a 70 degree elevation angle. Aligning the BRS at this angle gives the smallest range of sag between 60 and 80 degrees, while still giving reasonable sky coverage. This method is obviously not suitable for a facility-class LGS, which would require a far greater operational range of elevation angles, and also provide greater pointing stability of the LGS on the sky. However, for a demonstration GLAO system, such as that described in this thesis, the trade-off between cost, complexity and operational range was deemed acceptable and the passive BRS was employed.

4.6 Beam Quality

The size and intensity profile of the LGS is highly dependent on the output beam quality of the laser. The BLT is essentially a magnification system that re-images a small input focal point to a large focal point a long distance away. Therefore the

minimum input spot size, as well as the BLT objective diameter, determines the angular diameter of the LGS on the sky. The requirements on laser beam quality are therefore extremely stringent.

For a frequency-doubled Diode-Pumped Solid-State (DPSS) laser, the starting point for the processes determining the output beam quality of the laser is the generation of the IR beam to be doubled. The IR beam quality is sensitive to thermal effects inside the solid-state lasing crystal rod. Figure 6 shows a typical DPSS layout for the generation of an IR laser beam. The pump diodes either side of the crystal rod provide photons to create a population inversion in the lasing medium. The pump diodes are extremely powerful (up to 40W in each diode bar) and so heatsinks at the top and bottom of the rod are used to remove excess heat from the crystal. Unfortunately, the non-uniform temperature gradient across the crystal results in differential expansion. This causes thermal lensing, and affects output beam quality.

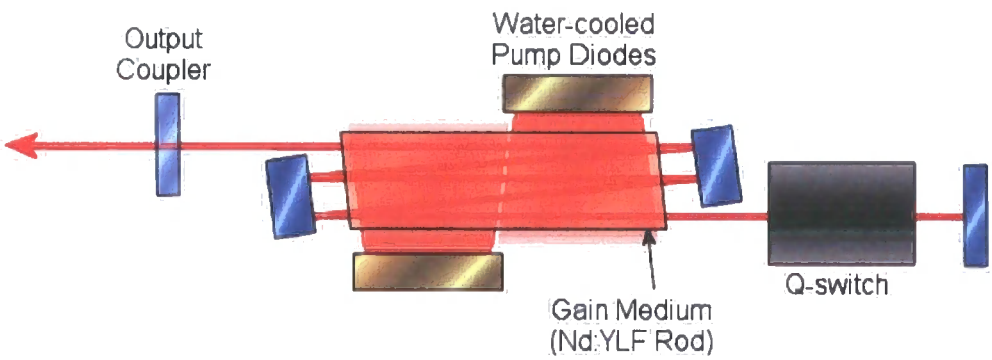

Figure 4.6 QPeak DPSS Q-switched cavity schematic. Two pump diodes excite electrons within the gain medium. The laser cavity is formed between the output coupler and mirror behind the Q-switch. Maximum gain is achieved by making multiple passes through the Nd:YLF rod. Output λ is 1046nm ~10W @ 7kHz pulse rate. The cavity has a TEM_{00} elliptical output.

The transverse electric modal (TEM) structure of a laser beam is generated inside the crystal rod also. Several mode structures are shown in Figure 4.7. The simple TEM_{00}

mode is generated when the optical cavity containing the rod only efficiently amplifies a single path through the crystal. If the optical cavity allows further paths, the laser exhibits further modes. If multiple paths are amplified through the crystal, the output beam no longer resembles the 2-dimensional gaussian of the TEM_{00} beam, but exhibits a complex modal structure. A laser beam focuses to the smallest spot size when in TEM_{00} mode. High power TEM_{00} DPSS lasers are frequently used as micro-machining tools, whilst the yet higher power, multimode DPSS lasers are generally employed in industrial cutting/welding applications.

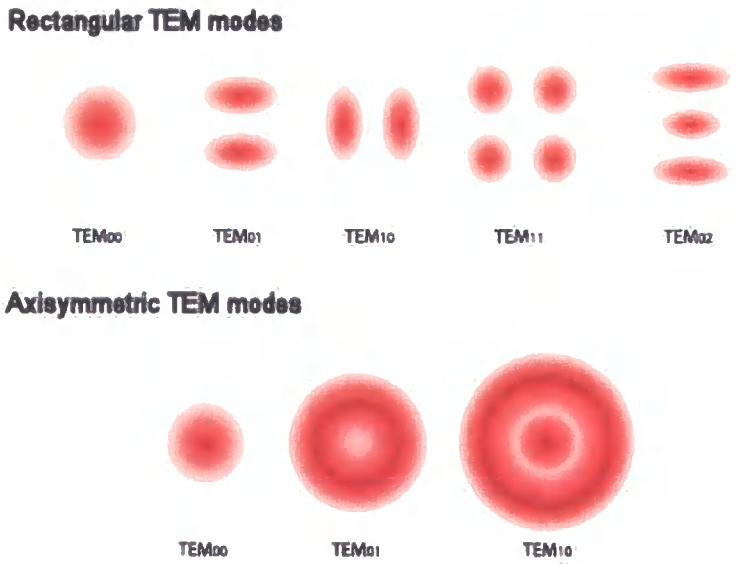

Figure 4.7 Lowest order rectangular and axisymmetric Transverse Electric Modes (TEM).

As can be seen in Figure 4.7, a perfect TEM_{00} output beam exhibits a Gaussian intensity profile in both dimensions. The M^2 value is the ratio of the laser beam's multimode diameter-divergence product to the ideal diffraction limited TEM_{00} beam diameter-divergence product. Thus for a TEM_{00} beam, the M^2 value is defined as 1. The minimum diameter to which a laser beam can be focused is determined not only

by the focusing optics but, as a first order approximation, is also proportional to the M^2 value of the beam. An analytical description of M^2 is defined in Chapter 5.

Beam divergence describes how the diameter of the collimated laser beam (irrespective of the intensity value defining the beam diameter) changes as the laser propagates. Diffraction causes light waves to spread transversely, so a perfectly collimated laser beam can never be produced and will always diverge slightly. However, unlike light beams examined using classical geometric optics, Gaussian beams do not diverge linearly. Close to the laser, the beam divergence is extremely small, but as the propagation distance increases, so does the beam divergence until it approaches an asymptotic limit. The beam radius along a focused laser beam is given in equation 4.2

$$\omega(z) = \omega_0 \left[1 + \left(\frac{\lambda z}{\pi \omega_0^2} \right)^2 \right]^{\frac{1}{2}}, \qquad \text{- 4.2}$$

where ω_0 is the minimum beam waist, λ is the laser wavelength, and z is the distance from the focused beam waist.

A focus term can be introduced into the wavefront to partially compensate for the observed asymptotic cone, optimising the beam diameter over a given range. Creating an LGS is an interesting problem, as a near-field diffraction pattern is created at what would normally be considered a far-field position i.e. 4km from the BLT objective, resulting in a very large diffraction limited spot at the focal point of the BLT. A full analysis of the propagation of a Gaussian laser beam through the atmosphere is presented in Chapter 5.

4.7 Beam Launch Telescope

The function of the BLT is to re-image an input focal point (real or virtual) at a given distance from the BLT to create a suitable LGS. Many factors must be considered in the design of the BLT. The first point, and arguably the most important of all, is the primary objective diameter. Larger diameter objectives generate smaller focal spots on the sky, but are heavier and require a larger space envelope for mounting. A larger diameter launch apertures also means the focusing laser beam samples a greater volume of atmosphere along the path to the LGS altitude (referred to hereafter as the 'uplink path' of the laser). If the launch aperture is too large, the turbulence sampled on the uplink can induce distortions in the laser wavefront great enough to increase the focused LGS spot size. Smaller diameter launch optics are far lighter, so mounting them on the main telescope structure would not affect balance, and reduces overall BLT cost.

The optimum BLT objective diameter is defined by the required LGS focal size in the sky, and the strength of the turbulence the propagating LGS beam will encounter on the LGS uplink. The effect of altering atmospheric conditions on the observed LGS spot size created by differing launch apertures was determined analytically using an atmospheric LGS propagation model. The results of this model are given in Chapter 5.

One of the initial decisions that must be made in the design of a BLT is the choice of a reflective or refractive design. Each has advantages over the other. An on-axis refractive design, e.g. a Newtonian telescope, is attractive because retro-reflection can be used for initial optical alignment of the BLT to the BRS. On-axis projection of the LGS through a Newtonian, Cassegrain or similar telescope does remove the central, highest intensity part of the laser beam due to the requirement for a secondary mirror.

Therefore the output laser power is reduced. However, the diffraction pattern from a truncated Gaussian beam with central obscuration does give a higher contrast ratio between peak intensity and intensity of the first diffraction ring of the airy profile than that observed from an unobscured truncated Gaussian source. Projecting from an off-axis reflective component removes the issues associated with the on-axis launch, but the cost and complexity of designing large off-axis components is often prohibitive.

The effect of the central obscuration on the relative intensity of the diffraction pattern is shown in Figure 4.8. The relative intensity of the first diffraction ring of the airy pattern decreases with an increase in central obscuration diameter until the beam is completely obscured. Although a Gaussian intensity beam forms a Gaussian intensity image when focused, the output intensity profile must be truncated at some intensity level by the clear aperture of the BLT. Truncation can cause diffraction rings to be formed around the Gaussian intensity central core. Truncation of the Gaussian profile is not desired in a BLT as it reduces power on sky. A focussed Gaussian beam with a central obscuration has a large fraction of the light in the central peak, with a small fraction of the remaining light distributed over a far greater area. The presence of a diffuse airy pattern around the LGS would have little effect on any measurement of LGS spot size, as any signal from the first airy ring would be swamped by read noise present on the WFS. In practice, the airy ring is rarely present around the LGS, as atmospheric turbulence on the uplink means the LGS never reaches the diffraction limit of the BLT. Therefore, the diameter of a central obscuration in a BLT should be minimised, or the obscuration avoided altogether, because it has no discernable effect on the angular diameter of the LGS, and only serves to reduce LGS intensity.

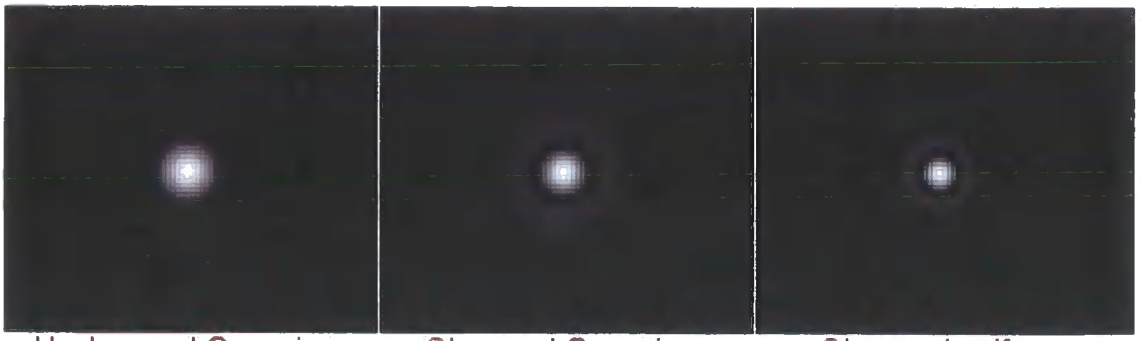

Figure 4.8 Focal points from obscured versus unobscured Gaussian input beams. Gaussian beams have been truncated at their $1/e^2$ intensity points. Central obscuration diameter is 29% that of pupil diameter. The obscured pupil image formed by a uniformly illuminated intensity profile is included for comparison.

Refractive designs have no central obscuration to contend with and as such are often preferred for launch optics because laser power is a critical factor in the performance of an LGS AO system. The large lens can also act as a window for the BLT, reducing the need for cleaning of any internal components.

A BLT must be designed with a method to allow for the BLT to be aligned to the main telescope. This process is referred to as 'bore-sighting' the BLT. After bore-sighting has been completed, the BLT points with the main telescope. Including a method for remote bore-sighting into a BLT design can be rather difficult as all optical elements in the BLT must rotate round a common point during adjustment to the main telescope, whilst retaining internal alignment, as well as alignment to the beam relay system. This requires reasonably complicated optical systems (which reduce overall efficiency of the BLT by including extra surfaces) and/or actively steered components (which require computer control systems, hence increasing cost and system complexity). Without any of these methods included in the BLT design, changing the bore-sighting of the BLT to the main telescope requires a realignment of

the BLT to the BRS. This can be a time-consuming operation requiring many alignment iterations before the BLT is near bore-sighted.

When trying to position the LGS with sub-arcsecond accuracy, mechanical backlash can be observed. If the optic being moved is large, very powerful motors must be used in combination with a mechanically-stiff kinematic mount to counter backlash. Powerful motors require large currents for operation and generate large amounts of heat, which is not a desirable feature for a telescope observing at IR wavelengths. The effect of backlash was reduced on-sky by adopting an alignment procedure whereby the LGS was steered from a point with large angular offset onto the WHT optical axis without reversing the direction of the BLT motors. This procedure was repeated if the LGS overshot the on-axis field point of the WHT.

Bore-sighting can be simplified by building off-axis tolerance into the BLT optics. Once the LGS points to a position within the tolerance of the BLT launch optics, a steering mirror can be used to bore-sight the LGS beam with arcsecond accuracy and without compromising the LGS spot size. This split bore-sighting method allows the use of a very stiff BLT structure thus reducing LGS motion due to BLT flexure and vibration. This can also be accomplished with very small steering components that do not suffer from backlash.

The focal altitude of the LGS can easily be controlled by a movable optical element in the BLT. For a sodium LGS, the focal altitude of the BLT must change with telescope elevation to ensure the BLT always focuses on the sodium layer at 90km altitude. Focal altitude for a Rayleigh LGS can be set at a fixed distance from the telescope, and as such can be a simple 'set and forget' system. The accuracy with which the focus must be set is dependent on both the required focal altitude and the BLT launch aperture diameter. For example, a 300mm BLT primary creates a 1" LGS at an

altitude 20km above the BLT. The LGS at this altitude has a physical beam waist of approximately 100mm. However, a 1.5 arcsecond LGS can still be used as a wavefront reference for most applications. Modelling the beam purely geometrically and ignoring any beam divergence or near-field effects, the beam described above still creates a 1.5" LGS between 13.5km and 38.5km altitude above the BLT launch aperture. This simple example demonstrates that there is a large degree of focus insensitivity for an LGS launched from a small aperture BLT. Figure 4.9 shows the altitude range that gives a 1.5" LGS diameter for a given LGS altitude.

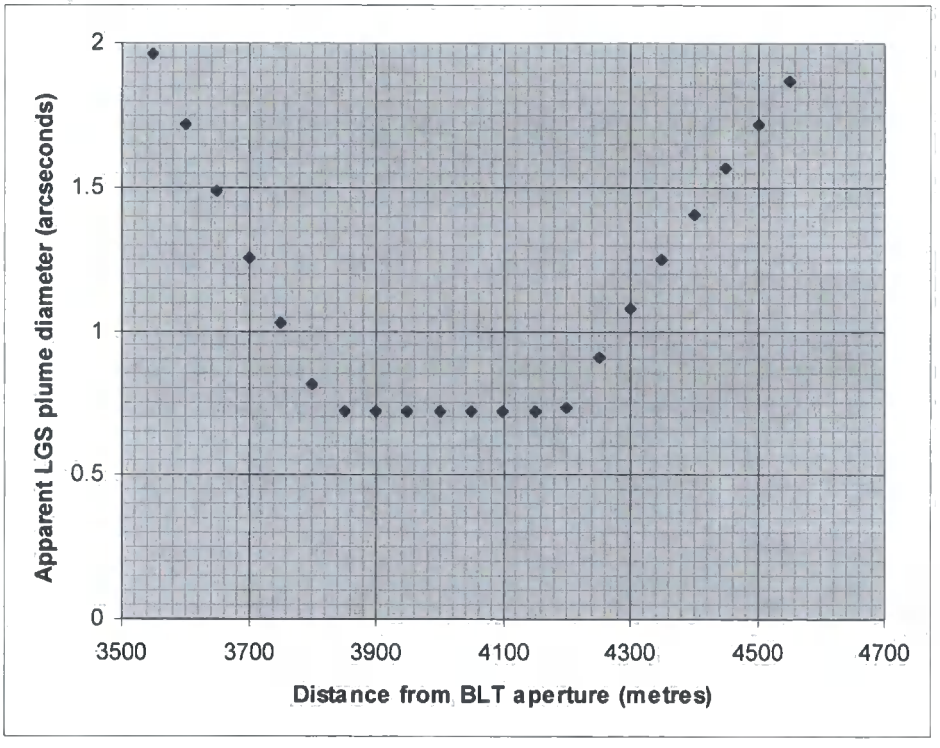

Figure 4.9 Altitude range for a 1.5" LGS modelling the LGS plume as a cone focused at the LGS focal altitude of 4km. To approximate diffraction effects when the cone diameter is less than the FWHM diffraction limit of the BLT (given by $2\lambda/D_{BLT}$), the LGS plume is replaced by a column of constant diameter that has an apparent diameter of $2\lambda/D_{BLT}$. Telescope defocus is not included, but the perspective narrowing of the beam is included.

For the optimum 4km range gate determined in Chapter 7, the 1.5" altitude range stretches between 3.65km and 4.43km. This implies that a coarse initial focus need

only position the LGS to within a few hundred metres of the required altitude before the WFS can be used to observe the LGS. At this point, determination of the LGS focal altitude can be accomplished using the full range gate system and a precise minimisation of the observed LGS diameter can be undertaken. Without the use of the range gate system for final focal altitude adjustment, the Rayleigh plume contaminates the WFS image, and the LGS is imaged along with an unwanted photon return from any non-range-gated altitude, thus increasing the apparent spot size as is shown in Figure 4.10.

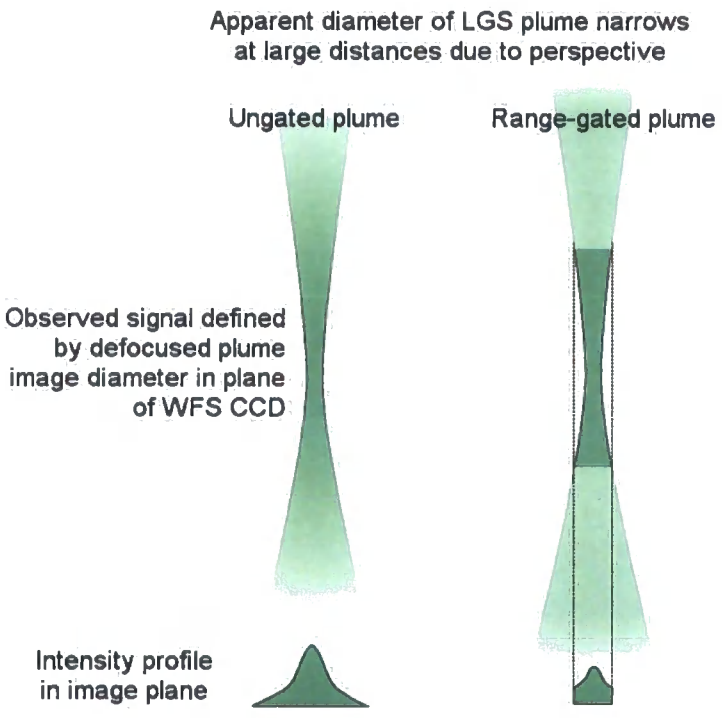

Figure 4.10 Diagram showing effect of viewing a non-gated Rayleigh plume versus range-gating of the plume on image intensity and apparent diameter. The apparent diameter of the LGS is greater for a non-gated plume.

A detailed model of BLT performance and LGS interaction with the WFS is presented in Chapter 5.

4.8 Laser Launch System Description

The laser was installed on the GRACE (GRound-based Adaptive optics Controlled Environment) Nasmyth platform of the WHT in the space envelope that is reserved for instrumentation using the NAOMI optical science port (Figure 4.11). The GRACE Nasmyth platform is a temperature and humidity controlled environment. When the laser is running, the temperature is set to the maximum available value of 19°C, as the laser power output has been observed to drop from the nominal 5W if the ambient temperature falls below 23°C. At 19°C, the maximum output laser power was measured using a Coherent LM-10 HTD thermopile sensor as 4.50±0.09W. The laser was aligned to the Nasmyth optical axis of the telescope by using a dielectric fold mirror. At this point the laser passed into the opposite Nasmyth platform where the GLAO system was situated.

Figure 4.11 Laser sitting in space allocated to the optical science port of NAOMI

The initial laser divergence was determined by placing a lens at the exit of the laser head (Relay Lens 1). A pair of cylindrical lenses placed at this point also allowed for reformatting of the beam from the normal elliptical output to a circular intensity profile. Once the laser was aligned to the optical axis of the WHT using the Nasmyth

targets (two opaque concentric ring targets that are accurately positioned on the WHT optical axis), a fold mirror (referred to as 'Relay Mirror 1') was attached to the primary mirror cell of the WHT such that it rotated with a change in telescope elevation angle (Figure 4.12). Relay Mirror 1 was mounted on an optical rail such that it could be moved to allow the laser to be used as a calibration source in GHRIL. The light was directed by Relay Mirror 1 through two 25mm holes drilled in the mirror cube and into a lightproof pipe with an internal diameter of 50mm. This bore encompasses the light path to the top end of the telescope (Figure 4.13).

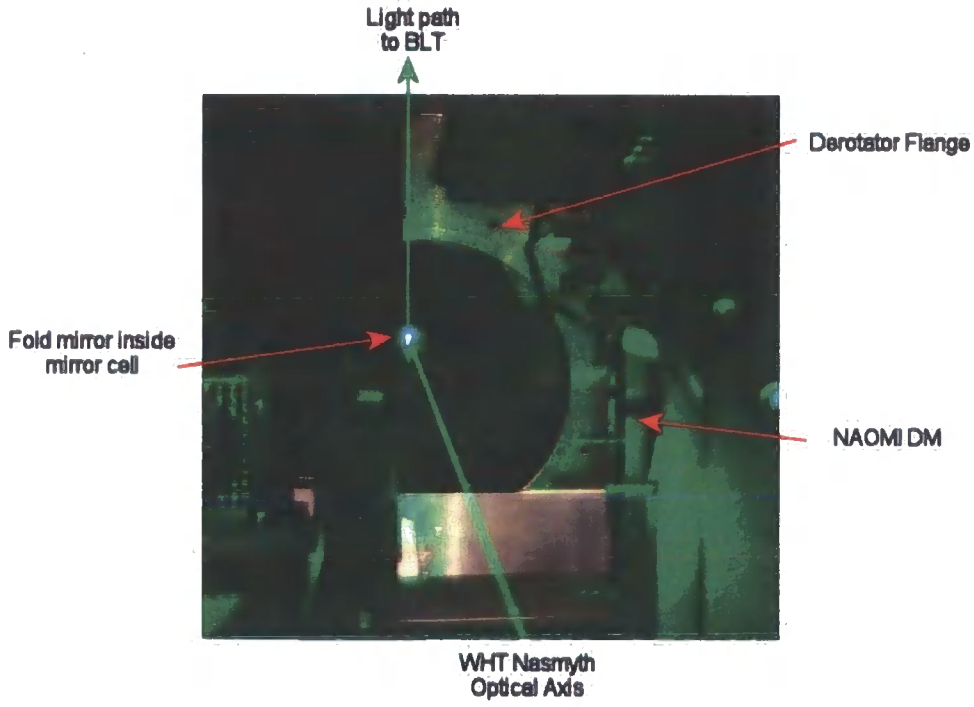

Figure 4.12 View along WHT optical axis in the GRACE Nasmyth platform to Relay mirror 1 in mirror cell that directs the light towards the top end of the BLT.

Figure 4.13 Enclosed beam path from WHT mirror cube to the BLT. Relay Mirror 2 is supported using the yellow-coloured structure attached to the top-end ring.

The light passed through two further holes (in this case bored through the top-end ring of the WHT) to a Relay mirror 2 positioned approximately 1.5m from the top-end ring surface on a rigid support structure (the yellow-coloured structure shown in Figure 4.13). Vibrations in this support structure were reduced in amplitude by cross-bracing tension cables. Relay Mirror 2 was enclosed in a light-tight neoprene box and directed light across the aperture of the WHT through a second 50mm diameter pipe. The introduction of this pipe reduced the light collecting area of the WHT by $0.075m^2$, which is an overall reduction in clear aperture of 0.6%. The effect of this 5^{th} vane on the image produced at the WHT focus is shown in Figure 4.14.

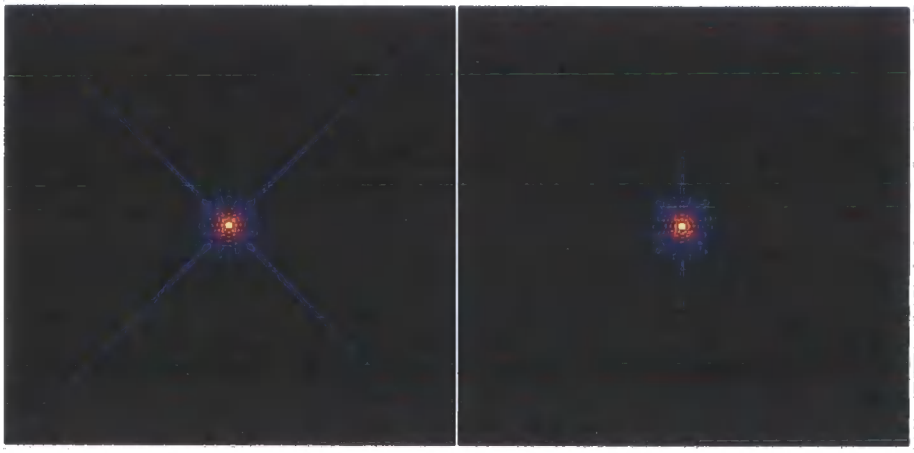

Figure 4.14 Theoretical spot pattern with (left) and without (right) 5th vane. Total intensity drops by 0.6% if 5th vane is included. Relative energy within the diffraction limited core increases with the inclusion of the 5th vane as energy is taken away from the diffraction spikes.

After passing through the final light pipe the beam entered the coarse focus mechanism. This consisted of a 100mm focal length 523nm AR-coated singlet lens (Relay Lens 2) of 25mm diameter mounted on a micrometer-driven translation stage. The divergence of the beam was adjusted by moving Relay Lens 1 such that the beam expanded inside the BRS from an initial 2mm diameter to the 12mm diameter required to produce an f/6 beam upon exiting the Relay Lens 2. This f/ratio was required to fill the full aperture of the BLT. Relay Mirror 3 (diameter 25mm) was placed on the optical axis of the BLT primary mirror. This mirror was glued to a miniature tip/tilt stage using a two-part epoxy adhesive to allow for easy alignment without any undue vignetting of the outgoing LGS beam. The support structure for this mount was an aluminium bar that created a 2mm wide obscuration across the BLT primary aperture. The support allowed Relay Mirror 3 to be centred above the BLT primary aperture, thus ensuring a good internal alignment of the BLT. Total vignetting of the BLT beam caused by Relay Mirror 3 and the support structure was calculated as 1.49% of the BLT primary aperture. In terms of power on-sky transmitted by the BLT, the actual vignetting factor is higher as the laser exhibits a

Gaussian intensity profile, whereas the above percentage would translate into a power on-sky only if a uniform intensity profile were assumed. Taking the non-uniform intensity into account, and assuming the $1/e^2$ diameter of the Gaussian intensity profile is 300mm, the actual transmitted power on-sky from the BRS input by the BLT becomes 4.06%

The BLT primary was an on-axis parabolic mirror, 300mm in diameter and with a focal length of 1833mm. This mirror was chosen as it allows a reasonable LGS to be created (1.4" LGS FWHM at 4km), and had been inherited from a previous project. The mirror was mounted on three worm drives powered by geared stepper motors to give fine tip/tilt and focus adjustment. Springs were used to balance the action of the motors. The springs were initially too stiff to allow the stepper motors to move freely and so were replaced with springs that provided enough resistance to allow the mirror to move without the motors slipping. However, the combination of the weaker replacement springs coupled with the mechanical design of the motor housings, which allowed the motors to twist slightly, meant the mirror drives could exhibit backlash. This only became apparent when the LGS was projected onto the sky and the fine tip/tilt adjustment was used. The degree of backlash was of the order of 3" and could not be observed without the very sensitive position adjustments that were visible with the LGS at 4.5km. Difficulties in positioning the LGS with arcsecond accuracy required many attempts before a good boresighting was achieved. Solving this problem by increasing the stiffness of the system required replacing the motors and springs, which was not a feasible option with the time and budget available, but twist supports were added to the motors to reduce any backlash present in the system from this source.

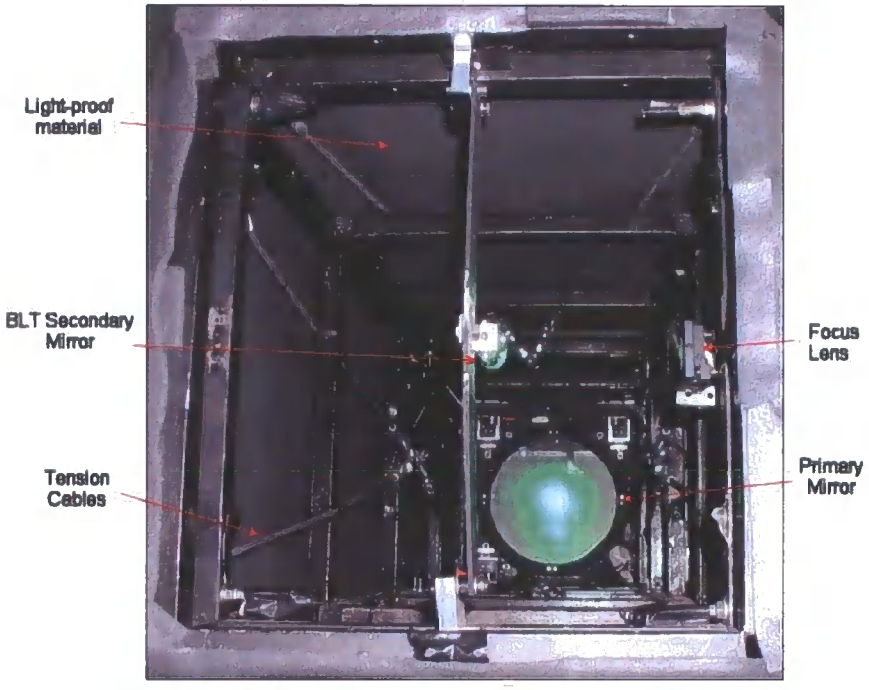

Figure 4.15 Photograph showing internal BLT structure.

The throughput of the system at the exit of the focus lens (i.e. the throughput of the BRS), and the reflectance of the BLT primary mirror were measured. The BRS power output was 3.6W from an input of 4.4W at 523nm. Relay Mirror 3 had a quoted reflectance of 99.5%, and the reflectance of the BLT primary was measured at 93%. Using 90% of the Gaussian intensity profile as the cut-off for the 300mm aperture, and with the BLT vignetting factor described above, the overall throughput of the laser launch system was 68%. As determined in Chapter 5, the optimum altitude that the LGS should be generated at is 4km. This meant that the position of the input focal point to the BLT from the BRS must be 1833.84mm from the BLT primary. From the relative magnification of the BLT input and output beams, to create a 1" focused LGS spot on the sky, the beam diameter at this point must be 8.73μm. The only beam profiling camera that was available had a pixel scale of 17μm, while scanning the focused beam waist with a knife edge would not have provided an accurate profile

due to the vibrations present in the telescope structure and dome. The input beam waist could not be measured using the equipment that was available for this project.

The launch system design presented above was one that allowed us to generate an on-axis LGS from a centre launch using the equipment and resources available. Although the design had several shortcomings (limited operating range, backlash, etc.), it overcame many of the problems of a shared launch system. It also provided a safe and easy-to-align system that would allow us to test the LGS on the sky within the project timescale. A description of the BLT optical input/outputs and associated parameters is given in Table 4.1 below.

Launch System	LGS focus (4km)	Units
BLT Primary Diameter	300	mm
Resolution	0.438	arcsec
BLT input f-number	6.0027	
BLT output f-number	13333.33	
Magnification	2221.222	
1" LGS requires input spot of diameter	8.73	μm
Throughput (on-axis)	0.68	

Table 4.1 Optical inputs/outputs of BLT.

4.9 Laser Safety

The safety precautions that must be taken when using high-power lasers are well defined when being used within a laboratory [7], and these were followed at all times when working with the laser, both in the laboratory and installed on the telescope. Creating the LGS required launching a focused high-power laser into the atmosphere, requiring consideration of several other safety aspects.

The first of these involves aircraft. Any aircraft passing through the beam will be illuminated by an output beam that has a minimum diameter of approximately 1" at a fixed distance of 4.5km from the WHT. When the WHT is pointing at zenith, this equates to a 22mm diameter beam at an altitude of 7km. If an aircraft cruising at

900km/h at this altitude is illuminated by a 5W laser with these parameters, the speed of the aircraft ensures that approximately 30 consecutive laser pulses could enter the aircraft cockpit (assuming a 1m length cockpit window). This gives a 20mJ flash lasting for 0.004s in the cockpit. The laser power becomes more hazardous if an observer is looking directly down the beam, but with a fully dilated pupil diameter of 7mm, at most, a single laser pulse could be observed and 1.4mJ will enter the eye. This is above the defined MPE (maximum permissible exposure) level. There is a no-fly zone in place above La Palma prohibiting aircraft from overnight flights within approximately 20km of the island and local air traffic control is informed and gives permission for the laser to be used. These safeguards ensure no planes will fly through the laser plume as long as the telescope does not track below 35°.

Similar problems exist for satellites in low-earth orbit at an altitude of ~300km above the surface of the Earth. However, a laser beam projected from a 300mm aperture and focused at 4.5km will be approximately 19.5m in diameter at an altitude of 300km. At this power density, the laser light does not pose a risk to the eye, although sensitive CCD cameras on satellites may become saturated.

4.10 Laser Launch System Alignment

Alignment of the LLS is a multiple stage process. The first stage, which has already been described, was alignment of the laser to the optical axis of the WHT. At low powers (below 100mW) this produced a very useful on-axis light source at the correct wavelength for the AO system in the opposite GHRIL Nasmyth platform, and by increasing the laser output power to 500mW, scattering at all the surfaces in the system made the beam footprint easily visible (Figure 4.16). This greatly simplified

the task of AO system alignment. Care was taken when running the laser at higher power not to damage any optical components in the GLAO system.

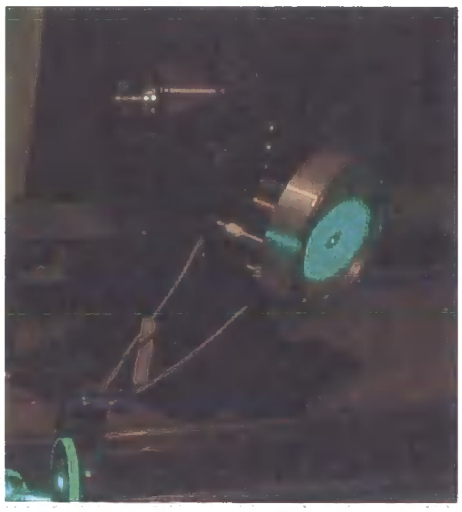

Figure 4.16 Beam footprint on NGS FSM demonstrating use of high-power laser to align large diameter collimated beam path.

After the laser had been aligned to the WHT optical axis, the next stage was the BRS alignment. Relay Mirror 1, like the laser itself, must also be very accurately positioned to the optical axis of the WHT, otherwise the beam pointing drifted as the telescope changed elevation angle, rather than just exhibiting vertical displacement due to the top-end sag. After alignment, Relay Mirror 2 directed light across the WHT aperture into the BLT. After the two relay mirrors were aligned, adjustments to the BLT and Relay Mirror 2 had to be undertaken whilst the WHT was horizontal. By removing Relay Lens 2, laser light could be retro-reflected from the BLT primary back down the relay system and an accurate alignment of the telescope to the BRS input achieved. The focus lens was then replaced at the approximate position to create a 4km LGS, and the BLT pupil pattern was projected onto the inside of the WHT dome. The WHT was then pointed 30 degrees from zenith and as expected, the top-end sag caused misalignment in the BRS. After re-alignment of relay mirror 1, the pupil pattern from the BLT primary aperture was again projected onto the inner

surface of the WHT dome. Changing elevation between 60 and 80 degrees at this point had little effect on the uniformity or position of the pupil pattern and the LLS was ready for on-sky alignment of the BLT to the optical axis of the WHT.

Bore-sighting the BLT and WHT can only be accomplished accurately with an on-sky alignment procedure. As previously mentioned, there are two stages to the on-sky alignment. The first stage was a coarse alignment procedure that required altering the pointing of the BLT structure, the second stage was carried out when the BLT pointing was within a small angle of being bore-sighted to the WHT. The first step was to choose a bright ($m_V = 2$) reference star and project the laser from the BLT. As the BLT had no bore-sight camera for alignment, the only way to determine the alignment was to utilise parallax to see where the LGS was pointing. By moving from one side of the open dome to the other and examining the apparent position of the laser on the sky relative to a star tracked by the WHT, the BLT could be bore-sighted to well within an arcminute. This task was simplified by using binoculars. At this point, the return could be observed within the GHRIL Nasmyth platform and the rough parallax alignment method was no longer required.

To change the initial alignment of the BLT, the telescope was lowered until it was horizontal. The BLT was then shimmed, and at this point required re-alignment to the BRS using the retro-reflection method described above. This was because re-pointing the BLT structure moves Relay Mirror 3 away from the BRS output. Thus the BLT was no longer in the retro-reflection condition and the primary mirror of the BLT was being used off-axis. This affected projected spot quality, with highly aberrated LGS's being created if the alignment was not accurate. Aligning the BLT to the WHT in this way required much time, but was the only method that was possible without including bore-sighting camera(s) and a means for remotely altering the pointing of the BLT.

The BLT retained bore-sighting over the course of the 5-day run with no need for further alignment.

Once the coarse bore-sighting had been achieved, the fine tip/tilt motors were used to move the LGS onto the optical axis of the WHT as observed in the Nasmyth platform. This was achieved despite the difficulties experienced with backlash on the motors. A wide-field (2.5 arcminute) acquisition TV camera was placed on a rail at the bare Nasmyth focus of the telescope to help with this task.

The next task was to tune the focal altitude of the LGS from the coarse initial focus that was defined by the position of Relay Lens 2. Previous experience of launching the LGS from a full aperture shared launch [8] had shown that the LGS focal point could be easily observed with the naked eye and standing approximately 6m from the optical axis of the telescope when the LGS was created at 4km. When the LGS focus could be directly observed from the 300mm aperture launch, the focal altitude was measured from off-axis observations as being below 500m. An increase in LGS plume intensity at the LGS focal altitude cannot be observed with the naked eye from a 300mm diameter beam focused at 4km.

The simplest means of determining the focal altitude of the LGS was achieved by moving the acquisition camera along the optical axis. This allowed the whole Rayleigh plume between 2km and 10km to be imaged. As the wide-field camera by definition has a small depth of field, the LGS at the altitude conjugate to the position of the TV camera was imaged. The image of the LGS was surrounded by a defocused image of the plume from altitudes non-conjugate to the position of the TV camera. The focal altitude of the LGS was clearly visible as the point where the LGS image was narrowest. Using this simple technique would not be possible if the laser were focused at a higher altitude because the distance between conjugate altitudes on the

telescope optical axis is much greater for low altitude rather than for high-altitude LGS's. The focus was then adjusted by returning the WHT to the horizontal position and adjusting the position of the top end lens. The BLT primary mirror drives were not used for final focusing as LGS motion was observed when the motors were moved. This was once again due to backlash in the mirror mount drives.

Four alternative methods of determining LGS focal altitude were used. By using the range gate system the conjugate altitude of the range gate could be moved up and down the Rayleigh plume until the LGS spot size was minimised. A second method used an off-axis monitoring telescope to image the LGS plume while the WHT was pointed at zenith. In this way, a direct and simple correlation existed between the elevation angle of the off-axis monitoring telescope and the altitude of the image of the plume. The LGS focus was then determined by finding the point where the imaged plume was narrowest. This method of focal altitude determination was used in the April 2004 observing run and the results are shown in Figure 4.17.

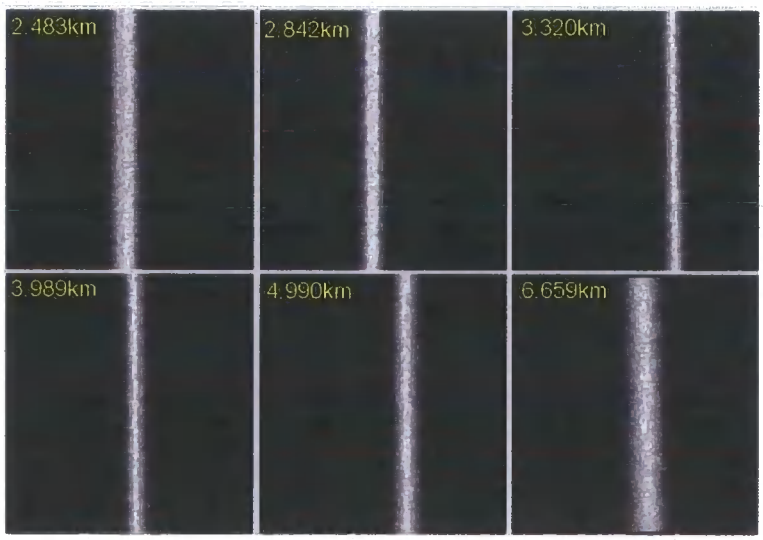

Figure 4.17 Off-axis images of the Rayleigh plume taken from a point 350m away from and 20m above the WHT. A 16" Meade telescope with Andor Ixon 128 camera was used. WHT (and hence BLT) was pointed at zenith and not tracking during these exposures. This allowed the zenith angle of the off-axis telescope to be easily translated into an altitude above the telescope.

The third method was to use a PMT with a small entrance aperture to determine the focal altitude. If the PMT is moved along the optical axis of the WHT (along the same rail as the acquisition TV camera to ensure optical alignment is retained) the PMT aperture acts as a field stop and blocks most light from all altitudes other than a small altitude range around the conjugate position of the PMT aperture. If this aperture is 2" in diameter (i.e. ~0.5mm in diameter) it is only when the LGS is below 2" in diameter that the return beam is unvignetted. The maximum return through the aperture can also be timed and compared to the trigger pulse from the laser. In this way a very accurate determination of the focal height was obtained.

The final focal altitude method is one that was not initially envisaged and involved utilising high layer cloud. On nights where thin cloud was present, the PMT registered a large return from the cloud layer. This altitude was measured by timing the return pulse. Then by viewing the LGS beam through the acquisition camera, the BLT pupil pattern projected onto the cloud was observed. The angular size of the pupil pattern on the cloud was measured from this observation and then the distance to the focal point of the LGS beam could be calculated. Another method that could be used in a cloudy sky is to decrease the telescope elevation until the cloud is 4.5km from the BLT aperture as measured by the PMT, and then minimise the LGS spot size in the acquisition camera, as the Mie scattered photon return from the cloud is far greater than that of the Rayleigh scattered photon return from the LGS plume. This is useful as it allows preparatory work to be carried out on the LLS even though the night may be completely useless for astronomical observations. However, it would of course be unwise to discard the other methods of altitude determination in favour of using the intense photon return from high-altitude clouds.

4.11 LGS Quality Testing

Once the focal altitude and boresighting of the BLT were set, the next task was to characterise the quality of the LGS, and hence the LLS. A series of tests were performed, including photon return, LGS spot size, LGS spot motion, polarisation tests, long-exposure images and LGS stability compared with elevation angle. The results are given below.

6000 images of the un-gated LGS plume were taken using the WHT on the 24th September 2004 between 0114 and 0121 GMT. The images were taken as 2 sets of 1000 and 2 sets of 2000 images, each image with an exposure of 1ms. The frame rate was limited by the readout speed of the camera and was measured at a later stage as 29.6Hz. The WHT was tracking SAO49528, but the 2nd magnitude star did not contaminate the observed photon flux of the LGS as the defocused infinity image was approximately 35mm across. This allowed the LGS image to be positioned inside the secondary obscuration of the stellar image. The camera, a Qimaging Retiga 1300, was conjugated to a distance of 5km from the WHT. At the 5km focus, the WHT has a plate scale of 4.41arcsec/mm. A single lens was used to increase the field of view of the camera, although this was at the expense of field uniformity. Field uniformity and pixel scale were determined by imaging a piece of graph paper (see Figure 4.18) The pixel scale at the mean LGS position in the field was determined at 0.47arcsec/pixel.

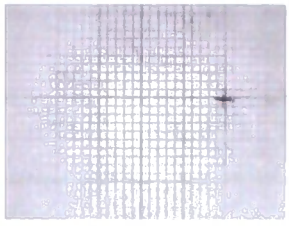

Figure 4.18 Calibration chart for LGS plume camera showing uniformity across CCD FOV. Pixel scale at the image centre is 9.37 pixels/mm.

4.11.1 LGS Spot Size

Images of the Rayleigh plume were taken at the bare Nasmyth focus of the WHT. Although the photon return at this point is not range-gated, a bright central core can be observed that is surrounded by a diffuse halo, and not a sharp spot that is required for high-order WFSing through a lenslet array. A sample LGS image from the data set is shown in Figure 4.19.

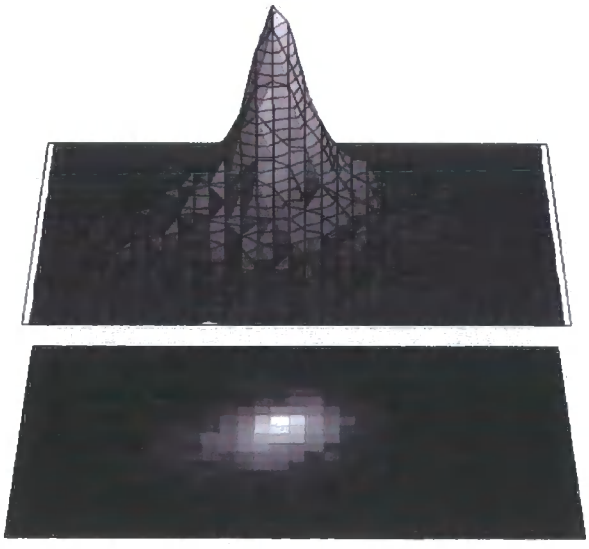

Figure 4.19 A 1ms exposure image and associated profile of the un-gated Rayleigh plume taken at the bare Nasmyth focus of the WHT. Pixel scale is 0.47 arcsec/pixel.

The mean FWHM was 2.29" with a standard deviation of 0.28". The FWHM was calculated by azimuthally averaging the image around the spot centroid. The mean spot $1/e^2$ diameter was 5.33" with a standard deviation of 0.34". For a pure Gaussian intensity profile, the ratio between FWHM and $1/e^2$ diameter is constant given by $\sqrt{-\ln(0.5)/2} = 0.588$. The ratio measured from the LGS images is 0.425, showing that the intensity profile is not Gaussian, and has more energy within the wings of the beam.

Without using a range gate, the LGS spot diameter cannot be measured directly when observing on-axis. The off-axis plume data shown in Figure 4.17 was analysed to determine plume diameter. The CCD used to take the off-axis images had a scale of 1.21" per pixel. The $1.22\lambda/D$ diffraction limit of the 16" Meade telescope used for observation was 0.32". The camera had been focused on the plume at a zenith angle corresponding to 4km, and the degree of defocus observed on the CCD as the zenith angle changes can be simply calculated with knowledge of the telescope optics and camera pixel scale.

Laboratory testing of the Retiga 1300 CCD with a 1ms pulsed light source confirmed that when a 1ms exposure time was set using the camera internal electronics, a 1ms exposure time was achieved on-sky. The frame rate returned by the control software was 0.2Hz slower than the true frame rate of the camera. This discrepancy is due to the overhead of transferring and processing the data within the computer.

After accounting for the degree of defocus in each image, a plot of plume FWHM versus altitude was made and is shown in Figure 4.20.

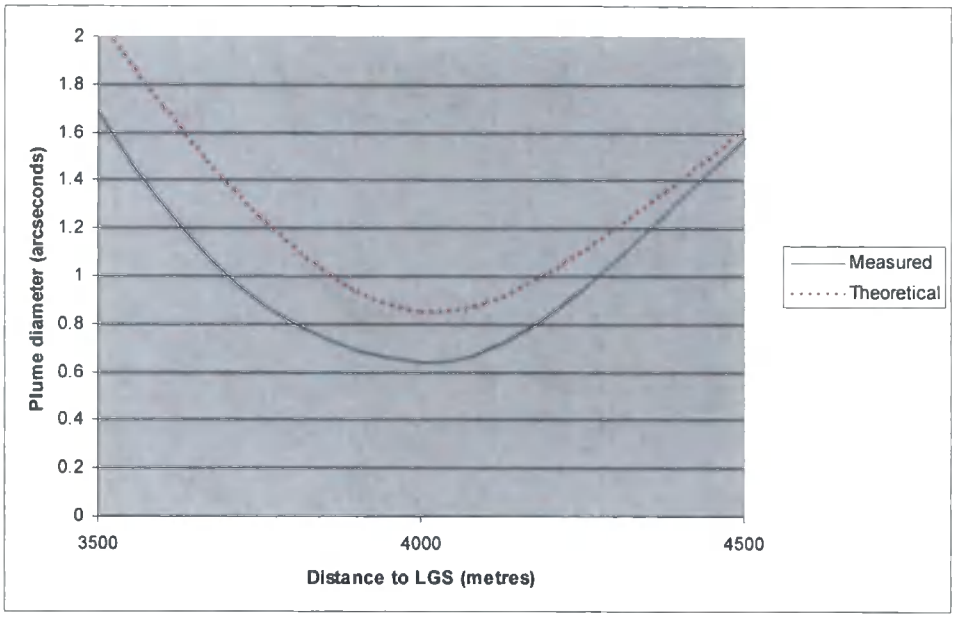

Figure 4.20 Plot of $1/e^2$ plume diameter versus altitude taken from the off-axis plume images. Telescope defocus has been corrected over the altitude range shown. Theoretical plot was created using the method presented in Chapter 5.

For the focused plume image at an altitude of 3.989km, the ratio between FWHM and $1/e^2$ diameter was measured as 0.412. The actual FWHM values after correcting for defocus only matched over the small altitude range shown in Figure 4.20. Without correcting for the telescope focus, the FWHM measured from the off-axis telescope was far greater than the FWHM measured using the WHT. Several external factors were thought to cause this. First, telescope jitter from both the WHT and off-axis telescope would increase the apparent plume diameter. The effect of atmospheric turbulence must also be considered as this would increase the apparent diameter of the plume.

4.11.2 LGS spot motion

A high-speed camera was used to record the centroid position of the LGS. This value is affected by both the atmospheric conditions but also by any vibrations that are present within the LLS.

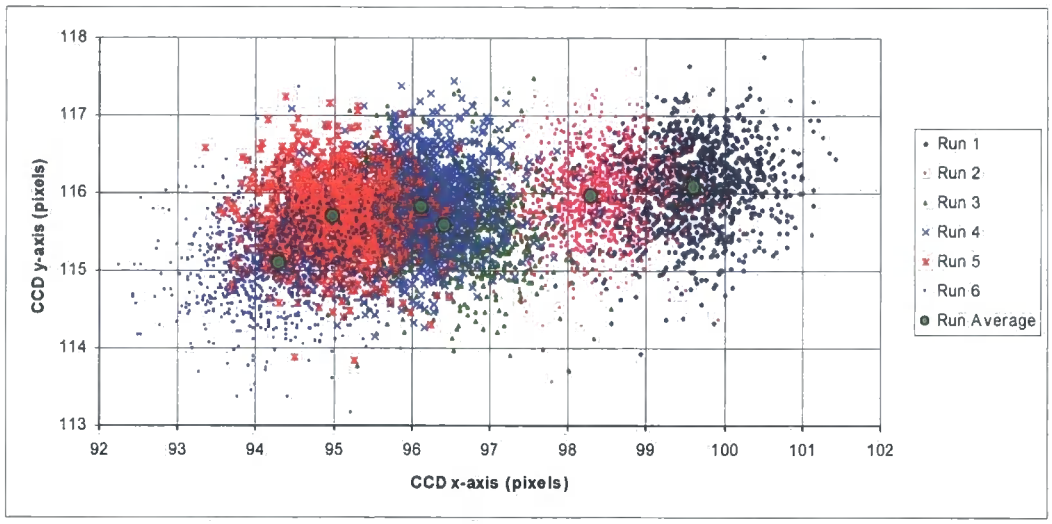

Figure 4.21 X and Y centroid values in terms of CCD pixels plotted for each set of 1000 images. Mean position of each set is indicated by a green circle.

The general trend in mean centroid position shown in the figure above was due to the effect of telescope sag on BRS alignment. The telescope altitude angle at the midpoint of each run is given in Table 4.2, along with the associated top end sag of the telescope. A second order polynomial was fitted to the measurements taken of the WHT top-end sag so that the small changes in elevation angle could be determined. Over the entire altitude range of the WHT, the fitted polynomial matched the observed sag of the WHT to within 25μm.

Set	Altitude	Sag (mm)
1	51.6	0.601212
2	51.4	0.607369
3	50.6	0.631915
4	50.5	0.634975
5	50.2	0.64414
6	50.1	0.647191

Table 4.2 Telescope altitude axis angle and modelled top-end sag for the sets of LGS plume images. WHT modelled sags match measured sags across a 0° to 90° elevation angle to ±25μm.

Although over a very short baseline, the modelled sag can be compared to the LGS spot offset to determine the pointing stability of the LGS while tracking. An analysis

of these two sets of data shows that the LGS moves on-sky by 51.14 ± 1.48" for every millimetre of top-end sag.

With the BRS aligned at 70°, the telescope can track until the top end sag has moved the LGS outside the FOV of the LGS WFS. If the loop is closed, the LGS FSM can then correct for the drift of the LGS. The FOV of the LGS WFS is 2.11", meaning that the top end can sag by 0.041mm. This corresponds to a change in telescope elevation angle of ±3° if the LGS has been aligned at a 70° elevation angle.

At the latitude of the WHT, the LGS drift observed when the telescope tracks an object will result in the LGS moving across the WFS FOV in approximately 20-30 minutes, depending on the declination of the star being tracked. The loop must be closed within this period, or a new star must be found.

4.11.3 LGS Launch Jitter

Once the LGS spot motion due to telescope sag had been measured and calibrated, the instantaneous spot jitter could be measured. A histogram showing the magnitude of observed instantaneous spot jitter is plotted in Figure 4.22.

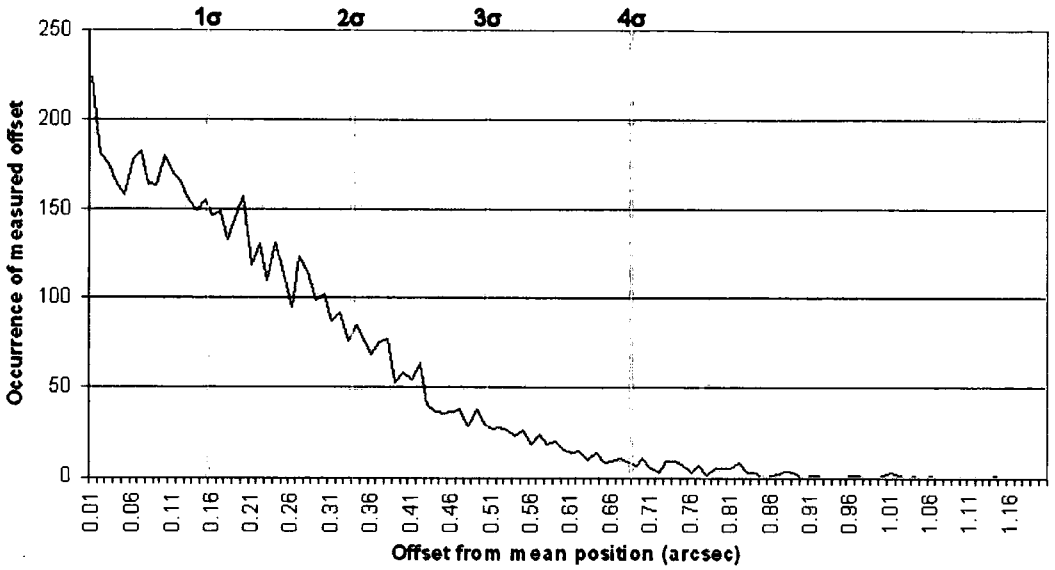

Figure 4.22 Histogram of LGS spot jitter observed from a 4km LGS. Slow spot motion due to telescope sag has been removed. 1,2,3 and 4σ points on the histogram are indicated. 3σ spot jitter is ±0.51"

The observed ±3σ spot jitter is close to the predicted spot jitter of 0.74", as detailed in Chapter 5. As the atmospheric C_n^2 profile was not known at the time the measurements were made, the launch jitter model cannot be verified. However, that the observed LGS jitter was less than 0.8" shows that a 1" LGS with up to 0.3" of elongation can be observed by the LGS WFS without contamination of adjacent subapertures.

4.11.4 LGS Photon Return

The intensity of the un-gated plume images was measured. The gain of the camera used for determining the photon return was established such that an absolute photon return count could be established. The effect on photon return of changing telescope elevation angle was also examined.

A plot of the total intensity measured in each image was made for each set of exposures as shown in Figure 4.23. All images exhibited an approximate 24%

fluctuation in observed signal that had a characteristic frequency of 1.3Hz. This was thought to be partly due to aliasing between the 1ms exposures and the 7kHz pulse rate of the laser as the photon flux from 6 or 7 pulses was measured. Sampling 6 or 7 pulses should only reduce the observed intensity by 14%, so another cause of the fluctuation must be present. Jitter in the CCD exposure time meaning 5, 6 or 7 pulses had been sampled could give rise to the intensity variation, but the intensity plotted below does not exhibit 3 distinct intensities. This effect was therefore ruled out.

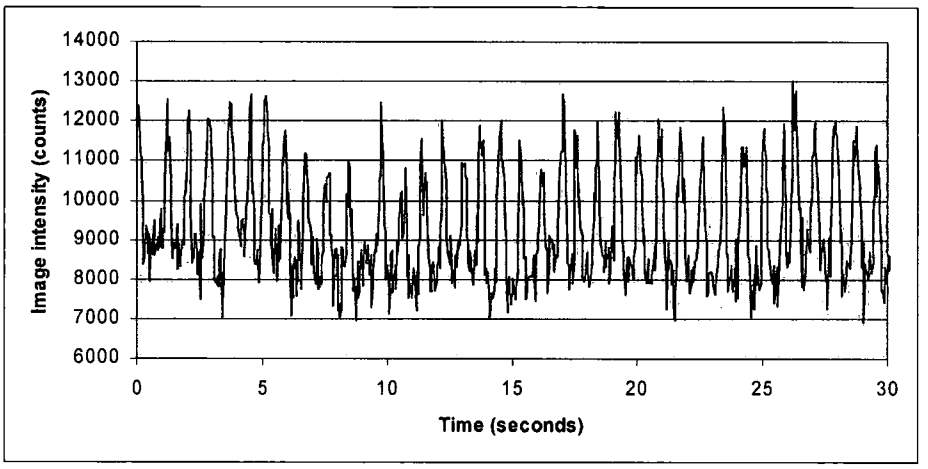

Figure 4.23 Plot of LGS plume intensity versus time for 1000 images taken with an exposure time of 1ms at a frame rate of 29.6Hz.

The intensity variation was not present at the laser output, where a 1.3Hz 24% power fluctuation would have been observed on the power meter output. The only other possible cause of error was due to telescope vibrations inducing misalignment in the BRS, causing vignetting and a drop in output power.

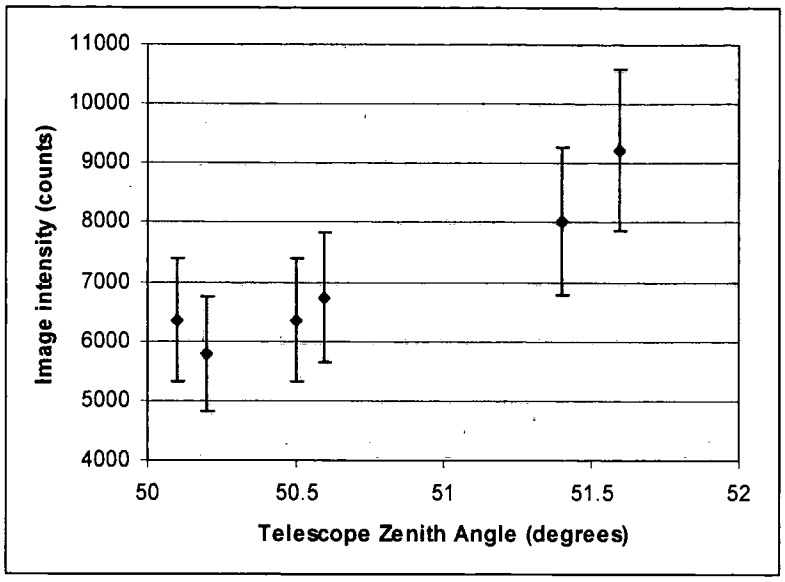

Figure 4.24 Observed mean image intensity versus telescope zenith angle. Each point represents the mean intensity of 1000 images. Error bars show the $\pm 1\sigma$ intensity point.

As can be seen from Figure 4.24, the mean intensity changes with telescope zenith angle, and hence also with top-end sag. This can cause large variations in observed power that are of a similar magnitude to account for the 24% observed power fluctuation. A 24% power drop corresponds to change in the altitude angle of the telescope by 0.9° from an initial value of 51°. At this altitude angle the top-end sags by approximately 27.6μm. If the observed drop in power is caused solely by telescope jitter, the top-end exhibits a vibration that has an amplitude of 27.6μm at a frequency of 1.3Hz.

We were unable to accurately calibrate the Qimaging Retiga 1300 camera in the laboratory to determine the detected photon flux from the LGS plume due to a lack of calibrated photon sources and/or a calibrated power meter. This is one outstanding piece of work that will be undertaken at the earliest opportunity when the correct equipment becomes available.

4.11.5 Polarisation Tests

The polarisation of the Rayleigh photon return was studied and compared with outgoing polarisation purity. As Rayleigh backscattering retains the polarisation state of the launch beam, any deviation from this initial polarisation state is due to either multiple Rayleigh scattering within the atmosphere, or other scattering processes.

Qualitative tests were carried out by viewing the plume by eye through a linear polariser on each of the three nights that the LGS was launched. At the time of checking on the first and final nights that the plume was linearly polarised and would disappear almost completely when the polarisation state of the laser and polariser were crossed. On the second night, rotating the polariser had no visible effect on the plume, suggesting that the backscattered photons were unpolarised. There were no visible or detected changes in atmospheric conditions between each night, with no visible clouds in the sky, and meteorological data showed only a slight increase in humidity.

The supposed reason for this was due to other scattering processes within the contributing to the observed photon return. Scattering from atmospheric aerosols (particularly ice crystals and dust particles) does not retain the polarisation state of a backscattered photon e.g. see Ref. 15 (and references therein). Although the degree of random polarisation was not measured, the fact that polarisation could not be discerned visually using the simple method outlined above suggests that the observed beam was only very slightly polarised. This degree of random polarisation have not been observed at other sites, although LIDAR measurements have never been made at the ORM where changes in the aerosol densities show very large variation, dependent upon atmospheric *calima*. It is not thought that changes to the launch system and laser

between observing runs caused a random *output* polarisation. These qualitative tests showed that the photon return of a Rayleigh LGS is not guaranteed to be linearly polarised, and a range gate system that can shutter unpolarised light must be employed if detected photon flux in the WFS is to be maximised. A full study of the return polarisation of the backscattered light would require a comprehensive monitoring campaign and specialised LIDAR equipment and was therefore not possible within the scope of this project.

4.12 Conclusions

The design and performance of the laser launch system used for the GLAO system has been described and characterised. Although a calibrated measure of photon flux was not derived, several other LGS quality metrics were analysed. The LGS plume diameter from the off-axis monitoring matched that predicted by the LGS WFS propagation model (presented in Chapter 5) to within 24% at the LGS focal altitude.

LGS spot motion highlighted the effect of telescope sag on the laser launch system. For a common-user instrument, this would have to be compensated for, or minimised in some other way. The magnitude of the observed launch jitter was also close to that predicted, although a direct comparison cannot be made without full knowledge of the C_n^2 profile.

There are many ways in which this experimental LLS could be improved, primarily through the use of a closed loop jitter correction system in the beam relay system. Design decisions that have compromised the performance of the system, such as the use of an on-axis Newtonian launch telescope and 5th vane across the WHT pupil have been examined.

4.13 References

1. '*Laser Guide Star Adaptive Optics for Astronomy*' edited by N. Ageorges and C. Dainty, NATO ASI Series, Kluwer Academic Publisheres (2000)
2. Piironen, P., '*A High Spectral Resolution Lidar Based on an Iodine Absorption Filter*', PhD thesis, University of Joensuu, Department of Physics. (1994)
3. DeSlover, D.H., '*Analysis of Visible and Infrared Cirrus Cloud Optical Properties Using High Spectral Resolution Remote Sensing*', M.S. Thesis, University of Wisconsin-Madison (1966)
4. King, D.L., '*Atmospheric Extinction at the Roque de los Muchachos Observatory, La Palma*', RGO/La Palma Tech. Note 31 (1985)
5. Myers, R.M. et al, '*NAOMI adaptive optics system for the 4.2m William Herschel telescope*', Proc. SPIE, Volume 4839, pp. 647-658 (2003)
6. Measures, R. M., '*Laser Remote Sensing: Fundamentals and Applications*' Krieger Publishing Co., Florida. (1992)
7. British Standards Insititute, 'Safety of Laser Products Part 1: Equipment Classification, Requirements and User's Guide', BS EN 60825-1:1994 (1994)
8. Clark, P. et al., 'Rayleigh guide star AO demonstrator for the 4.2m William Herschel Telescope', Proc. SPIE, Volume 4839, pp. 516-523 (2003).
9. Fotiadi, Andrei A.; Megret, Patrice; Blondel, Michel, '*Stimulated Brillouin scattering in optical fibers and fiber lasers: 1-D dynamics*', Proc. SPIE, Volume 4829, pp. 971-972 (2003).
10. Knight J.C., Broeng J., Birks T.A., and Russel P.S.J., '*Photonic band-gap guidance in optical fibers*', Science 282, 1476 (1998).
11. Bonaccini, D. et al. '*ESO VLT laser guide star facility*', Proc. SPIE Vol. 4494, p. 276-289 (2002)
12. Bonaccini, D. et al. '*VLT laser guide star facility*', Proc. SPIE, Volume 4839, pp. 381-392 (2003)
13. Bonaccini, D.; Hackenberg, W.; Taylor, L. '*Pushing Technologies: ESO Fibre Laser Development for Laser Guide-Star Adaptive Optics*', The Messenger, No.114, p. 15-19 (2003)
14. Jolley, P, '*WHT Top-end Sag*', Private communication, Isaac Newton Group (2001)
15. Vaughan, G. and Wareing, D.P., '*Stratospheric aerosol measurements by dual polarisation LIDAR*', Atmos. Chem. Phys. Discuss. 4, p.6107-6126 (2004)

Chapter 5: LGS WFS Model

5.1 Introduction

The LGS WFS model, which is described below, was developed in order to examine the performance of the WFS with an LGS, and to optimise the system optical design parameters.

The LGS WFS model comprised three modules that collectively described the dependence of the WFS performance on many LGS parameters. The first component used an analytical model of the propagation of the laser through the atmosphere to examine the performance of the Beam Launch Telescope (BLT). This module then calculated the beam diameter at any point along the focused LGS plume. The second module calculated the Rayleigh photon return observed by the WHT from a given slice of the Rayleigh plume. The final module used geometric optics to produce a WFS image, and then added random photon noise and read noise. By combining these three modules, an accurate determination of the WFS centroiding performance was produced whilst exploring the parameter space of the BLT, LGS and WFS.

Each module will be described in turn, followed by a section detailing the results of the modelling, and the conclusions drawn.

5.2 BLT Modelling

The analyses of AO system performance presented in Chapters 1 and 2 used purely statistical means to determine AO performance. While statistical methods have been used to analyse AO system performance since the first AO systems, several problems are better described using analytic, rather than statistical, models. One such example

is the modelling of the BLT/LGS/WFS interaction, which is described primarily using a geometric model of the LGS plume and optics. The advantages of using a geometric model are that the WFS image can be created with a reduced computational load and then analysed using exactly the same algorithms as those used within the control system. The technique presented below uses a semi-analytic model that combines a statistical representation of the effect of the atmosphere on the laser beam propagation with a geometric model of the LGS and WFS interaction.

The BLT propagation model used an approach similar to that taken in Parenti and Sasiela [1] to determine the short exposure Strehl ratio and from that, the spot diameter. For a Gaussian beam being focused by a diffraction-limited lens, the diameter of the focussed beam waist, ω_0, in metres, is

$$\omega_0 = K \times \lambda \times f/\# \qquad \text{- 5.1}$$

where K is a constant dependant on where the truncation point of the Gaussian beam and the intensity point at which the beam waist is to be measured [2]. To determine the focused beam waist at the $1/e^2$ intensity point, the factor K is given by

$$K = 1.6449 + \frac{0.6460}{(T - 0.2816)^{1.821}} - \frac{0.5320}{(T - 0.2816)^{1.891}} \qquad \text{- 5.2}$$

where T is the so-called truncation ratio of the input Gaussian beam. Eq. 5.2 is not valid for determining the focused beam waist at other intensity points e.g. FWHM. The truncation ratio is defined as

$$T = \frac{D_b}{D_{BLT}} \qquad \text{- 5.3}$$

where D_b is the $1/e^2$ diameter of the input Gaussian beam and D_{BLT} is the clear aperture diameter of the lens. For the purposes of this analysis, the Gaussian beam diameter is always measured at the BLT primary aperture.

Global tilts account for the majority of phase variance within any series of wavefronts perturbed by the atmosphere. The tilt component of the wavefront also varies slowly in comparison with higher-order modes. By calculating the variance of a wavefront with the tilt components removed, the instantaneous wavefront variance of the higher spatial order Zernike modes can be determined. This residual variance determines the instantaneous shape of the focused LGS spot, irrespective of its actual position on the sky. Assuming that the tilt component of the LGS will be removed by a closed-loop fast-steering system, this residual variance therefore describes the minimum spot size of the LGS as would be observed by the WFS. For a beam launch telescope with a launch aperture of diameter D_{BLT}, and an atmospheric coherence length of r_0, the tilt-removed turbulent wavefront variance for Kolmogorov turbulence is given by [2]

$$\sigma_{Tilt}^2 = 0.134\left(\frac{D_{BLT}}{r_0}\right)^{5/3} \qquad \text{- 5.4}$$

The total wavefront variance of the focusing LGS beam will also include a component due to the quality of the launch optics. Assuming that the optics are designed to give diffraction-limited performance, the Maréchal approximation gives a wavefront variance due to the launch optics of 0.223rad^2, corresponding to a Strehl ratio of 0.8 at the laser wavelength. The total wavefront variance is

$$\sigma_{Total}^2 = \sigma_{Tilt}^2 + \sigma_{Optics}^2 \qquad \text{- 5.5}$$

The short exposure coherence length, ρ_0, is defined by Yura [4] as

$$\rho_0 = r_0\left[1 + 0.37\left(\frac{r_0}{D_{BLT}}\right)^{1/3}\right] \qquad \text{- 5.6}$$

The approach of Parenti and Sasiela allows a short-exposure Strehl ratio, $Strehl_{SE}$, to be calculated using the quantities determined in equations 5.1 -5.6.

$$Strehl_{SE} = \exp\left(-\sigma^2_{Total}\right) + \left[\left(1 - \exp\left(-\sigma^2_{Tilt}\right)\right) \Big/ \left(1 + \left(\frac{D_{BLT}}{\rho_0}\right)^2\right)\right] \qquad \text{- 5.7}$$

The short-exposure Strehl defines a scale factor, F, which relates to the spot size.

$$F = 1 \Big/ \sqrt{Strehl_{SE}} \qquad \text{- 5.8}$$

such that the LGS spot radius, D_{LGS}, in radians, is given by

$$D_{LGS} = \left(\omega_0 F / H_{LGS}\right), \qquad \text{- 5.9}$$

where H_{LGS} is the distance from the launch telescope to the LGS focus.

The BLT model must include the performance of a real-world laser by incorporating a measure of the laser beam quality. A perfect Gaussian intensity beam has a Transverse Electronic Mode (TEM) of 00, commonly notated as TEM_{00}. TEM modal structure in a laser beam is caused by multiple paths within the laser cavity stimulating emission. The multiple paths mutually interfere with one another, resulting in an output laser beam that exhibits structure. A selection of TEM profiles were shown in Figure 4.7 [2].

A laser suitable for creating a tightly focused LGS in the sky obviously requires a TEM_{00} structure. However, even a TEM_{00} laser will not exhibit the beam divergence and minimum beam waist equal to that of a perfectly Gaussian beam. As previously defined, the laser beam quality, or M^2 value, describes how closely a laser resembles a

perfect Gaussian beam. M^2 is the ratio of the product of the beam divergence, θ, and minimum beam waist, ω_0, for both beams and is given by

$$M^2 = \frac{\omega_{0R}\theta_R}{\omega_0\theta}, \qquad \text{- 5.10}$$

where the suffix R denotes the property of the real laser beam.

A laser that has a focussed beam waist and divergence product equal to that of an ideal Gaussian intensity beam has an M^2 of 1. Values between 1.2 and 1.5 are typical for high-power TEM_{00} lasers, whereas high-power multimode lasers can have M^2 > 30. In the specific case of LGS AO, the laser M^2 value effectively describes the minimum diameter of the focused LGS spot in the absence of atmosphere [2]. A mixed-mode beam that has a waist M (not M^2) times larger than the embedded Gaussian will propagate with a divergence M times greater than the beam diameter of the embedded Gaussian. Consequently, the beam diameter of the mixed-mode beam will always be M times the beam diameter of the embedded Gaussian, which was determined in equation 5.9. The effect of beam quality on the LGS spot radius is therefore given by

$$D_{LGS} = (\omega_0 FM / H_{LGS}) \qquad \text{- 5.11}$$

With the optical performance of the BLT modelled, a model of the system can be made that determines the angular diameters of the plume at all points along the axis of propagation. The diameter of the Rayleigh plume, D_i, at an altitude H_i above the launch aperture of the telescope can be determined geometrically if the focal altitude of the LGS and launch aperture diameter are known using Eq 5.12.

$$D_i = D_{BLT}\left|1-\left(H_i/H_{LGS}\right)\right| \qquad \text{- 5.12}$$

However, once the beam approaches the focal altitude of the LGS, the beam waist diameter will not approach 0, as predicted by Eq 5.12, but ω_{0F}, as shown in Figure 5.1.

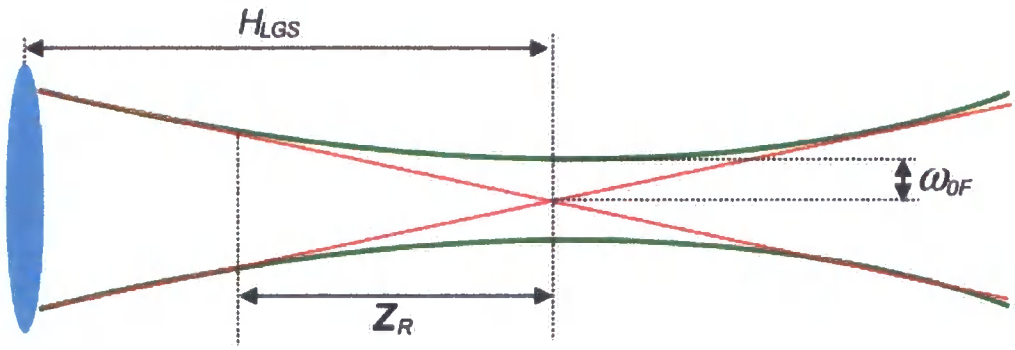

Figure 5.1 Cross section of Rayleigh plume showing the deviation from the geometrical model (shown in red) of a focused real laser beam (shown in green) The Rayleigh range, z_R, and minimum beam diameter, ω_{0F} are indicated

The Rayleigh range of a real focused laser beam, z_R, is defined as the distance between the plane of the focused beam waist and the plane at which the diameter has increased to $1/e^2$ the minimum beam width. For a real beam, this Rayleigh range is given by

$$z_R = \frac{\pi \omega_{0F}^2}{\lambda} \qquad \text{- 5.13}$$

The diameter of the beam at a distance, z, from the focus of the plume in a vacuum is given by

$$D_{vac}(z) = 2\omega_0 \left[1 + \left({}^{\lambda z M^2}\!/_{\pi \omega_0^2} \right)^2 \right]^{1/2} \qquad \text{- 5.14}$$

The above equation does not include the effects of atmospheric turbulence on the propagation of the beam. The Rayleigh range of a beam propagating through atmospheric turbulence does not change, so the term inside the square root remains constant irrespective of the effect of the atmosphere. At $z = 0$ i.e. the focused beam waist, the beam diameter from equations 5.1 and 5.14 increases to $\omega_0 FM$ giving,

$$D_{atm}(z) = \frac{K\lambda FHM}{D_{BLT}}\left[1+\left(\lambda z M^2 / \pi\omega_0^2\right)^2\right]^{1/2} \qquad - 5.15$$

ω_0 is derived by equating the $1/e^2$ beam radius at the launch aperture to the launch aperture of the BLT i.e. when $z = H_{LGS}$, $D_{atm}(H_{LGS}) = TD_{BLT}$

$$K\lambda FHM\left[1+\left(H_{LGS}\lambda M^2 / \pi\omega_0^2\right)^2\right]^{1/2} = TD_{BLT} \qquad - 5.16$$

$$\left(\frac{1}{\omega_0^2}\right)^2 = \left[\left(\frac{TD_{BLT}^2}{K\lambda FHM}\right)^2 - 1\right]\left(\frac{\pi}{\lambda HM^2}\right)^2 \qquad - 5.17$$

Equation 5.17 also predicts when a beam will not form a focused Rayleigh plume in the atmosphere. ω_0 becomes complex, and therefore unphysical, when

$$\left(\frac{TD_{BLT}^2}{K\lambda FHM}\right)^2 < 1 \qquad - 5.18$$

5.3 Photon Return

The photon flux observed by the WFS is a product of the system throughput and the photon return flux generated by the Rayleigh beacon. The throughput of the system (at the LGS wavelength) can be optimised by minimising the number of surfaces that

are present in the system, and choosing suitably high-reflectance and transmittance coatings.

The precise return photon flux of a Rayleigh LGS is dependent on the exact composition of the atmosphere, and is therefore difficult to determine. The dominant source of elastically backscattered photons within the atmosphere is through collisions with molecular nitrogen and oxygen. The number of backscattered photons is dependent on the scattering cross section and number density of scattering particles within the volume of the LGS. These molecular scattering properties can be calculated either using meteorological data or estimated using an atmospheric model.

Although the nitrogen and oxygen molecules are the numerically dominant species in the atmosphere, other more complex species can have a far larger scattering cross section, and therefore the distribution and number density of more complex molecules must be included to get an accurate representation of the full Rayleigh backscatter. The inclusion of more complex molecules, commonly called aerosols, requires knowledge of their vertical distribution. The inclusion of aerosol backscatter in the return photon flux is particularly difficult in La Palma where the close proximity of the Sahara desert can fill the atmosphere with fine sand. During a so-called '*calima*' event, the return from a Rayleigh LGS will be affected. The effect of aerosol backscattering is relatively small compared to the number of photons received through Rayleigh backscatter alone. For this reason, the effect of aerosols was not included in the number of photons backscattered.

The photon return flux (due to a single elastic scattering process within the atmosphere) for a single laser pulse can be calculated using the LIDAR equation [5,6,7].

$$N_\gamma = \frac{Q\sigma T_{sys} QE_{CCD} \lambda \rho(H_{LGS}) D_{slice} A}{4\pi hc H_{LGS}^2 f_L}, \qquad \text{- 5.19}$$

where N_γ is the number of detected photons for a single pulse,

Q is the output laser power in watts,

σ is the molecular scattering cross-sectional area in m^2,

T_{sys} is the end-to-end system optical throughput,

QE_{CCD} is the Quantum Efficiency (QE) of the WFS CCD at the LGS wavelength,

ρ_H is the atmospheric scattering particle density at a height H_{LGS},

D_{slice} is the scattering depth in the atmosphere,

A is the diameter of the collecting area of the WFS subaperture being studied,

f_L is the laser repetition rate

T_{sys} is the combined optical system throughput given by Eq 5.20.

$$T_{sys} = T_{telescope} T_{optics} T_{launch} T_{atmos}^2 \qquad \text{- 5.20}$$

$T_{telescope}$ is the transmission of the WHT telescope to the Nasmyth focal point, which has been measured [8] as 0.8 for a newly cleaned and coated mirror.

The number of elements in the GLAO design presented in Chapter 6 could not be minimised within the budget available in order to optimise T_{optics}. The calculated throughput to the LGS WFS was 22%, which is very low, but the versatility of a Rayleigh LGS is that the distance to the LGS can be reduced to increase signal level on the WFS. This obviously increases the error between LGS and NGS wavefronts,

and therefore the degree of AO correction attainable, but for this demonstrator system, this trade-off was deemed acceptable.

The launch system had a measured throughput of 0.64 at the output aperture of the launch telescope. This figure includes the effects of truncation of the Gaussian wings of the beam so is an accurate measure of the output power to sky.

The processes governing the optical transmission of the atmosphere for low power lasers are similar to those giving rise to the backscatter that the system utilises, namely Rayleigh and Mie scattering. To precisely calculate the atmospheric transmission, once again one must know the full chemical distribution of aerosols in the atmosphere. On La Palma, knowledge of the altitude, depth and particle density of the *calima* is particularly important for calculating the optical transmission, especially if the laser beam is focused above the *calima* layer.

As the vertical distribution of aerosols above the observatory was not known, the optical transmission was estimated by using calculated values for the optical transmission per unit airmass above the telescope and scaling this value by the cumulative density of the atmosphere traversed by the laser. The atmospheric density at a given altitude is given by,

$$\rho(H) = \rho_0 \exp\left(-{}^{(H)}\!/_{S_{atm}\theta_z}\right) \qquad \text{- 5.21}$$

where ρ_0 is the particle density of the atmosphere at sea level,

H is the altitude of the LGS above sea level in metres,

S_{atm} is the characteristic scale height of the atmosphere in metres,

θz is the zenith angle at which the observation is taking place.

The cumulative density between two altitudes, H1 and H2 is therefore given by

$$\int_{H_1}^{H_2} \rho(H) \partial H = \rho_0 S_{atm} \theta_z \left[\exp\left(-H_1 / S_{atm} \theta_z \right) - \exp\left(-H_2 / S_{atm} \theta_z \right) \right] \quad \text{- 5.22}$$

For an observatory at altitude H_{obs}, the cumulative density of a single airmass, ρ_A, is given by

$$\rho_A = \rho_0 S_{atm} \theta_z \exp\left(-H_{obs} / S_{atm} \theta_z \right) \quad \text{- 5.23}$$

The atmospheric extinction for a unit airmass calculated for the Roque de los Muchachos Observatory (ORM) at 525nm is 0.11mag/airmass [9]. This value is calculated using an atmospheric scale height [10] of 7400m, and at a zenith angle of 0°. As atmospheric extinction is directly proportional to atmospheric density the optical transmission between launch and LGS focus at any altitude is given by

$$T_{atmos} = K_A \rho_0 S_{atm} \theta_z \left[\exp\left(-H_{obs} / S_{atm} \theta_z \right) - \exp\left(-\left(H_{LGS} + H_{obs} \right) / S_{atm} \theta_z \right) \right] \quad \text{-5.24}$$

where K_A is a constant (for 525nm light) equal to $100^{-0.11/5}$ (= 0.9036).

The response curve for the EEV-39 CCD is given below [11].

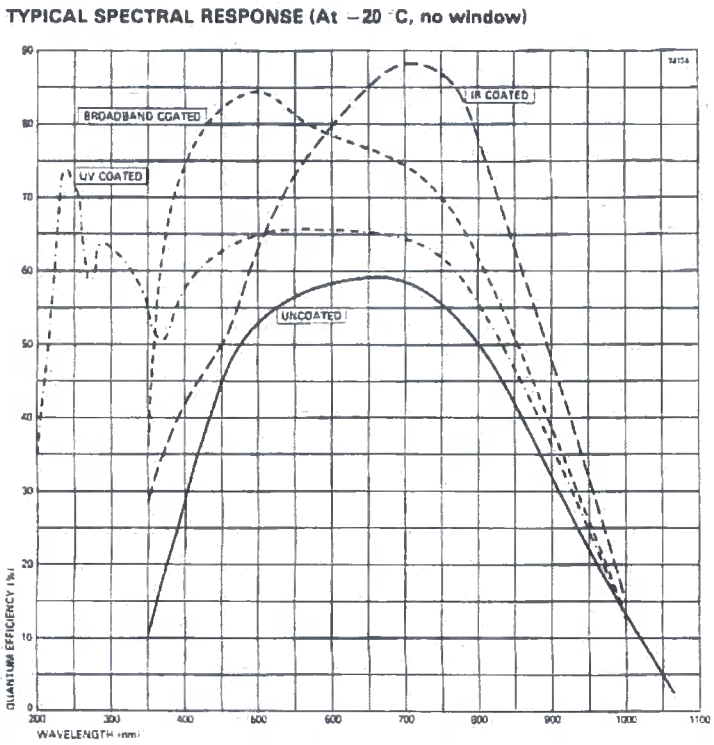

Figure 5.2 E2v back-illuminated CCD 39 spectral response curve. The CCD used was water cooled to approximately -20°C and was broadband coated giving a QE at 523nm of 0.82

The scattering cross sectional area, σ, is dependent on the relative proportions of the major scattering species in the atmosphere. σ is given by [12]

$$\sigma = \frac{A\lambda^{\left(-B+C\lambda+(D/\lambda)\right)}}{10000} m^2 \qquad - 5.25$$

where the parameters A, B, C and D are wavelength dependent and are given in the table below. It must be noted that the wavelengths are defined in μm, and σ must be scaled to square-metres, hence the factor of 10000.

	λ < 500nm	λ > 500nm
A	3.01577E-28	4.01061E-28
B	3.55212	3.99668
C	1.35579	0.00110
D	0.11563	0.02714

Table 5.1 Table showing the Rayleigh scattering coefficients for laser wavelengths less than and greater than 500nm

5.4 WFS Model

The WFS response was modelled by assuming the WFS was perfectly conjugated to the focal altitude of the LGS and that the pixel scale across the 8 pixels of the subaperture was constant. This meant that if the focal point of the Rayleigh plume was imaged by the WFS, the resulting WFS spot would form at the centre of the subaperture. The angular offset from the focal altitude to a given altitude of the Rayleigh plume was then determined and this offset was converted to a pixel offset on the WFS using a defined pixel scale. This method is illustrated in Figure 5.3.

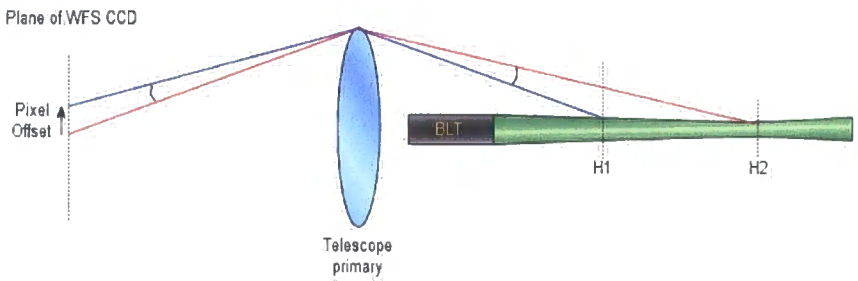

Figure 5.3 Schematic diagram showing the method used to calculate subaperture spot elongation to create a model of the WFS. The angular offset is preserved through the telescope optics, translating to a pixel offset (and defocus) on the WFS CCD.

By co-adding slices of the Rayleigh plume from a range of altitudes and generating a Gaussian intensity spot for each slice with the pixel offset calculated above, the diameter determined in section 5.2, and the intensity determined in section 5.3, an accurate model of the WFS could be made.

The effect of the contrast ratio of the WFS shutter system was also included in this model by calculating the photon return from a range of altitudes and dividing the calculated photon return from each slice by the shutter contrast ratio when the slice lay outside the pre-defined range gate depth. The shutter-open throughput is included

in the optical transmission of the WFS system. In this way, either a Pockels Cell shutter system or conical rod passive range gate could be simulated. Methods of range gating are investigated in section 6.6.

The ability for a highly-elongated WFS spot (or a spot with a large offset) to contaminate adjacent WFS subapertures was also included in the model.

Poissonian shot (photon) noise and read noise was added to the WFS image to simulate the effects of CCD read noise. The image was then clipped at a signal level equal to

$$Sig_{\min} = R(e^-)\left(1 + R(e^-)\right) \qquad \text{- 5.26}$$

where $R(e^-)$ is the rms CCD read noise in electrons.

5.5 LGS Spot Motion

Angle of arrival statistics for the atmosphere determine the magnitude of spot offsets that should be observed for a given atmospheric turbulence profile and telescope diameter. This should allow us to link the input spot offsets to an atmospheric r_0. However, angle of arrival statistics do not take into account the LGS spot jitter, (due to vibrations within the laser launch system and the different paths that the laser light takes on the uplink and return paths) and non-common path errors that will be present between the science camera and WFS.

The (Kolmogorov) turbulence-induced angular tilt variance of an incoming wavefront is given by [2]

$$\sigma_{tilt}^2 = S\left(\frac{D_{atm}(z)}{r_0}\right)^{5/3}\left(\frac{\lambda}{D_{atm}(z)}\right)^2 \qquad \text{- 5.27}$$

where S depends on the aperture geometry. For a circular aperture, S is 0.164, for a square aperture, S is 0.184. Both the BLT and WHT have circular launch apertures. When examining the effect of a turbulent atmospheric profile where the turbulence is contained within discrete layers, the vertical distribution of the layers also affects the observed LGS offset. Lower layers have more of an effect on the LGS spot offset than higher layers. To include this effect, the distance between layers must be included in Eq. 5.27 to give

$$\sigma_{offs}^2 = 0.164\left(\frac{D_{atm}(z)}{r_0}\right)^{5/3}\left(\frac{\lambda}{D_{atm}(z)}\right)^2 z^2 \qquad \text{- 5.28}$$

where z is the distance between a layer and the next. For the highest turbulent layer, this is the remaining distance to the LGS.

Fried's parameter is dependent on the vertical distribution of turbulence. An LGS propagated to some altitude above the launch telescope samples a cone of the atmosphere equal to the volume occupied by the Rayleigh plume profile determined in Eq. 5.15. The tilt variance present in the beam on both uplink and downlink can be modelled by calculating the strength of turbulence and the diameter of the Rayleigh plume at each turbulent layer.

The value of r_0 for a given turbulent layer in the atmosphere, r_{0i}, is given by,

$$r_{0,i} = r_0\, s_i^{-3/5} \qquad \text{- 5.29}$$

where s_i is the relative strength of the turbulence at layer i.

The actual LGS offset induced in the wavefront at each layer, σ_i^2, on the uplink is given by,

$$\sigma_{uplink}^2 = \sum_{i=0}^{\infty} \sigma_i^2 \qquad \text{- 5.30}$$

where σ_i^2 is given by Eq. 5.28, with a layer altitude of z_i.

The return beam diameter along the path from the LGS focus to the observing telescope of diameter D_{tel} can be calculated using the geometrical relationship

$$D_{down,i} = D_{tel}\left[1-\left(z_i/H_{LGS}\right)\right] \qquad \text{- 5.31}$$

When $D_{atm} << D_{down}$, the tilt variance between uplink and downlink is essentially uncorrelated [13] allowing the tilt variance on uplink and return path to be added. The total turbulence-induced tilt covariance is given by,

$$\sigma_\alpha^2 = \sigma_{uplink}^2 + \sigma_{return}^2 \qquad \text{- 5.32}$$

The covariance between σ_{uplink}^2 and σ_{return}^2 must be considered as $D_{atm} \rightarrow D_{down}$. However, the inclusion of the uplink and downlink tilt covariance only has the effect of reducing the overall tilt-variance, so equation 5.32 gives a 'worst-case' value.

One further error source that must be included in the overall tilt signal is the effect of launch jitter. The magnitude and effect of telescope vibrations and wind-shake on the apparent position of the beam can be derived, but require precise measurements of all telescope and beam relay system vibrations at all telescope elevation angles, under all wind conditions and all telescope loadings. Due to this, approximations must be made to get a rough order of magnitude estimate for the launch jitter. If the magnitude of vibrations between the point where the laser is mounted (in the case of the Durham GLAO system, at the Nasmyth focus of the WHT) and the point where the BLT is mounted (behind the WHT secondary), a worst case value can be derived by converting all the observed vibrational motion into a pointing term that is dependent on the distance between the launch aperture and centre of rotation. This variance of this term could then be calculated from this angular displacement and the vibrational

data and expressed as wavefront variance. This term can then be included in Eq. 5.32 giving,

$$\sigma_{\alpha}^{2} = \sigma_{uplink}^{2} + \sigma_{return}^{2} + \sigma_{jitter}^{2} \qquad \text{- 5.33}$$

Using the above equations, the standard deviation of tilt across the LGS WFS can be determined for a given atmospheric turbulence profile. Although this only gives the 1σ angular displacement across the pupil, for one to be confident that the WFS will perform under a given atmospheric profile, it must be expected to return an accurate centroid for a 3σ displacement; therefore the determined rms value must be multiplied by a factor of 3 to give the magnitude of spot motion that will be observed. For example, if the tilt variance across the pupil gives rise to a standard deviation of ±0.3arcseconds, the WFS must be able to return an accurate centroid for angular displacements of ±0.9arcseconds. This will allow a fast steering mirror to lock onto the WFS spot pattern and remove the majority of the tip and tilt that are present in the LGS wavefront. As tip and tilt account for the majority of wavefront variance across an aperture [2], closing the LGS TT (Tip/Tilt) loop removes much of the spot motion observed on the WFS. The magnitude of the global spot motion that will be observed by the LGS WFS is therefore given by,

$$\alpha_{LGS} = \pm 3\sqrt{\sigma_{\alpha}^{2}} \qquad \text{- 5.34}$$

The magnitude of angular correction that that the LGS FSM must provide is then half this value and is given by [14],

$$\alpha_{FSM} = \pm \frac{D_{tel}}{2D_{FSM}} \alpha_{LGS} \qquad \text{- 5.35}$$

5.6 Results

The methods described in sections 5.2-5.5 were used to optimise the performance of launch and return systems. It should be noted that many of the optical components present in the system were purchased for a laboratory AO system, and were not fully optimised for use with an on-sky GLAO system, as would be the case for a facility instrument. The standard La Palma atmosphere [15] was used as the model for all calculations.

The standard atmosphere defines layers at 0km, 2.5km and 7.5km. Initial photon return calculations showed the 5W laser could not create an effective LGS at altitudes above ~6km, so the highest layer could not affect the performance of the LGS in any way. The ground and middle layers have a cumulative strength of 0.8 of the total atmospheric r_0 value. From equation 5.29, this means that the r_0 experienced by the LGS on uplink and downlink was increased by the factor $0.8^{-3/5}$, and the relative strengths of each layer were made equal at 0.5.

	Parameter	Value	Unit	Description
Atmosphere	S_{atm}	7400	m	Characteristic scale height of atmosphere
	r_0	0.14	m	Atmospheric Fried parameter
	H_i	0, 2.5, 7.5	km	Turbulent layer altitudes
	s_i	0.4, 0.4, 0.2		Turbulent layer relative strengths
	V_{atm}	0.11	mag	Atmospheric extinction ratio
Telescope	D_{tel}	4.2	m	Telescope diameter
	D_{2ndary}	1.2	m	Telescope obscuration diameter
	T_{tel}	0.67		Transmission of telescope optics
	H_{obs}	2269	m	Altitude of observatory
WFS	N_{subap}	8		Number of WFS subapertures
	F_{subap}	2.11	arcsec	Field of view of individual subaperture
	P_{subap}	8	pixels	Pixels per subaperture
	FR_{WFS}	300	Hz	WFS frame rate
	QE_{CCD}	0.84		WFS CCD quantum efficiency
	$R(e^-)$	6	electrons	WFS CCD read noise
	Contrast	1000		Contrast ratio of shutter system
LGS	H_{LGS}	4500	m	Distance to focus of LGS
	H_{RGD}	50	m	Range Gate Depth
	θ_z	0	°	Zenith angle
Laser	λ	523	nm	Laser wavelength
	Q	4.5	W	Output laser power
	f_L	7000	Hz	Laser pulse rate
	Tl_{aunch}	0.64		Launch system transmission
	S_{launch}	0.8		Strehl Ratio of launch system
	D_{BLT}	0.3	m	Diameter of launch telescope
	T_{launch}	0.83		Gaussian beam truncation ratio
	M^2	1.3		Laser M^2 value
AO System	T_{optics}	0.22		Transmission of AO system optics
	D_{FSM}	0.1	m	Diameter of LGS FSM

Table 5.2 GLAO system base parameters.

The WFS images output by the model were analysed by examining each WFS subaperture in turn and calculating the position of the centroid within a subaperture. This value was then compared with the known centroid to determine an angular offset. The angular offset of the subapertures was assumed to wholly correspond with a wavefront tip/tilt across a subaperture. The measured-actual angular tilt discrepancy could therefore be scaled to give a corresponding subaperture wavefront variance. The

rms value of all subaperture wavefront variances gives a global wavefront variance, and therefore Strehl ratio.

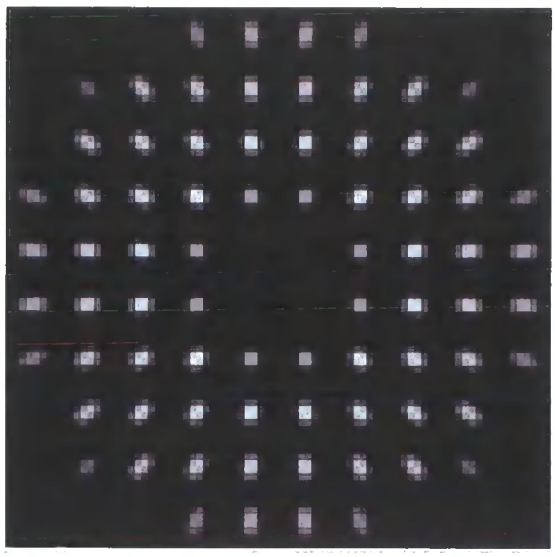

Figure 5.4 Simulated WFS images for a 10x10 subaperture Shack-Hartmann system imaging 10m, 25m and 50m sections of a Rayleigh plume focused at 4.5km with a lenslet field of view of 2.11" from a 523nm 5W laser with an M^2 value of 1.3, an end to end system throughput of 0.22, with an atmospheric r_0 of 0.19m (La Palma median seeing) corresponding to an LGS r_0 of 0.20m.

5.6.1 LGS Spot Size

The on-sky LGS spot size for different truncation ratios and atmospheric conditions was determined from equation 5.15. The launch telescope aperture was fixed at 300mm, as this component had already been procured, although alternative launch aperture diameters are examined.

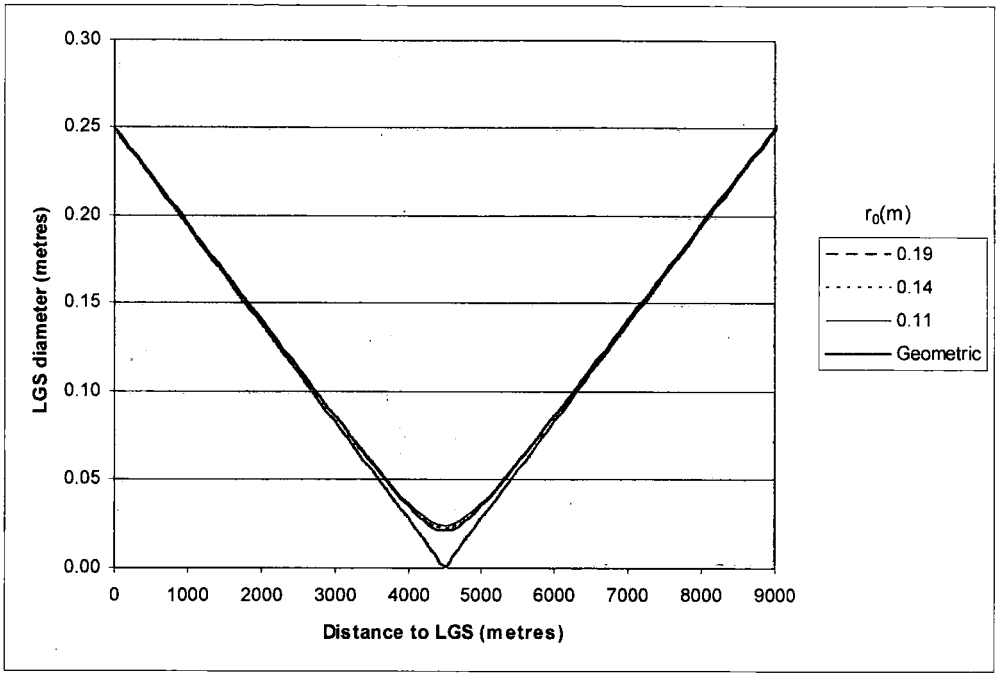

Figure 5.5 Effect of changing atmospheric r_0 on the LGS plume diameter from the BLT launch aperture to twice the LGS focal distance. Geometric plume diameter is shown as a comparison

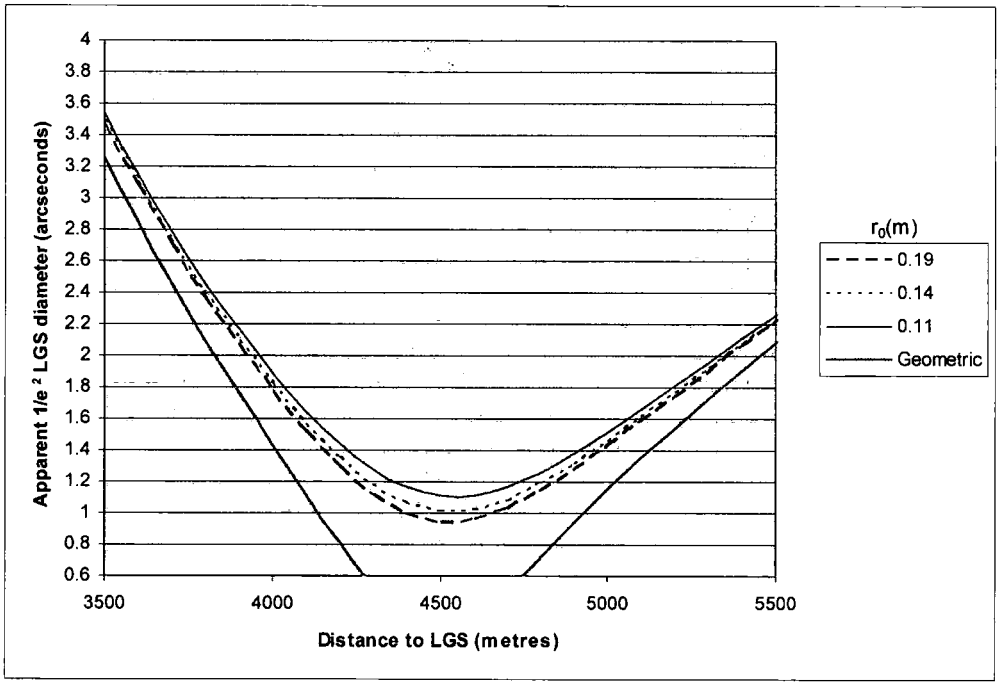

Figure 5.6 Effect of changing atmospheric r_0 on focused LGS beam waist

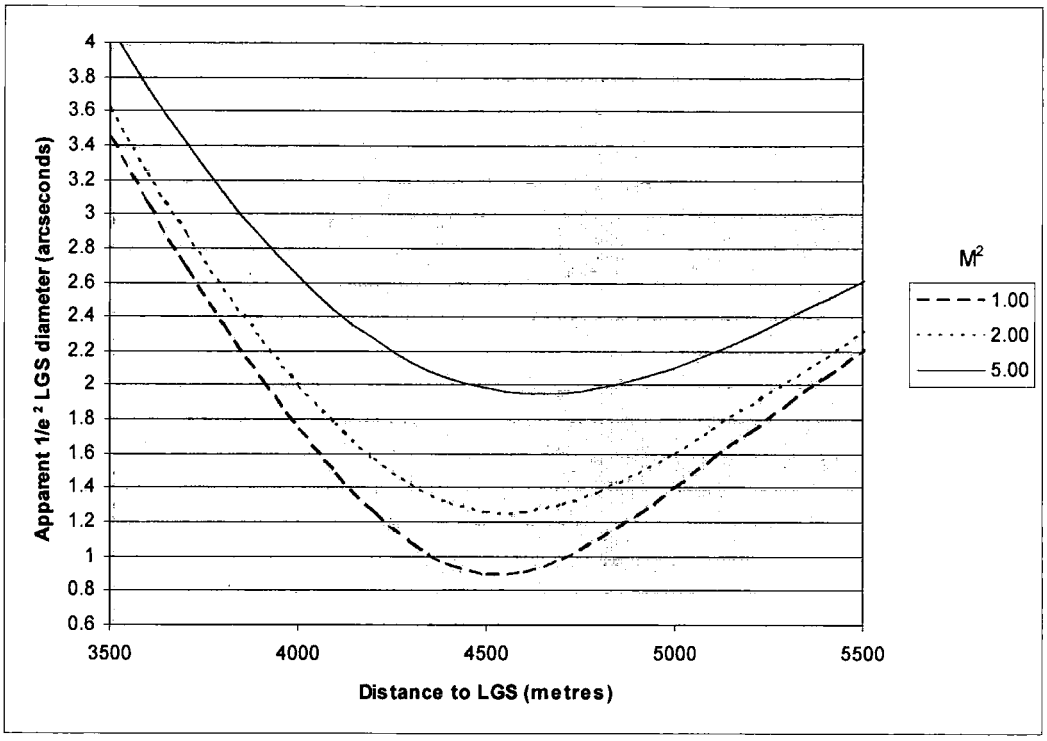

Figure 5.7 Effect of decreasing laser beam quality (i.e. increasing .M^2) on focused LGS beam waist

The importance of a high-beam quality laser is emphasised by Figure 5.7. Lasers with large M^2 values cannot create a low-altitude sub-arcsecond LGS, irrespective of the BLT launch aperture. Lower-quality lasers can however create LGSs at higher altitudes if the launch aperture diameter is increased to counter the increased beam divergence of the laser.

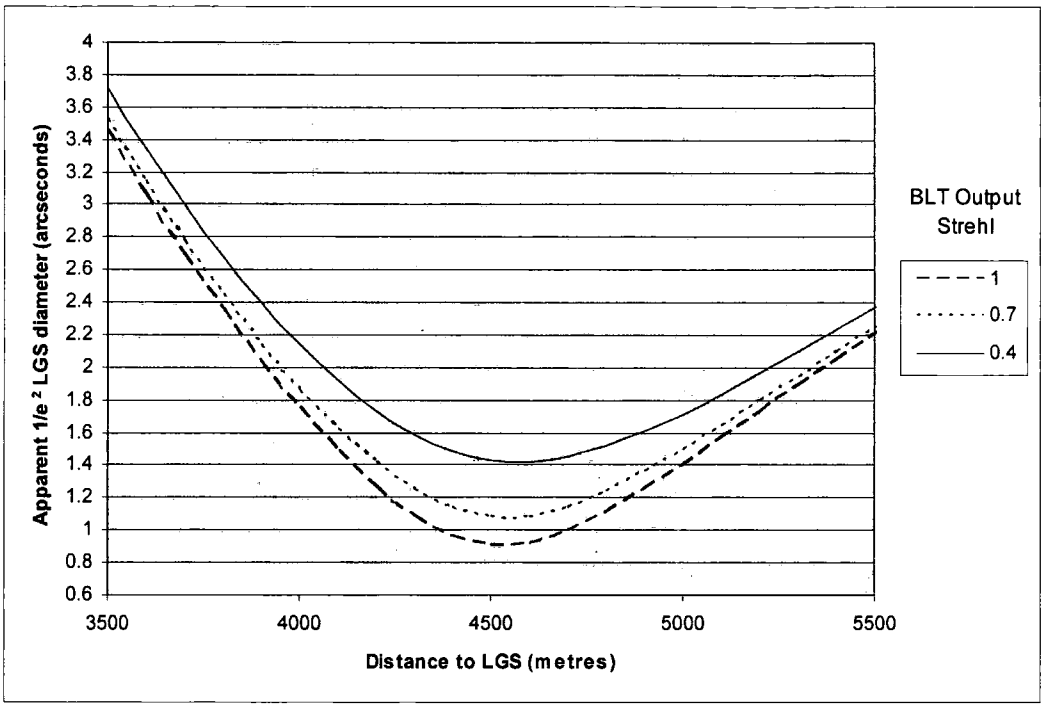

Figure 5.8 Effect of increasing transmitted wavefront quality on focused LGS beam waist

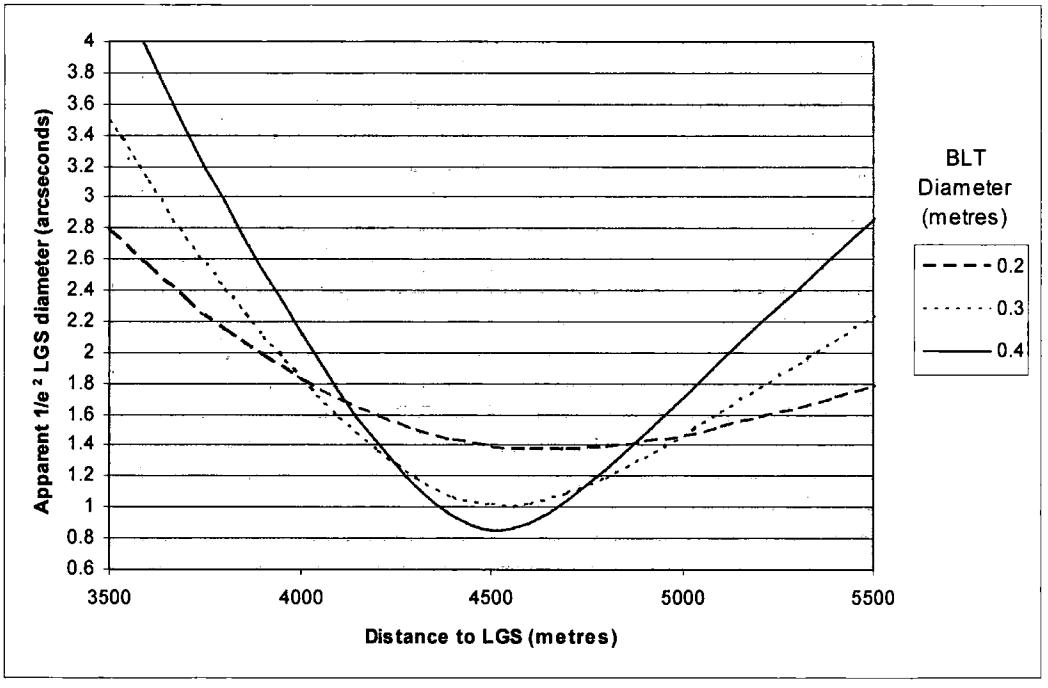

Figure 5.9 Effect of increasing launch aperture diameter on focused LGS beam waist

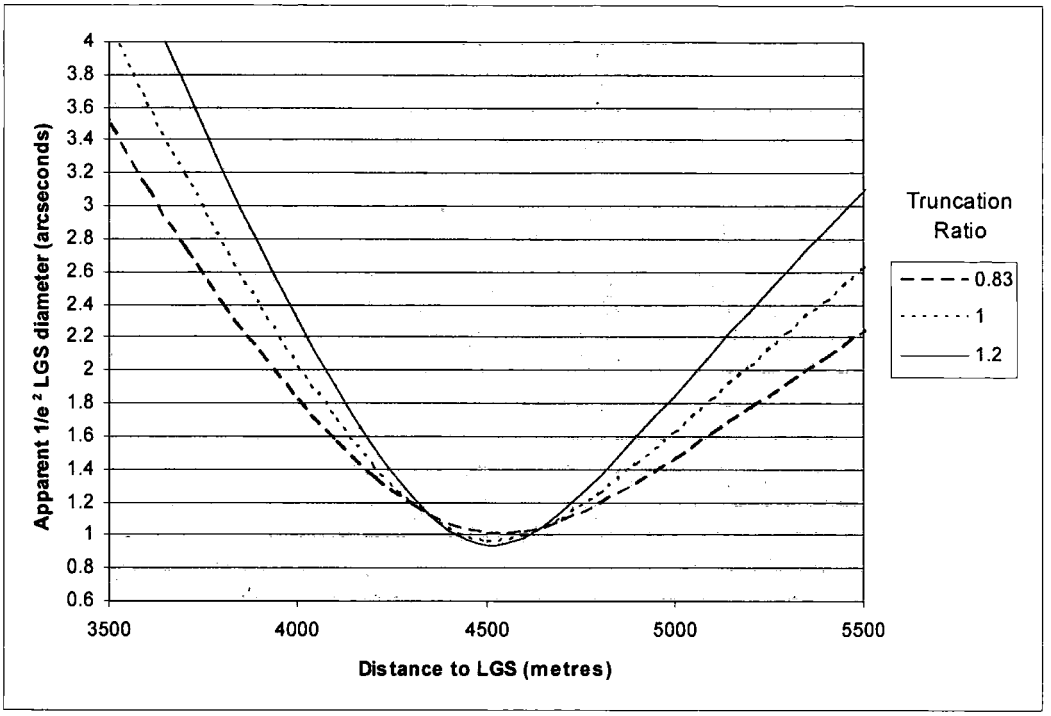

Figure 5.10 Effect of changing truncation ratio on focused LGS beam waist

As can be seen from the figures above, the 0.3m BLT primary aperture will be able to create a sub-arcsecond LGS at 4.5km under median to good seeing conditions.

One interesting feature is demonstrated in Figure 5.9. Although the BLT is focused at a distance of 4.5km, the smallest apparent diameter for the plume from the 0.2m launch aperture is placed at 4.6km. This effect is caused by perspective narrowing of the beam having a greater effect than the divergence of the Gaussian beam. This has implications for telescopes using similar launch apertures to those described here (<1m) that create a focused spot at higher altitudes. The apparent LGS focus will not be at the set focal point of the BLT, and the change must be accounted for in the BLT design.

Truncation ratio has very little effect on minimum LGS diameter, as does moving from a 0.3 to 0.4m BLT launch aperture. One interesting point to note is that as the beam geometric cone angle decreases, either by focusing at a higher altitude,

launching from a smaller BLT aperture or decreasing the truncation ratio, the maximum range gate depth can increase. Figure 5.10 demonstrates that even though the minimum LGS diameter increases, the range gate depth where the diameter stays below a threshold of 1.4" increases. This has important implications for LGS AO systems that employ dynamic refocus mechanisms. A dynamic refocus mechanism increases the range gate depth that can be used by tracking the laser pulse as it propagates along the Rayleigh beam path. To achieve this, the dynamic refocus mechanism must continuously reconjugate the LGS WFS to the instantaneous position of the laser pulse in the atmosphere.

5.6.2 LGS FSM

The LGS FSM corrects for any global tip-tilt that is observed on the LGS WFS. The degree of spot motion that would be observed was derived in section 5.4. Using equations 5.27 to 5.33, a relationship between atmospheric conditions (in this case, r_0) and maximum observed spot offset can be found.

The effect of launch jitter is not included in this analysis as no accurate data on the degree of jitter in the launch system, or in the WHT structure were available.

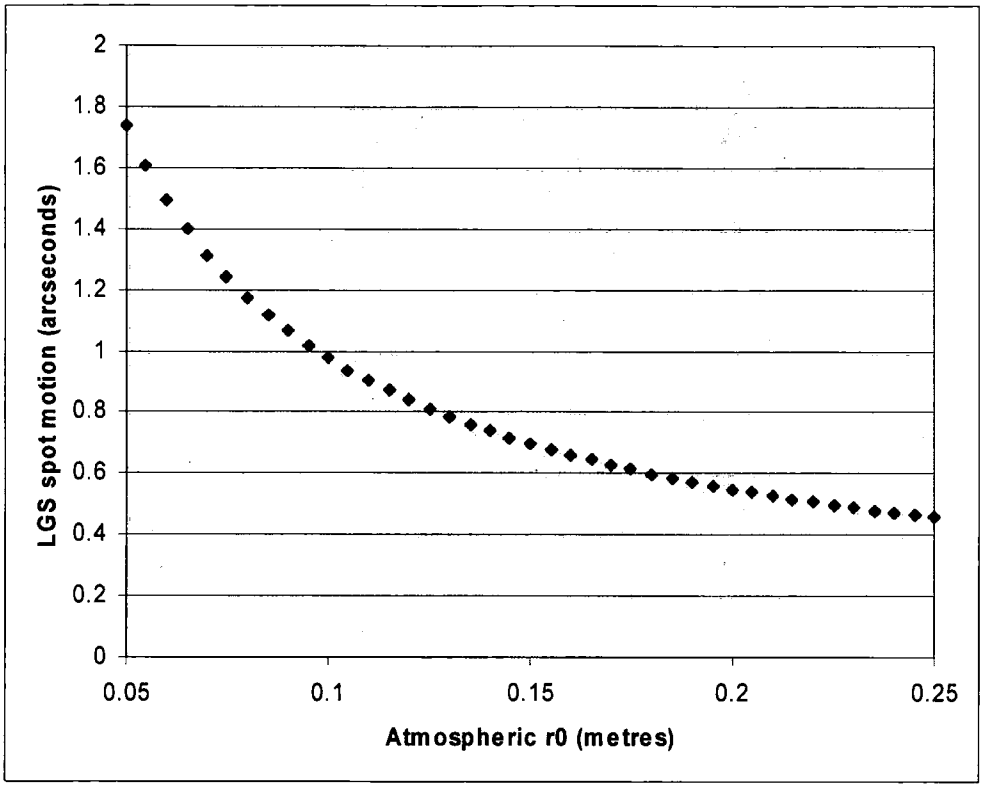

Figure 5.11 Effect of changing atmospheric r_0 on observed LGS spot motion

Under median seeing conditions of 0.14m, the observed spot motion should be 0.74 arcseconds. This means that a tip-tilt mirror with a diameter of 0.05m must have a full range of at least ±31.08" to correct for LGS motion under median seeing conditions, rising to ±37.84" for 75th percentile seeing of 0.11m. The actual degree of correction required will be greater than this value, as launch jitter must also be corrected by the FSM. An FSM correction range of ±50" should suffice for most atmospheric conditions.

After the LGS TT loop is closed and the global LGS jitter is removed, the range gate depth can be increased to take advantage of the stabilised WFS spots and provide a greater SNR. For a RLGS, this can be achieved by opening the Pockels cell shutter for a longer time period. This effect is studied in section 5.6.4.

5.6.3 Optimum LGS Parameters

A wide parameter space must be examined in order to optimise the system as the effect of range gate depth, contrast ratio, subaperture field of view, LGS spot size and LGS focal altitude are interlinked, with all affecting WFS performance in some way.

The subaperture field of view is defined by the Shack-Hartmann lenslet array focal length and lenslet pitch. The lenslet array being used was a commercially-available 188μm pitch 8mmm focal length lenslet from Adaptive Optics Associates (AOA), which gives a field of view of 2.11 arcseconds per subaperture. This is a smaller field of view than would normally be used for an LGS WFS as the subaperture must accommodate any elongation present due to the finite depth of the range gate, but an alternative lenslet could not be purchased with the budget available for the project. This set stringent limits on the performance of many aspects of the system.

To determine the optimum LGS altitude requires three pieces of information. First the minimum WFS signal level must be determined. This allows range gate depth and LGS focal distance combinations that can provide adequate return flux to the WFS to be determined. Due to the exponential decay of atmospheric pressure with altitude, to get a constant signal level on the WFS, the range gate depth must be increased at a faster rate than the LGS focal distance increases. This means at higher altitudes the angular magnitude of WFS spot elongation increases.

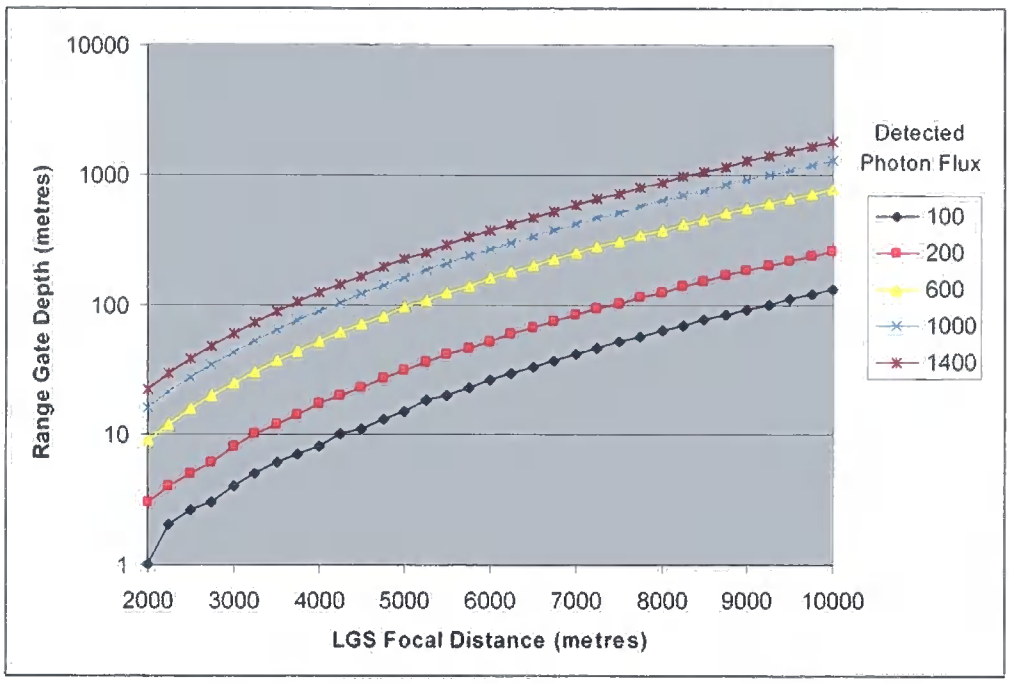

Figure 5.12 Range Gate Depth and LGS focal distance combinations that provide a given detected photon flux to a 10x10 SH-WFS on a 4.2m telescope using the parameters defined in Table 5.2. Telescope is pointing at zenith.

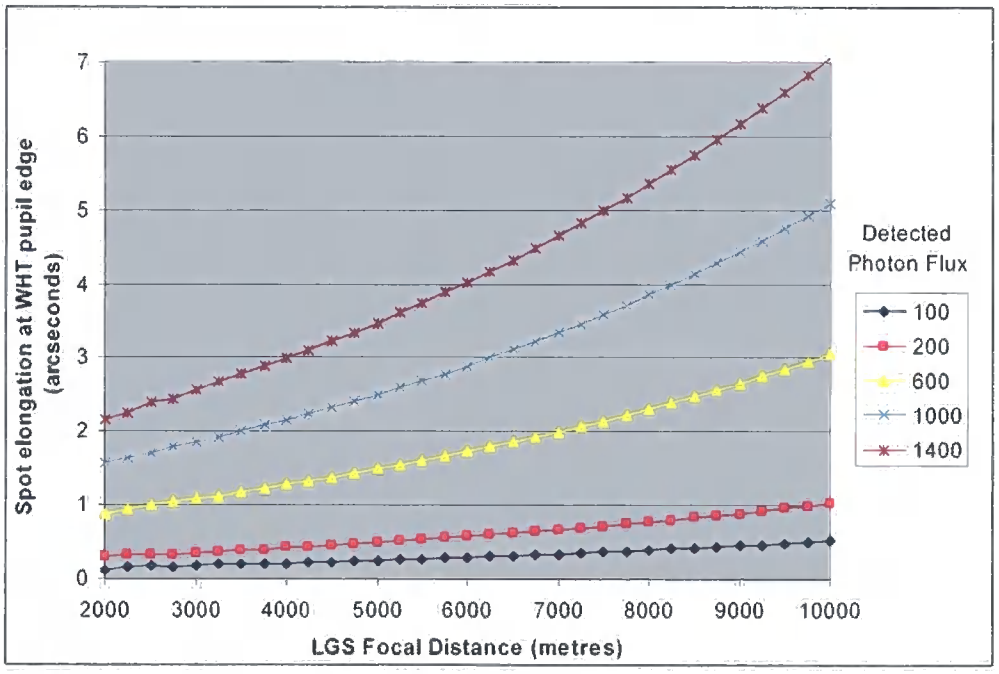

Figure 5.13 Spot elongation observed by a WFS subaperture at the WHT pupil edge for LGS focal distances from 2km to 10km. For a 10x10 SH-WFS the centre of the subaperture is positioned 1.9m from the pupil centre.

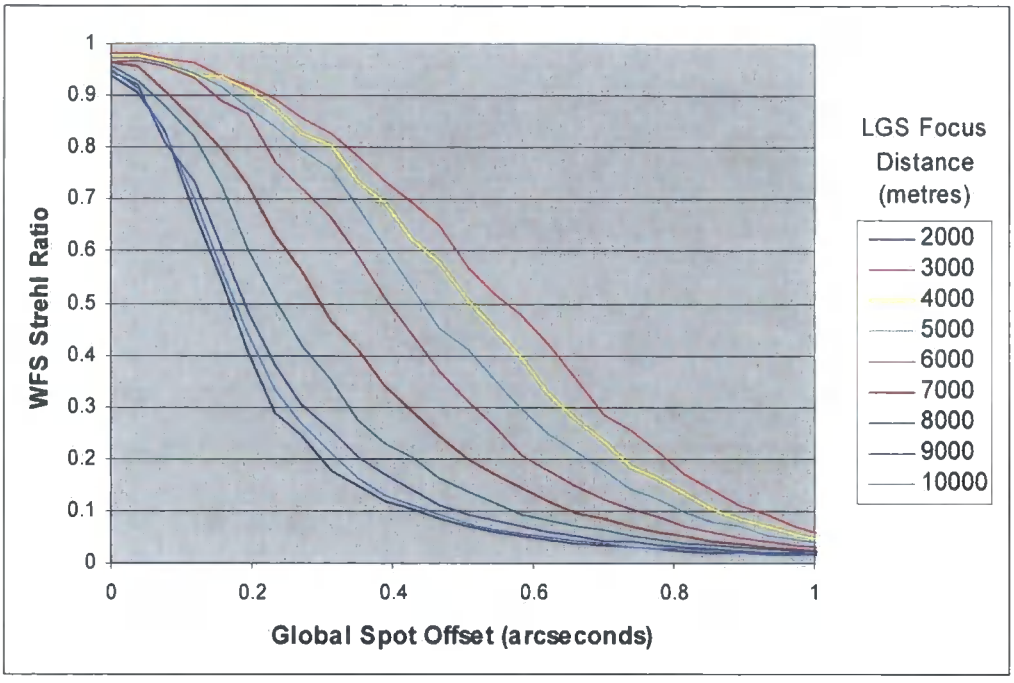

Figure 5.14 Effect of increasing spot elongation on WFS performance. Each line plots the Strehl ratio returned by a 10x10 SH-WFS when the spots are globally offset from the centre of the subaperture for an average flux of 800 photons per subaperture per WFS frame. To retain the signal level as the LGS focal distance is increased, the range gate depth must increase also, increasing apparent spot elongation. After introducing read noise into the WFS image 250 frames were averaged to create the plots shown above.

Figure 5.14 demonstrates the effect of spot elongation on WFS performance. The performance was studied by globally offsetting all the LGS spots by a small amount, i.e. introducing a tilt across the LGS wavefront, and reconstructing the measured wavefront. If the WFS can measure the tilt, there will be no difference between the measured LGS wavefront and true LGS wavefront and a zero wavefront variance between the two wavefronts will be returned. For this discussion, the term WFS Strehl ratio has been used as the metric with which to define the LGS WFS performance. The global spot offset introduced emulates the LGS launch jitter as this is observed as a global spot offset on the WFS. As is to be expected, increased spot elongation reduces the global spot offset, and hence the magnitude of launch jitter at which the

wavefront measured by the WFS will match the true LGS wavefront to a given Strehl Ratio (SR).

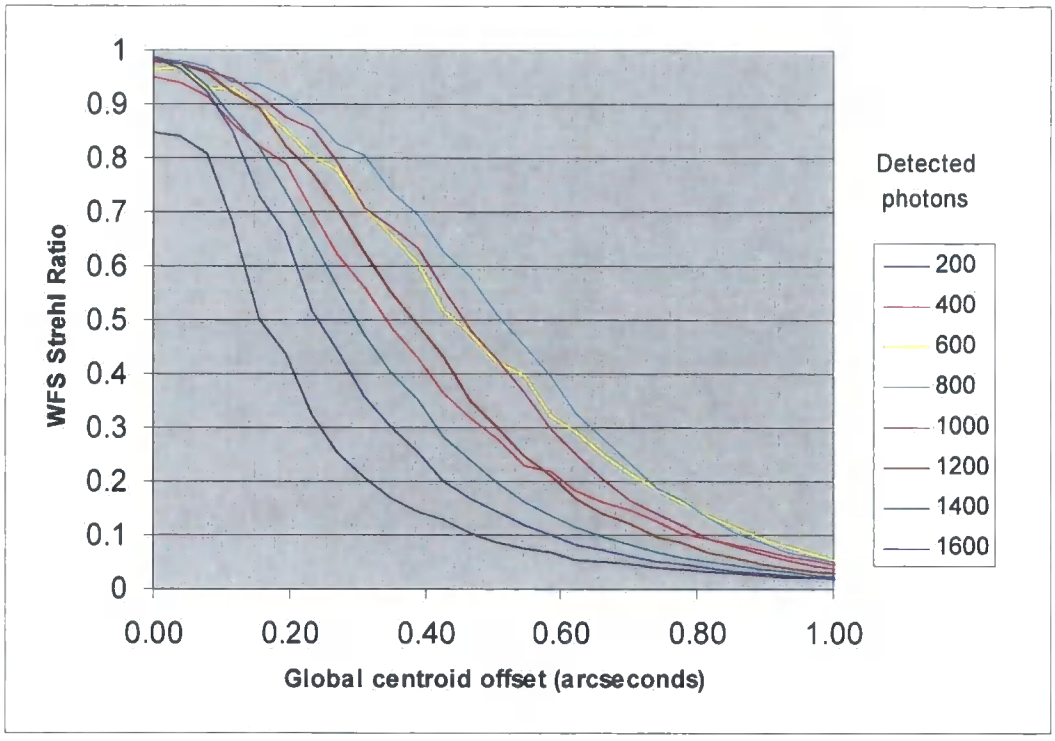

Figure 5.15 Effect of increasing detected photon flux on WFS performance for an LGS at 4km distance. This shows the effect of increasing spot elongation at a single altitude. After introducing read noise into the WFS image 250 frames were averaged to create the plots shown above.

Figure 5.15 shows the effect of increasing the photon flux (and elongation) while the LGS focal distance is a constant 4km. As can be seen, an average signal level of 200 photons cannot provide optimum performance from an LGS WFS with 6e^- read noise. Optimum performance is not seen until photon flux is increased to 600 photons. However, increasing the return flux by increasing range gate depth as is shown in Figure 5.15 also reduces the magnitude of LGS spot jitter that can be observed before wavefront variance between the measured and true LGS wavefronts increases. For each LGS altitude, there is an optimum signal level that draws the best compromise

between WFS SNR and contamination of adjacent subapertures caused by elongated spots. This is demonstrated by Figure 5.16 and Figure 5.17.

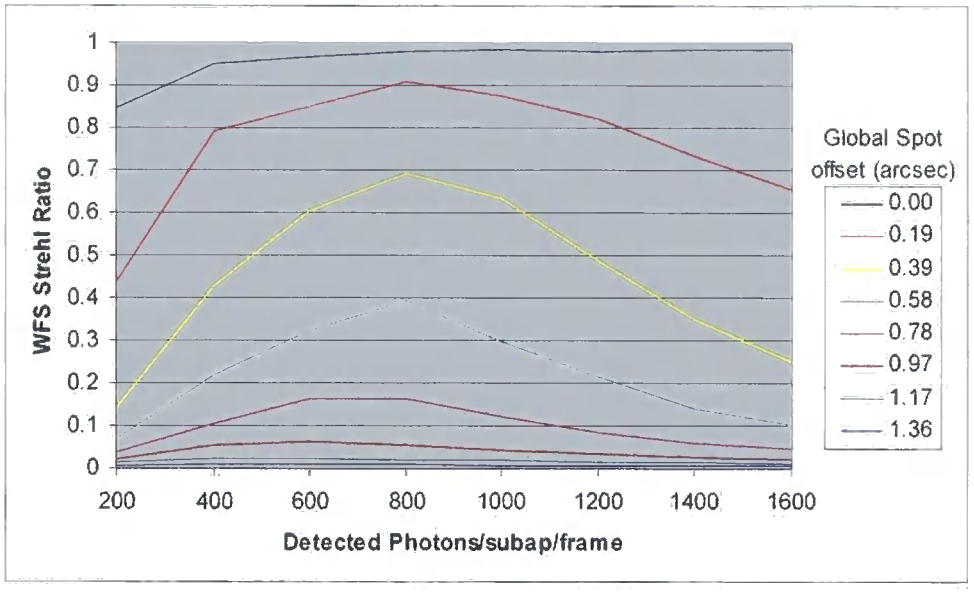

Figure 5.16 Effect of increasing range gate depth, and therefore detected photon flux and spot elongation on several different global spot offsets for an LGS at 4km distance

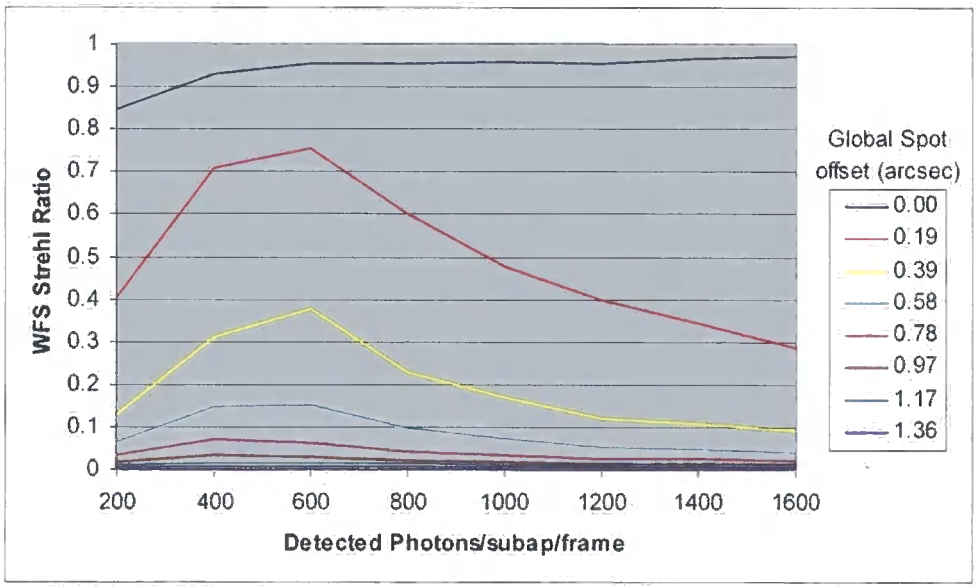

Figure 5.17 Effect of increasing range gate depth, and therefore detected photon flux and spot elongation on several different global spot offsets for an LGS at 8km distance

Figure 5.16 shows that for an LGS created 4km from the telescope pupil, an average signal of 800 photons per subaperture gives the best performance between WFS SNR and spot elongation. For an LGS created at 8km from the telescope pupil, as shown in Figure 5.17 this flux has dropped to 600 photons per subaperture. This is because a longer spot elongation is required to provide the same photon flux, therefore decreasing the WFS Strehl ratio for a given spot offset. Figure 5.17 shows that even small global spot motions will impair WFS performance. An 8km LGS with the demonstrator system is therefore not a viable option. Plotting Figure 5.16 and Figure 5.17 for all LGS altitudes between 3km and 10km shows that the optimum photon flux is between 600-800 photons over this range of LGS altitudes.

To allow the LGS tip/tilt loop to close and the gross spot motion due to launch jitter to be removed from the wavefront, the WFS Strehl ratio must be greater than zero. Numerical simulations [16] of the loop closing on offset spot patterns have shown that a WFS Strehl ratio of 0.05 will always allow the LGS tip/tilt loop to close. Combining this Strehl Ratio with the 0.74" spot jitter that was determined in section 5.6.2 allows us to determine a set of range gate depth and detected photon flux combinations that will allow the LGS FSM loop to close. These combinations are plotted in Figure 5.18 and show that there are a wide range of possible LGS focal altitudes that can be used with the GLAO WFS system.

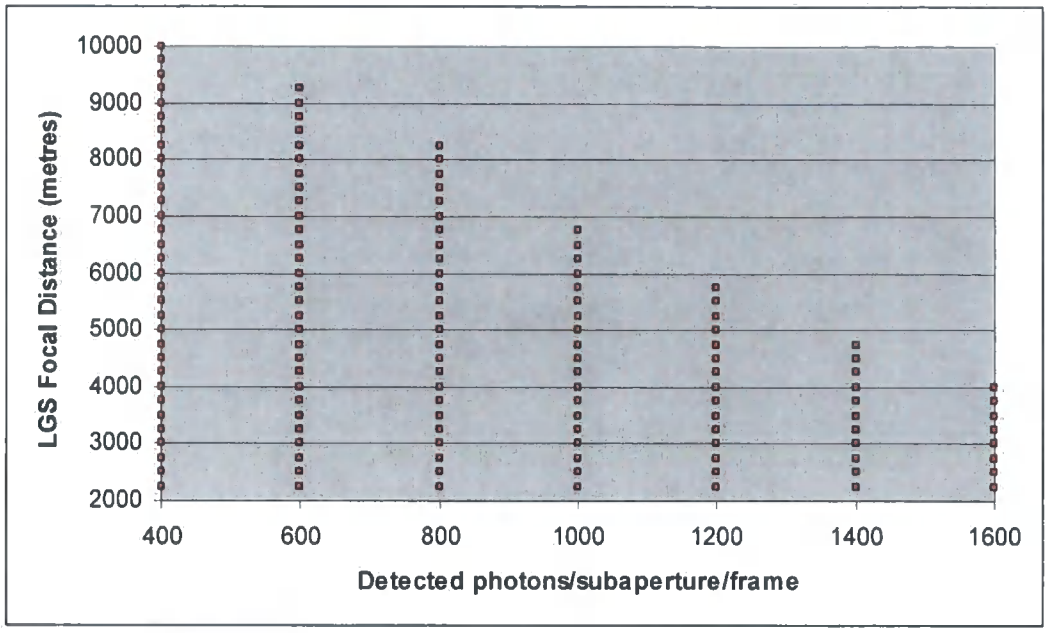

Figure 5.18 LGS Focal distance and detected photon flux combinations that provide a Strehl ratio of 0.05 or greater at a global spot offset of 0.74"

Once the LGS tip/tilt loop is closed, the residual spot motion is reduced and the WFS Strehl ratio improves. As previously stated, the optimum photon flux is between 600 and 800 photons per subaperture for LGS focal altitudes between 3km and 10km. From the analysis presented in chapter 7, the optimum LGS altitude is at 4km. This allows us to define an optimum range gate depth of 69m. The resulting optimised WFS pattern is shown in Figure 5.19.

The performance of the optimised WFS, with the effect of the 6e- read noise is shown in Figure 5.20. It can be seen that for residual spot motions below 0.25", the WFS achieves a 'diffraction-limited' Strehl of 0.8, irrespective of the effects of noise in the WFS signal. Once both the LGS tip/tilt loop and LGS high-order loop have closed, the LGS WFS spot motion will be reduced to a minimum. If the spots are stabilised to within ±0.25", the WFS will have a diffraction limited performance. In reality, the WFS Strehl should be higher than 0.8, as other error sources will also reduce the

overall system performance, but the extent of these errors cannot be determined without a full system error budget.

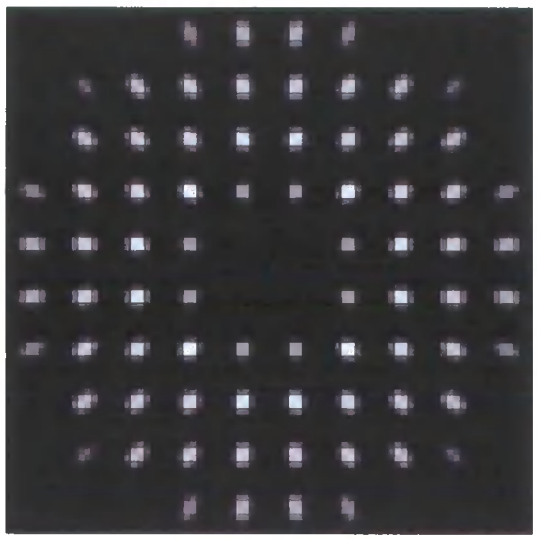

Figure 5.19 Optimum LGS WFS spot pattern for a 4km LGS with a 69m range gate.

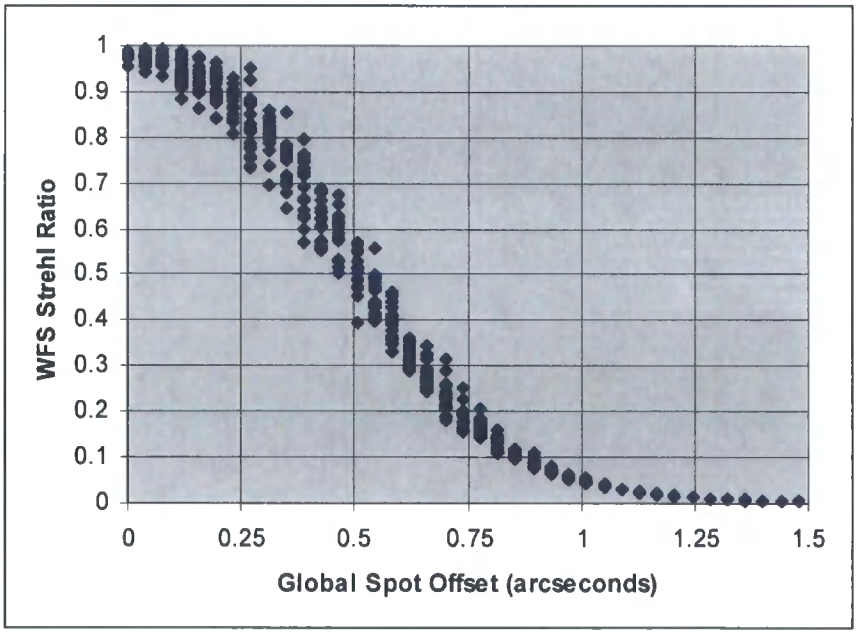

Figure 5.20 Performance of optimum LGS WFS out to a 1.5" spot offset from the centre of the subaperture. Variation is caused by the addition of read noise into the WFS pattern. Residual spot motions less than 0.25" will always provide a 'diffraction-limited' Strehl ratio of 0.8.

5.6.4 Variable Range Gate

Temporal control of the range gate depth of a Rayleigh LGS allows the photon flux to be optimised depending on the regime that the AO system is currently operating under. Three stages, and a set of associated conditions, can be defined before high-order correction of the LGS wavefront can occur.

The first stage involves correcting the apparent motion of the LGS. As was seen in Chapter 2, the apparent motion of the LGS at a finite altitude bears no (or at most, a minimal) relationship to the wavefront coming from a NGS situated at infinity. The observed LGS motion is a combination of differential tilt on the LGS uplink and return paths and launch jitter due to telescope vibrations. For the LGS fast-steering loop to close and suppress the observed LGS motion, the LGS WFS must be able to detect global tip/tilt from the WFS pattern. The field of view of the lenslet must be great enough that the elongated spots do not contaminate adjacent subapertures and degrade the WFS performance. For a given subaperture FOV, the magnitude of allowed spot elongation is dependent on the magnitude of launch jitter and the LGS angular diameter.

Once the LGS fast-steering loop is closed, the observed motion of the WFS spots is reduced and the second stage is reached. The reduced WFS spot motion allows the range gate depth to be increased to fill pixels that are no longer used. Alternatively, the altitude and range gate depth can be increased to reduce the effects of focal anisoplanatism, although this requires reconjugating the WFS to the new LGS focal distance. This increases the WFS SNR and improves performance. For a given subaperture diameter, the elongation allowed in this second stage is dependent wholly on the turbulent properties of the atmosphere.

The final stage is the spot motion that is observed once the loop has been closed. The residual spot motion at this stage is the smallest and therefore the range gate depth and LGS altitude can be increased to its maximum value. The spot elongation allowed in this final stage is dependent on the atmospheric turbulence profile and the closed-loop AO performance.

One drawback to the use of a variable range gate is that as LGS range gate depth is increased, the non-uniform illumination of the LGS plume on the WFS CCD biases the centroid away from the centre of the subaperture. This is interpreted by the WFS and control system as a wavefront focus term, and the appropriate correction will be applied to the DM. This will cause the science image to become defocused. Fortunately, this effect is purely geometrical and can easily be modelled. The geometry is assured by the accurate control of the range gate depth and LGS focal altitude. Sodium LGSs cannot rely on the geometry of the LGS remaining fixed and so rely on a secondary low-bandwidth NGS WFS that takes time-averaged exposures to determine focus errors in the wavefront and apply correction to the LGS WFS. A similar method can be used to determine the correction to apply Rayleigh LGS WFS image.

An alternative method to increasing the range gate depth in three closed-loop steps is to use only the least elongated spots to close the LGS fast-steering loop. These will be the WFS subapertures closest to the telescope pupil centre. As wavefront tip and tilt are partially correlated in adjacent subapertures, stabilising the inner ring of subapertures will reduce spot motion on the next ring of subapertures. The process is repeated, adding more subapertures until the full WFS pattern is used to sense tilt. Using this method, launch jitter can be removed using the optimised range gate depth as a starting point.

The techniques presented in this section, including varying the LGS range gate depth and focal distance during different stages of closed loop operation and using only the central WFS subapertures to initially close the LGS loop, have not to the author's knowledge, been presented before this work.

5.7 Conclusions

Using a model of the semi-analytical model of the LGS, BLT and atmosphere, the optimum photon flux was determined. By including the result of numerical modelling of AO system performance given in Chapter 7, an optimum LGS distance of 4km with a range gate depth of 69m was determined. This LGS focal altitude and range gate depth combination optimises both WFS performance and PSF uniformity across the field of view of the experimental GLAO design presented in Chapter 6. The study has shown that there exist many other LGS focal distance and range gate depth combinations that would allow the LGS WFS to function, albeit with reduced performance. The freedom this gives allows some redundancy in the system design in case photon fluxes are not as bright as predicted, LGS spot jitter is greater than predicted, or atmospheric turbulence increases the LGS spot size.

The use of novel techniques to improve LGS WFS SNR, such as variable range gates and the concept of staggered loop closing introduced. Both these methods allow for increased SNR in the WFS as a longer LGS range gate can be used.

5.8 References

1. R. R. Parenti and R. J. Sasiela, '*Laser-guide-star systems for astronomical applications*', J. Opt. Sci. Am. A 11 288-309 (1994)

2. '*Gaussian Beam Optics*', Melles Griot Optics Guide. http://www.mellesgriot.com/pdf/CatalogX/X_02_6-9.pdf (07/09/05)
3. Noll, R. J., '*Zernike polynomials and atmospheric turbulence*', J. Opt. Sci. Am. Vol. 66, p. 207-211 (1976)
4. H. T. Yura, '*Short-term average optical beam spread in a turbulent medium*', J. Opt. Sci. Am. 63 567-572 (1973)
5. Piironen, P., '*A High Spectral Resolution Lidar Based on an Iodine Absorption Filter*', PhD thesis, University of Joensuu, Department of Physics. (1994)
6. DeSlover, D.H., '*Analysis of Visible and Infrared Cirrus Cloud Optical Properties Using High Spectral Resolution Remote Sensing*', M.S. Thesis, University of Wisconsin-Madison (1966)
7. Measures, R. M., '*Laser Remote Sensing: Fundamentals and Applications*' Krieger Publishing Co., Florida. (1992)
8. Benn, '*NAOMI Throughput*', http://www.ing.iac.es/~crb/wht/aothruput.html (2003)
9. D. L. King, '*Atmospheric extinction at the Roque de Los Muchachos observatory, La Palma*', ING La Palma Technical Note 31 (1985)
10. Weisstein, E.W., '*Pressure Scale Height*', Eric Weisstein's World of Physics. http://scienceworld.wolfram.com/physics/PressureScaleHeight.html. (07/09/05)
11. '*CCD39-01 datasheet*', e2v technologies, Document number A1A-CCD39-01 Back Illuminated Issue 5, April 2003.
12. A. Bucholtz, '*Rayleigh-scattering calculations for the terrestrial atmosphere*', Appl. Opt. 34 15 2765-2773 (1995)
13. Wilson, R. W.; Jenkins, C. R., '*Adaptive optics for astronomy: theoretical performance and limitations*', MNRAS, Volume 278, Issue 1, pp. 39-61
14. J. W. Hardy, '*Adaptive Optics for Astronomical Telescopes*', Oxford University Press, Chapter 6, p210 (1998)
15. J. Vernin and C. Muñoz-Tuñón, '*Optical seeing at the La Palma observatory*', A&A 284 311-318 (1994)
16. Wilson, R.W., Private Communication, August 2005

Chapter 6: GLAO design

6.1 Introduction

This chapter describes the design of the GLAO system used and looks at factors that affect performance, and how they were minimised within the scope of the budget and project timescale. Much of the hardware and software utilised in the GLAO design was developed in conjunction with the NAOMI system that is deployed on the WHT, and so many of the issues that have been studied in order to optimise NAOMI apply directly to the GLAO system.

The main purpose of this chapter is not to detail the work done by others on many aspects of the GLAO system (especially the real-time control software), but more detailed description of some technical aspects of the system will in some cases be required.

As with the previous chapter, this chapter first examines the technical issues that must be addressed with any GLAO optical design, then goes on to detail the design itself. A conventional AO system comprises of three main components, a wavefront sensor (WFS), a wavefront corrector, normally some form of deformable mirror (DM), and a control system linking what the WFS senses to what shape must be employed on the DM surface to flatten the incoming wavefront. Each part will be examined in detail along with a study of theoretical performance. The system performance itself, both on-sky and in the laboratory, are studied in chapters 7 and 8 respectively.

6.2 GLAO Overview

GLAO is a method of correcting only the lowest altitude turbulence present in the atmosphere above a telescope in order to provide a wide-field partial correction of image quality due to atmospheric effects. To achieve this, either tomographic sampling of the atmosphere must be employed to determine the ground layer turbulence profile, or more simply, a laser guide star can be projected to an altitude where only the lowest level turbulence is sampled. The latter was the method employed for this system.

The use of a low-altitude LGS introduces the problem of pupil misrepresentation on the deformable mirror (DM) surface that is not present in any LGS-enabled AO systems currently in routine operation, as they all rely on the excitation of sodium atoms to form a wavefront reference at an altitude of 90-100km. With a low-altitude beacon, the difference in positions between the LGS focus (conjugate to approximately 4.5km) and the infinity-focused starlight (hereafter referred to 'NGS' or 'Science' light) can be large (Figure 6.1), whereas the difference in position between the sodium LGS and the infinity focus NGS light is small. If this extra path length is not compensated for, although the optics will ensure that the pupil is re-imaged onto the DM surface, the footprint of the NGS and LGS beams will be of different sizes at all optical surfaces that are not conjugated to the telescope pupil. This will introduce static aberrations between the LGS and NGS paths that will increase as the LGS altitude is reduced. Other than this problem, the low-altitude GLAO design shares many design considerations with a conventional LGS-enabled AO system.

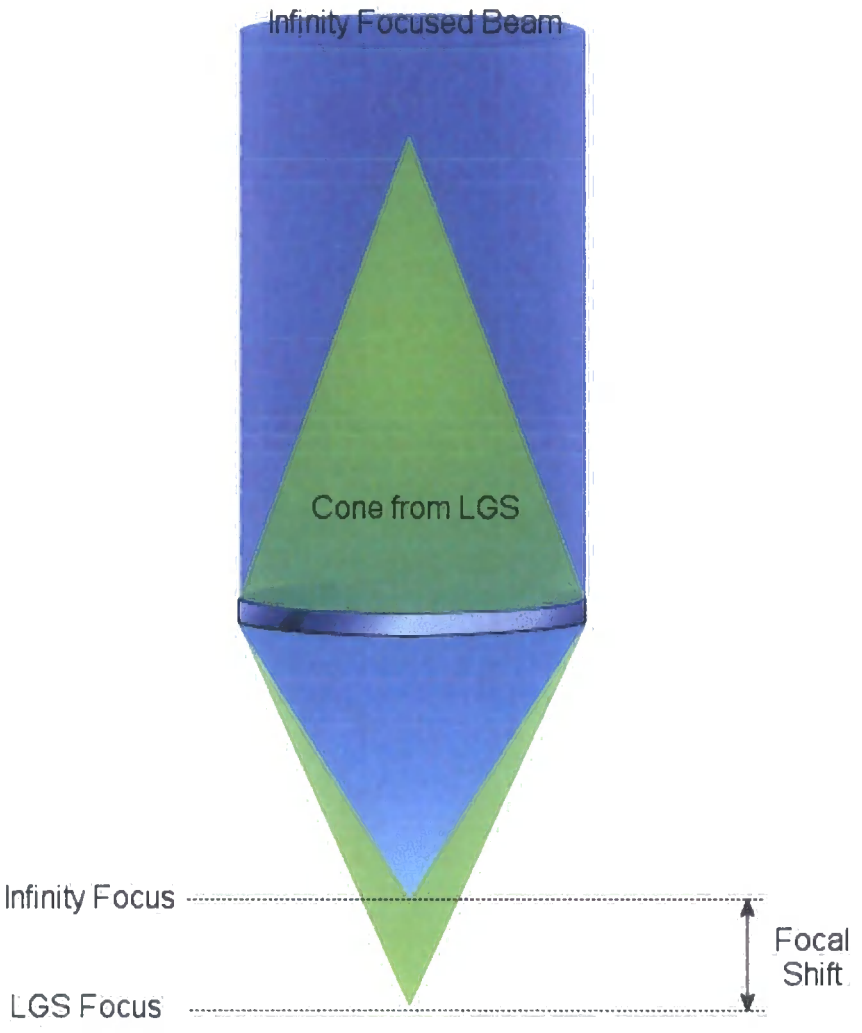

Figure 6.1 Focal shift between NGS and LGS foci. For 4km and 4.5km LGSs on the WHT the focal shifts are 48cm and 54cm .

6.3 Wavefront Correction

The performance and design of the wavefront corrector are at the heart of an AO system, and drive many other aspects of an AO system design such as WFS resolution, physical size of the optics, and the complexity of the control system to name just a few. The most important specification for a wavefront corrector, from an optical design standpoint at least, is the diameter of the phase controlling surface. For the control system, the number of actuators, and thus control channels, is the most important specification. The WFS design is affected by both the actuator geometry

and number of actuators. As this demonstrates, once the wavefront corrector has been chosen, much of the design is defined along with it, so the choice of wavefront corrector is one that defines system performance as a whole.

Many components of the GLAO system described here were previously purchased before work on this thesis had commenced, so many aspects of the design were already defined. The wavefront corrector, wavefront sensor and control system were already in place as part of a laboratory AO simulator, so a comparative study of different wavefront corrector and WFS technologies is outside the scope of this work, but it is shown how the GLAO system was designed to maximise performance of each of the components within the budget and timescale possible.

6.4 System Components

As was seen in Chapter 2, the most commonly used type for astronomical AO is a continuous phase sheet DM. The primary manufacturer of these DM's is Xinetics Inc. in the United States of America. A Xinetics DM was inherited for use with this project. The Xinetics DM has a regular grid actuator geometry with a 7mm actuator pitch. Along with the number of actuators, the actuator pitch defines the physical size of the DM. The Xinetics DM used has 97 actuators in an 11x11 square array as shown in Figure 6.2. This gives the reflective phase surface of the DM a 78mm clear aperture. The WFS is based around a 4-port EEV-39 CCD, using a controller designed and built by Rutherford Appleton Labs. A 25mm diameter square-lenslet array with an actuator pitch of 188 microns and a focal length of 8mm creates the Shack-Hartmann spot pattern. The control system is a parallel 8-processor Texas Instruments C40 DSP system, with a 9th DSP for diagnostics and monitoring purposes. The real-

time control software was developed in-house [1], but system calibration tools still required development to maximise performance.

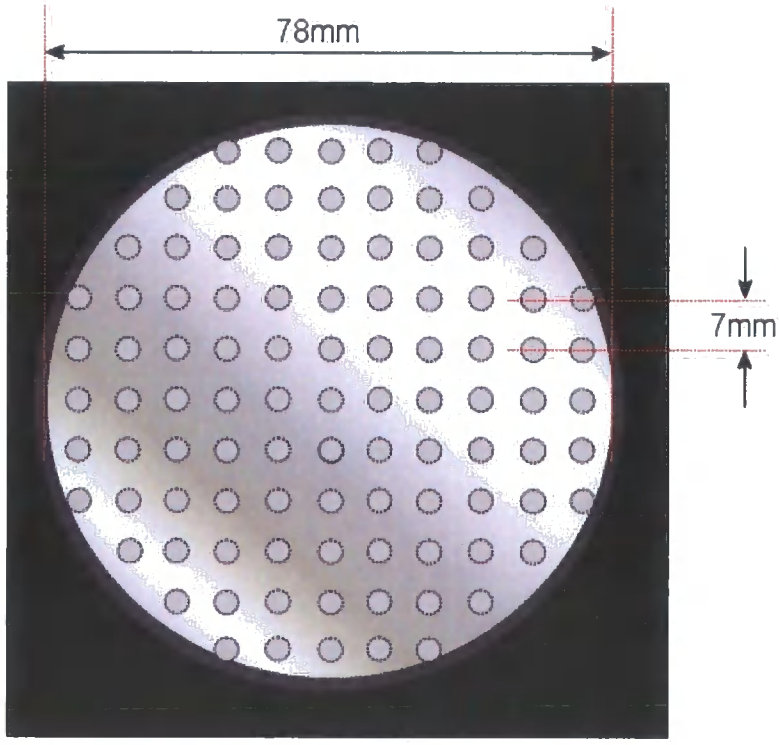

Figure 6.2 Actuator map of Xinetics 97. The actuators are arranged in an 11x11 regular array with a 7mm pitch. The edges of the phase sheet are not secured. The clear aperture is 78mm.

6.5 AO system design

The optical design of any AO system must accomplish four main tasks. First, it must accept light from the main observing telescope. Secondly, it must expand this beam onto the surface of the wavefront corrector. Thirdly, it must provide inputs to both WFS and science camera. Finally, it must do this with a high optical throughput, basically meaning the fewer the surfaces, the better.

The starting point for the optical design of an AO system is the clear aperture diameter of the wavefront corrector, in this case a Xinetics DM. To correct for the

most complex wavefronts, the wavefront corrector needs to have as many degrees of freedom as is possible, and this means using all the actuators. The highest-order AO systems have wavefront correctors with 941 actuators, but use a guard ring of actuators around the main active area that tracks nearby actuators in order to minimise edge effects. Edge effects are caused by the mirror not being constrained outside the outer ring of actuators at the edge of the pupil. Without this guard ring, the response of the unbound mirror edge will reduced system performance. Actuator response can also be affected by their proximity to the edge of the phase surface due to tension within the phase sheet. With DM's that have fewer actuators, utilising a guard ring reduces the number of actuators by such an amount that the performance improvement that should be observed is countered by the fact that the DM has a reduced number of degrees of freedom. Interferometric measurements of the DM showed that edge effects were not noticeable if the used aperture of the DM did not exceed the outer ring of actuators. This condition is shown in Figure 6.3 and resulted in a DM clear aperture of 77mm.

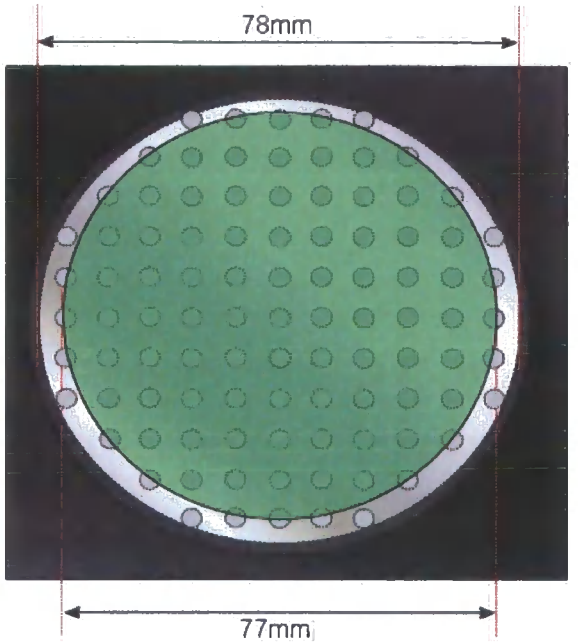

Figure 6.3 Usable area of Xinetics DM shown in green. If the Fried WFS-DM geometry is enforced, then subapertures at the pupil edges become highly vignetted.

The clear aperture of the DM also defines the physical size of the optics that must be used to direct the beam around the AO system. A generic AO system takes the focusing light beam output by the telescope and collimates it at the correct size to fill the clear aperture of the DM. If the DM is 10mm in diameter, this is a simple optical design and cheap off-the-shelf optics can be used. However a 10mm diameter DM, using current technologies cannot contain more than a few corrective elements, and would not be able to correct the complex wavefronts seen at visible or NIR wavelengths. For an 11x11 Xinetics DM, the clear aperture is 78mm, meaning all surfaces must be at least 80mm in diameter, and even larger if a large field of view is to be transmitted through the AO system. For the next generation of ELT AO systems, DM's may measure meters in diameter requiring significantly large, heavy and expensive optics.

The use of a collimated beam in the system allows the DM to be placed at a height that is conjugate to the most turbulent layers in the atmosphere. The effect of DM misconjugation on the performance of an AO system has been studied in several papers [2,3]. For a GLAO system correcting ground layer turbulence only, regardless of the altitude of the turbulent layers in the atmosphere, the DM must be conjugated to the pupil of the telescope.

After the wavefront has been corrected, the collimated beam is then refocused into the WFS and science cameras. The normal method for doing this is to use a pair of matched off-axis parabolic mirrors to collimate and refocus the beam. Large diameter off-axis parabolic mirrors with a high surface accuracy are both expensive and difficult to align, as they require a 6-axis alignment procedure, while on-axis components only require 5-axis alignment as they are rotationally symmetric. On-axis parabolic mirrors are not usually used as they require an extra surface to feed the light onto the optical axis of the parabolic mirror, and this extra surface can not only limit the field of view of the system but also reduce overall throughput.

The optical design must also include dichroic elements for separating different wavelengths of light into the WFS and science cameras. For NGS AO systems, the wavefront is usually sensed over a small bandpass at visible wavelengths, with NIR light being fed into the science camera. Chromatic separation of the visible light from the NIR maximises throughput to both the WFS and science CCD. AO correction is simpler at longer wavelengths as the atmosphere has less effect on longer wavelength light. A small apparent improvement in image quality at a visible wavelength can give a diffraction-limited image if the same wavefront is studied at NIR wavelength of 1 micron or longer. For an LGS AO system, only a very small wavelength bandpass is required of maybe +/- 1nm. Dichroic beamsplitter technology has improved greatly in

recent times. Rugate notch filters capable of transmitting wavelengths from UV to NIR with an average 95% efficiency except for a 10nm bandpass positioned almost anywhere within the wavelength range that reflects nearly 100% of the light [4,5]. The availability of this technology allows LGS light to be removed with great ease from the system and fed into an LGS optimised WFS without adversely affecting visible or NIR throughput.

The field of view of the AO system is also a consideration for the optical design. As discussed in Chapter 1, as the angle between the wavefront reference source and the object being studied is increased, the AO correction degrades. For most conventional AO systems, the wavefront reference is either a NGS or a high-altitude LGS, and so the AO corrected field is very small, of the order of an arcminute at the very most, so the field of view of the system need not be much greater than this. LGS AO system also require a separate faint NGS wavefront reference to determine global tip/tilt from the atmosphere (see Chapter 2) which must be positioned within a small radius of the LGS, so the transmitted field of view must also allow for this. For a GLAO system, depending on atmospheric conditions, the corrected field of view can be far greater than either an NGS or LGS-enabled AO system, so GLAO includes the requirement for a far larger field of view in the optical design.

6.6 Range-gating the Rayleigh return

The range gate is an essential part of a Rayleigh LGS AO system, as an altitude at which the LGS is to be created must be selected. Without this, the Rayleigh plume contaminates the WFS image and using the Rayleigh backscatter as a wavefront reference source becomes impossible. The type of range gate used is dependent on the

pulse rates of Rayleigh lasers that vary between 200Hz and 10kHz, depending on the type of laser being used. For the slower, 200Hz pulse rate lasers, the complexity of the system is obviously reduced, as it becomes feasible to use mechanical devices to assist with shuttering, but for the high repetition rate lasers, an electro-optic range gate becomes necessary to select a required depth around the LGS focal altitude. Electronically shuttered CCDs are also available. These include elements on the CCD that drain photoelectrons when a trigger is set, such that an external range gate is not required. Obviously, if on-chip range-gating can be achieved, the use of an external range gate becomes redundant, and including a range gate in the design is not necessary. Although the gated CCD described above is available and in use in Rayleigh LGS observations, it was not available for this project so an external range gate was needed.

Electro-optic range gates work by altering the polarisation state of light passing through it. By placing the electro-optic cell between crossed polarisers, a shutter capable of very fast on/off switching times and with very high (10000:1) extinction ratios is achievable. The problem with using an electro-optic range gate is incorporating it into the optical design. The difficulty and expense of growing large crystals suitable for use as an electro-optic cell means the cell is often long and narrow and extended in the z-direction, which severely limits the field of view that the cell can transmit. If the aperture of the cell is increased, then a higher electric field is required to induce the $\pi/2$ polarisation change that is required for shuttering. Higher electric fields not only require higher voltage power supplies and electronics for their generation, but the rapidly changing rate (10kHz) of the electric field can also introduce piezoelectric effects inside the crystal, introducing aberrations in the transmitted wavefront. The piezoelectric effect also causes oscillations in the angle of

retardation immediately after the cell is switched. This behaviour is known as 'ringing' and reduces the shutter contrast ratio. The piezoelectric effects can be reduced, or even removed entirely, by changing the type of electro-optic crystal, but this comes at a price and often the piezoelectric effect free crystal cannot be found with suitable apertures and lengths.

The reliance of the system on the electro-optic cell to create the range gate can be relieved by the use of sophisticated baffling systems in the return path. Figure 6.4 shows a schematic of a conical rod Rayleigh noise suppression system that can be used to passively vignette the returning LGS beam before it enters the WFS. By using a passive optical baffle, most unwanted return light from the Rayleigh plume can be removed from the system without introducing any further wavefront aberration into the system or a reduction in throughput to the WFS. A ZEMAX model of the performance of this system was made, and the results of this are given later in this chapter.

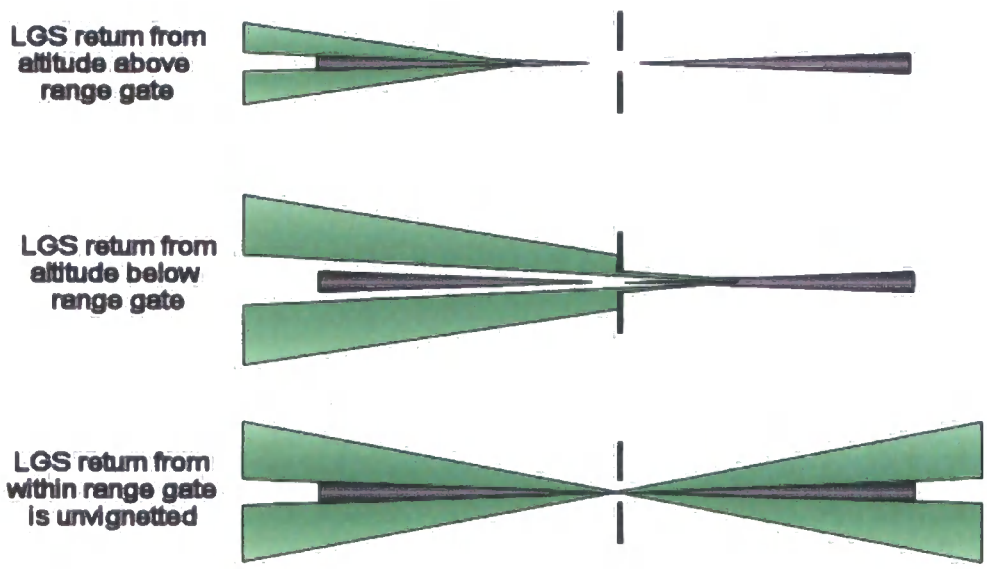

Figure 6.4 Optical baffling scheme used to suppress Rayleigh plume around LGS focal distance

6.7 LGS WFS

The WFS must also be positioned with great accuracy, as for best performance it must be aligned not only to the return beam, but also to the wavefront corrector. The type of wavefront corrector used and wavefront sensor geometry are closely linked. For example, the actuator geometry present in a Xinetics-style DM is very similar to the geometry present in a normal square-geometry Shack-Hartmann WFS, while the curvatures applied to the wavefront by a bimorph mirror are better measured by a curvature sensing system. Similarities between the corrector and sensor geometry can improve the performance of a system, as cross-talk between control channels is reduced. This allows simplification of the control system, as performance can be tuned by using sparse-matrix methods for example [6].

In the case of the Xinetics DM and SH-WFS used for this system, the actuator and lenslet geometry required careful alignment. The ideal alignment requires positioning an actuator at the corner of each WFS subaperture such that adjustment of an actuator affects only the four adjacent WFS spots. This alignment is known as the Fried geometry. In the event that a lenslet lies directly above an actuator, a change in position of the actuator does not affect the position of the WFS spot. If this occurs, the WFS spot experiences a focus/defocus term and becomes blurred. For a SH-WFS that works by determining wavefront slopes, this is a situation that needs to be avoided. This can not generally be achieved in a conventional reflective astronomical AO system using regular actuator/lenslet geometries, due to the need for the light to reflect off the wavefront corrector at an angle. This angle means that the apparent

actuator density will be different in x and y dimensions and the actuator/lenslet alignment condition described above cannot be met.

Spot elongation is caused by imaging the LGS from an off-axis position. The degree of spot elongation observed on a WFS image is a product of LGS altitude, range-gate depth, the distance from the BLT to the optical axis of the observing telescope and the position of the subaperture from the centre of the pupil plane. For a LGS projected from behind the secondary mirror of the observing telescope, the maximum spot elongation is observed at subapertures at the edge of the WFS. Although this example describes spot elongation as it is observed on a SH-WFS, all WFS are affected by spot elongation. On a curvature sensing system, spot elongation is observed as a blurring of the pre- and post-focal images. The blurring is due to the difference in focal positions between the return from the lowest altitude of the range-gate to the highest. The field of view of each WFS subaperture must be taken into account when determining the maximum allowed range gate depth for the LGS. Without taking this into account, larger and larger range-gates can be selected to allow a greater photon return, but the defocused return from the extremes of the range gate will separate and can overlap adjacent WFS subapertures. At this point, wavefront determination is affected and AO system performance is reduced. A model of the LGS was made to examine the performance of the LGS-WFS and the impact of changing LGS parameters on the optical design and is presented in Chapter 5.

6.8 System Design

6.8.1 Optics

The GLAO system was to be situated on the GHRIL Nasmyth platform of the WHT and had to accept the photon return from a low-altitude Rayleigh LGS. The space envelope available within the GHRIL Nasmyth platform is shown in Figure 6.5. The optical axis is 150mm above the optical bench surface. As has previously been mentioned, a GLAO design must observe both the infinity and LGS focal points. At the WHT Nasmyth focus, the difference between focal points at the optimum LGS altitude of 4km (determined in Chapter 7) and the infinity focus was 540mm. The difference in focal positions also precludes the use of the field derotator as it possesses too small an aperture to pass the low-altitude return without vignetting. The field derotator was therefore removed. The removal of the derotator meant that the field would rotate around its centre as the telescope tracked. For the AO system to retain alignment to the NGS while the telescope was tracking either the NGS had to be on-axis, or short exposures where field rotation would not be apparent would have to be used. For off-axis science objects, exposures times had to be long enough such that the seeing was averaged, but short enough such that field rotation was not apparent.

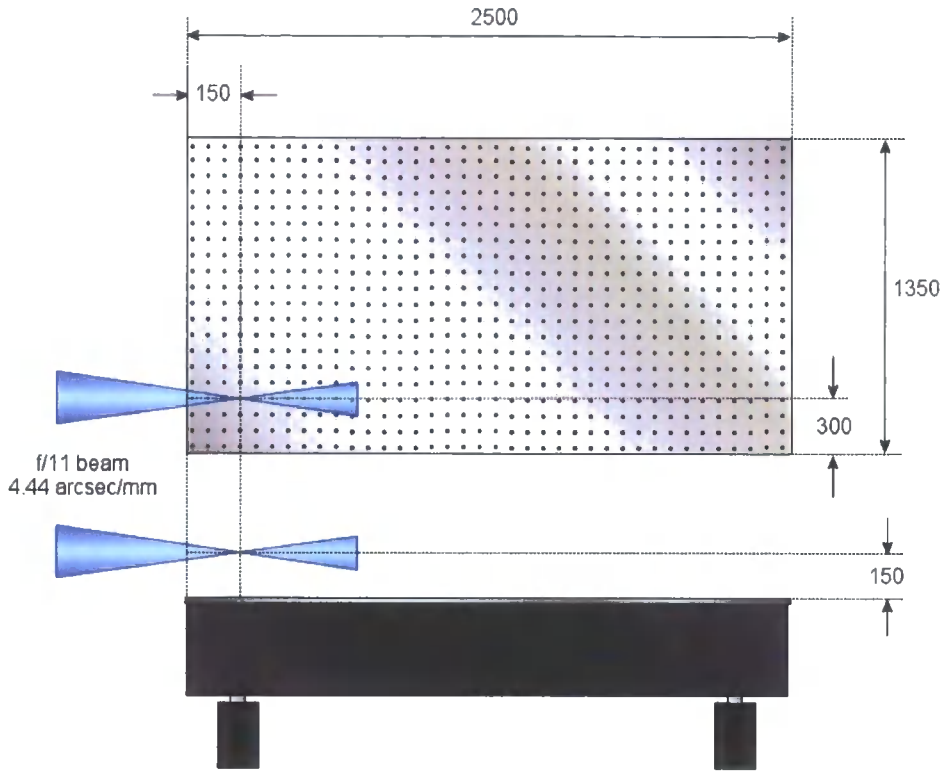

Figure 6.5 GHRIL bench space envelope

An overview of the optical design used is shown in Figure 6.6 and a description of the optical components given in Table 6.1. The first element used in the system was a dichroic beamsplitter that separates the 4km focused LGS light and the infinity focused NGS/science light. The beamsplitter used was a 110mm dichroic that reflects all wavelengths between 650nm and 850nm and transmits all others. The dichroic beamsplitter was 10mm thick and had been borrowed from the OASIS spectrograph feed, thus saving the expense of a high-quality custom dichroic, although a custom dichroic would have been a preferable solution.

At 523nm at an incident angle of 45 degrees, the dichroic transmission was measured as 85%. At NIR wavelengths (λ > 1 micron), the dichroic transmission was not known, but was estimated to have 20% efficiency. The true reflectance of NIR wavelengths by the dichroic beamsplitter was not important as a brighter reference

source could always be found. For this demonstrator system, improving sky-coverage or IR throughput was not feasible with the available project budget. At longer wavelengths than the J-band, the increase in isoplanatic patch size in the atmosphere meant that the wide field performance of the system could not be studied due to the limited field of view of the GLAO design.

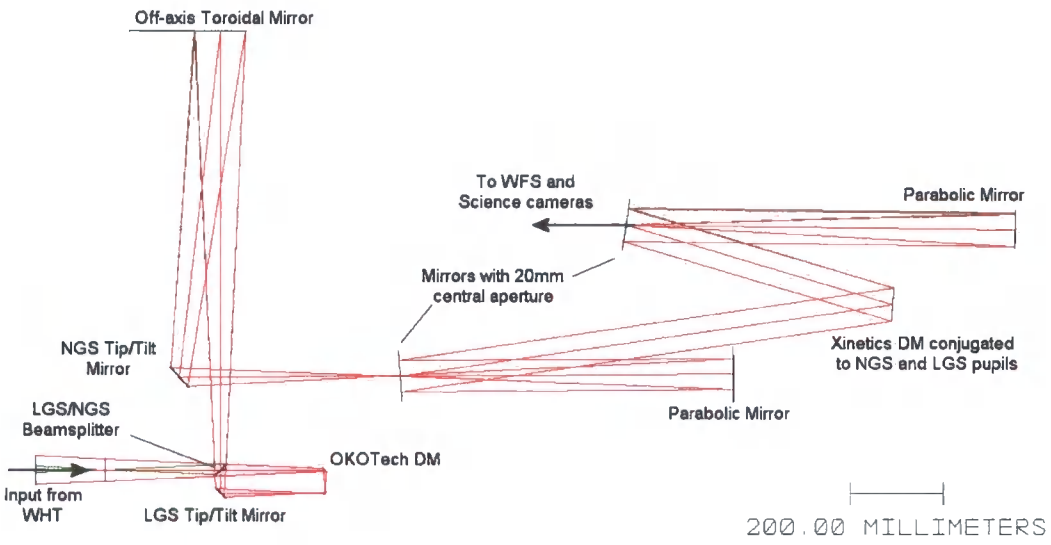

Figure 6.6 GLAO optical design. Red lines denoted return beam from LGS focus, green beam shows infinity focused beam. LGS path length compensation occurs after the initial LGS/NGS beamsplitter.

AO path from:	Infinity Focus	LGS focus (4km)	Units
Input f-number	11	11.13	
Output f-number	11.74	11.64	
Input plate scale	4.44	4.46	arcsec/mm
Output plate scale	4.16	4.26	arcsec/mm
Magnification	1.067	1.047	
FOV (unvignetted)	84.24	87.12	arcsec
Pupil Diameter at DM	73	72.6	mm
Throughput	Unknown	0.34	
Wavefront Quality (optimised)	200	Unknown	nm

Table 6.1 Overview of designed optical performance in GLAO system optical train shown in Figure 6.6.

	Diameter (mm)	Curvature (mm)	Conic Constant	Off-axis distance (mm)
OKOTech DM	19	2400	-1	0
Parabolic Mirror 1	120	1514	-1	0
Parabolic Mirror 2	120	1680	-1	0
Xinetics DM	140	600	-1	70

Table 6.2 Optical Description of powered components in Figure 6.6

The LGS light then entered a reconjugation system that removed the excess path length between the LGS and NGS light. Three reflective elements were used in the reconjugation system. The first was a 37-element OKOTech electrostatic deformable mirror. This mirror was included in the design as it allowed the LGS wavefront to be manipulated independently from the visible NGS light. Using the OKOTech DM in this way allowed for repeatable, calibrated turbulence profiles to be injected into the system both for alignment and closed-loop system testing. Software was written to convert atmospheric phase maps into actuator values that took into account the 45 degree angle of incidence that was present in the optical design. The OKOTech mirror was also used to remove any static aberrations present in the LGS-specific parts of the AO system to present as flat a wavefront into the LGS WFS as was possible. By doing this, the spot elongation only varies due to the factors detailed in Chapter 5, and the LGS WFS will only see slopes that are present in the wavefront due to atmospheric turbulence, and not due to aberrations in the optics.

The final function of the OKOTech DM was to change the focal ratio of the LGS beam to match the NGS beam. The input f/ratio of the NGS beam was 10.96, while the LGS beam was f/11.11. This difference was small and only required a small wavefront curvature to be added, but the ability of the OKOTech DM to approximate a toroidal surface was used to change the LGS beam f/ratio without introducing the extra wavefront aberration that would be added if an off-axis parabolic mirror were used. To decrease the f/ratio of the LGS beam, the DM could only be placed before the LGS focus as the default mirror shape of the electrostatic DM is parabolic and so can only place a focus term on a reflected wavefront.

The next element in the LGS reconjugation system was a fast-steering mirror (FSM) for tip/tilt correction of the LGS wavefront. This mirror was used to correct for any global spot motion that was observed on the LGS WFS without affecting the tilt across the NGS wavefront. This mirror had to correct for the dual effects of atmospheric tip-tilt on both the uplink and return paths of the laser, and also any spot motion due to vibration in the LLS and telescope structure. The maximum spot motion due to the atmosphere was of the order of twice the seeing limit. Any spot motion observed over this limit was thought to be due to telescope vibrations affecting the position of the generated LGS.

The design of the LGS FSM therefore had to allow for correction for angles at least twice those produced by the worst seeing conditions that could be reasonably expected, and with an extra allowance for the correction for telescope vibrations. When the expected wavefront tilt is scaled from the 4.2m WHT aperture to the 50mm diameter of the LGS FSM the maximum angular offset value was estimated (see Equation 5.35) as ±50". Figure 6.7 shows an image of the completed LGS FSM. Two Physik Instrument (PI) actuators with a maximum stroke of 15 microns were positioned equidistant to a central pivot point, with one actuator vertically below and the other horizontally level with the pivot. The maximum angular deviation of the mirror was defined by the stroke of the actuators and their distance from the pivot. The actuators were 20mm from the pivot point defining the maximum angular deviation as ±77". The output 14-bit DAC used to control the actuator gave an LGS FSM resolution of 0.037". Two compression springs were placed in opposition to each actuator to provide a countering force. By increasing the stiffness of these springs, the resonant frequency of the FSM could be increased, but at the cost of an increase in hysteresis effects. The resonant frequency of the FSM had to be above the

loop speed of the WFS and control system, as this would determine the update rate of the mirror pointing.

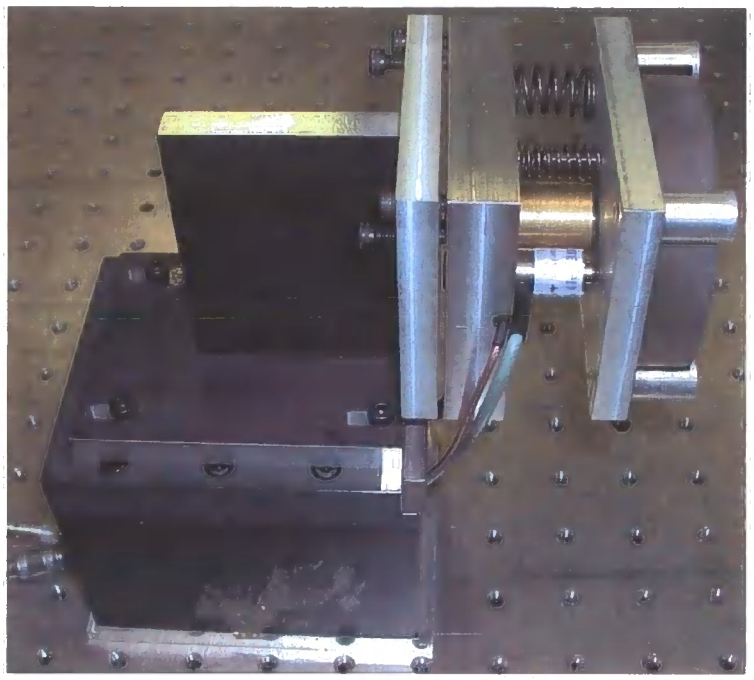

Figure 6.7 Side view of LGS FSM.

The lowest resonant frequency of the mirror was measured by placing a high speed camera at a point 1m from the FSM. A laser beam was then reflected from the mirror and into the high speed camera. A sinusoidally varying voltage was applied to each actuator in turn and the full range of spot motion was recorded. The frequency of the sine wave was then increased, taking care to avoid aliasing with the frame rate of the camera, until the full range of motion decreased by $1/e^2$ of the full range of spot motion. This was observed at 450Hz.

The final element in the LGS reconjugation optics was a simple fold mirror that directed light back through the dichroic beamsplitter, where the reconjugated LGS beam was recombined with the NGS beam. The LGS reconjugation path can reconjugate light from different altitude LGSs by moving the DM and FSM along the

optical axis of the GHRIL bench. The altitude limits of the LGSs that can be observed with this system are imposed by the clear aperture of the dichroic beamsplitter. The clear aperture of the 110mm beamsplitter (tilted at 45°) was placed 300mm from the NGS focus and therefore limited the lowest possible altitude of the LGS to approximately 2km. The focal point of a 2km beam is 1.09m from the NGS focal point.

The beamsplitter and electrostatic membrane DM were also easily removable such that the bare Nasmyth focus could be easily accessed. This was useful, as explained in Chapter 4, for studying the Rayleigh photon return over all LGS altitudes.

The LGS FSM could not be conjugated to the WHT pupil, therefore LGS pupil footprint would wander over the surface of the DM once the LGS FSM loop was closed. The LGS FSM was conjugated to a distance of 19.1km from the telescope primary. As determined in section 5.6.2, the observed spot motion under median atmospheric conditions will be 0.74". Using the LGS FSM at a conjugate distance of 19.1km to correct for a tilt of this magnitude will cause the WHT pupil to shift by 6.8cm. This corresponds to a pupil shift on the DM of approximately $1/6^{th}$ of the interactuator distance. In terms of LGS closed-loop stability, changing the position of the LGS pupil on the DM in this manner essentially means that the WFS-DM interaction matrix[3] becomes inaccurate, thereby affecting performance. There was insufficient time available to fully quantify or measure this effect, however, empirical evidence from laboratory-based closed-loop testing showed that the AO loop would still close and provide some degree of correction with this offset.

---

[3] see section 8.5 for further description of the WFS-DM interaction matrix

Once the LGS and NGS beams had been recombined, both beams were expanding and were too large to pass through the central aperture of the first Newtonian fold mirror. An off-axis toroidal mirror, originally used in the MARTINI AO system [7], was placed 1.2m from the NGS focus. The toroidal mirror served a dual purpose of not only refocusing the beam into the main AO path (comprising the beam expander/collimator mirror, DM, refocusing mirror and annular fold mirrors), but it also created the first of two approximately 70mm diameter WHT pupil images that were present in the system. As the WHT pupil image is, by definition, conjugated to the ground layer, the NGS FSM and high-order Xinetics DM were placed at these points.

The NGS FSM (Figure 6.8) was of a similar design to the LGS FSM, but required a much larger active element to avoid vignetting the 70mm diameter beam. To compensate for this, PI actuators with twice the stroke of those used in the LGS FSM were used. The actuators and springs were placed twice the distance from the pivot such that a similar angular range as the LGS FSM could be achieved. The compression of the springs could be tuned to increase the resonant frequency of the mirror. The resonant frequency of this mirror did not have to reach the closed loop update speed of the high-order LGS loop, as it was driven from a separate closed loop NGS system that ran at a maximum of 100Hz, due to a combination of slower speed tip-tilt sensor and a simple control system. The resonance of the NGS FSM was determined as above 300Hz, at which point measurements were stopped, as the maximum update rate was limited to 100Hz, and so resonance should not be encountered.

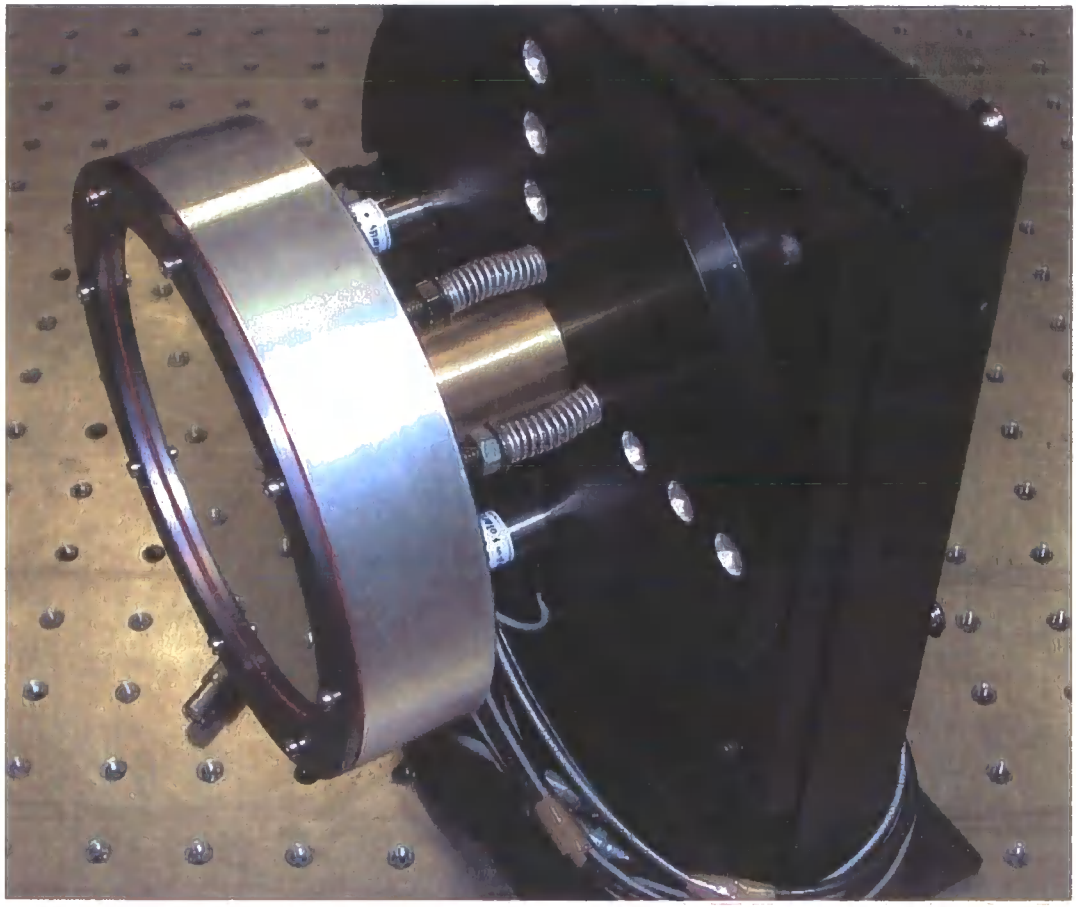

Figure 6.8 NGS FSM. Brass cylinder is central pivot point. Actuators (silver and white) and counterpoised springs can be seen. Clear aperture of mirror was 90mm.

The main AO path was a double Newtonian system that expanded the beam to the 75mm diameter required to fill the Xinetics DM clear aperture. The on-axis parabolic elements were stock items from Edmund Optics and as such, the position of the pupil plane was defined by what focal length mirrors were available. This led to a very long path that the collimated beam must traverse above the optical bench. Turbulence on the bench was observed, so baffling was used to disrupt air currents flowing across the bench surface. The main design consideration, other than the choice of collimating mirror, is to reduce the angle of incidence of the light onto the DM surface. This was achieved as far as possible by minimising the size of the optical mounts.

Although using a double Newtonian collimation/refocusing system reduces cost and complexity of alignment, the 20mm central aperture of the two fold mirrors limits the field of view of the AO system to 80". Increasing the system field of view by increasing the size of the central aperture increases vignetting for off-axis field angles. The maximum aperture size is defined by the ratio of the WHT central obscuration to the WHT primary mirror. The WHT central obscuration is 28% of the diameter of the full beam. For a 75mm collimated beam with the same vignetting ratio, this maximum diameter of the fold mirror central aperture is 21mm. Due to the tilt of the Newtonian fold mirror, vignetting occurs due to this aperture when an off-axis angle of 5" is reached. This gives a 10" unvignetted field of view for the system. The portion of the wavefront obscured by the central aperture of the Newtonian fold mirrors is the major source of vignetting until the maximum off-axis angle of 40" is reached. Past this point, the pupil edge also becomes vignetted by the central aperture of the Newtonian fold mirrors and system throughput rapidly diminishes.

After exiting the main AO path, the light is split into three wavelength bands, as shown in Figure 6.9. An IR dichroic beamsplitter is used to reflect wavelengths longer than 900nm into the NIR science camera. An achromatic IR lens is used at this point to focus light onto the CCD. The remaining visible wavelengths are then separated by a 500nm +/- 40nm bandpass filter from Andover, which has a broadband reflective coating. This filter was chosen as it has a nominal maximum 75% throughput at normal incidence, whereas filters with a smaller pass band were quoted as having a maximum transmission of only 55%. The 523nm transmission of the bandpass filter was examined over a wide range of incident angles and the results are plotted in Figure 6.10. By tilting the bandpass filter, the optimum angle to maximise throughput to the LGS WFS was found and the reflected visible wavelengths (650-850nm) could

be directed into the two visible wavelength cameras present in the system with a minimal impact on the throughput to the WFS. The optimum transmission of 0.86 was found at filter tilt angles between 15° and 35°.

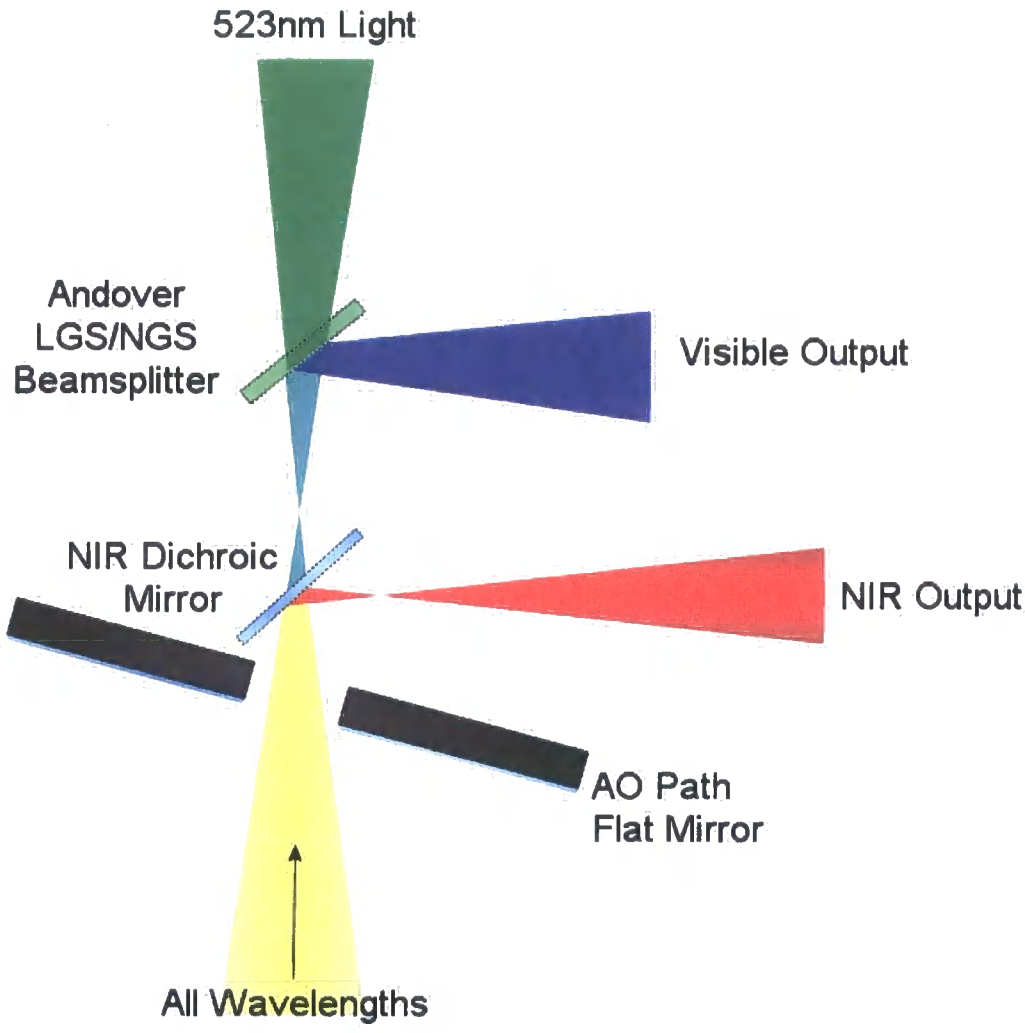

Figure 6.9 Diagram showing separation of wavelengths into NIR for science imaging, visible wavelengths for NGS Tip/Tilt WFS, and 523nm light into the LGS WFS.

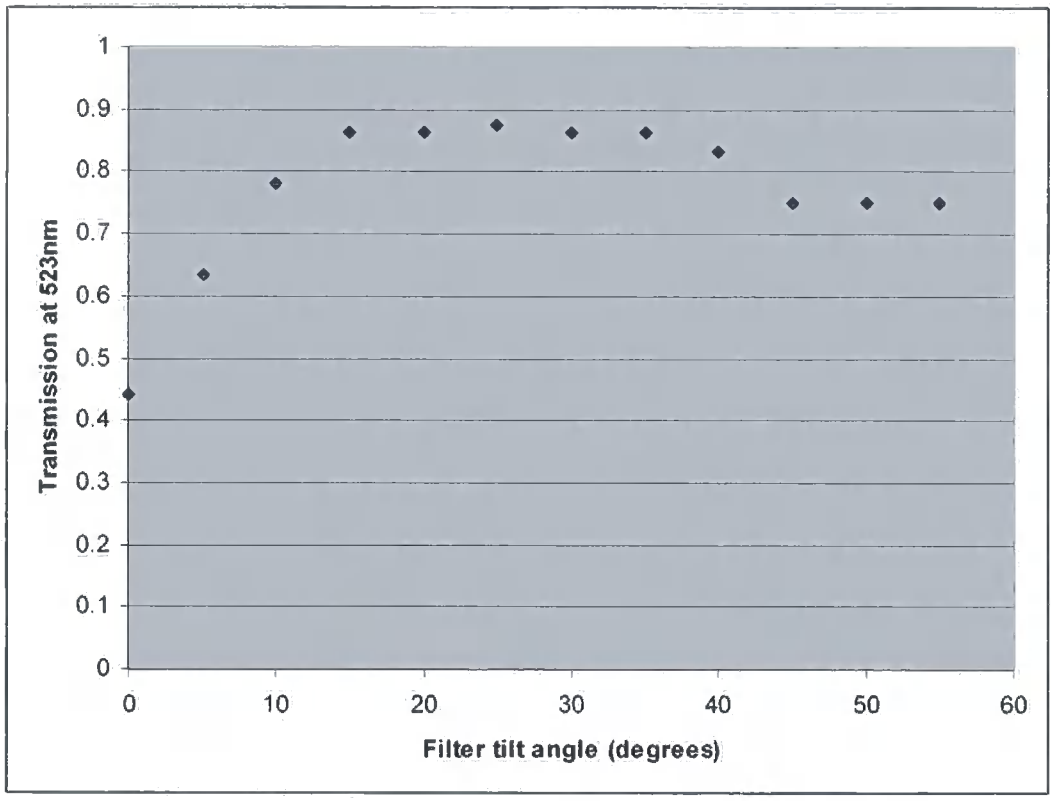

Figure 6.10 523nm transmission curve of Andover bandpass filter when tilted over a range of incident angles from 0° to 55°. Optimum transmission of 0.86 is found at any angle between 15° and 35°.

The 523nm light then entered the range gate system. This was a two-stage process comprising of a passive optical baffle and a pockels cell. The passive optical baffling system is shown in Figure 6.11. Two conical rods were manufactured by stacking and then gluing hypodermic needles together (in a similar fashion to a car aerial) and spray-coating with Nextel. Black Nextel absorbs 99.5% of visible light that is incident upon it [8]. The needles were cut such that the assembled rod would fit exactly inside the secondary obscuration that would be present in an on-axis f/10 beam output from the AO system. The focal ratio of the input beam to the conical rods was tuned by moving a lens to ensure the rods worked at peak efficiency.

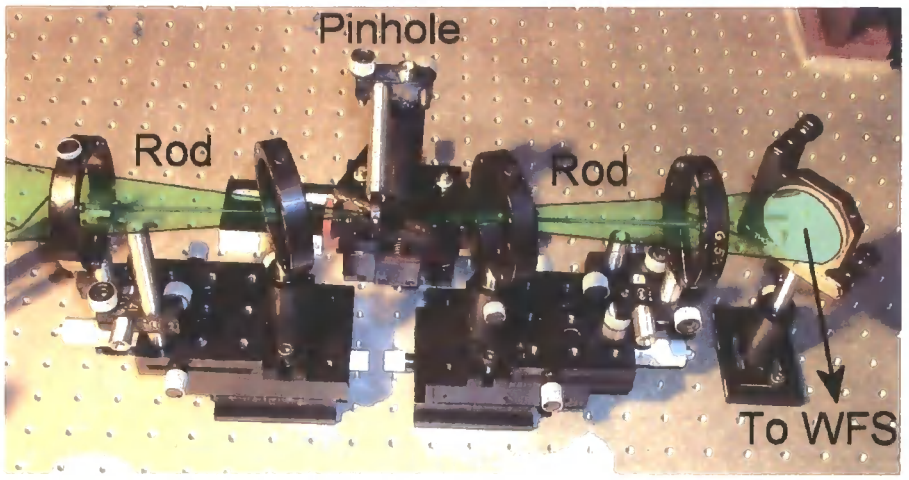

Figure 6.11 Photograph of conical rod optical baffle. Light path has been shown in green. Each rod was mounted on an independent XY stage. Rods were suspended on a fine wire.

The next element in the LGS beam was the pockels cell electro-optic range gate. As the initial polarisation state of Rayleigh backscattered light is preserved if the backscattering angle is 180 degrees from the direction of propagation, a half-wave plate on a rotation stage was placed so as to orient the polarisation state of the linearly polarised light vertically. Due to the on-axis elements in the Beam Relay System and the removal of the field derotator, the polarisation state output from the laser was preserved on observation in GHRIL and did not vary with a change in WHT elevation angle. This meant that the half-wave plate would not require active control.

Light then passed through the 4mm aperture Pockels cell where the polarisation state was unchanged if the range gate was closed, or rotated 90 degrees if the range gate was open. A linear polariser, oriented horizontally, was placed at the output of the Pockels cell. The efficiency of the range gate is determined by the accuracy with which the polariser and Pockels cell can be aligned to each other, and the incoming beam, as well as their respective contrast ratios, and contrast ratio of the initial polarisation state of the laser. Laboratory tests of the Pockels cell system at 633nm showed that the contrast ratio between the open and the closed states was

approximately 150:1. The $1/e^2$ transmitted altitude range of the conical baffle (conjugated to an altitude of 4.5km with a rod separation of 6mm and a 0.6mm aperture placed at the focus) was determined using ZEMAX as between 4.39km and 4.61km. The peak throughput of the baffle at 4.5km was 0.89. However, an off-axis deviation of 1" from axis of the rods and aperture increased the $1/e^2$ transmitted altitude range to between 4.38km and 4.63km with a peak throughput of 0.52. Increasing the LGS off-axis angle past this point rapidly increased the $1/e^2$ transmitted altitude range (a 2.5" offset had a $1/e^2$ transmitted altitude range of over 2km). The LGS had to be stabilised to within 1" of the optical axis for the conical rod range gate to function, although optimal performance would only be achieved once the LGS fast-steering loop had been closed.

A trigger signal to open the shutter was provided by relaying the launch pulse signal from the laser in the GRACE Nasmyth platform to the GHRIL Nasmyth platform. The length of cable that was required to relay the signal introduced a large delay between the time of the laser pulse firing, and the time the pulse was received at the timing electronics. This delay was measured during calibration and alignment when the laser was firing into GHRIL. The pulse was registered on a PMT as this was the only nanosecond resolution photon detector available. The time delay between the optical PMT pulse registering and the electronic trigger signal was measured as 114 microseconds. Without this calibration data, the range gate could not be set to an altitude accurately. The overall throughput of the Pockels cell system was highly dependent on alignment of all the polarisation optics. After the range gate had been cleared, the LGS light enters the LGS WFS.

The LGS WFS was mounted on a 3-axis translation stage for accurate positioning. The lenslet array could also be moved in 3 axes independently of the WFS CCD to

simplify alignment of the lenslets to the mirror actuators. To detect the ground layer turbulence accurately, the lenslet had to be conjugated to the WHT pupil. ZEMAX modelling of the optical design showed that the subaperture formed by each lenslet had a 2.11" field of view before overlapping an adjacent subaperture. However, guard pixels around the edge of each subaperture limit active area of each subaperture on the CCD and therefore reduced the field of view of on the CCD to 1.58". This determined the maximum spot elongation that could be usefully observed, and thus helped determine the maximum altitude at which an LGS could be created (given in Chapter 5).

The NGS light reflected by the dichroic beamsplitter over 650-850nm was directed into a secondary 10 x 10 SH-WFS. The secondary NGS WFS was aligned to the LGS WFS to allow a direct comparison between the motion of LGS spots and NGS spots. The camera used for this was a Qimaging Retiga 1300EX that connected via a firewire camera to a desktop PC (Pentium III 800Mhz running Windows 2000). The 10 x 10 SH spot pattern was analysed in the desktop PC at a frame rate of 70Hz, although this rate was limited by the frame rate of the camera. Analysis of the wavefront in this manner allows the overall tip and tilt of the NGS wavefront to be determined and fed to the NGS FSM. Global spot motion of the NGS WFS was measured and a closed-loop 'leaky box' accumulator was used to determine the correction to apply to the NGS FSM. The readout speed of the CCD was the limiting factor in the speed of the close loop system.

The NGS WFS was also used as a low-bandwith WFS (LBWFS) [9] to continually study a time-averaged wavefront from the NGS. As a time-averaged wavefront will not observe any high speed fluctuations caused by atmospheric turbulence, but instead will see the seeing-limited image, the LBWFS gives a continuous measure of how the

alignment of the entire AO system is changing. Any deviations observed in this wavefront from the initial optimised wavefront could be fed back into the control system to ensure that the optimised wavefront was always being transmitted to the science camera no matter what was occurring with regards to WHT flexure, LGS quality, or any other of the factors that could affect system performance. The primary source of error that the LBWFS was expected to observe was due to WHT top-end sag causing aberrations in the LGS spot on the sky during star tracking. Thirty seconds of NGS WFS was co-added to generate the LBWFS data. A scaling ratio between the offsets observed on the LGS WFS and LBWFS was measured by studying the effect of perturbing single actuators and comparing the resulting spot motion on each WFS. The scaling ratio was determined using off-sky calibration sources. A LBWFS was used on both the SOR sodium LGS and Keck I/II AO systems to correct for changes in the LGS due to the change in apparent distance of the sodium layer (which is at a fixed height above the observatory) as the telescope tracked.

6.9 Optical Optimisation

The initial input state of a closed loop AO system is critical to AO operation as the system always attempts to flatten the wavefront as sensed by the WFS. However, optical elements that are present in the path to the science camera can introduce aberrations that are unsensed by the WFS. If the initial state of the AO system is not optimised, the aberrations present in the science path degrade the science image quality, even if the wavefront at the WFS is flat.

The presence of two wavefront correctors within the system allowed the removal of any static aberrations present between the science light path and LGS light path.

Optical optimisation to remove these non-common path errors involves altering the shape of the two wavefront correctors to input flat wavefronts into the science camera. This is a two-stage process, first involving flattening the DMs present in the system, then using an image sharpening algorithm to optimise the output at the science camera.

6.9.1 DM Flattening

In the laboratory at Durham, the initial surface flatness of the Xinetics DM with all actuators at 0V was measured as 127nm peak-to-valley using a FISBA interferometer. However, the surface flatness measured while the mirror was installed at the GHRIL Nasmyth platform of the WHT was 220nm P-V. This change was due to a difference of 10°C in the ambient temperatures between the two locations causing a warp in the actuator support structure. The ambient temperature in the Durham labs was approximately 22°C, while the ambient temperature present at the GHRIL Nasmyth platform was approximately 11°C. The only other environmental differences between the two locations were the air pressure and humidity. Because the Xinetics DM is not air tight, changes in pressure could not cause the change in surface flatness observed. The performance of the actuators was also changed by the cooler temperatures present in GHRIL. Tests on similar Xinetics DMs have shown [10] that the maximum stroke of the mean actuator increases from 5μm to 6.5μm for a drop in temperature from 20°C to 10°C. The actuator response curve to an input voltage becomes increasingly non-linear as temperature falls below 20°C. Non-linear response of the actuators introduces an error in the shape placed on the DM.

The temperature dependence of the performance of the DM was determined as one of the limiting factors in the performance of the system as a whole. Temperature variations between 0°C and 10°C are routinely observed over the course of a night, which using the figures taken from the manufacturer's own analysis [10], changes the average actuator stroke by up to 1.5μm. The 0V DM surface has a 127nm P-V at 20°C, allowing one to measure the manufacturing accuracy of the system. When the midrange voltage is placed on all the actuators the DM surface exhibits a 310nm P-V. This gives an error in the actuator stroke of $\pm(310-127)/2 = \pm 92$nm over the midrange actuator stroke of 2.5μm. Extrapolating this accuracy to the extended stroke of 6.5μm at the DM average operating temperature of 10°C, the DM will have a midrange surface of 3.25μm±120nm, or a wavefront P-V of 240nm. This result is close to the observed P-V surface accuracy of 220nm at a temperature of 10°C and within the measurement accuracy (±20nm) of the FISBA interferometer used. Assuming that the DM was flattened and calibrated at 20°C and the loop closed on the system at 10°C the DM would exhibit a P-V wavefront error of 56nm, or an rms error of approximately 16nm. As the wavefront is reflected from the front surface of the DM, this wavefront error must be doubled. For observations at 850nm, this corresponds to a wavefront accuracy of approximately $\lambda/27$.

To compensate for the effect of changing temperature on the DM, the calibration of the DM should be performed several times over the course of a night before observing is due to begin. The temperature of the calibration can then be recorded and the calibration recalled at any time. Due to time constraints at the telescope, only a single calibration was made at the night-time ambient temperature of 8°C. The small

wavefront error (<λ/27) any change in temperature causes will minimally affect AO performance.

The calibration of the Xinetics DM followed the basic method outlined by Sivaramakrishnan and Oppenheimer [11] that iterates towards a flat mirror. An attempt was made to use this method to flatten the wavefront through the entire optical train by injecting light from the interferometer into the system. A mirror placed at the system focus retroreflected the light back into the interferometer and so a double pass was made through the entire system. However, vibrations present on the GHRIL optical bench meant that optimisation of the output wavefront in this fashion was impossible. The flattening procedure could still be carried out if the DM and interferometer were tightly fastened to one another. This ensured that all vibrations experienced by the DM and interferometer were common, and stable wavefront measurements were possible.

6.9.2 Simplexing

The second stage of optical optimisation was undertaken by placing a camera at the IR output and examining the image quality of an on-axis focused spot. An image of the focused spot was fed into one of two image quality metrics (equations 6.1 and 6.2). The shape placed on the surface of the high-order Xinetics DM is then adjusted and a new image obtained. Through the process of iteration, a mirror shape is eventually arrived at that cancels out all static aberrations in the system that the DM can correct. A simplex algorithm [12] was used to control the shape on the DM. The simplexing algorithm works by generating a set of mirror shapes and examining their effect on the metric. The worst stored mirror shape (as defined by the metric) is then

compared to the best stored mirror shape, and a new mirror shape is generated through a series of geometrical transformations. Over the course of many iterations, the best and worst mirror shapes slowly converge to a solution. The operation of the simplex metric is described in Numerical Recipes [13].

$$M = \frac{\sum_{i=0}^{i=n} P_i(r > a)}{\sum_{i=0}^{i=n} P_i(r < a)} \qquad \text{- 6.1}$$

where r is the distance in pixels of the i^{th} pixel to the image centroids, P_i is the number of counts detected in the i^{th} pixel and M denotes the value of the image metric. When $M = 0$ all the light will be concentrated within a circle of radius a pixels. Note that if the defined radius used in equation 6.1 is reduced, both metrics essentially accomplish the same task (concentrating the light inside a small area). However, the first metric was used initially as it gave far better results when dealing with a more aberrated spot as was present after initial optical alignment. Care must be taken with the use of the metric given in equation 6.1 as light that leaves the CCD image plane also registers as an improvement in image quality. A case where the above metric fails is where the DM shape concentrates a small fraction of light inside the circle of radius a pixels on the CCD and the rest of the light is directed out of the CCD field-of-view. This causes numerator of equation 6.1 to equal zero and the simplexing algorithm will observe no further reduction in the value of the metric. Fortunately, the CCD was large when compared to the initial focused spot size, so by positioning the spot in the centre of the CCD this situation could be avoided. Equation 6.2 examines both the intensity and light-concentration of the focal point.

$$M = \frac{\left(\sum_{i=0}^{i=n} P_i\right)^2}{\sum_{i=0}^{i=n} P_i^2} \qquad \text{- 6.2}$$

Equation 6.2 describes the final image sharpening metric where M is the metric value. $M = 1$ when all the light is concentrated inside a single pixel. $M > 1$ if any light falls outside a single pixel. Use of this metric not only concentrates light around a given point, but the metric also improves with an increase in peak intensity. This was useful as it registered the extra presence of photons that would normally be lost in the noise. For example, 1000 photons spread across 100 pixels could easily be 'lost' in the background noise, and their presence would not affect the metric in any way, but an accurate solution could not be converged upon. 1000 photons concentrated across a few pixels would make a large difference to the second metric, even if they were initially lost in the background noise. The results of the simplexing algorithm are shown in Figure 6.12.

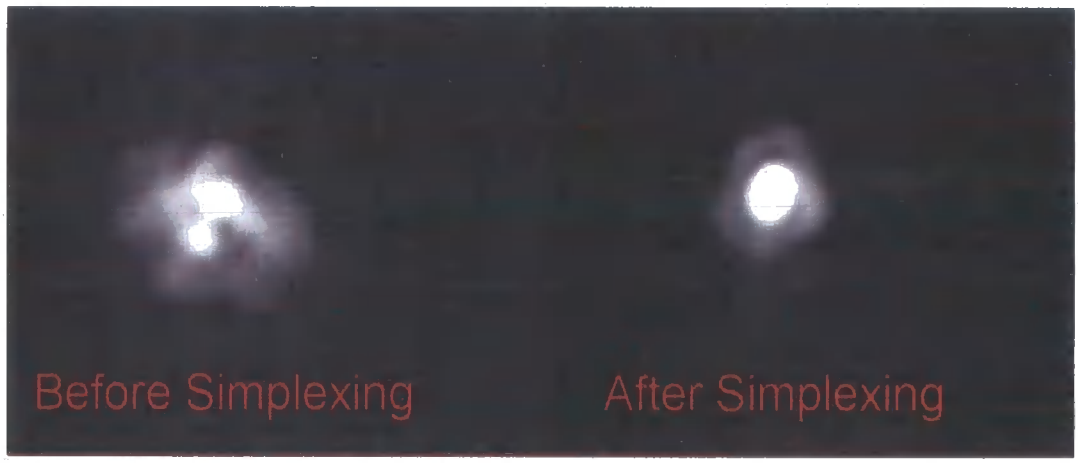

Figure 6.12 Effect of simplexing on the image quality at the science focus. First diffraction ring is visible in simplexed image.

Once the simplex algorithm has converged to a solution, the mirror is said to be 'simplexed'. The simplexed mirror shape gives the optimum spot quality at the focal

position of the IR science camera. The process was repeated at the focal point input to the LGS WFS, but this time using the OKOTech DM as the wavefront corrector. The 523nm calibration source was used as the reference for this optimisation. Running a second simplex was deemed necessary as the Andover filter was not of a high optical quality, and a flat wavefront transiting through this component would become very aberrated, to the point where using it for WFSing would become difficult and contain inaccuracies. The actuator values present on the OKOTech DM were then recorded and not altered.

Once both simplexes had been completed, the WFS image itself was studied and the spot offset from the centre of each subaperture was recorded. Although the two simplexes should remove most aberrations from the system, some residual offsets will still be present due to higher order static aberrations within the system. The offsets present at this point define the wavefront that the DM/WFS coupling is trying to reproduce, and hence a flat wavefront into the IR science camera. The simplexed mirror shape is also the starting point for all calibration procedures, as the atmosphere produces a turbulent profile that fluctuates around a flat wavefront which this mirror shape recreates.

While simplexing both mirrors, care was taken not to approach the limits of the linear response regime of the actuators. The Xinetics DM uses piezo-magneto-restrictive actuators that only have a linear response over a small voltage range. Each actuator in the OKOTech DM also exhibits a response that is not just proportional to the applied voltage, but is also related to the position of that actuator relative to the edge of the electrostatic membrane. The linearity of actuator response is not a critical issue in this case, as the OKOTech DM input a static aberration during AO operations. However,

using the linear regime of the Xinetics DM actuators is critical to the closed-loop operation of the AO system as the control system relies on a linear actuator response.

After simplexing, a phase map of the Xinetics mirror surface was made, showing an increase from the 20nm rms surface value of the flattened DM to approximately 200nm rms. This value combines wavefront errors due to the quality of the optics used in the AO system and how well the AO system has been aligned. Minimising this value is essential because any DM stroke used for correcting static aberrations cannot be used to correct for turbulence, essentially decreasing the dynamic range of the DM. For a Xinetics DM with a stroke of 6.5μm, a 200nm rms wavefront error uses only 3% of the DM stroke, leaving up to 12.6μm of full-range correction (doubled due to reflection from the mirror surface) available to the AO system. This is sufficient to correct for strong atmospheric turbulence observed at the LGS wavelength at a good astronomical site. A phase map of the OKOTech DM could not be made as there was not sufficient space on the optical bench to position the interferometer, however, as the OKOTech DM is used to inject static aberrations only, the DM stroke used to correct for these aberrations is irrelevant, just so long as the aberrations can be corrected.

Assuming that all mirrors used in the system have a transmitted wavefront quality (TWQ) of 126.6nm (corresponding to a λ/10 surface measured at 633nm), all lenses and beamsplitters have a TWQ of 158.25nm (λ/4), the combined wavefront quality to the LGS and NGS WFSs are given in Table 6.3 below. The combined wavefront errors shown are relatively large, but these are a consequence of the limited project budget, and are all within the correction range of the Xinetics and OKO DM's.

Path	Mirrors	Lenses	Beamsplitters	RMS Error(nm)
LGS WFS	12	5	4	704
NGS WFS	8	2	3	558
Science	8	1	2	492

Table 6.3 Optical quality of optical design assuming mirrors have a λ/10 rms surface accuracy, and lenses and beamsplitters have a λ/4 rms transmitted wavefront quality. Total RMS error was calculated from the root of the quadratic sum of errors from each component.

The simplexed DM surface of 200nm rms shows that either the optical quality of the system was better than that predicted above.

6.10 On-sky performance

This section discusses the optical performance of several components in the AO system when used on-sky with the LGS.

6.10.1 Range Gate

Although the conical rod baffle worked, and a dark annulus was observed around the bright core of the LGS, the top-end telescope sag while tracking the NGS caused the LGS to drift away from the centre of the alignment of the rod system, and the contrast ratio between LGS and plume dropped. The finite diameter of the LGS also meant that the contrast ratio was lower than expected. The rod system could work as a range gate if the AO loop was already closed and the LGS spot was diffraction limited and jitter/sag corrected.

The Pockels cells were of limited use due to their small clear aperture (4mm) and length (130mm). The physical dimensions of the crystals limited the field of view of the Pockels cell to approximately 1" on-sky at the LGS altitude. As was seen in

Chapter 4, the on-sky FWHM diameter of the Rayleigh plume was 2.45" at approximately 4km when viewed through the WHT. Even though the diameter of the LGS embedded within this plume should be sub-arcsecond, to range gate this plume the Pockels cells must have a clear aperture of at least 3" in order to cope with the finite size of the LGS and LGS jitter. When the Pockels cells were used on the LGS, they achieved a contrast ratio of 343:1, but only on the subsection of the LGS that could be imaged through the clear aperture of the Pockels cell.

6.10.2 WFS

During the course of the LGS AO run, one quadrant of the WFS failed, and could not be repaired in the time available. Although this failure did not rule-out attempting closed-loop operation, the AO system performance could no longer match predicted performance.

Although simplexing the Xinetics DM could optimise the image quality in the science camera, the OKOTech DM did not have the range to correct for the aberrations that were observed in the LGS WFS. The poor image quality to the WFS was caused primarily by the dichroic used to separate visible light from the LGS wavelength. A higher quality dichroic could not be purchased with the budget available.

The 188μm pitch of the lenslet required an input 1.88mm diameter collimated beam. With the poor LGS WFS wavefront quality that was observed, intensity variations due to aberrations within the collimated beam were increased resulting in a very poor WFS image. Although several attempts to improve the LGS wavefront were made, the combination of the small field of view of the range gate system, the small lenslet pitch requiring collimating optics to be placed near the aberrated focus, and the limited time available for system commissioning prevented any improvement over the WFS image

presented in Figure 6.13. The LGS WFS image shown obviously cannot provide a wavefront to an AO system expecting a 10x10 spot pattern, and this ultimately prevented closed loop operations on-sky. Analyses of the section of the LGS wavefronts that could be measured were undertaken and the results presented in Chapter 8 of this work.

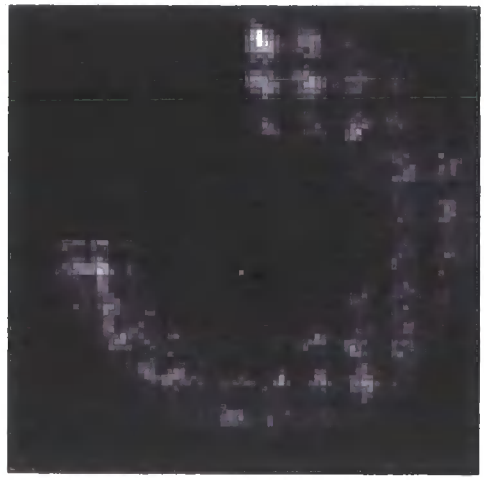

Figure 6.13 Sample LGS WFS image showing failed quadrant and poor wavefront quality.

6.11 Conclusion

This chapter presented the optical design of the AO system as commissioned on the telescope. The performance of several system components was analysed. Due to both the limited commissioning time and available project budget several non-optimal optical components were used. The combined wavefront errors from these components resulted in a poor-quality LGS wavefront being observed by the LGS, and ultimately prevented stable closed loop operations. However, LGS wavefronts were reconstructed from the LGS WFS data and these will be compared to wavefronts reconstructed from simultaneous NGS data in Chapter 8.

6.12 References

1. Myers, R.M. Longmore, A.J., et al '*NAOMI adaptive optics system for the 4.2m William Herschel telescope*', Proc. SPIE, Volume 4839, pp. 647-658 (2003)
2. Racine, Rene; Ellerbroek, Brent L., '*Profiles of nighttime turbulence above Mauna Kea and isoplanatism extension in adaptive optics*', Proc. SPIE Vol. 2534, p. 248-257 (1995)
3. Flicker, R; Rigaut, F.J.; Ellerbroek, B.L., '*Comparison of multiconjugate adaptive optics configurations and control algorithms for the Gemini South 8-m telescope*' Proc. SPIE Vol. 4007, p. 1032-1043 (2000)
4. Johnson, W.E.; Crane, R.L., '*Introduction to rugate filter technology*', Proc. SPIE Vol. 2046, p. 88-108 (1993)
5. Bartzsch, H.; Lange, S.; Frach, P.; Goedicke, K., '*Silicon oxynitride rugate filters grown by reactive pulse magnetron sputtering*', Proc. SPIE, Volume 5250, pp. 502-510 (2004)
6. Ellerbroek, B.L., '*Efficient computation of minimum-variance wave-front reconstructors with sparse matrix techniques*', J. Opt. Sci. Am. A. Vol. 19, p. 1803-1816 (2002)
7. Doel, A. P.; Dunlop, C. N.; Buscher, D. F.; Myers, R. M.; Sharples, R. M.; Major, J. V., '*The MARTINI adaptive optics instrument*', New Astronomy, vol. 5, p. 223-233. (2000)
8. Egan, W.G. and Hilgeman, T., '*Retroreflectance measurements of photometric standards and coatings*'. Appl. Opt. 15, p1845. (1976)
9. Rhoadarmer, T.A.; Ellerbroek, B.L, '*Method for optimizing closed-loop adaptive optics wavefront reconstruction algorithms on the basis of experimentally measured performance data*', Proc. SPIE Vol. 2534, p. 213-225 (1995)
10. '*Xinetics General Mirror Performance*', Xinetics Inc, (13/09/2005) (www.ucolick.org/~max/289C/Reading/General%20Mirror%20Performance.pdf)
11. Sivaramakrishnan, A.; Oppenheimer, B.R., '*Deformable mirror calibration for adaptive optics systems*', Proc. SPIE Vol. 3353, p. 910-916 (1998)
12. Nelder, J.A. and Mead, R., '*A simplex method for function minimization*', Comp. J. 7 p308-313 (1965)
13. Press, W.H., Teukolsky, S.A., Vetterling, W.T., Flannery, B.P, '*Numerical Recipes in C: The Art of Scientific Computing*', 2nd Ed., Cambridge University Press, Cambridge (1992)

Chapter 7: System Modelling

7.1 Introduction

This chapter details the numerical modelling of the AO system. Monte Carlo simulation code, originally developed by Richard Wilson of the University of Durham and similar in approach to that described by Ellerbroek et al [1], was used to model the full AO system. The Monte Carlo simulation is referred to hereafter as the numerical simulation. An analytic WFS model was also created (by the author) that can quickly and accurately determine the performance of a particular LGS concept. AO system modelling forms an essential part of the design process for any AO system, and impacts the system design by quantifying the effect of design tradeoffs on system performance. This chapter first details the models used, followed by a presentation of the simulation results and the predicted system performance.

7.2 Numerical AO Model Overview

The simulation itself is a modular, parallelised code capable of handling diverse AO system setups. Each module describes a different component of the experimental setup and allows complete configurability of the LGS, NGS, atmosphere, DM, WFS and AO control system. The software architecture is illustrated in Figure 7.1.

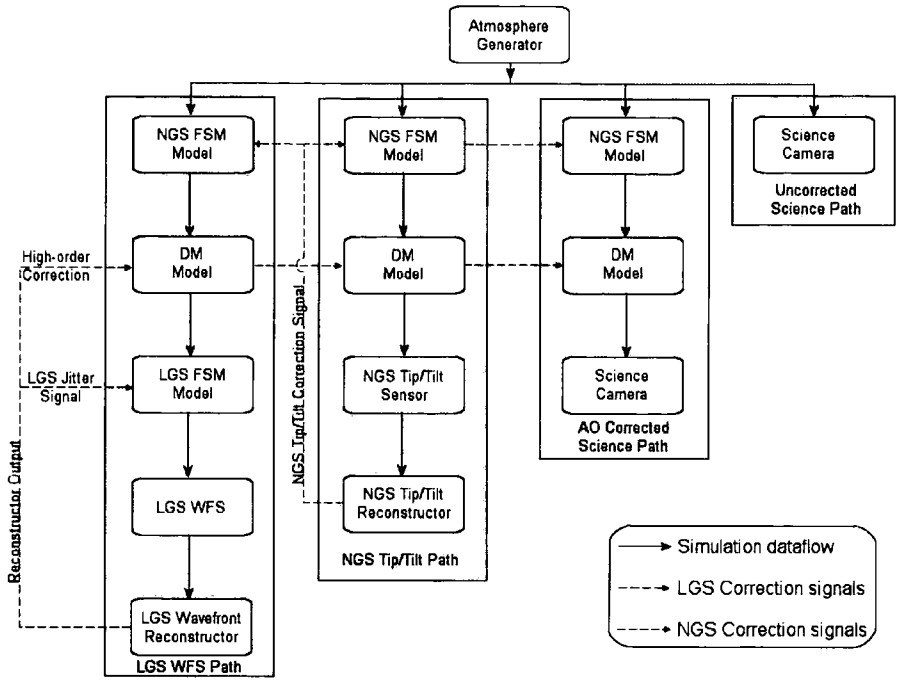

Figure 7.1 Model AO System overview. The modular makeup of the system allows multiple paths to be defined, allowing multiple NGSs, LGSs and field points to be sampled in a single simulation run. The uncorrected path verifies the simulated atmospheric turbulence accurately represents the requested conditions.

7.2.1 Atmosphere

The atmospheric model used was a 3-layer model, with 40% of the turbulence placed at the ground layer, 40% of the turbulence placed at a layer 2.5km above the telescope, with the remaining 20% at an altitude of 7.5km i.e. the "standard" La Palma atmosphere [2]. Atmospheric seeing was limited to 2 cases, with r_0's equating to median La Palma V-band seeing of 0.74", and good V-band seeing of 0.54". System stability tests were carried out by gradually reducing r_0 to investigate the point where the AO system would fail to work.

The system time-period, or 'heartbeat' frequency, was defined by the speed at which the phase screen moves across the telescope. All timings within the system, including WFS integration periods and system latencies are by necessity, integer multiples of

the heartbeat frequency. For a system running at approximately 300Hz, a 3ms system time-period would be acceptable. If a faster AO frame rate, wind speed, or sub-3ms system latencies are required, a shorter time period must be used.

7.2.2 NGS

The NGS was modelled as a single wavelength point source of fixed brightness. The flux (in photons/sec/WFS subaperture) detected by the WFS was set to match reasonable throughputs expected from the system model. For this demonstrator system, the NGS magnitude was arbitrary. If system performance was seen to be limited by the signal on the NGS tip-tilt WFS, a brighter NGS could be selected. The flux to the NGS WFS was therefore set at 100000 photons per NGS WFS frame. This corresponds to approximately a 6^{th} magnitude star at the NGS wavelength of 600nm. This flux is at a level well above the predicted signal threshold for the NGS WFS. The NGS could be positioned at any angular distance from the on-axis LGS. Three cases were studied, with the NGS positioned on the WHT (and hence LGS) axis, and 40" and 120" off-axis.

7.2.3 LGS

The LGS is modelled by placing an NGS at a finite altitude within the atmosphere. The turbulence sampled by the LGS wavefront is then given by the geometrical cone that the returning beam samples on the path from the LGS to the full telescope aperture.

The model of the LGS that was presented in Chapter 5 was integrated into the simulation to provide an accurate depiction of the BLT-LGS interaction. The effects of launch jitter and centroid anisoplanatism [3] on the LGS uplink were not included in the model. To accurately model uplink effects requires a full physical optics propagation model [4,5] which would increase simulation run-times to the point where numerical simulations of the atmosphere would become unfeasible to accomplish within an acceptable timescale. Across a 300mm aperture, such as that of the BLT, the dominant wavefront aberrations are tip and tilt. The effect of uplink jitter was examined in Chapter 5 and showed that the GLAO WFS performance should not be impaired by LGS launch jitter. The effect of centroid anisoplanatism on the LGS uplink also introduces an apparent tilt on the wavefront as the intensity profile of the LGS can be distorted from a Gaussian. Over a 300mm aperture, this effect will be small when compared to the effect of launch jitter.

7.2.4 DM

A precise definition of the surface of the Xinetics DM within the model requires using complex (and therefore computationally costly) code that uses finite element analysis to determine the shape of the DM surface that has been deformed by the influence of an actuator. A simple mathematical approximation to the surface of the Xinetics DM can be used that utilises cubic interpolation to approximate the phase surface.

An 11x11 actuator grid is passed to the interpolator that rescales the grid to a predefined number of pixels (in the case of this simulation 80x80). The resulting DM phase map is then scaled to the full linear range of the DM and applied to the incoming wavefront. An initial investigation into the accuracy of this approach

showed that an interpolated DM can reproduce the response of the DM to a given actuator pattern to better than an rms wavefront error of λ/3 at 633nm when the DM lies within its linear range. This match can be enhanced by improving the accuracy of interferometric measurement and through modification of the interpolation geometry. A comparison of an interferometer image of the Xinetics phase sheet with the output of the interpolated model phase sheet is shown in Figure 7.2.

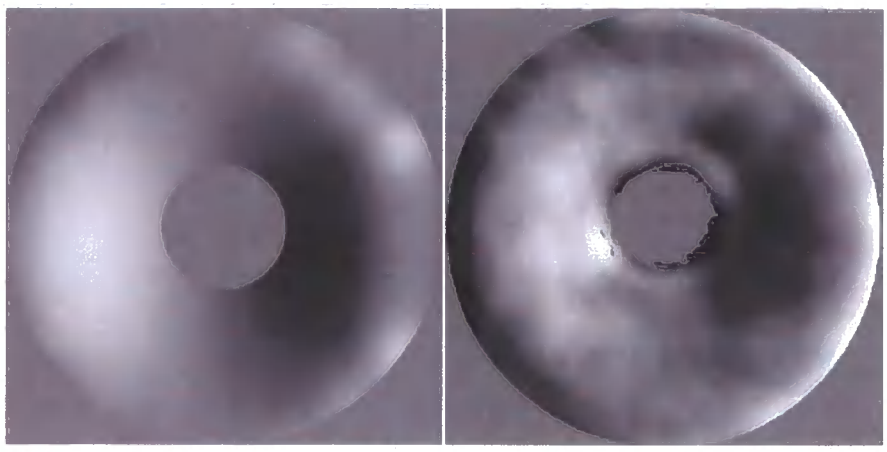

Figure 7.2 Model DM phase surface produced by interpolation and DM phase surface as measured by a FISBA interferometer. Zernike mode 7 corresponding to classical wavefront coma was both modelled and measured. After normalisation, the rms error between the two wavefronts was λ/3.08 at 633nm.

For comparative purposes, the original DM model was constructed using either a linear superposition of Zernike terms up to a given radial order approximating the response of the DM, or a segmented mirror with each segment capable of independent tip/tilt and piston movements. Whilst a Zernike-based analysis comparison favours a Zernike-type DM, the only true measure of DM model suitability is a comparison between a measured DM phase profile and a modelled DM phase profile. The project timescale did not allow for this comparison to be made, as a full calibration of each DM actuator had not been undertaken, and was not required for closed-loop operation. The fact that the AO loop was able to close and provide correction proved the concept

of using an interpolated DM in a closed-loop AO simulation. Further work is required to fully characterise the performance of the interpolated-DM technique and compare it to both the performance of current DM models and the measured performance of a real Xinetics DM.

7.2.5 WFS

The WFS module defined an 80x80 pixel CCD, divided into 10x10 8 pixel subapertures. Each subaperture has a 1 pixel guard ring, giving a 6x6 WFSing element. The effect of a read noise of $6e^-$ was included in the WFS image.

The elongated WFS spot pattern created by the LGS model presented in Chapter 5 was convolved with the output of the LGS propagation through the atmosphere on a subaperture by subaperture basis to give an elongated spot pattern. The pixel scales output by the WFS model and the LGS simulation were matched so this convolution was accurate. The 188μm pitch, 7.6mm focal length WFS lenslet, defined a pixel scale of 0.263" per pixel

7.2.6 AO control system

The control system processed the WFS data and reconstructed the wavefront to display on the DM. This was achieved by measuring the system WFS-DM interaction matrix and using Singular Value Decomposition (SVD) to create a pseudo-inverse system control matrix. Poorly sensed modes were removed from the control matrix at this point using a threshold value on the SVD diagonal matrix. This concept is discussed further in Chapter 8.

The AO control system also included the ability to define subsystem latencies to accurately simulate the response of the system. Latencies were simulated by withholding data from the control system to the DM for a given period of time. Although in reality latencies occur at all stages where data must be transferred or processed, the total latency between end of WFS exposure and the correct shape settling on the DM encompasses all sub-system latencies. As such, it is the only the total system latency that requires definition.

The GLAO system had the added complexity of having two control systems, one controlling the high-order LGS system and LGS jitter correction mirror, and the other controlling the NGS tip/tilt loop. The two loops could potentially compete with one another. The NGS tip/tilt would be observed by the LGS WFS as an additional component of the launch jitter. Provision was included in the on-sky system to feedback the NGS signal into the high-order LGS loop so the NGS-induced jitter would not be observed by the LGS WFS, but the added complexity this introduced into the simulation meant this provision was not included here.

7.3 LGS WFS Model

A model that was able to rapidly determine the performance of a particular WFS concept using real atmospheric profiles and simulated turbulent phase screens was developed. This model generated an atmosphere in an identical fashion to the full closed loop AO simulation detailed in section 7.2.1. Vertical slices through the atmosphere were used to create LGS wavefronts. The finite altitude of the LGS was simulated by projecting the light from the LGS onto each turbulent layer. The illuminated area of a turbulent layer was selected and then the selection was rescaled

to the diameter (in pixels) of the telescope pupil, as is shown in Figure 7.3. Wavefront rescaling was performed using bicubic interpolation. Wavefronts at any points across the science field could also be created by slicing vertically through the atmosphere. Global tip and tilt were subtracted from the wavefront to simulate the effect of using a separate NGS as a tip/tilt reference source. Wavefront piston terms were also ignored. The model then calculated the variance between the WFS wavefront and science wavefront. This process was repeated for several hundred randomly generated atmospheres with the same C_n^2 profile to determine mean WFS performance. The LGS WFS model was far simpler, and therefore less computationally intensive, than the full numerical simulation AO model, allowing rapid analysis of a given WFS geometry. The performance predicted by this model is obviously an optimistic measure of WFS performance as many sources of AO system error are ignored.

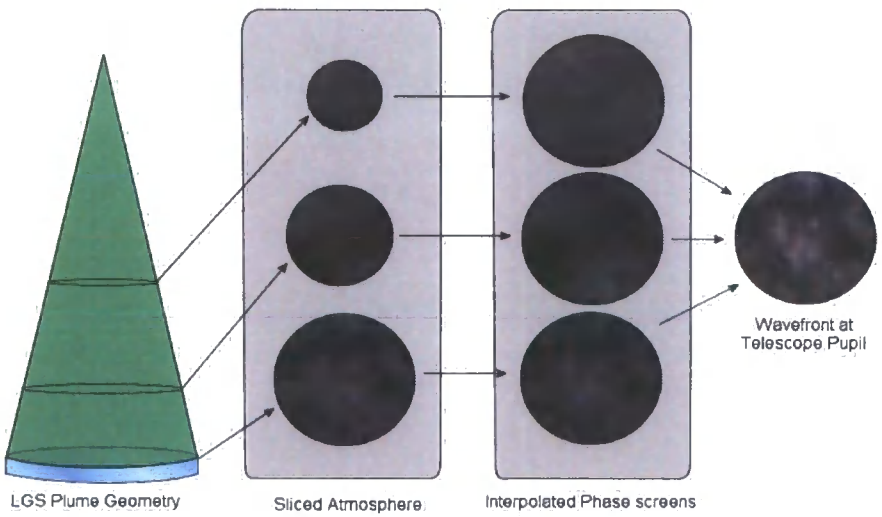

Figure 7.3 WFS model method of operation. The plume is modelled geometrically and the diameter of the plume determined at each turbulent layer. A section of the phase screen is sampled and then scaled by pixel interpolation to the same diameter in pixels as the telescope pupil. The interpolated phase screens are then summed (after removing piston terms) to create wavefront that the telescope would observe. Science paths are determined using the same method but require no interpolation as the slices are always the same diameter as the telescope pupil.

7.4 Results

The choice of analysis metric is dependent on the AO system application. As was shown by Ellerbroek et al [6], performance metrics (the specific case of slit coupling versus Strehl ratio was examined in the given reference) can be insensitive to different levels of AO correction, demonstrating that the choice of performance metric can affect the system optimisation. The system Strehl ratio was the preferred performance metric for system analysis/error budgeting, allowing simple experimental verification of AO performance, and could be compared with the equations presented in Chapter 1 and 2 detailing error sources in terms of residual wavefront variances. However, due to the partial wavefront correction achieved by a GLAO system, the Strehl ratios achieved were very low and not indicative of the GLAO system performance as a method of improving astronomical performance. The FWHM of the AO-corrected image was therefore used to describe and optimise performance in the numerical simulation, although this metric is not directly comparable with the methods presented in Chapters 1 and 2.

The wavefront variance, which is related to the Strehl ratio by the Maréchal approximation for small wavefront variances, was used as a metric for the LGS WFS analyses in sections 7.4.1 and 7.4.3. This was primarily because it allowed rapid and simple analysis of the LGS WFS performance without having to form an image of the AO-corrected PSF.

7.4.1 GLAO with a low-altitude LGS

Simulations of the performance demonstrator GLAO system on the WHT were made to determine the optimum altitude to which the low-altitude LGS should be projected. The distance between telescope pupil and LGS was increased from 2m to 10km in 1km steps to determine the optimum altitude for a low-level GLAO LGS. The optimum altitude is defined as the altitude that gives the lowest overall wavefront variance across the instrument FOV. The science field of view of the demonstrator system was approximately 80".

From Figure 7.4 it is clear that when using a 3-layer La Palma atmosphere with an instrument that has a field of view of 80", the best performance is achieved by minimising the wavefront error due to focal anisoplanatism and using a sodium LGS. However, the variance between LGS and science wavefronts increases rapidly as angular anisoplanatism is increased. For comparison, the average tilt-removed wavefront variance of the science path, before the LGS wavefront was subtracted was $28rad^2$. The results presented below are all modelled at a wavelength of 500nm with an r_0 of 0.11m. This corresponds to a 'bad-seeing' case on La Palma.

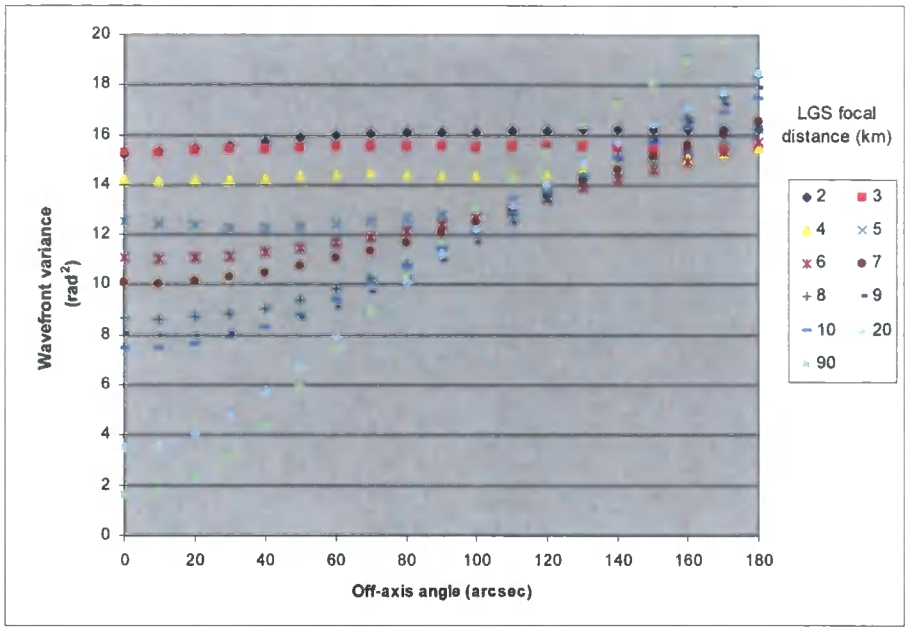

Figure 7.4 Performance of several low-altitude LGSs on the WHT using the standard La Palma 3-layer atmosphere. Field angles up to 180" from the LGS position are plotted. A 20km ('conventional' Rayleigh) and 90km (sodium) LGS are shown for comparative purposes. Uncorrected wavefront variance was 28 rad^2.

This performance is highly dependent on the input turbulence profile. The middle layer at 2.5km was dropped to 1km to examine this effect. A change of this magnitude is one that could be observed over the course of a night. Figure 7.5 shows that, as one would expect, the overall performance increases as the mid-altitude layer is moved from 2.5km to 1km.

An 2' FOV is obviously too small to make full use of the potential of GLAO with the turbulence profiles used to create the plots in Figure 7.4 and Figure 7.5. A field-averaged wavefront variance could be used to determine optimum LGS altitude for maximising performance across a given field. The field averaged wavefront across a 6' FOV is plotted for both test atmospheres in Figure 7.6.

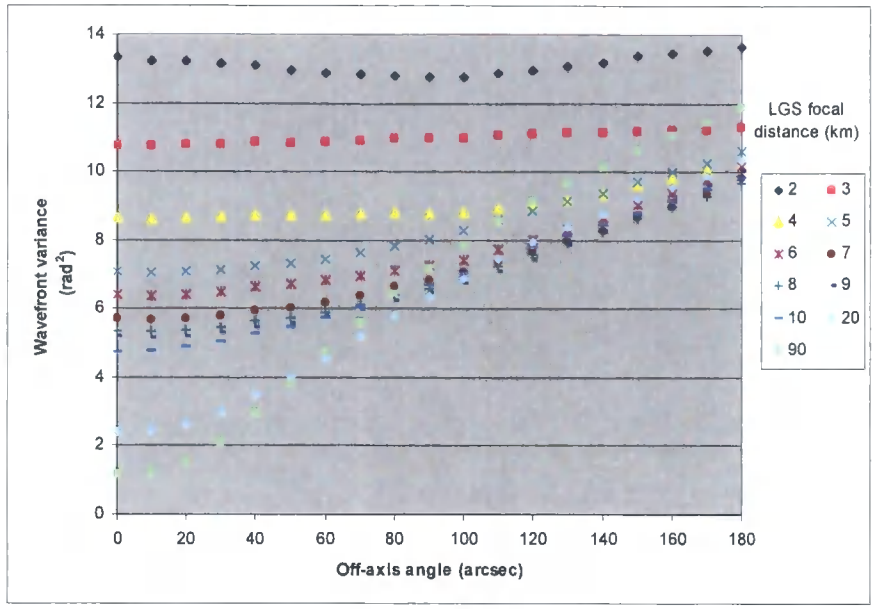

Figure 7.5 Performance of several low-altitude LGSs on the WHT using a 3-layer atmosphere with 40% of the turbulence at the ground layer, 40% at 1km, and 20% at 7.5km. Field angles up to 180" from the LGS position are plotted. A 20km ('conventional' Rayleigh) and 90km (sodium) LGS are shown for comparative purposes. Uncorrected wavefront variance was 28 rad^2.

The optimum altitude depends on the degree of PSF uniformity that is required and the FOV it is to be corrected over. In the specific case of the demonstrator system with an 80" FOV, the optimum altitude is defined by the return photon flux, as an increase in altitude will always improve performance. However, with a 4km LGS, very little change in PSF should be observed across the 80" field. From Figure 7.6 it can be seen that a 4km-distant LGS will not perform as well as a more distant LGS.

The metric for examining field uniformity was defined as the standard deviation of the wavefront variance across the field of interest, described by

$$\sigma_{\text{var}} = \sqrt{\frac{1}{(n-1)}\sum_{\theta=0}^{n}\left(\sigma_\theta^2 - \overline{\sigma^2}\right)} \qquad \text{- 7.1}$$

where σ_{var} is the PSF uniformity metric, n is the number of field sampling points, and σ_θ^2 is the wavefront variance between the LGS wavefront and the NGS wavefront that

is sampled at a field angle of θ arcseconds. Figure 7.7 shows that for an LGS created at an altitude above 4km, the field uniformity drops rapidly, irrespective of changes in the altitude of the middle turbulent layer. The LGS altitude should therefore not be increased above 4km because, although this will improve on-axis performance, off-axis performance will begin to degrade rapidly beyond an off-axis angle of 90".

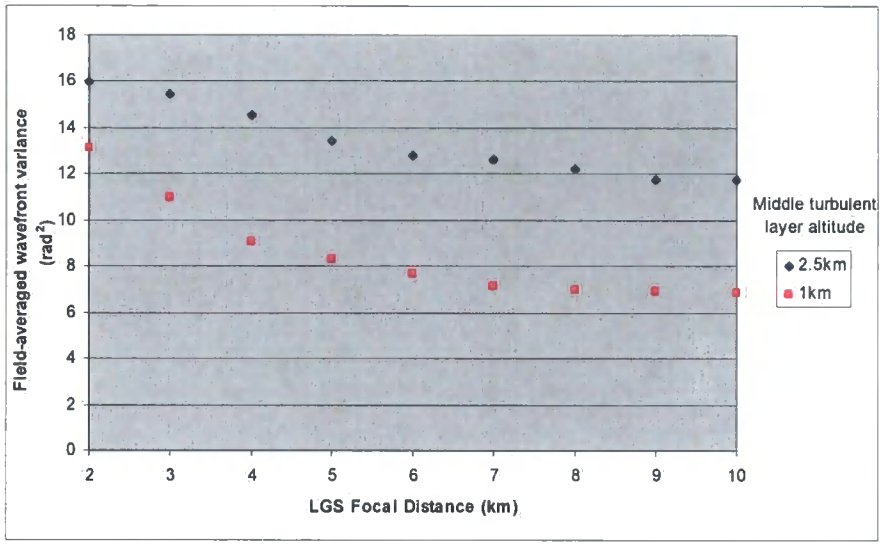

Figure 7.6 Field-averaged wavefront variance over a 6' FOV for two 3 layer atmospheres. 40% of the turbulence is at the ground layer, 20% at 7.5km. The two plots show the effect of changing the middle layer from an altitude of 2.5km to 1km.

For the maximum 40" off-axis field (80" FOV) which the experimental system will allow without vignetting, the PSF will be fairly uniform across the field irrespective of Rayleigh LGS altitude as is shown in Figure 7.8. Optimum PSF uniformity across the 80" field will be observed if the LGS is projected to 4km. At distances less than 4km, PSF uniformity across this field actually decreases.

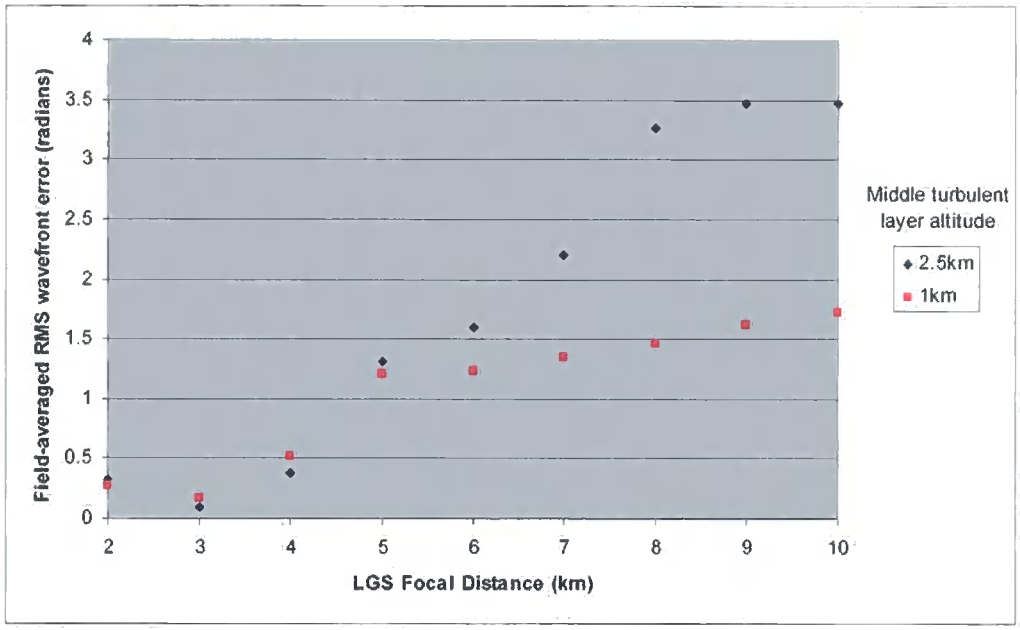

Figure 7.7 Model results showing a plot of field uniformity across a 180" field for low-altitude LGS observed using a 4.2m telescope. Smaller values signify a more uniform PSF across the field. The two plots show the effect of changing the middle layer from an altitude of 2.5km to 1km.

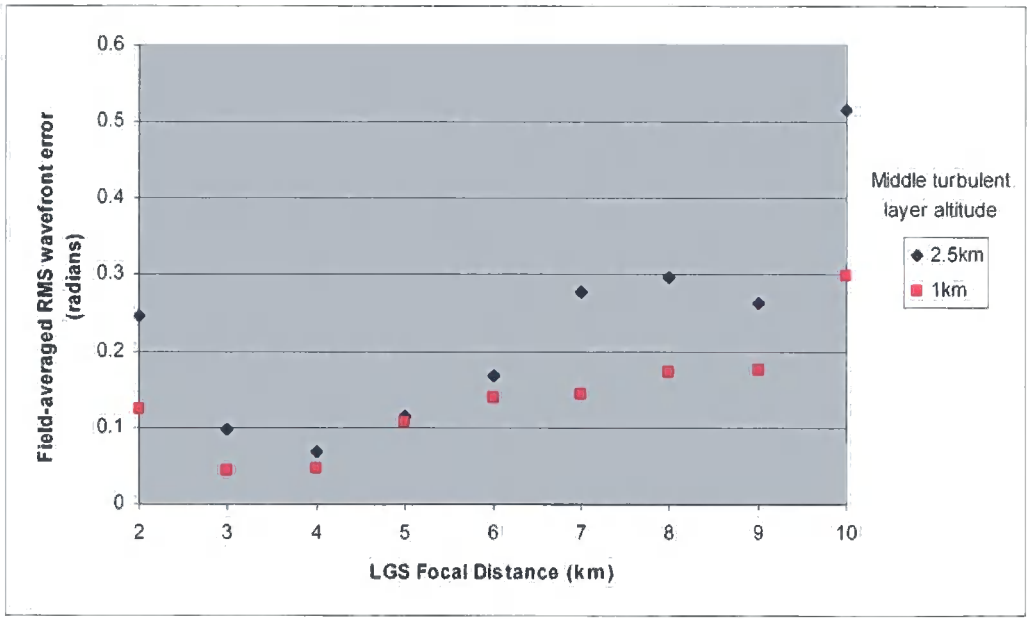

Figure 7.8 Model results showing a plot of field uniformity across a 40" field for low-altitude LGS observed with a 4.2m telescope. Smaller values signify a more uniform PSF across the field. The two plots show the effect of changing the middle layer from an altitude of 2.5km to 1km.

An indication of the potential of low-altitude LGSs to provide GLAO correction is when performance is studied over a wider field than 2'. As can be seen from Figure 7.4, although the 90km (sodium) and 20km (high-altitude Rayleigh) LGS perform well over a narrow field, for field-angles greater than approximately 2', a 8-10km altitude LGS on La Palma would provide a better degree of correction. The performance of a low-altitude LGS below 5km can provide extremely uniform correction across wide fields, up to the 6' modelled here.

7.4.2 GLAO System Performance

The closed loop performance of the experimental GLAO system was modelled using the full numerical simulation. The simulation parameters are given in Table 7.1 and were used unless stated otherwise. LGS WFS flux was calculated using the model described in Chapter 5 using the optimal LGS altitude of 4km and a range gate depth of 69m.

Two simulations runs were undertaken to examine the performance of the low altitude LGS under more realistic conditions. Test runs were made to determine the number of SVD modes to use in the control matrix and examine loop stability with the standard La Palma atmospheric turbulence profile. The outcome of the tests showed that the photon flux within partially illuminated subapertures, even at the optimised values determined in Chapter 5, resulted in closed loop instability. It was observed that the subapertures at the edge of the telescope pupil could not be tracked by the centroiding algorithm due to the smaller collecting area of these partially illuminated subapertures and the greater spot elongation causing lower SNR. Although the analysis presented in Chapter 5 suggested that this WFS should work, the effect of atmospheric

turbulence coupled with the elongation reduced the SNR to a point where centroiding became inaccurate.

Variable	Value						Description
Simulation Params							
	LGS	NGS	1	2	3	Uncorrected	
source_lam	523	600	1250	1250	1250	1250	Source wavelength (nm)
source_alt	4000	∞	∞	∞	∞	∞	Source Altitude (m)
source_theta	0	0	0	40	120	0	Source off-axis angle (arcsec)
gate_depth	69						LGS Range gate depth (m)
sim_duration	60						Simulation run time/Integration time (sec)
tstep	0.005						Simulation time step (sec)
Telescope							
npup	80						Pupil array size (pixel)
tel_diam	4.2						Tel aperture diam (m)
tel_sec	1.2						Tel secondary diam (m)
Atmosphere							
n_layers	3						Number of phase screen layers in model
nscrn	1024						Phase screen size (pixels)
r0	0.14						r_0 (m @ 500nm)
l0	30						Outer scale (m)
			1	2	3		
str_layer			0.4	0.4	0.2		Layer relative strengths
v_wind			6.6	8.8	12.4		Layer wind velocity (m/s)
theta_wind			45	0	-80		Layer wind direction (degrees)
altitude			0	1000	7500		Layer altitude (m)
NGS Tilt Sensor							
tilt_nfft	8						Number of pixels in FFT
tilt_nimg	8						Number of pixels in tilt sensor
tilt_int	0.01						Tilt Sensor Exposure Time (secs)
tilt_mag	1						NGS Reference source magnitude
tilt_thruput	0.22						Throughput to tilt sensor
tilt_read	8						Tilt sensor read noise (e-)
tilt_ncen	6						Centroid box size (pixels)
tilt_gain	0.5						FSM Closed loop gain
LGS WFS							
wfs_nsubx	10						LGS WFS SH array size (pixels)
wfs_fov	2.11						Subaperture FOV (arcsec)
wfs_n	8						Subaperture size (pixels)
wfs_minarea	0.6						Min unvignetted subaperture area to use
wfs_int	0.005						LGS WFS Exposure Time (secs)
wfs_read	6						WFS Read noise (e-)
wfs_lat	0.005						LGS Loop latency (secs)
Reconstructor							
pokeamp	3						Amplitude of DM influence function (radians)
gamma_loop	0.8						LGS Closed loop gain
n_modes_corrected	91						Number of SVD Modes used

Table 7.1 Model AO system parameters used for simulation runs.

Once one subaperture has become unstable, the poor correction spreads to adjacent subapertures due to the continuous phase sheet of the DM. This instability was apparent irrespective of the number of modes of the SVD used. To increase the photon flux to the WFS without changing the 4km altitude of the LGS, the frame rate

of the WFS was reduced from 300Hz to 200Hz. The lower SNR of the most elongated spots can be observed in the image of the WFS taken whilst running closed loop shown in Figure 7.9.

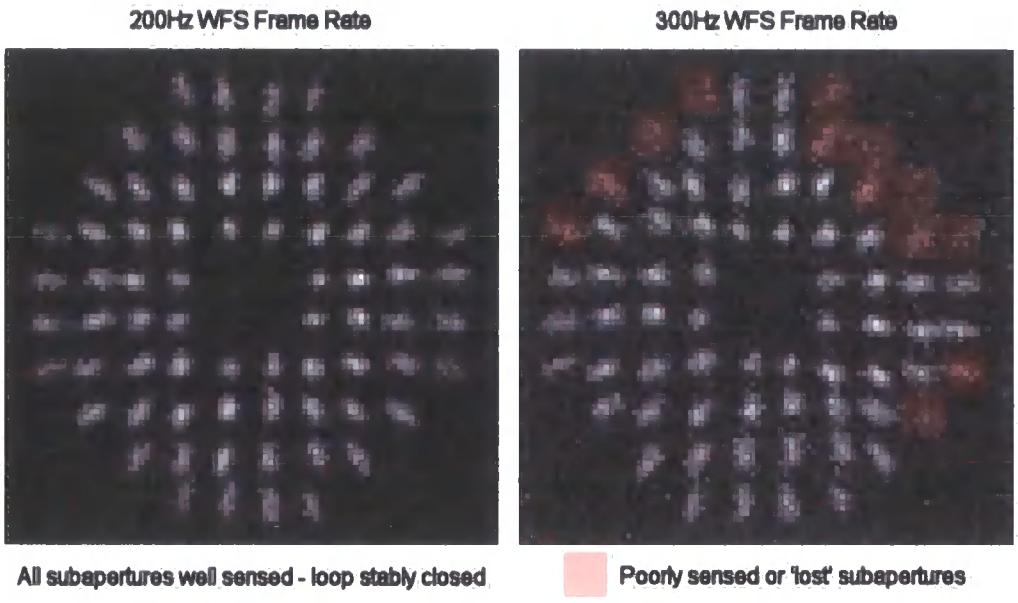

Figure 7.9 WFS image taken from the closed loop simulation, demonstrating stability of AO loop with increased WFS SNR. The 200Hz WFS runs stably and all spots are well defined and within an 8x8 pixel subaperture. Several subapertures around the edge of the telescope pupil (marked in red) on the 300Hz WFS have been 'lost', or are poorly defined, due to an incorrect mirror figure on the DM.

The effect of cancelling singular value decomposition modes in the control matrix performance was studied and the results shown in Figure 7.10. Optimum performance of the AO system both on-axis and at a field angle of 40" was found when the loop was closed with all but 2 modes cancelled.

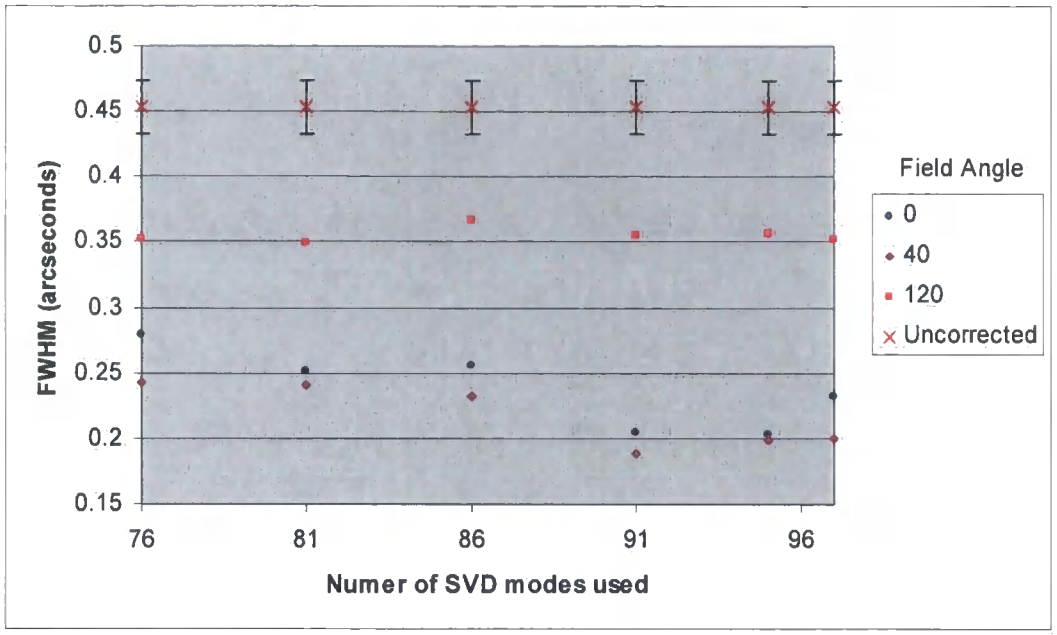

Figure 7.10 Effect of cancelling SVD modes in the control matrix on AO system performance in terms of corrected image FWHM at a closed loop gain of 0.2

The closed-loop gain was then increased until the loop became unstable. Although the loop was able to close with a gain of 1, increasing the gain beyond this point resulted in a bistable WFS pattern as the wavefront became over-corrected. Increasing WFS read noise also reduced the stable closed-loop gain, although this effect was not quantified. The results of these simulations are shown in Figure 7.11. The optimum gain was determined as 0.6. It must be mentioned that running the real system closed loop with a gain of 0.6 had not been achieved in the laboratory closed loop tests. The maximum stable gain had been between 0.1 and 0.2. The difference between the theoretical optimum gain and real maximum gain highlights the inherent problems of using an idealised system to describe a real-life system.

With the optimum closed loop parameters determined by following a similar method to that which would be used on-sky, the performance of the AO system was analysed. The simulation results showing the effect on FWHM of decreasing the mid-altitude layer from 2.5km to 1km are shown in Figure 7.12.

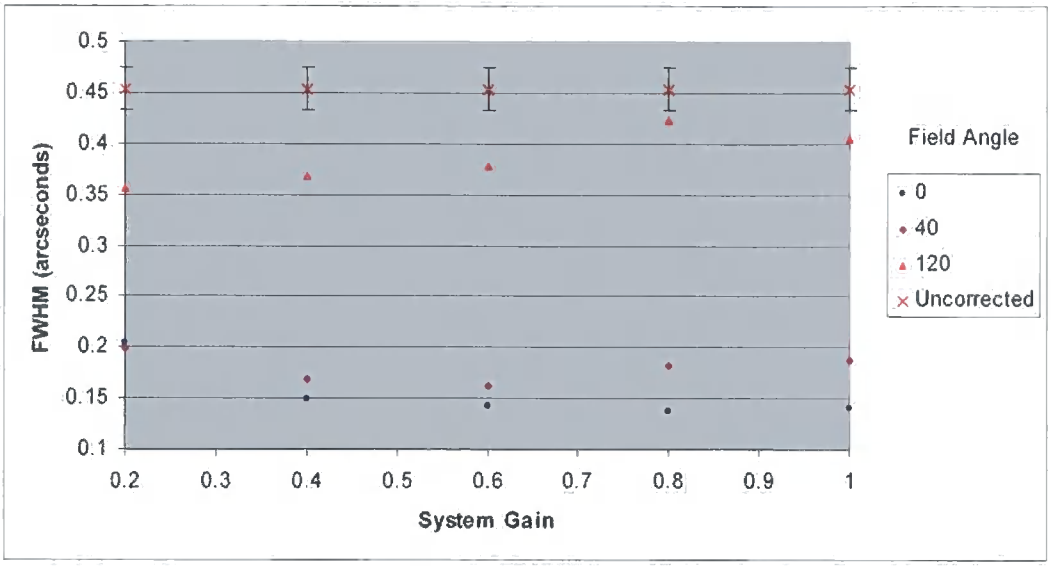

Figure 7.11 Effect of increasing closed loop gain on AO system performance in terms of corrected image FWHM with 95 SVD modes used in the control matrix

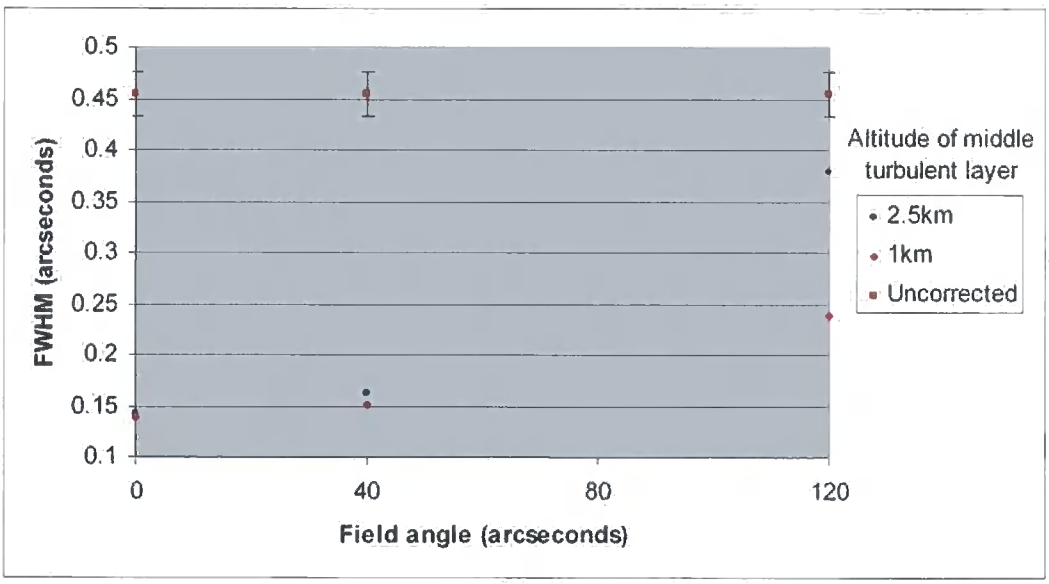

Figure 7.12 Plot of AO-corrected FWHM versus field angle for standard 3-layer La Palma atmosphere and 3-layer atmosphere with middle layer placed at 1km at a wavelength of 1250nm. Error bars on uncorrected FWHM indicate 1σ point returned from all simulations.

As predicted by the analysis presented in section 7.4.1, the FWHM of an image corrected by a 4km distant LGS remained relatively constant at field angles up to 40", but dropped when a wide field of 120" was examined. One point to note is that performance apparently improved as one increased the field angle between LGS and

science path for the initial case of placing the mid-altitude layer at 2.5km. This however was within the statistical accuracy of the simulation as indicated by the $\pm 1\sigma$ error bars plotted on the uncorrected FWHM. The effect of dropping the mid-altitude layer to 1km from 2.5km showed an overall improvement in performance. However the uniformity of correction decreased as the sampling of mid-altitude layer increased.

The effects on system performance of changing the vertical distribution of turbulence without changing the overall strength of the turbulence highlight the need for an accurate C_n^2 profiles if a real-life AO system is to be compared with a simulated version of itself. While r_0 can be determined from WFS data, off-axis performance is wholly dependent on the vertical structure of turbulence, and no comparison is valid unless the same distribution of turbulence is used for the simulation as was encountered by the AO system while on-sky.

The effect of changing atmospheric conditions on system performance was further studied by changing the value of r_0, Fried's parameter.

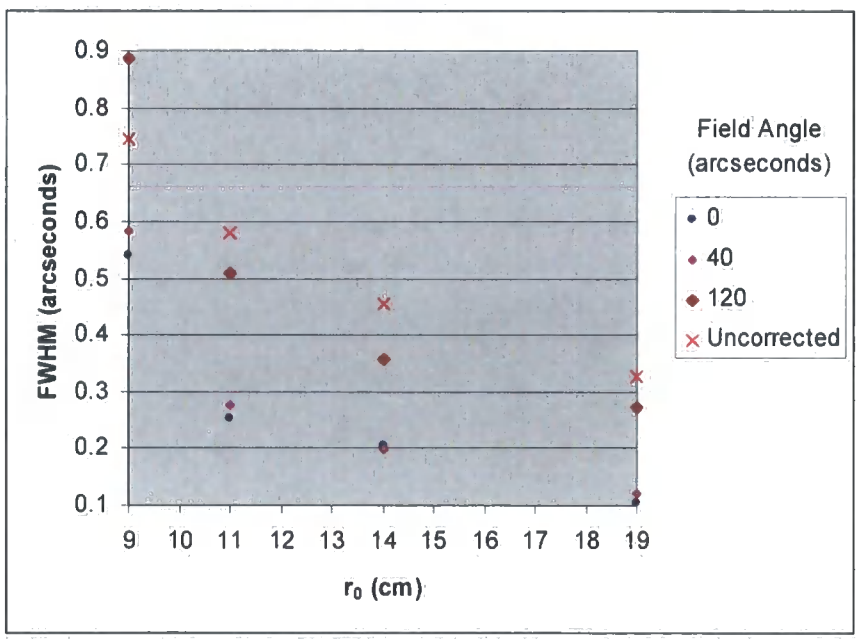

Figure 7.13 Effect of changing r_0 on AO system performance.

As expected, increasing the strength of the turbulence increases corrected FWHM at all field angles. The system remained stable down to an r_0 of 0.11m, confirming that AO correction should be achieved under all but the worst atmospheric conditions at the WHT. An r_0 of 0.11m corresponds to the 75th percentile seeing value at the WHT. The loop was closed on an atmosphere with an r_0 of 0.09m, but did not remain stable for the duration of the 60 seconds of simulated time. The on-axis correction observed here was as a result of the period of time that the wavefront remained stable. Sample PSFs from across the field are shown in Figure 7.14. Although the FWHM of the PSF remains relatively constant out to an off-axis angle of 40", elongation of the PSF in the direction of the LGS and NGS can be observed. This is primarily due to angular anisoplanatism caused by the on-axis NGS reference source.

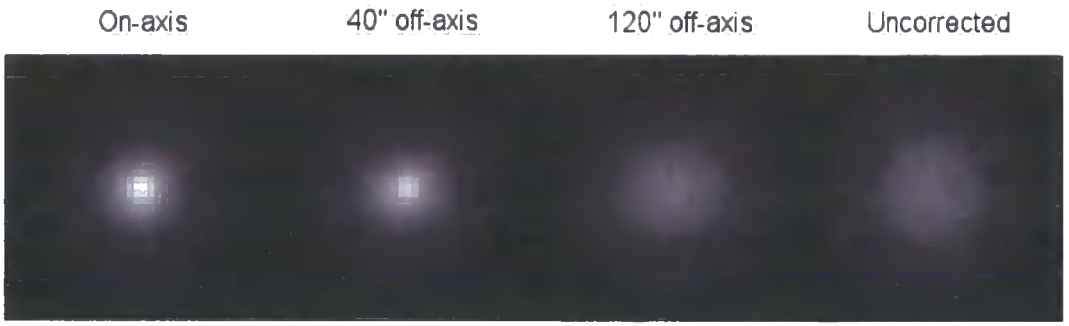

Figure 7.14 Sample PSFs taken from points in the field offset from the LGS and NGS by 0", 40" and 120" at a wavelength of 1250nm. Atmospheric r_0 is 0.14m. The uncorrected PSF is also shown. The square root of the intensity has been plotted to show fine structure in halo of the PSF. Intensities are to scale. Pixel scale is 0.031arcsceonds/pixel.

The effect of system latency on AO performance was examined. The base system latency depends on the exact algorithms used in the control system, but was set to a high-range value of 5ms for these simulations. This value is comparable with the closed-loop latency of NAOMI (3ms), which uses the same CCD and similar control architecture. The value of 5ms was used to reduce the simulation run time as this corresponded to 1 iteration of the simulation at a WFS frame rate of 200Hz. The

latency was increased from 0 to 20ms and the results of the simulations are shown in Figure 7.15.

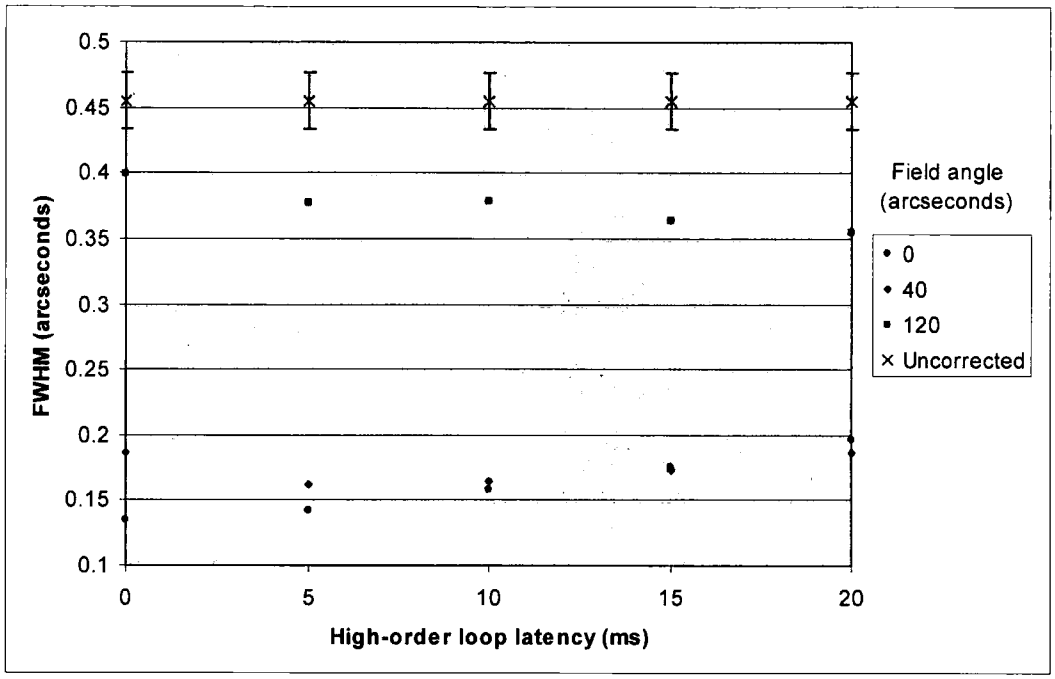

Figure 7.15 Effect of increasing system latency on AO system performance.

The apparent improvement of off-axis performance with increasing latency that is shown by Figure 7.15 is due to the effect of the velocity of the turbulent layer and the field sampling point. For equal correction of the PSF at any rotational angle around the field, the latency of the control system must be zero. This effect could be measured in an AO system to determine the velocity and altitude of the most turbulent layer if the system latency is known.

7.4.3 GLAO with a Rotating LGS

The rotating LGS introduced in Chapter 2 as a technique that would measure a GLAO wavefront was modelled using the LGS WFS code. To simulate the effect of the

rotating LGS, the model calculated the number of laser pulses per WFS frame. This was rounded to the nearest integer value which in the case of a 5kHz laser and 300Hz WFS, was 17 pulses per frame. The rotational angle of each pulse was then defined as $2\pi/17$. The sliced wavefront for each pulse was determined and then summed to create the rotating LSG wavefront. The resulting summed phase was divided by the number of pulses in the frame for scaling to the science wavefront. The rotating LGS wavefront was then subtracted from the wavefront from science paths out to 60" arcseconds off-axis, and the residual wavefront variance measured. This process was repeated for 1000 separate atmospheres to ensure a good statistical sample. The diameter of the circle traced out on the sky by the LGS rotation was increased from 0" to 120". The atmosphere used was the standard 3-layer La Palma atmosphere. The LGS was created at a distance of 20km from the 4.2m WHT telescope primary.

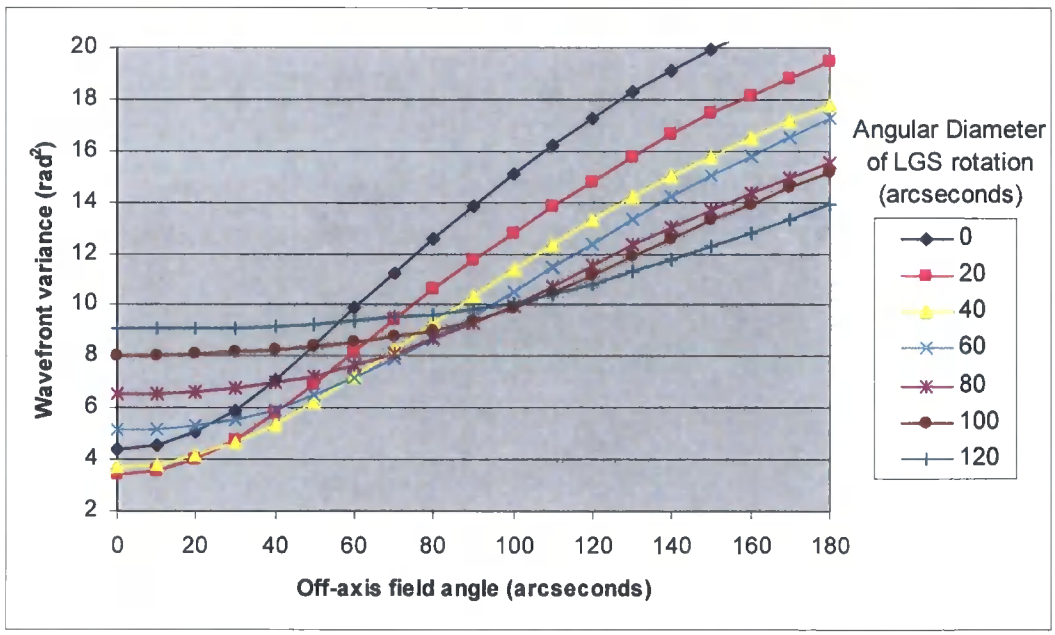

Figure 7.16 Performance of a rotating LGS created at a distance of 20km from a 4.2m telescope pupil. The diameter of the circle traced out on the sky by the rotating LGS was increased from 0", corresponding to a conventional LGS, to 100" in 20" steps. The rotating LGS wavefront was subtracted from the wavefront from several field angles up to 180" away from the centre of rotation of the LGS.

As can be seen from Figure 7.16, the off-axis performance increase introduced by rotating the LGS is substantial. One interesting point to note is that once the LGS is rotated, on-axis performance improves. This is thought to be due to anti-correlation between the highest layer of turbulence at 7.5km and the wavefront coming from the science target at infinity. At the 7.5km layer, the illuminated cone from an LGS at 20km is 62.5% of the telescope pupil diameter. Only tip and tilt across the wavefront will be correlated between the science and LGS wavefronts at this layer. Wavefront tip and tilt are removed in the model, as they would be in reality by using a separate NGS tip/tilt reference source.

The observed on-axis improvement should decrease with increasing LGS altitude as the highest layer is sampled well. The effect of rotation of a sodium LGS at 90km distance was also modelled and the results are shown in Figure 7.17.

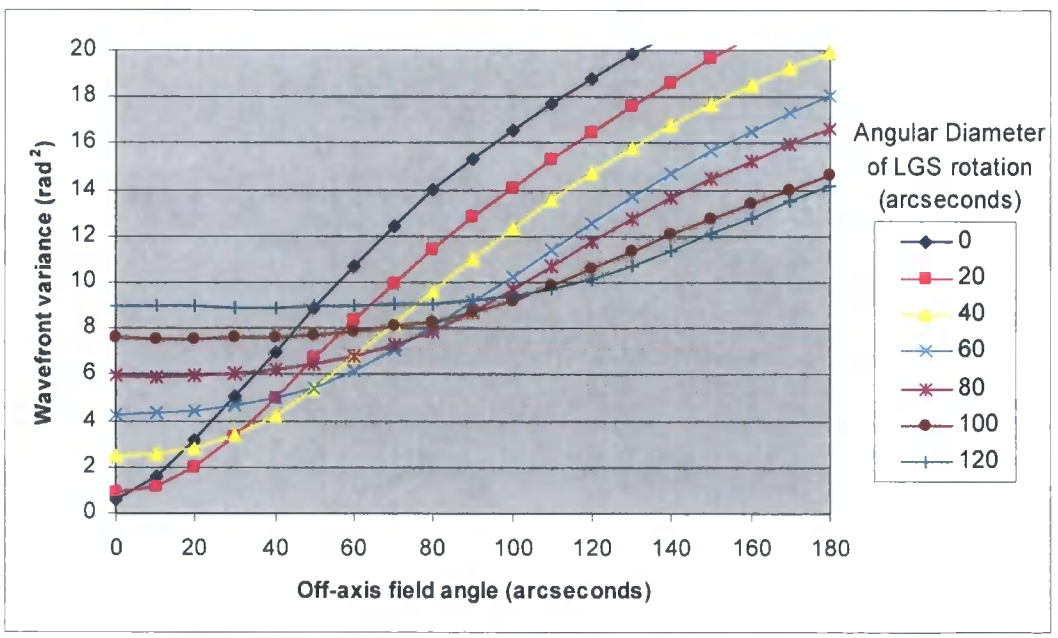

Figure 7.17 Performance of a rotating sodium LGS at 90km up field angles of 180' (i.e. a 6' FOV). Diameter of the circle traced by the rotation of LGS has been increased from 0" to 120".

The on-axis performance increase seen by rotating the 20km LGS is not observed when the LGS distance is increased to 90km. This shows that there is a good correlation between NGS and LGS wavefronts at the highest turbulent layer in the atmosphere for a sodium LGS. A comparison of the performance of a rotating LGS at 20km and 90km is shown in Figure 7.18. The off-axis improvement achieved by the rotating the LGS is comparable for both a 20km and 90km LGS. Once a rotational diameter of 120" is achieved, the performance of the 90km LGS across the field is particularly uniform out to a field angle of 90", showing that wide-field correction can be achieved using a single rotating sodium LGS at a distance of 90km.

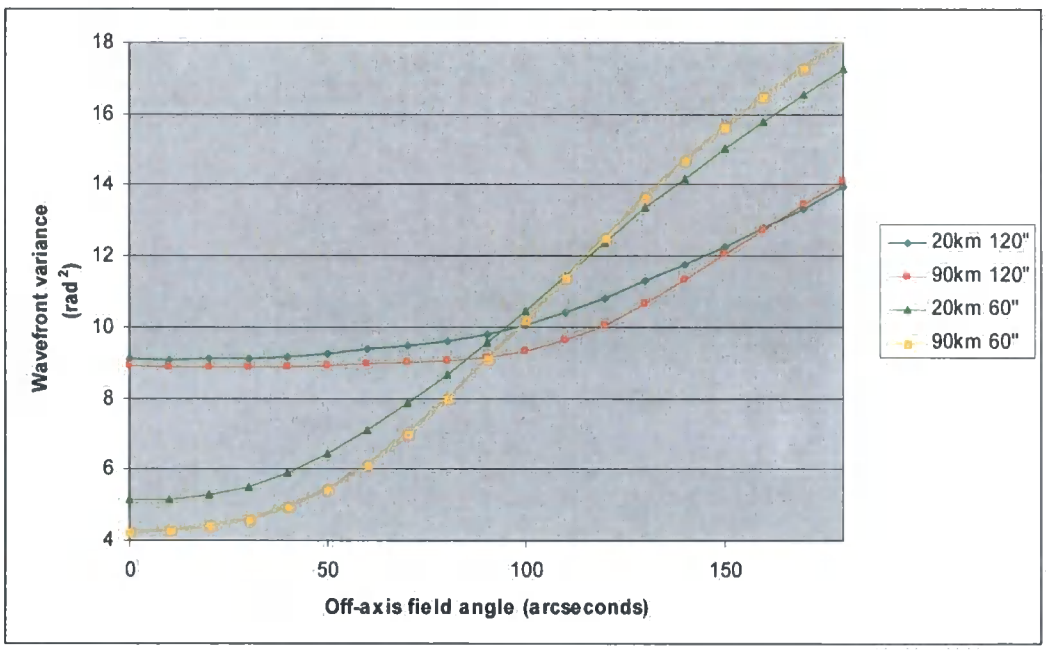

Figure 7.18 Performance of rotating sodium LGS at a distance of 90km (orange lines) compared to a rotating Rayleigh LGS at 20km (green lines). The performance of rotating LGSs with angular diameters of 60" and 120" are comparable in terms of PSF uniformity across the field and overall degree of correction.

Figure 7.19 compares the performance of a low-altitude LGS method for creating a GLAO wavefront to a rotating LGS at 20km using four example systems. The example systems were chosen to have a similar PSF uniformity across a 4' FOV. A rotating LGS can provide a uniform PSF across a field that shows as much variation

as the correction provided by low-altitude LGS, as is shown by the similar curvature of the two blue lines and the two red lines in Figure 7.19. This demonstrates the viability of rotating LGSs as a tool for wide-field imaging. The rotating LGS however has a far lower wavefront variance, implying that better correction would be observed if the technique were employed instead of a low-altitude LGS.

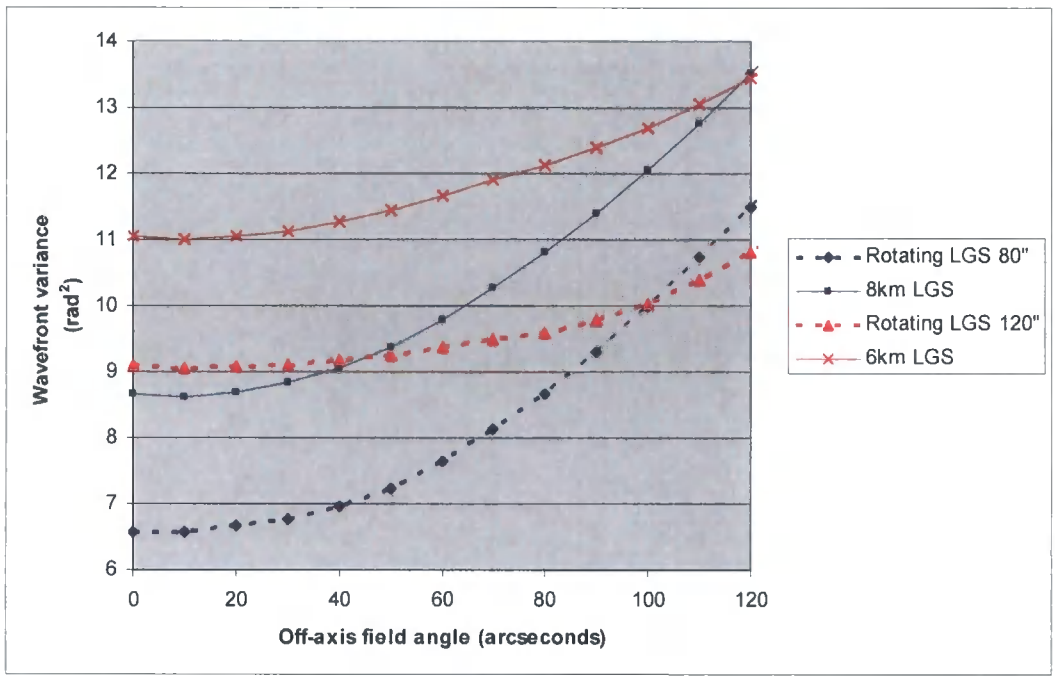

Figure 7.19 Comparison of low-altitude LGS performance to rotating LGS performance over a 4' FOV. Solid lines show the performance of the low-altitude LGS system. Dashed lines show the performance of a rotating LGS system. The two blue lines compare low-altitude and rotating LGS systems that have a lower PSF uniformity across the field. Red lines compare low-altitude and rotating LGS systems that have poor on-axis performance, but better PSF uniformity across the field.

7.5 Conclusions

The optimum altitude at which to project a low-altitude LGS, using the standard 3-layer La Palma atmosphere, to minimise PSF variation across fields of view up to 6' in diameter is 4km when observing with the 4.2m WHT. However, the overall

performance will be improved at the expense of PSF uniformity if the distance to the LGS is increased.

Creating a low-altitude Rayleigh LGS is technically less complex than creating a Rayleigh or sodium LGS at high altitude, simply as power requirements on the laser are reduced. This makes the system far cheaper to build, and as such, maybe a comparison between the two techniques is unfair. However, rotating a 20km or 90km LGS will provide better off-axis performance, albeit at the cost of reducing on-axis performance in the case of a sodium LGS. Corrected fields of up to 3' in diameter will exhibit a uniform PSF if the LGS traces a circular path with an angular diameter of 2' for both 20km Rayleigh and 90km sodium LGS.

On-axis performance of a Rayleigh LGS will be improved by rotating the LGS as poorly sampled higher layers are averaged and only global tip and tilt (which is removed through referencing to an NGS and therefore ignored by the LGS WFS) will be observed. This feature depends upon high layer turbulence being at an altitude where the diameter of the actual area sampled by the cone from the finite altitude LGS is a small fraction of the full diameter of the telescope pupil. Further work modelling the effect of the rotating LGS on WFS performance, and not just through the comparison of rotating LGS and science wavefronts, is required to fully explore this concept.

The full AO system simulation analysis presented in section 7.4.2 showed the theoretical on-sky performance of the experimental GLAO system. A comparison between the closed-loop gains at which the theoretical and laboratory systems could provide stable correction confirmed that the simulation is more stable than in reality, and that other differences between the simulation and reality could well exist. The simulation can be said to describe optimum system performance, but the validity of

this statement cannot be tested without comparison of theoretical to actual results under identical atmospheric conditions.

7.6 References

1. Ellerbroek, B.L., '*First-order performance evaluation of adaptive-optics systems for atmospheric-turbulence compensation in extended-field-of-view astronomical telescopes*', J. Opt. Sci. Am. A **11**, pp.783-805 (1994)
2. J. Vernin and C. Muñoz-Tuñón, '*Optical seeing at the La Palma observatory*', A&A 284 311-318 (1994)
3. Yura, H.T. and Tavis, M.T, '*Centroid anisoplanatism*', J. Opt. Sci. Am. A **2**, p765-773 (1985)
4. Lawrence, G.N., '*Optical Modeling*', Applied Optics and Optical Engineering, Volume **11**, R. R. Shannon and J. C. Wyant, eds., Academic, New York (1992).
5. Goodman, J.W., '*Introduction to Fourier Optics*', McGraw-Hill, New York (1968).
6. Tyler, D.W., Ellerbroek, B.L., '*Spectrometer slit-power-coupling calculations for natural and laser guide-star adaptive optics*', Appl. Opt. **37**, p4569-4576 (1998)

Chapter 8: System Performance

8.1 Introduction

This chapter examines the performance of the AO system during both on-sky and laboratory testing. The laboratory tests are primarily concerned with the stability of the closed-loop control system, while the on-sky tests examine both the feasibility of GLAO correction, as well as the performance of the separate elements of the LLS and AO design. An on-sky demonstration of closed-loop GLAO correction was not possible due to reasons that will be outlined later.

The initial state of the GLAO system on starting the work for this thesis was as a laboratory demonstration NGS AO system. The optical layout is identical to one previously used in an NGS AO demonstrator on the WHT [1], except that the segmented mirror was replaced by the Xinetics DM. In this state, the lab AO system would vignette most light from the LGS and would be unusable on-sky. Therefore a complete redesign of the system was essential, and these modifications were presented in chapter 4. The initial AO design, referred to hereafter as the AO design (as opposed to the GLAO design presented in chapter 4) was in a state such that it should achieve closed-loop turbulence correction, but AO correction had never been achieved. The first task therefore was to examine the control system to attempt stable closed-loop operation. The initial AO system layout is presented in Figure 8.1.

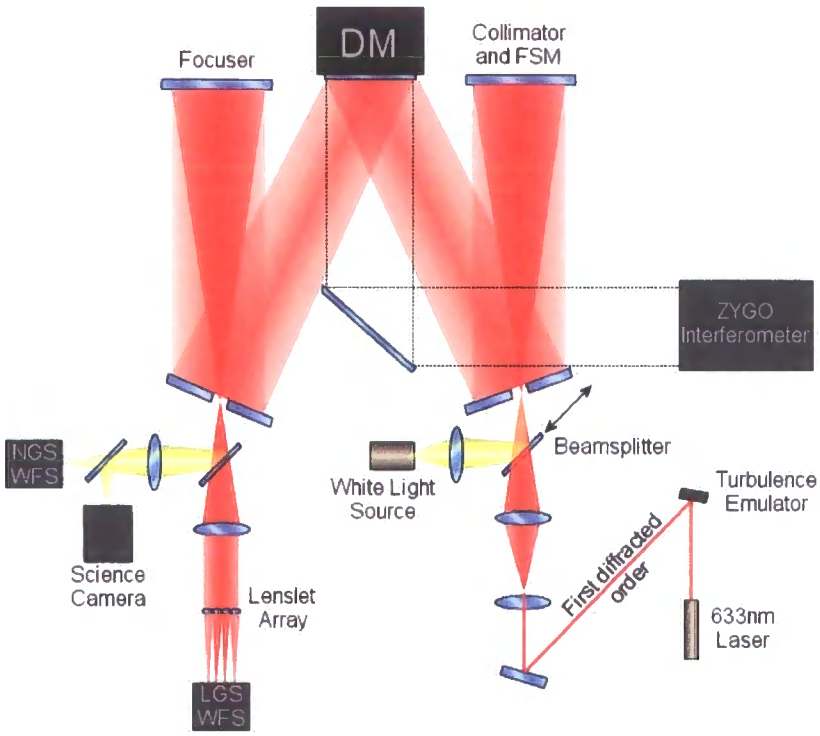

Figure 8.1 Laboratory AO system layout showing turbulence emulator and FSM location

8.2 Laboratory AO system design

Although the AO system design used for laboratory testing shows similarities with the design presented in chapter 6, there are a few important differences that must be highlighted.

8.2.1 Turbulence Emulation

A 256x256 pixel spatial light modulator (SLM) was used in place of the OKOTech DM for turbulence emulation [1]. A distorted phase grating representing the turbulent phase screen was placed on a pixellated binary SLM. Each pixel was capable of

producing a 0 or π phase shift. The SLM was illuminated by a laser and the distorted grating caused a diffraction pattern. The wavefront of the first diffracted order could be controlled in this manner. Using the SLM as a turbulence emulator allowed for repeatable turbulence profiles to be injected into the system, so that changes made to the control system or optical alignment could be examined under identical atmospheric conditions. The SLM was replaced in the final AO system design by the OKOTech DM for various reasons. First, the SLM can only work at a single wavelength of light, therefore diffraction effects are enhanced at the science focus. This can have a large effect on spot optimisation routines, such as simplexing. Secondly, the use of the first order diffraction pattern means that the light source is very dim and difficult to align optically. This meant a secondary laser had to be employed for alignment purposes. Finally, due to hardware limitations, only 128 frames of turbulence could be uploaded to the device at a single time. This gave approximately 1 second of real-time turbulence before looping, although this time was dependent on the turbulence being emulated (faster turbulence requiring faster frame rates). The OKOTech DM suffered no such limitations, allowing polychromatic real-time playback of turbulence, using the same light source that was used for alignment. The response of the OKOTech DM did require calibration before turbulence could be accurately emulated.

8.2.2 Optics

None of the optical components that were required to reconjugate the LGS to the NGS focus, or deal with range-gating of the LGS were used in the original laboratory design as they simply added complexity to the system, and had no effect on the

control system performance. The off-axis toroid and NGS FSM were also not used in the AO system. The first collimating mirror was placed on the LGS FSM stage to test the stability of the control loop with the presence of a secondary wavefront tip-tilt corrector. Aberrations caused by the off-axis use of the first parabolic element were not detected by the WFS.

8.3 DM Characterisation

The Xinetics DM had 97 PMN (lead magnesium niobate) electrostrictive ceramic actuators arrayed on a square grid 7mm apart. The actuators were capable of delivering a 5μm mechanical stroke with a 100V change in applied drive voltage. It is possible that if adjacent actuators are set to 0V and 100V, the bond between the actuator and the deformable phase sheet could break. The maximum interactuator stroke was therefore limited to 1.25μm by zener diodes linking each actuator channel to its neighbours. The zener diodes accomplish this by limiting the maximum voltage difference between neighbours to no more than 26V.

The performance of PMN actuators in terms of range of mechanical stroke, the linearity of actuator response and hysteresis is highly dependent on temperature. At room temperature of 20°C, the hysteresis of the actuators is quoted in literature [3] provided by the manufacturer as 2% from 0V-100V-0V. The response of the actuators is linear between 40V and 90V, giving a midrange value of 65V. The midrange voltage should be applied to all actuators as a starting point before optimisation of the optical performance of the AO system. This way the optimised DM surface after simplexing should be as close as possible to the middle of the linear range of the DM, allowing maximum dynamic range for correction.

The electronics controlling the DM require digital input values between 1 and 4095. This value is passed through a digital-to-analogue converter (DAC) and a high-voltage amplifier (HVA) that scales this value to a voltage between 0 and 100 volts. 4095 gives an output of 0V, while 1 gives an output of 95.8V. There are 4 DAC cards that each controls up to 25 actuators. There is a possibility that the actual voltage across an actuator could then exceed 100V during the very rapid changes that occur in actuator settings during closed loop operation. The actuators themselves are rated to 120V. The midrange value of 65V, measured interferometrically as the centre of the linear range of the DM, corresponds to a DAC value setting of 1400.

The shape of the phase screen was studied using a Zygo PTI phase-shifting interferometer. The Zygo PTI can be used to measure surfaces to very high accuracy that was quoted on delivery as $\lambda/20$; our specific model of Zygo PTI uses a He-Ne laser with a wavelength of 633.9nm, giving a measurement resolution of 31.69nm. The interferometer beam reflects off a flat mirror tilted at 45° to strike the phase screen of the DM face-on as shown in Figure 8.1. Any surface map made of the DM also includes phase changes that are introduced by reflection from the tilted flat. While studying the shape of the DM phase screen, it was noted that setting all DAC values to give HVA outputs other than 0V resulted in large wavefront changes in the peak-to-valley and rms wavefront error values across the DM phase map. The two images in Figure 8.2 show the phase map of the DM surface measured with all actuators set to a DAC value of 4000 and then with each actuator set to 1000. These 2 global DAC values correspond to mean HVA outputs of 2.1 and 75.0 volts respectively. The residual peak-to-valley wavefront error increases by a factor of 2.5 between these two mirror 'flats'.

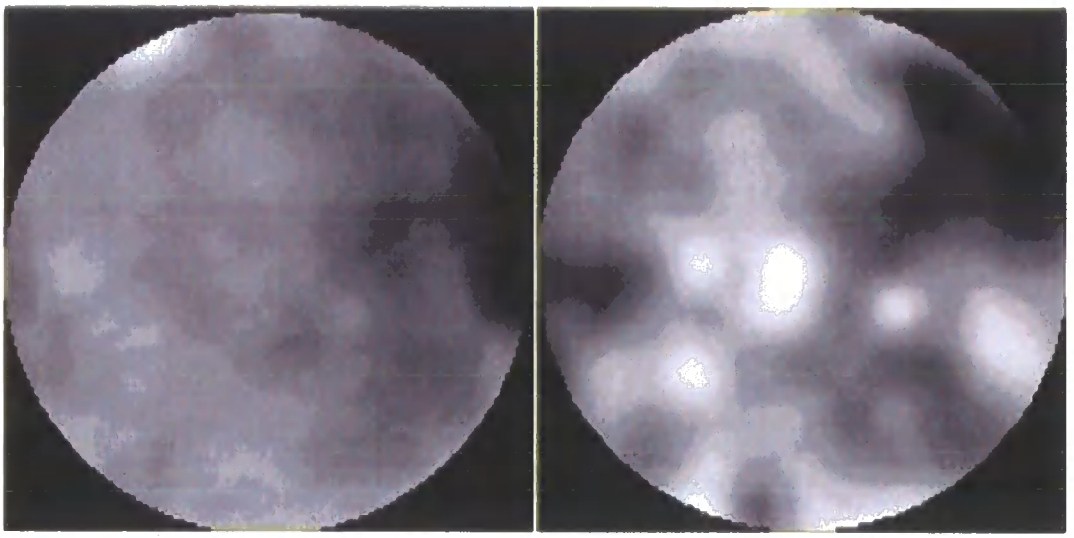

Figure 8.2 Phase screen at actuator average values of 2.1V and 75V respectively showing change in 'flat' mirror shape brought about by non-linearities in the DM and control electronics. P-V wavefront distances are 0.2λ and 0.49λ repsctively.

To determine the source of error, the voltage that was passed across each actuator was measured for a range of DAC values. Figure 8.3 plots the mean HVA output from each DAC card, showing DAC card 2, which controls actuators 26 to 50, consistently output a higher voltage.

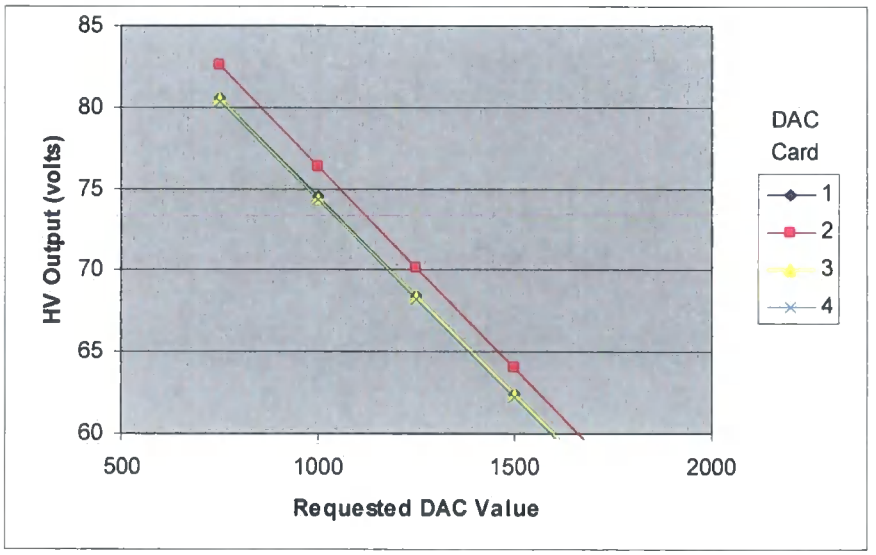

Figure 8.3 Mean requested DAC value and resulting HVA output voltage plotted for each of the four DAC cards.

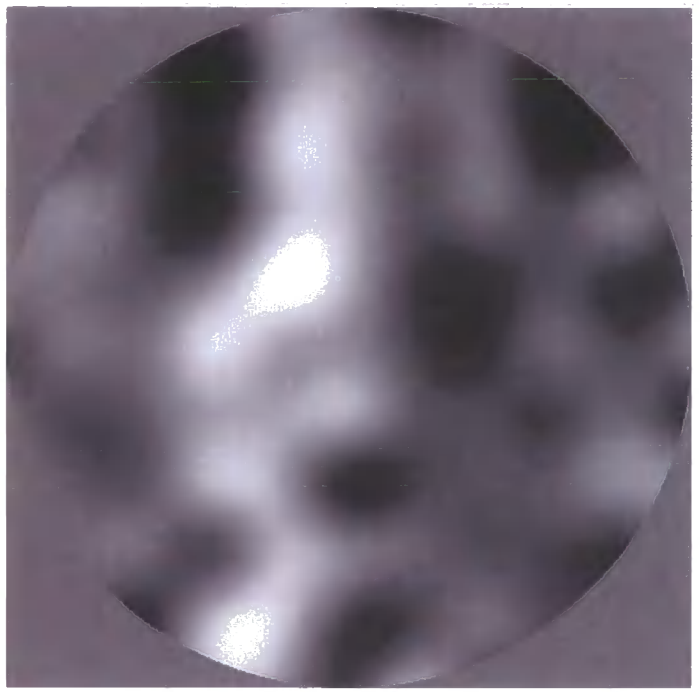

Figure 8.4 HVA output mapped onto DM actuator grid for a requested DAC value of 1000, corresponding to an average HVA output of 74.92V. Image has undergone bicubic interpolation from 11x11 actuators to 500x500 pixels to approximate phase sheet. Before interpolation, RMS Error in voltage was 1.06V, corresponding to an RMS error on the DM phase sheet of 0.08λ at 633nm. Corresponding P-V error is 0.47λ. The actuators controlled by DAC card 2 can clearly be seen as a thick vertical band across the mirror surface

Smaller errors between different channels on the same DAC card were noticed. As each channel has its own dedicated HVA these aberrations are most likely to be caused by differences between components within these. Looking at the HVA outputs at high voltage (DAC value of 750), there are 8 channels that register voltages greater than 2% from the DAC mean value.

Errors in output DAC voltages do not affect closed-loop performance as information on the actuator-to-actuator response of the DM is observed by the WFS and encoded within the system calibration matrix. They can however affect the open-loop performance of the system as known aberrations cannot be placed upon the DM phase surface. An optical calibration of each actuator must be made in order to use the DM, as an example, to inject calibrated turbulence into the WFS.

The effect of the zener diodes on adjacent actuators was also measured. A single actuator was poked from a DAC value of 1 to 2900 (corresponding to a voltage range of 95.8V down to 29.6V) while keeping adjacent actuators set at 1400 (~65V). The graph in Figure 8.5 shows the effect of the zener diodes limiting the voltage between adjacent actuators. It was noted that as the 26V limit was reached, non-diagonal adjacent actuators were also affected by the voltage difference, with their actuator voltages changing by up to 1.2 volts. Actuators that were diagonally adjacent to the poked actuator were not affected by any reverse voltage leak.

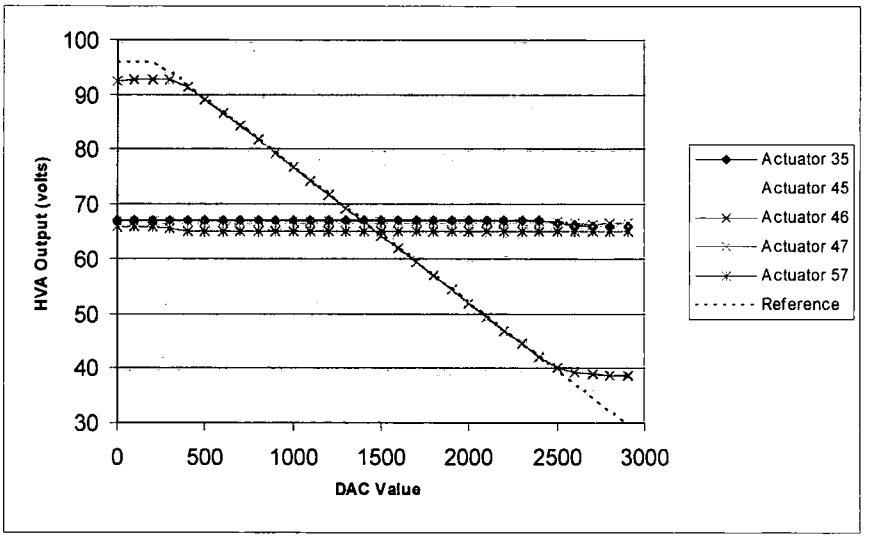

Figure 8.5 Effect of zener diode links between actuators on HVA output voltage limiting inter-actuator voltages to 26V for non-diagonally adjacent actuators. Diagonal actuators (not plotted) are not linked by zener diodes. The reference line was created by increasing all actuators.

The effect of the zener diodes is not encoded within the pokematrix (defined in section 8.5), and can affect the corrective performance. A 1.2V change in output voltage corresponds to a 1.46λ path length increase in a reflected beam at the LGS laser wavelength, which will have a large effect on the observed WFS spot motion, and AO corrected PSF. However, for current leakage through the zener diode link to occur, the difference in voltage between adjacent subapertures must equal 26V. This

corresponds to an optical path length difference greater than than 5λ. Dislocations of this magnitude are possible between adjacent subapertures [4], but only under the poorest seeing conditions. The effect of the zener diode links should be minimal under normal atmospheric conditions.

8.4 WFS Performance

Plane wavefronts with a gradually increasing tilt value were created using the SLM turbulence generator with a 633nm laser. The x- and y-centroid motion of all the WFS spots was then measured and plotted.

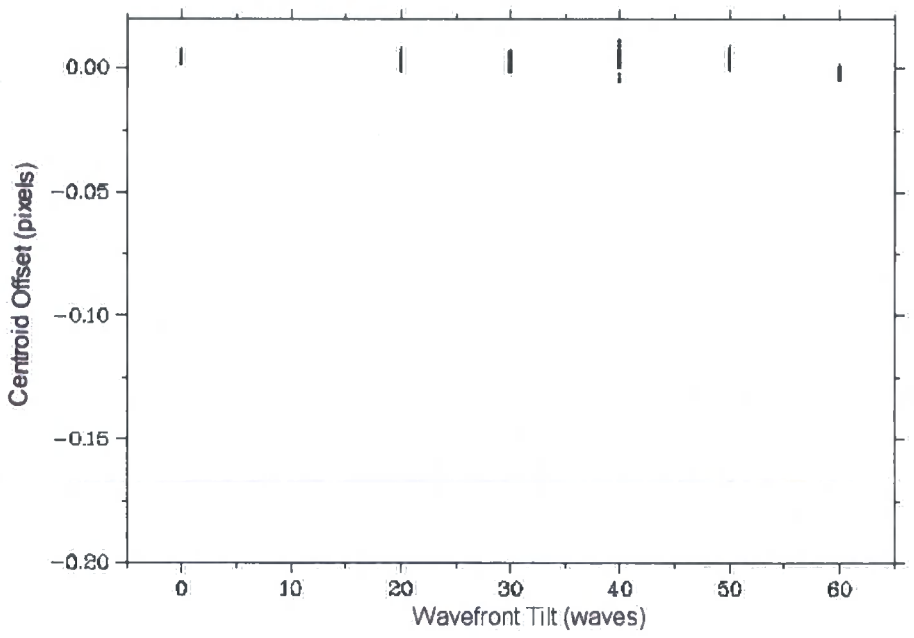

Figure 8.6 Effect of increasing vertical offset (wavefront 'tip') on recorded centroid values in the horizontal (wavefront 'tilt') plane

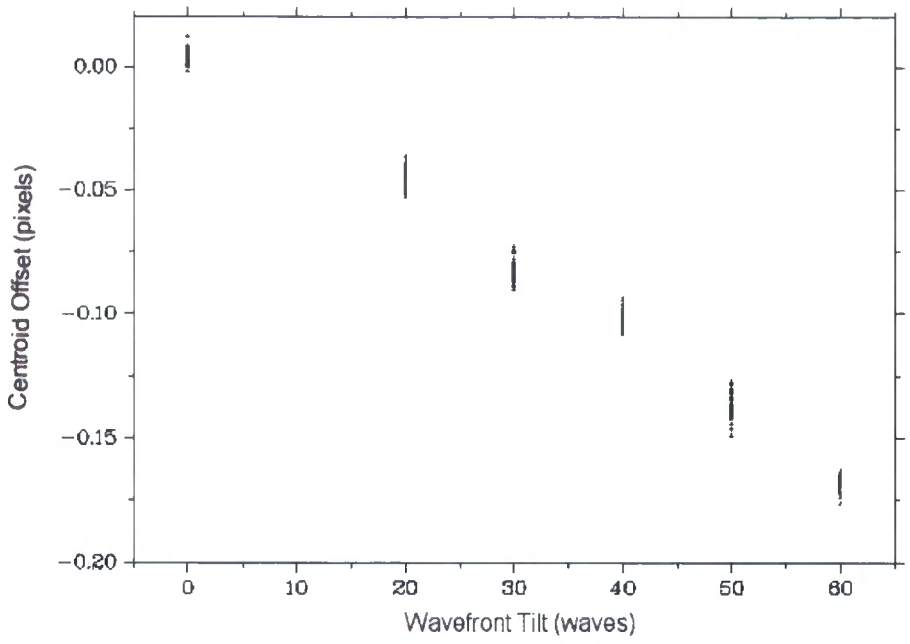

Figure 8.7 Effect of increasing vertical offset (wavefront 'tip') on recorded centroid values in the vertical plane

The centroid motion of spots in the horizontal (x-) plane was not affected by changing the wavefront tilt values as is shown in Figure 8.6, confirming that the WFS lenslet array and SLM turbulence generator were aligned accurately. The slope in Figure 8.7 was clearly linear across the range of values of wavefront slopes displayed on the SLM. A least squares fit to this plot showed a 0.00295 pixel motion for a 1-wave change in tilt across the aperture.

8.5 Control System Operation

A DSP (Digital Signal Processor) control ring interfaces the WFS to the Xinetics DM actuators. A DSP is a specialised microprocessor designed to rapidly analyse digital data, such as the digitised pixel intensities output by the WFS. The calibration of the DSP link is critical to the operation of the closed loop system. One of the most

important factors in the calibration of the AO system is the interaction matrix that measures the WFS spot motion for a known actuator motion. This matrix is produced by placing a known shape on the mirror and examining the effect of this shape on the WFS. In this way, a matrix linking actuator motion to wavefront is produced. A linear model of the WFS is assumed that links the incoming phase of the wavefront, ϕ, to the set of gradients representing the WFS measurements, S, such that

$$S = A\phi \qquad - 8.1$$

The normal method of creating the interaction matrix, A, using a SH-WFS and Xinetics DM is to increase (or decrease) each actuator value in turn by a known amount from its flat mirror value and record the corresponding effect of this aberration on the WFS. We refer to an interaction matrix produced by poking the actuators in this fashion as a pokematrix. An example pokematrix is shown in Figure 8.8.

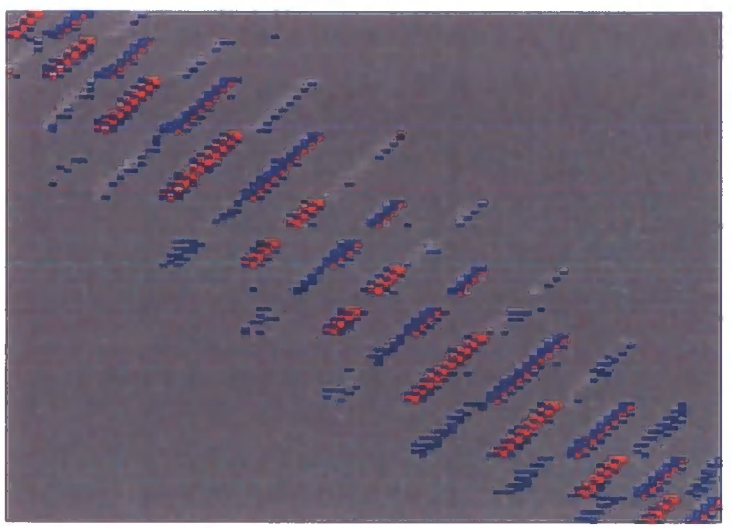

Figure 8.8 Example pokematrix with each row describing the response of the WFS subapertures to the action of a single actuator. Each pair of columns give X and Y pixel centroid motion within a single subaperture. Red pixels denote positive centroid motion in the pokematrix; blue pixels denote negative centroid motion in the pokematrix. Grey pixels denote a measured centroid motion that was less than 5% of the maximum centroid motion, effectively describing WFS channels that did not exhibit a response upon poking an actuator

The x and y motion of each spot (numbered 1 to 76) is scaled by the DAC value that each actuator has been poked by (e.g. When poking actuator 1 by a DAC value of 100, spot 1 moves in the positive x-direction by 4 pixels. The pokematrix value for actuator 1 and the spot 1 x-motion becomes 4/100). The scaling process assumes that the response of each actuator is linear over the entire range of possible actuator setting. This is not the case for voltages outside the 40 to 90 volt linear range of the DM. These voltages correspond to a pathlength change of over 15λ in a reflected beam at a wavelength of 0.5μm. Actuator values when running closed loop should not approach these limits, unless significant tilts are being corrected using the DM. From running the system closed-loop on emulated turbulence (using the holographic turbulence emulator described in Section 8.2.1), it has been seen that actuator DAC values rarely differ by more than 700 from the initial mirror DAC value of 1400. The effect of WFS noise was reduced by setting large poke values, as spot motions are larger compared to random noise motions. After scaling down by the large poke value, noise in the pokematrix was reduced.

The pokematrix in Figure 8.8 shows the response of all WFS spots to each single mirror actuator. Under closed loop operation however, we need the inverse of this information, as we measure the motion of a single WFS spot and must derive from this the motion of many actuators. The generated pokematrix (which has encoded within it measurements of the actuator response and WFS/DM co-alignment) must be inverted to give a control matrix, *B*, such that

$$\phi = BS \qquad - 8.2$$

When applied to a Xinetics DM and SH-WFS, the phase, ϕ, is described as a set of actuator values, and S, a set of wavefront slopes across each WFS subaperture. At no

point in the control loop is the true phase of the wavefront determined, with the physical surface of the DM providing the mathematical transform from actuator space to phase space. From a simple comparison of equations 8.1and 8.2, it can be seen that B is the inverse of A. As neither matrix is square, the simple inverse cannot be made and B has to be calculated by the singular value decomposition (SVD) of the interaction matrix A, creating a least-squares control matrix that minimises wavefront measurement error. A least-squares control matrix attempts to minimise the measurement error ε_m of a wavefront when a correction is applied to the DM.

$$\varepsilon_m = \|S - A\phi\|^2 \qquad \text{- 8.3}$$

Every m x n (where $m > n$) matrix, such as the actuator interaction matrix, A, has a SVD that is given by

$$A = UDV^T \qquad \text{- 8.4}$$

The process of SVD generates two orthogonal matrices, U and V, linked by a diagonal matrix, D. U is an m x n matrix and V and D are both n x n matrices. The inverse of A, which in this case is B, the system control matrix can therefore be given by

$$B = VD^{-1}U^T \qquad \text{- 8.5}$$

The inverse of the diagonal matrix D represents the gains of each of the system modes in the control loop, which themselves are represented by columns in the two orthogonal matrices U and V. High values in the inverted diagonal matrix correspond to system modes that are poorly sensed by the WFS. High values are typically one to two orders of magnitude greater than the majority of values in the inverted diagonal matrix. Setting these values to zero prevents the control system trying to correct these modes on the DM. If the large gains are not zeroed, the system could effectively

attempt to correct for random noise while ignoring the large spot motions caused by true wavefront slopes.

Figure 8.9 and Figure 8.10 show control matrices generated with no modes cancelled and the control matrix generated with the 13 poorest sensed modes removed. The matrix in Figure 8.10 somewhat resembles the original pokematrix, which is preferable as there is an obvious direct relationship between the motion of a spot and its 4 surrounding actuators. It is obvious that this relationship between actuator displacement and subsequent WFS spot motion should be dominant in both the poke and control matrices and not masked by noise within either matrix if the system is to perform well.

As further system modes are zeroed, the system becomes less sensitive to small signals on the WFS. If this is taken to the extreme and all modes are cancelled, the control system becomes insensitive to all observed modes on the WFS and the DM does not respond, irrespective of the measured wavefront. The response of the system to an input control matrix can be optimised by removing enough modes to cancel noise, but retain those modes that are associated with real WFS signals. The optimum performance point can be defined as a gain threshold in the SVD diagonal matrix. The gain threshold for a given system is dependent on optical alignment between DM and WFS, WFS SNR, closed-loop gain and calibration accuracy.

When the system is aligned in a known geometry the points in the interaction matrix where a WFS subaperture should register a motion when an actuator is displaced can be theoretically determined. One such alignment is the so-called 'Fried' geometry [5] which describes a WFS-DM alignment where an actuator is positioned at the vertex of four lenslets. A pokematrix measuring a WFS and DM in the Fried geometry sees a maximum of 4 spots only move for each actuator, and the points in the interaction

matrix where these signals will be placed are defined. This knowledge allows signals that lie outside the points of interaction to be zeroed, reducing noise, although the values in the interaction matrix would still require determination. In reality, WFS signal noise will cause errors on all the centroid positions and these will be interpreted by the control system as an actual effect of moving an actuator. Averaging spot motion over many WFS frames reduces the effect of noise on a pokematrix, but it is still a problem as can be seen by the slight variations seen in the background (grey) pixels in Figure 8.8. Further frame averaging could reduce these variations, but the generation of an interaction matrix can take a significant amount of time. During this time period, several factors that can affect the stability of the system, primarily due to temperature variations affecting both actuator response and system alignment, can reduce the accuracy of the interaction matrix, and invalidate the assumption of a linear WFS response. A theoretical mask that maps which WFS subapertures should measure a response for a given DM actuator can be placed over the pokematrix to remove spurious noise entirely, but this requires knowledge of the actuator influence functions and precise alignment between WFS and DM. A filter can also be used that zeros all small signals, but care must be taken not to zero true spot motions. Even using a masked pokematrix, genuinely affected subapertures still measure a wavefront slope that is affected by noise, and there will always be some error that propagates through to the control matrix.

AO correction of an aberrated point source was measured for a set of control matrices. The set of control matrices was created by sequentially cancelling system modes from the SVD and closing the loop on the point source. Results of this study are presented in section 8.6.2. Two example control matrices generated using the pokematrix in Figure 8.8 are presented in Figure 8.9 and Figure 8.10.

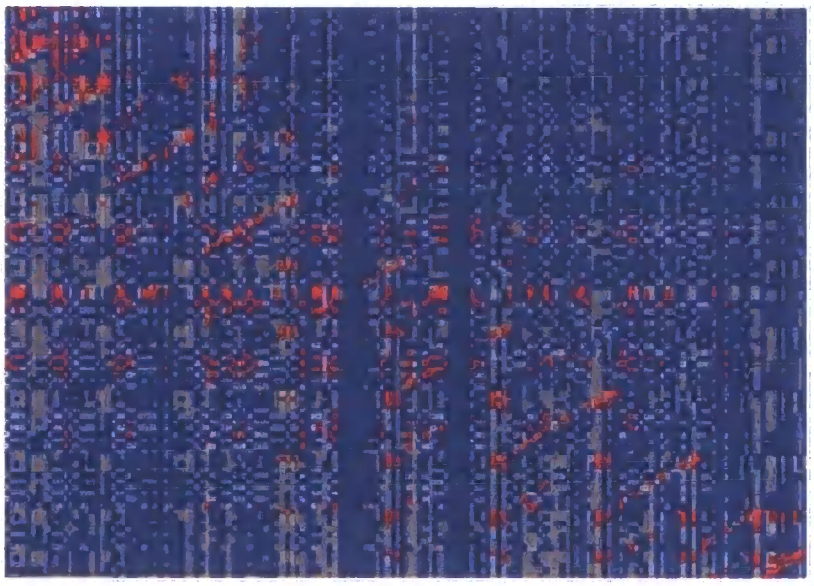

Figure 8.9 Control matrix generated by inverting the pokematrix shown in Figure 8.8. No system modes have been cancelled. Each pair of columns give X and Y pixel centroid motion within a single subaperture. Red pixels denote positive centroid motion in the pokematrix; blue pixels denote negative centroid motion in the pokematrix. Grey pixels denote a measured centroid motion that was less than 5% of the maximum centroid motion, effectively describing WFS channels that did not exhibit a response upon poking an actuator

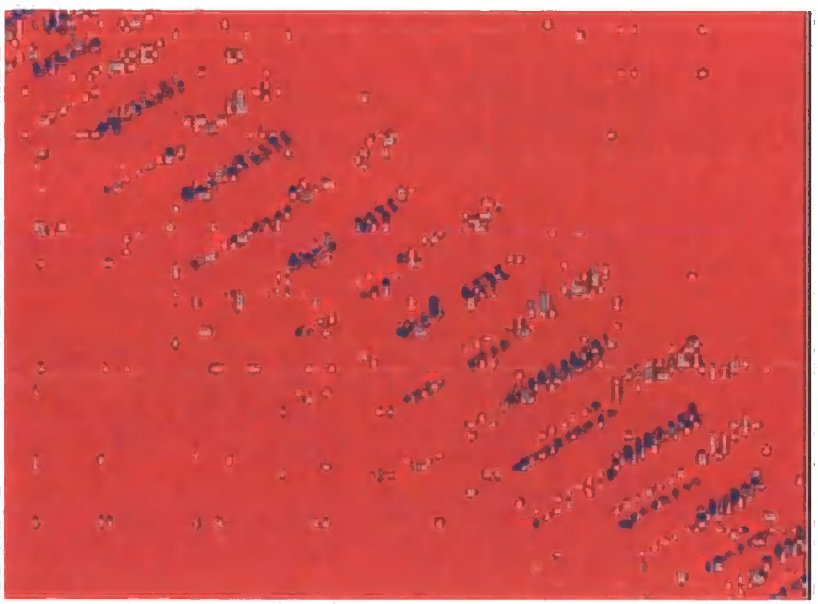

Figure 8.10 Control matrix generated by inverting the pokematrix shown in Figure 8.8. The 13 system modes with the highest gains have been cancelled. Each pair of columns give X and Y pixel centroid motion within a single subaperture. Red pixels denote positive centroid motion in the pokematrix; blue pixels denote negative centroid motion in the pokematrix. Grey pixels denote a measured centroid motion that was less than 5% of the maximum centroid motion, effectively describing WFS channels that did not exhibit a response upon poking an actuator

A qualitative visual comparison of Figure 8.9 to Figure 8.10 allows several conclusions to be drawn. The control matrix should show a clear link between WFS spot motions and actuator motion, and should therefore resemble the input pokematrix and show a set of clear points where WFS spot motion is linked to movement of an actuator. An actuator/subaperture pattern can be seen in Figure 8.9, but is masked by noise (blue pixels). By cancelling system modes with the highest gain (13 in this example), Figure 8.10 is derived. Here a clear link between WFS and DM can be seen above the background noise as demonstrated by the similarity between Figure 8.8 and Figure 8.10.

Figure 8.10 also shows that by cancelling modes, the average value of the control matrix changes. By looking down the first column, one can see that most actuators have a small positive reaction (denoted by the red pixels) to the particular spot motion the first column describes. Each iteration of the closed loop system will therefore add a small piston term to the mirror. This will quickly take the mirror to the point where the actuators become non-linear and system performance will decrease. Simply subtracting a constant offset from the control matrix would reduce the accuracy of the control matrix further, so the control system was modified to include a 'piston bleed' algorithm.

The piston-bleed algorithm worked while the loop was closed by attempting to maintain the average DAC value at the default midrange level of 1400. If the average DAC value deviated from this norm, the difference between true average and midrange was multiplied by a gain term and subtracted from all DAC outputs. This ensured that any large offsets that were built up by the non-zero average of the control matrix were removed before being displayed on the DM. Without an input calibration the piston bleed algorithm has no knowledge of actuator linearity therefore reduces

system performance. This can be minimised by reducing the piston bleed gain to the point where the piston bleed corrections are small enough that the WFS cannot observe the difference that removing the piston makes to the wavefront. This value is of the order of 10 DAC units per closed loop operation which corresponded to a 12nm actuator movement. To the author's knowledge, the use of a piston-bleed algorithm as a method for keeping the DM within its linear regime has not been suggested before.

8.6 Control System Performance

A study of the performance of the AO system under closed loop-control was made in the laboratory.

8.6.1 Single Actuator Response

A simple test of closed loop performance is to record DAC values for a single actuator when that actuator value is changed externally. Figure 8.11 demonstrates the system correcting this external change in actuator value.

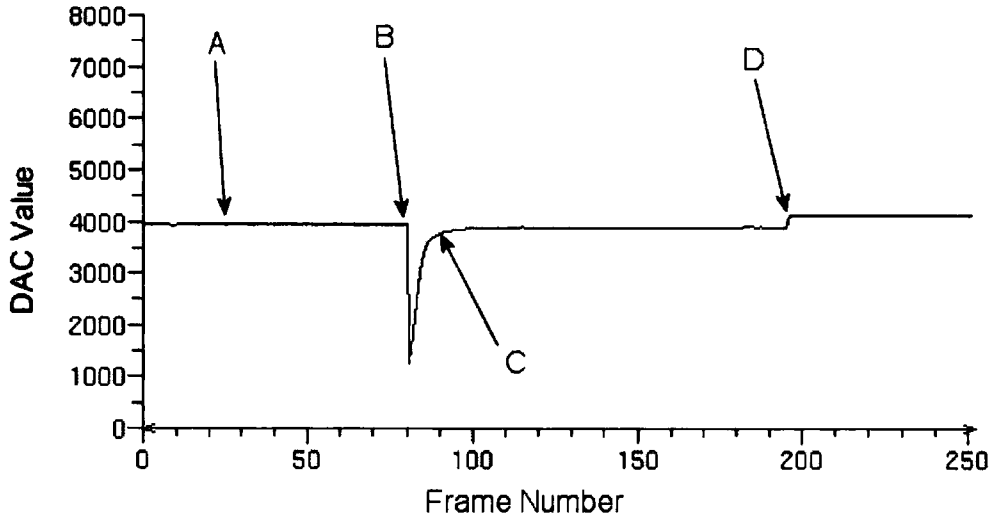

Figure 8.11 Plot of DAC Value versus WFS frame number for a closed loop run. The loop is closed at point A. The actuator value is changed externally at point B. The system corrects the actuator to return the mirror to a flat state by point C. The loop is opened at point D and the mirror reset to a global 0V. The frame rate of the system was ~300Hz. Closed Loop gain was 0.1.

As can be seen in Figure 8.11, after the actuator impulse the system does not return the actuator to its initial value, but to a slightly lower value. This shows the DM settling to a new average value, and that the poked actuator has been corrected to this new average mirror value. This demonstrates the need for a Xinetics DM to implement some kind of piston-correction. The piston-bleed algorithm had not been implemented at this stage, allowing the DM piston to float in this manner.

From points B to C in Figure 8.11 is a time period of 55ms. A correction on this timescale corresponds to a closed loop bandwidth of 18Hz, which is slow for an AO system trying to correct atmospheric turbulence. From looking at the DAC units, it can be seen that the requested DAC value of the poked actuator exceeded the voltage limit set by the zener diode, therefore the actual voltage on the actuator would have been limited to 26V, which would correspond to a DAC value of ~3000. The time taken for the actuator to change from 3000 DAC units to point C is 30ms,

corresponding to a closed loop bandwidth of 33Hz. This corresponds to the closed loop gain of 0.1 that was being used.

8.6.2 Control Matrix performance

A study of the effect of cancelling modes in the control matrix on system performance was undertaken. A set of 97 control matrices was created by decreasing the number of zeroed SVD modes from 97 (all modes cancelled) to 0 (all modes used). The loop was closed using each control matrix and the resulting AO corrected image from a non-turbulent point source was examined. Non-common path errors between the science camera and WFS had been removed, and the simplex algorithm used to maximise the science image quality.

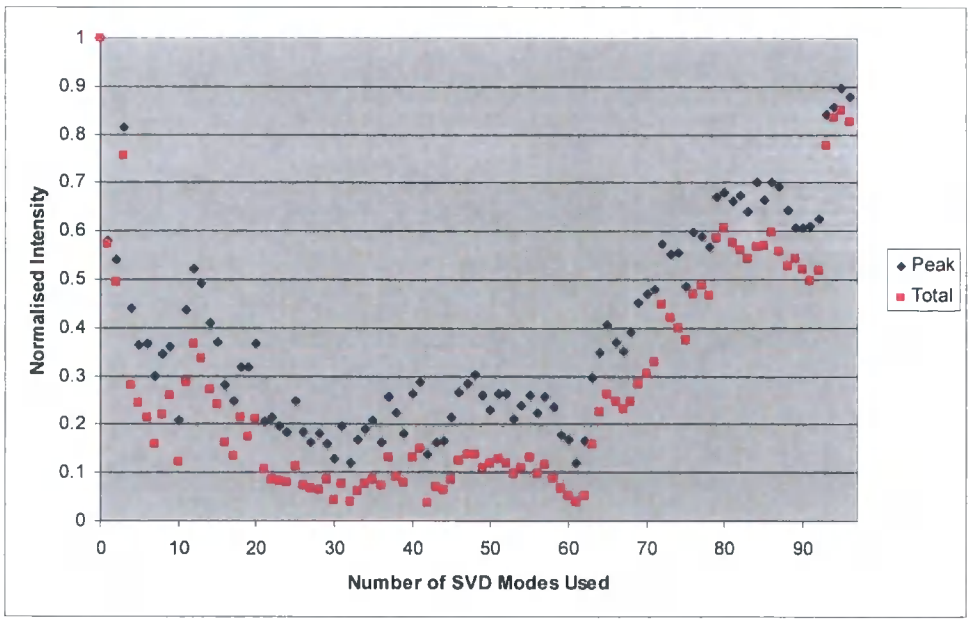

Figure 8.12 Normalised Total and Peak intensity of AO corrected science image versus number of SVD modes cancelled in the control matrix modes.

Using a bright, non-turbulent point source as a wavefront system means there is little correction for the AO system to perform. Air currents through the AO beam path will

be corrected, but the effect of these are likely to be small on output image quality. With all modes cancelled, the system has no response when the AO loop is closed. The first point plotted in Figure 8.12 therefore shows the measured peak and total intensities of the uncorrected PSF. The system should not be able to improve on the image quality of the diffraction-limited point source once the loop is closed, irrespective of control matrix used, as sources of noise in the WFS and error in the control matrix will introduce distortions, albeit small, into the wavefront. This is exhibited in Figure 8.12 as a drop in science image peak (and average) intensity between the closed-loop performance with all modes cancelled, i.e. no correction, and the best closed-loop performance achieved with only a single mode cancelled. Figure 8.12 shows that very few modes should be cancelled in order to optimise performance. These results also suggest that cancelling no modes will achieve almost optimal performance, however, an AO system using a full control matrix is highly unstable. The above experiment can only be performed with a non-turbulent, high-light level point source and requires very careful alignment of the DM to the WFS to minimise sources of noise in the system. The normal method of operation on a turbulent point source would be to start with no-modes cancelled and remove modes until the loop became stable. Using the emulated turbulent source with an r_0 of 0.14m and a frame rate of 100Hz, which corresponded to a ground layer wind speed of 5m/s, the loop was closed and remained stable using 90 modes and a closed-loop gain of 0.1.

8.7 On-sky performance

On-sky performance was to be measured at several points across the field using an IR sensitive camera at the AO-corrected feed. However, a quadrant of the WFS camera suffered a failure at the start of the observing run and could not be repaired, leaving the AO system with three quarters of a wavefront camera. The large degree of static aberrations present in the LGS WFS path also reduced the fraction of the wavefront that could be reconstructed.

The measured LGS and NGS wavefronts were reconstructed using an SOR algorithm. The average centroid offset was removed as well as the global tip and tilt across the wavefront. This removed the effects of static aberrations and differential tilts from both wavefronts. Sample NGS and LGS output wavefronts are shown in Figure 8.13

Figure 8.13 Sample LGS (left) and NGS (right) reconstructed wavefronts.

The recorded wavefront data had been synchronised by interrupting both beams twice. This also allowed the frame rates of the two WFS to be compared relative to one another. To increase SNR the exposure of the LGS WFS had been increased to 50ms. The NGS WFS was run at its maximum possible frame rate of approximately 60Hz.

A comparison was made between the two sets of WFS data to determine the correlation between the X and Y centroids returned by the LGS and NGS WFS. Global tip and tilt and static aberrations were removed from the wavefronts before comparison. Two methods for synchronising the LGS and NGS WFS frames were used. The first synchronisation method averaged the centroids from a number of NGS frames corresponding to a single LGS frame. Two or three NGS frames were averaged for each LGS frame. The second synchronisation method performed the correlation using a single NGS frame taken at the midpoint of the LGS exposure. Correlation between the X any Y centroid motion on a subaperture by subaperture basis was not observed using either synchronisation method. There are some possible reasons why the correlation between the LGS and NGS WFS frames was not observed. The most obvious of these is that the LGS WFS FOV was too restricted and vignetted the LGS. The lack of correlation could also have been due to inaccuracy in the NGS WFS, although this is less likely because the image from the NGS WFS showed a well separated spot pattern. NGS WFS SNR was not a major source of error with the 2nd magnitude star that was being used as the NGS. Another possibility is that during the course of the observations, the majority of the atmospheric turbulence was at a high altitude. This theory cannot be confirmed without knowledge of the vertical distribution of turbulence but could mask any small correlation between NGS and LGS wavefronts.

The correlation of global tilts across the wavefront was examined but also showed no instantaneous correlation between LGS and NGS tilts, but this was as predicted. For two sets of data, it was observed that the global tilt of the LGS wavefront had changed in magnitude with time from its initial value, suggesting that the LGS WFS was tracking the slow LGS drift caused by the WHT top-end sag. This is shown in Figure

8.14. The fact that the gradients of the two independent measurements are well matched lends support to this theory.

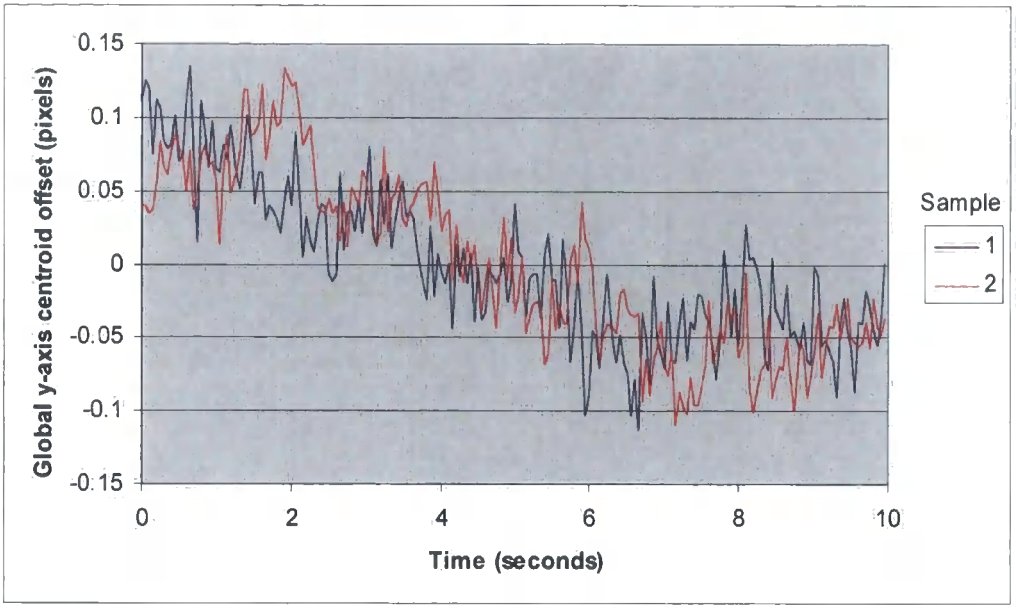

Figure 8.14 LGS WFS tracking LGS drift due to WHT top-end sag affecting pointing of the launch telescope. The time between the two sets of data being taken was approximately 5 minutes.

Figure 8.14 illustrates the problem of the restricted FOV of the LGS WFS. The global tilt changes from a value approximately 0.1 pixels to -0.1 pixels over the course of 4 seconds then stabilises. This corresponds to an LGS drift of 0.04" over this time period. The instantaneous LGS spot jitter measured from the un-range gated plume (see Chapter 4) taken using 1ms exposures showed a 3σ spot jitter of 0.5", suggesting that the LGS was vignetted and what is actually being tracked is the movement of the peak intensity of the Gaussian LGS intensity profile through the central 0.04" section of the LGS WFS FOV.

8.8 Conclusion

The on-sky performance of AO system was restricted by the limited FOV of the range gate system and no correlation was observed between the NGS and LGS centroid motion. A change in global tilt was observed for two sets of LGS WFS data that was consistent with the LGS WFS tracking the slow LGS drift caused by the top-end sag of the WHT.

Laboratory characterisation of the closed loop performance on a non-turbulent point source showed that due to effect of noise in the WFS and error in the control matrix, the corrected PSF would not match the peak intensity of the optimised PSF with the AO loop open. The effect of cancelling SVD modes in the control matrix on the closed loop performance of the AO system showed that optimum performance is achieved when a minimum number of modes are cancelled.

Open-loop calibration of the DM and characterisation of the DM electronics showed that the high-voltage signal output from one of the DAC cards was approximately 2V higher than the average DAC output across the linear range of the actuator response curve. This caused a section of the DM to become offset as voltages were increased, and this offset was observed both in an interpolated model of the DM phase surface and from interferometric data. This suggested that the major source of open loop wavefront error in the DM surface was due to the offset input voltage of the second DAC card.

A piston bleed algorithm was created to force the DM surface to move towards the midrange value once the AO loop was closed. This ensured that the DM actuators remained within their linear range and thus the control matrix remained valid.

8.9 References

1. Zadrozny, A., Chang, M.P.J.L, Buscher, D.F, Myers, R.M., Doel A.P., Dunlop, C.N., Sharples, R.M., Arnold, R.L., '*First atmospheric compensation with a linearised high order adaptive mirror – ELECTRA*', in '*ESO/OSA Topical Meeting on Astronomy with Adaptive Optics*' Ed. Bonaccini D. ESO Conf. Workshop Proc. (56) p459-468 (1999)
2. Kelly, T-L; Buscher, D.F.; Clark, P.; Dunlop, C.N.; Love, G.D.; Myers, R.M.; Sharples, R.M.; Zadrozny, A., '*Dual-conjugate wavefront generation for adaptive optics*', Optics Express, vol. 7, Issue 11, p.368 (2000)
3. '*Xinetics General Mirror Performance*', Xinetics Inc, (13/09/2005) (www.ucolick.org/~max/289C/Reading/General%20Mirror%20Performance.pdf)
4. Voitsekhovich, V.V.; Kouznetsov, D.; Morozov, D.Kh., '*Density of turbulence-induced phase dislocations*', Applied Optics LP, vol. 37, Issue 21, pp.4525-4535 (1998)
5. Fried, D.L., '*Least-square fitting a wavefront distortion estimate to an array of phase-difference measurements*', J. Opt. Soc. Am. 67, pp. 370-375, (1977)

Chapter 9: Conclusions

9.1 Introduction

The large number of systems that are currently being designed that will rely on, or can utilise, GLAO correction, means that an on-sky demonstration of a GLAO system is an event the adaptive optics community is eagerly awaiting. This work presented the design and performance of the first dedicated GLAO system to be fielded on a astronomical telescope, and the first to use the backscattered light from a very low-altitude Rayleigh LGS as a wavefront reference. This thesis also described the performance optimisation of a laboratory-based AO system upon which the GLAO design was based. Numerical simulations of the GLAO system were made to determine the theoretical system performance and provide a comparison for the tests undertaken during commissioning at the WHT.

With reference to the project aims (defined in Chapter 1), this chapter draws conclusions made as a result of the work on the demonstrator GLAO system, and describes the scientific lessons learned from the project. Finally, possible modifications to the GLAO system have been outlined that use the experiences gained during this project that will allow a further modified/upgraded system to achieve wide-field GLAO correction using a Rayleigh LGS

9.2 System Performance

An overview of the system performance is given in Table 9.1.

Parameter	Designed/ Modelled	Actual	Units	Comments
LGS				
Altitude	*4*	*3.9*	*km*	*Determined from off-axis viewing and observed return through WHT primary*
Range Gate Depth	70	N/A	m	Narrow FOV of range-gate system
LGS plume diameter at 4km	*0.65*	*0.75*	*arcsec*	*LGS plume diameter measured from off-axis obesrvations of LGS plume*
LGS spot size	>2	2.29	arcsec	Designed LGS spot size dependent on
Flux	*800*	*Unknown*	*(a)*	*Calibration of camera not possible with*
±3σ LGS spot motion	0.74	0.51	arcsec	
Output power	*5*	*3.5*	*W*	*Combined effect of LGS system throughput and thermal effects on laser*
AO System				
Frame Rate	*300*	*200*	*Hz*	*Low-light level in partially illuminated subapertures caused loop instability*
Field of view	80	80	arcsec	
LGS Throughput	*0.34*	*Unknown*		*Uncalibrated LGS WFS camera*
Wavefront Quality				
(LGS)	704	Unknown	nm (RMS)	Full reconstruction of LGS wavefront not possible using 3/4 of LGS WFS
(NGS)	492	400	nm (RMS)	Actual RMS error is twice that of DM
SVD Optimisation	*91*	*96*		*Number of SVD modes used in control*
Closed Loop performance				(with 91 SVD modes used, uncorrected
on-axis	0.21	Unknown	arcsec	Loop closed in laboratory, Unable to close
40" off-axis	0.18	Unknown	arcsec	Unable to close loop on sky
120" off-axis	0.35	Unknown	arcsec	Outside AO system FOV

Table 9.1 Designed or modelled performance compared with actual system performance (where possible) Units for (a) are in photons per subaperture per 5ms frame

The first two project aims were concerned with the laser launch system performance and the characteristics of the resulting LGS. The theoretical performance of the low-altitude GLAO system showed that across the 80" FOV of the experimental system, an LGS projected to a distance of 4km from the telescope primary optimised field uniformity when using the "standard" La Palma 3-layer atmosphere. The 5W laser and launch system design presented in Chapter 4 were capable of projecting an LGS at this altitude that would create a Rayleigh plume with a minimum apparent diameter of 0.65 arcseconds. When viewed with a 10x10 subaperture Shack-Hartmann WFS running at a frame rate of 200Hz, an average signal of 800 photons per frame would be observed if an LGS range-gate depth of 70m was used. The interaction of the laser launch system with the LGS WFS was examined in Chapter 5 and showed that even

with the restricted FOV imposed by the available lenslet array, a SH-WFS pattern that would provide stable closed loop correction was possible, and that LGS launch jitters of up to ±1" would not prevent a provide a signal that would allow the LGS fast steering loop to close. Numerical simulations of the GLAO system presented in Chapter 7 using this LGS as a wavefront reference showed that such an LGS could provide a stable wavefront reference for a closed-loop AO system. With these analyses, it was shown that the aims relating to the laser lauch system performance were met, although on-sky confirmation of several of these parameters was not possible with the equipment available for this project.

The restricted operational parameters (operating only with 60-80 degrees elevation) allowed a relatively simple launch system design. The launch system utilising both Nasmyth platforms of the WHT allowed an on-axis LGS to be created at the correct focal altitude within a few hours of going on-sky. The measured performance of the laser launch system matched the modelled performance in several areas, including LGS plume diameter near the focus, and the observed LGS launch jitter. A complete comparison of the launch system model to the actual LGS plume was not fully possible due to a malfunction of the LGS WFS CCD, low contrast ratio achieved by the passive range-gate system and large static aberrations within the system. However, as the GLAO system did not include instruments for the determination of the atmospheric C_n^2 profile, an accurate comparison of model to system performance would have had to have to been based on the assumption of the standard La Palma 3-layer atmosphere.

The GLAO system design presented in Chapter 6 allowed simultaneous NGS and LGS WFS over an 80" FOV that was restricted by the entrance aperture of the double Newtonian beam expander. The modifications that were required to allow the original

laboratory NGS AO system to be fielded on a telescope using a low-altitude LGS were extensive, necessitating a complete redesign of the system. The design presented in Chapter 6 confirmed that project aim of determining if the laboratory-based AO system could be modified had been achieved; however, the system could only provide a single 10" diffraction-limited FOV at any field point in the full 80" patrol field. The performance of the on-bench implementation of this system was impaired due to the budgetary limitations imposed on the project and did not meet the diffraction-limited optical design. A large number of surfaces had to be included within the design that reduced the system throughput and resulted in a poor quality wavefront being presented to the LGS WFS. This ultimately prevented closed-loop GLAO system verification on-sky. Assuming that suitable optical quality components could be procured, the design itself was capable of using a low-altitude LGS as a wavefront reference, thereby fulfilling the third project aim.

The final aim of the project was to determine both the theoretical and actual performance of the GLAO system itself. The system did perform closed loop correction in the laboratory and allowed control matrix performance to be investigated using a real system under controlled conditions. For a well-aligned system with little or no sources of noise within the WFS, the control matrix that generated the smallest reduction in PSF peak and total intensity when compared to the optimised (simplexed) PSF was found with only a single mode cancelled. This result was confirmed using the numerical simulation in Chapter 7, where optimum control matrix performance was found when only 2 modes were cancelled, albeit with a much higher closed-loop gain than was achieved with the laboratory system. The similar effect of cancelling modes in the modelled and actual SVD's show that the performance of the laboratory-

based AO system matched the response of the modelled system in terms of system stability and optimisation techniques.

Closed loop simulations of the GLAO system demonstrated that a higher SNR than predicted from the inclusion of WFS read noise only in the simulation was required when the effects of seeing within a subaperture were simulated. This necessitated reducing the frame rate of the LGS WFS from 300Hz, as was originally planned, to 200Hz. Using the standard La Palma atmosphere and values of r_0 ranging between 0.11m and 0.19m, corresponding to 75^{th} and 25^{th} percentile seeing on La Palma, showed the FWHM of the corrected PSF was approximately half that of the uncorrected PSF, although the associated improvement in Strehl ratio was minimal. The Strehl ratio only shows large improvements when describing near diffraction limited performance. The GLAO corrected PSF was still far from diffraction limited as was seen from the simulated PSFs shown in Chapter 7.

The interpolated model of the Xinetics DM that was used was, to the author's knowledge, a novel method for rapidly generating a DM surface within a closed loop numerical simulation. Modelling of a Xinetics DM within simulations is usually achieved using simplistic linear models, or a modal representation of the DM, but these do not model the fitting error of a Xinetics DM with the accuracy of the interpolated DM. As was noted within the text, the accuracy with which the interpolated DM matches Xinetics DM performance will be further compared with alternative DM models to determine the benefits of this method.

Several results of this project have directly influenced the design of the facility-class Rayleigh laser system for the WHT called GLAS (Ground Layer Adaptive optics System). The unpolarised photon return observed during one night of the AO run necessitated modifications to the GLAS launch and range gate systems, which had

assumed that the linearly polarised light output by the laser would be preserved on return into the shutter system. The experience gained using the demonstrator system on-sky has proved invaluable in many areas of GLAS system design and modelling. The models used in the work have also been used to simulate GLAS performance and determine the system error budget.

The LGS WFS model presented in Chapter 5 has also formed the basis for a design study commissioned by ESO to examine the feasibility of performing GLAO correction for the MUSE spectrograph and HAWK-I NIR imager using Rayleigh beacons.

The presented system design was capable of fulfilling all the project aims as defined in Section 1.3, but was let down by poor-quality optics, a lack of telescope commissioning time and the inter-dependence of characterisation tests on system components (requiring the LGS range gate system to work before the LGS spot size could be determined is an example of this problem). As such, the project aims were all met to differing degrees of success. Many of the difficulties that were encountered on-sky would have been discovered and investigated if extensive system testing had been performed in a laboratory environment, proving the need for adequate testing when commissioning a complex instrument such as this.

9.3 System Development

After the final LGS GLAO run, the decision was made to upgrade the AO system to create a more general LGS AO system test-bed for the WHT. Testing new LGS concepts is essential to the development of LGS AO systems for proposed ELT AO

systems. A conceptual design was made, drawing on experiences gained from using and aligning the laser launch system and demonstrator AO system.

With the failure of the WFS camera, a new gated CCD is being procured to allow the LGS WFS system to be greatly simplified through the removal of the Pockels cell shutters. The double Newtonian beam collimating/focusing system is also being replaced with a single, large, parabolic mirror that will greatly increase the ease of alignment and the FOV of the demonstrator system. A new LGS/NGS dichroic beamsplitter is being purchased that has excellent transmitted and reflected wavefront quality. The proposed system will have a very high throughput to both the LGS and NGS WFSs, allowing the altitude of the LGS to be increased or range gate depth reduced. The wide field of view of the conceptual design will also allow off-axis data to be collected with far greater ease. An integrated SLODAR turbulence profiler is also being included in the system to provide a real-time atmospheric C_n^2 profile for system analysis.

This work has shown that a low-altitude LGS will not perform as well as a rotating LGS, and with the purchase of a high-power laser for the GLAS project, the concept of wide-field correction using a low-altitude LGS for GLAO is being abandoned, at least for the future of this project. The GLAS laser launch system will be modified to create a rotating LGS at a distance of 20km from the WHT primary and therefore should match the performance of the rotating LGS presented in Chapter 7. The GLAS laser also has a fully engineered launch system that will automatically compensate for the WHT top-end sag, reducing one of the major difficulties discovered during LGS tests. The upgraded AO system, using a rotating LGS created using the GLAS laser launch system should achieve substantially flat field correction across the entire WHT Nasmyth field of view.

This project has confirmed that commissioning an LGS AO system requires a lot of dedicated telescope time. Although the time allocated to the project by the ING has been very generous, the total time on-sky used for this project was approximately 6 full nights of telescope time (over the course of 4 years), which is not long enough to fully commission and characterise such a LGS-based GLAO system such as this.